Study of GdBaCo2-xMxO5+δ (M=Ni, Fe; x = 0, 0.1, 0.2,...) as new cathode materials for IT-SOFC application

Yang Hu

ÉCOLE CENTRALE DES ARTS
ET MANUFACTURES
« ÉCOLE CENTRALE PARIS »

THÈSE
présentée par

HU Yang

pour l'obtention du

GRADE DE DOCTEUR

Spécialité : Science des Matériaux

Laboratoire d'accueil : Structures Propriétés et Modélisation des Solides
UMR 8580 CNRS / Ecole Centrale Paris

SUJET :

Study of $GdBaCo_{2-x}M_xO_{5+\delta}$ (M=Ni, Fe ; x = 0, 0.1, 0.2, …) as new cathode materials for IT-SOFC application

Soutenue le : 25 mars 2011

Devant un jury composé de :

M. Gilles CABOCHE	Professeur à l'Université de Bourgogne	Président
M. Alain THOREL	Maître de Recherche à Mine Paris	Rapporteur
Mme. Rose Noëlle VANNIER	Professeur à L'ENSCL	Rapporteur
M. Guilhem DEZANNEAU	Chargé de recherche à ECP	Directeur de thèse

Numéro d'ordre : 2011ECAP0017

Acknowledgements

This work has been done in Laboratoire Structures Propriétés et Modélisation des Solides (SPMS) of the Ecole Centrale Paris (ECP) and Centre National de la Recherche Scientifique (CNRS, UMR 8580), with financial support from China Scholarship Council (CSC).

I would like to express my gratitude to my thesis supervisor, Professor Guilhem DEZANNEAU, whose guidance, encouragement, and instructing have extremly helped and inspirited me.

I would also like to sincerely thank M. G. CABOCHE, Professor of the University of Bourgogne, for accepting to be the referees of my thesis. I would also like to sincerely thank Mme. R.N. VANNIER, Professor of the University of Lille, and M. A. THOREL, Maître de recherche of University of Paris Mines for accepting as the examiners of my thesis.

I am also very grateful to the fellow students of our group: Emile Bévillon, Marc-david Braida and Yanzhong Wang, for their valuable helps and advices, as well as all the joyful time we have spent together. I would also like to thank Jean-Michel KIAT, the director of Labo SPMS, and professors Brahim DKHIL and Maud GIOT, for their encouragement, help and kind attention.

I would also like to thank the laboratory engineers and technicians: Christine BOGICEVIC and Fabienne KAROLAK for their help in chemistry related experiments, Gilles BOEMARE for the very time-costing TGA/TG measurements, Jacques CHEVREUL and Nicolas GUIBLIN for XRD, Françoise GARNIER for SEM, and other people like Thierry MARTIN, Agnès BÉNARD, Fabien DEBRAY, Obadias MIVUMBI, Claire ROUSSEL. Thanks to their great help I could accomplish all the experiments of thesis.

I am thankful to M. Jean-Hubert SCHMIT, the director the research department of ECP, who has helped me to find financial support of the postponing period, as well as Geraldine

CARBONEL and Catherine LHOPITAL from the secretariat de l' Ecole doctorale for their help, encouragement and kind attention.

I am eternally grateful to my family. My parents have contributed me with their confidence and forever support. Thanks to you, I could passed the most difficult time and come to this accomplishment.

Résumé

Etude de $GdBaCo_{2-x}M_xO_{5+\delta}$ (M = Ni, Fe ; x = 0, 0.1, 0.2,…) comme nouveaux matériaux de cathode pour l'application de IT-SOFC

$GdBaCo_2O_{5+\delta}$ a été présenté récemment comme un matériau de cathode potentiel pour pile à combustible à oxyde solide. Cependant, sa réactivité chimique avec la zircone yttriée et son fort coefficient de dilatation constituent une limite importante à son utilisation. L'objet de ce travail est l'étude des composés $GdBaCo_{2-x}M_xO_{5+\delta}$ (M = Ni, Fe, x = 0, 0.1, 0.2…) i.e. substitués au fer et au nickel pour objectif d'améliorer les propriétés du composé original pour l'application pile à combustible. Tout d'abord, différentes méthodes de synthèse ont été essayées et comparées, les méthodes par voie chimique montrant un net avantage pour l'obtention de taux de substitution élevés. Les propriétés physico-chimiques des matériaux synthétisés ont été caractérisées. Si la structure des composés évolue avec la nature et le taux du substituant, les propriétés de ces composés en termes de conduction électronique ou d'évolution du contenu en oxygène sont relativement constantes. Finalement, les performances électrochimiques de plusieurs compositions sous forme d'électrodes poreuses ont été testées avec différents types d'électrolytes. Les résultats montrent que la substitution n'apporte rien pour ce qui concerne la dilatation des composés et par ailleurs ne semble pas améliorer significativement les performances électrochimiques.

Mots-clés: SOFC, $GdBaCo_2O_{5+\delta}$, substitution, synthèse, conduction, électrochimique, transport

Abstract

Study of $GdBaCo_{2-x}M_xO_{5+\delta}$ (M=Ni, Fe; x = 0, 0.1, 0.2,…) as new cathode materials for IT-SOFC application

$GdBaCo_2O_{5+\delta}$ has been recently introduced as a potential cathode material for solid oxide fuel cell. However, its utilization has been strongly limited by its chemical reactivity with yttrium-stabilized zirconia and its significant thermal expansion coefficient. This work focus on the study of compounds $GdBaCo_{2-x}M_xO_{5+\delta}$ (M = Ni, Fe, x = 0, 0.1, 0.2…) i.e. substituted by Ni or Fe in order to ameliorate the properties of original composition for fuel cell application. Firstly, different synthesis methods have been attempted and compared, and the chemical routes showed a clear advantage for obtaining high substitution proportion. The physico-chemical properties of synthesized materials have been characterized. The structure of these compounds evolves with the substitution nature and proportion, while their properties such as electrical conductivity or changes in the oxygen content are relatively constant. Finally, the electrochemical performances of several compositions serving as porous electrodes were tested with different types of electrolytes. The results exhibit that the substitution neither shows evident influence with respect to the thermal expansion of these compounds, nor significantly improves their electrochemical performance.

Keywords: SOFC, $GdBaCo_2O_{5+\delta}$, substitution, synthesis, conduction, electrochimical, transport

Table of contents

Chapter 1 Introduction

1.1 Fuel cells

1.1.1 Principles

The chemical energy stored in hydrogen and several hydrocarbon fuels is significantly higher than that found in common battery materials. This fact provides the impetus to develop fuel cells for a variety of applications, as well as the concerning of environmental consequences of fossil fuel utilized in modern industry. Fuel cells are an ideal primary energy conversion device for remote site locations and find application where an assured electrical supply is required for power generation, distributed power, remote, and uninterruptible power [1].

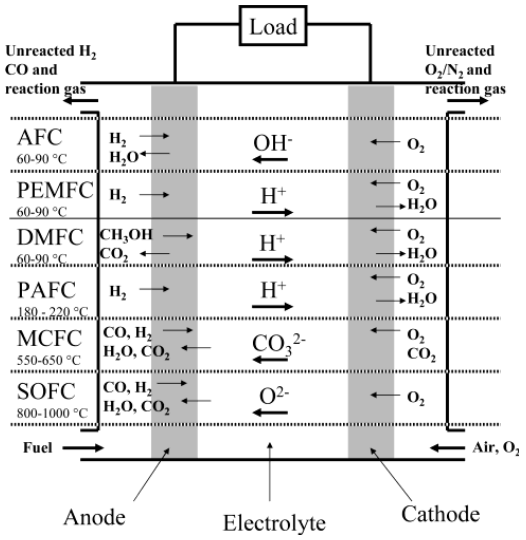

Figure 1.1 *Summary of the reactions and processes that occur in the various fuel cell systems [2].*

The basic physical structure of a fuel cell consists of an electrolyte layer in contact with a porous anode and cathode on either side. The fuel or oxidant flows through the anode or cathode, and generates electrical energy by the electrochemical oxidation of the fuel and the electrochemical reduction of the oxidant. Figure 1.1 depicts a schematic representation of various functional fuel cells with the reactant/product gases and ion-conduction trough the cells. Apart from batteries, the fuel and oxidant are not contained within the fuel cell component but supplied continuously from an external source. As long as the fuel and oxidant are fed in the system, the energy conversion process should theoretically remain persistent.

Fuel cells are quiet in operation and can be located close to the application. They produce much less green house emissions and can be more efficient in conversion of chemical energies in a fuel into

power than gasoline engines or utility thermal power plants. From an operational point of view, the fuel of choice is hydrogen gas, with the exhaust gas being water, which makes fuel cells the possible cleanest power generation. Moreover, fuel cells have been considered as a nearly ideal solution for the segments having significant incentives to develop alternate power sources, such as motor vehicle manufacturers, utility and nonutility generators, and portable devices. The comparison of advantages and disadvantages in fuel cell technologies is given below [2]:

Advantages:	*Disadvantages:*
Efficient energy conversion	Complex to operates
Modular construction	Best as primary energy source
Non-polluting	Impurities in gas stream shorten life
Low maintenance	Pulse demands shorten cell life
Silent	Expensive
Safe	Limited availability
High energy density	Lower power density per volume

Operating fuel cells are complex chemical plants that require sophisticated manufacturing techniques and control circuitry. Although nowadays, several fuel cell technologies are reaching technical maturity, the economics of a fuel cell stay unclear. The commercial potential of fuel cells is strongly limited by the costs of catalyst and other expensive materials used, as well as the cost for manufacturing the units.

1.1.2 Thermodynamics and efficiences

The overall electrochemical reaction of a fuel cell consists of two half-cell reactions taking place at anode and cathode, respectively, as can be described in Eq. 1.1:

$$aA + bB \rightarrow cC + dD \tag{1.1}$$

where the equilibrium potential E^0 of each half-cell reaction is given by the Nernst Equation:

$$Ox + ne^- \rightarrow Red \tag{1.2}$$

$$E^0 = E^\phi + \frac{RT}{nF} ln \frac{[ox]}{[red]} \tag{1.3}$$

E^ϕ: standard electrode potential

[*red*]: concentration of reducing species

[3]: concentration of oxidising species

n: number of electrons transferred per mole of reactants

R: gas constant

F: Faraday constant

The equilibrium voltage of the cell ΔE_0 is represented by the difference between the two half-cell reactions in the absence of current by Eq. 1.4, and the Gibbs free energy change of the chemical reaction is related to the cell voltage:

$$\Delta E_0 = E_C^0 - E_A^0 = E_C^\phi - E_A^\phi + \frac{RT}{nF}\frac{[C]^c[D]^d}{[A]^a[B]^b} \tag{1.4}$$

$$\Delta G = -nF\Delta E = \Delta H - T\Delta S \tag{1.5}$$

where ΔG is Gibbs free energy, ΔH is the enthalpy, ΔS is the entropy, with $T\Delta S$ being the heat associated with the organization/disorganization of materials.

The thermodynamic equilibrium potential described by the Nernst equation is an ideal case. Even under OCV condition, the mixed potential formation or other parasitic processes can make voltage of a fuel cell lower than the thermodynamic value [4]. Under actual operating condition, when a current flows, a deviation from the OCV occurs, which corresponds to electrical work performed by the cell. This deviation from the equilibrium value is called overpotential η, given by:

$$\eta = E_{OCV} - E_W \tag{1.6}$$

where E_{OCV} is the voltage of the cell at OCV and E_W is the terminal cell voltage with current I flowing. For a redox reaction at one electrode current density can be given by the Butler-Volmer equation:

$$i = i_0\left\{exp\left(\alpha_A F\eta / RT\right) - exp\left(-\alpha_C F\eta / RT\right)\right\} \tag{1.7}$$

i_0: exchange current density

α_A, α_C: transfer coefficients for the anodic (A) and cathodic (C) reaction

η: the overpotential driving the reaction

For a practical point of view, many other factors are also responsible for the potential losses, such as the electrolyte resistance, concentration polarisation from limited mass transport capabilities, the conductive diluent, current collectors, terminal, and contact between particles of the active mass, which could give rise to the ohmic polarisations. By considering the sum of resistances at cathode, anode and electrolyte as an internal resistance R, the cell voltage ΔE can be written as:

$$\Delta E = \Delta E_0 - Ri + \eta_C(i) - \eta_A(i) \tag{1.8}$$

Figure 1.2 schematically depicted the cell voltage, and a power density versus current density plot is shown as a useful representation from comparing different fuel cells [1,4]. It can be noticed that the overpotential losses are much higher at the cathode, due to slower kinetics of oxygen reduction reaction compared to the oxidation reaction of fuels at anode.

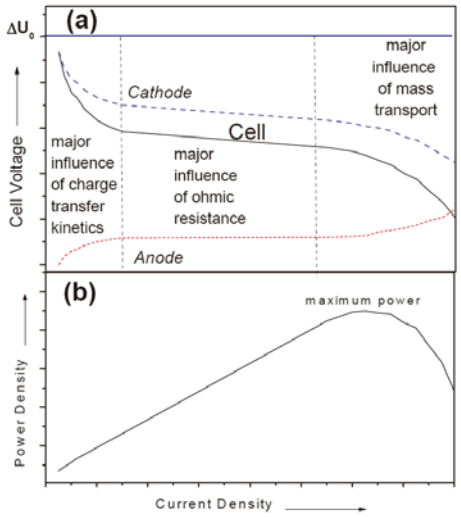

Figure 1.2 *Schematic of (a) fuel cell voltage, anode and cathode overpotentials versus current density (b) power density versus current density* [4]

One highlight of fuel cell technology is the high efficiency compared to traditional power generation systems. Take the combustion engines for instance, which converts chemical energy (heat) into mechanical energy or further electrical energy by using a rotating generator. In this system, the combustion of hydrocarbon is exothermic reaction which results in a rise in temperature, and the usual products are gases. The maximum efficiency is given by a theoretical thermodynamic derivation of the Carnot-Cycle, ε_E as follows:

$$\varepsilon_E = \frac{W_r}{(-\Delta H)} = \frac{T_1 - T_2}{T_1} \tag{1.9}$$

W_r: reversible work performed

ΔH: enthalpy change of the reaction

T_1, T_2: two absolute temperatures for the expiration of the heat engine (T_1,>T_2)

It shows that the maximum efficiency depends only on the temperature of the two thermal sources and decrease by lowering the temperature of thermal sources. Even under ideal conditions, this kind of systems cannot convert all the heat energy from combustion into mechanical energy. In general, these

efficiencies are beneath 40%-50% for most cases [5], and can reach to 85% with application of co-generation of heat and power.

On the other hand, fuel cell process is electrochemical and the maximum efficiency can be represented from the Gibbs free energy (ΔG) and the enthalpy change (ΔH) of the electrochemical reaction:

$$\varepsilon_{FC} = \frac{W_{el}}{(-\Delta H)} = \frac{nF\Delta E}{(-\Delta H)} = \frac{\Delta G}{\Delta H} = 1 - \frac{T\Delta S}{\Delta H} \tag{1.10}$$

where W_{el} is the maximum electrical work in a fuel cell operation for a constant temperature and pressure. In contrast to combustion engine, a decrease in temperature causes an increase in thermodynamic efficiency. Ideally speaking, the free energy of the reaction can be completely converted into electrical energy. In practice, in addition to the dependency of efficiency on the fuels and oxidants applied, the electrode overpotentials and electrolyte resistance prevent from obtaining the efficiency close to ideal value ε_{FC} = 1. However, intrinsically, fuel cells exhibit attractive thermodynamic efficiencies superior to those of combustion engines, approaching 60-70% even up to 90% in case of re-utilization of waste heat.

1.1.3 Various types of fuel cells

Fuel cells are typically classified by the type of electrolyte employed in the cell. The five major types of fuel cells are alkaline fuel cell (AFC), polymer electrolyte membrane fuel cell (PMEFC), phosphoric acid fuel cell (PAFC), molten carbonate fuel cell (MCFC), and solid oxide fuel cell (SOFC), as well as an exception to this classification: direct methanol fuel cell (DMFC), in which methanol is directly fed to the anode and electrochemically oxidized. A second grouping can be done according to the operating temperature for each of the fuel cell. An overview of the fuel cell types is presented in order of increasing operating temperature in Table 1.1 [1,4,6-9].

	Electrolyte	Charge carrier	T (°C)	Electrochemical reaction A: anode C: cathode Ce: cell	Application	Realised Power
AFC	KOH solution in a matrix	OH^-	<100	A: $H_2 + 2OH^- \rightarrow 2H_2O + 2e^-$ C: $1/2O_2 + 2H_2O + 2e^- \rightarrow 2OH^-$ Ce: $1/2O_2 + H_2 \rightarrow H_2O$	Transportation Space Military Energy storage	Small plants 5-150 kW modular

					systems	
PEMFC	Hydrated polymeric ion membrane exchange	H^+	60-120	A: $H_2 \rightarrow 2H^+ + 2e^-$ C: $1/2O_2 + 2H^+ + 2e^- \rightarrow H_2O$ Ce: $1/2O_2 + H_2 \rightarrow H_2O$		Small plants 5-250 kW modular
DMFC		H^+	60-120	A: $CH_3OH + H_2O \rightarrow CO_2 + 6H^+ + 6e^-$ C: $3/2O_2 + 6H^+ + 6e^- \rightarrow 3H_2O$ Ce: $CH_3OH + 3/2O_2 \rightarrow CO_2 + 2H_2O$		Small plants 5 kW
PAFC	H_3PO_4 soaked in a matrix	H^+	160-220	A: $H_2 \rightarrow 2H^+ + 2e^-$ C: $1/2O_2 + 2H^+ + 2e^- \rightarrow H_2O$ Ce: $1/2O_2 + H_2 \rightarrow H_2O$	Combined heat and power for decentralised stationary power systems	Small-medium sized plants 50 kW-11 MW
MCFC	Li_2CO_3, KCO_3, $LiAlO_3$	CO_3^{2-}	600-800	A: $H_2 + 2CO_3^{2-} \rightarrow H_2O + CO_2 + 2e^-$ C: $1/2O_2 + 2CO_2 + 2e^- \rightarrow CO_3^{2-}$ Ce: $1/2O_2 + H_2 + CO_2 \rightarrow H_2O + CO_2$	Combined heat and power for stationary decentralised systems and for transportation (trains, boats, …)	Small powder plants 100 kW-2 MW
SOFC	Ceramic ionic conductor	O^{2-}	600-1000	A: $H_2 + O^{2-} \rightarrow H_2O + 2e^-$ C: $1/2O_2 + 2e^- \rightarrow O^{2-}$ Ce: $1/2O_2 + H_2 \rightarrow H_2O$		Small power plants 100-250 kW

Table 1.1 Different types of fuel cells which have been realized and currently in use and development

1.2 Solid oxide fuel cells (SOFCs)

1.2.1 Principle and components

Solid oxide fuel cells (SOFCs) are complex electrochemical devices that contain a dense electrolyte which is sandwiched between a porous anode and a porous cathode, as a single cell shown in Figure 1.3. Fuel is fed to the anode, undergoes an oxidation reaction releasing electrons to the external circuit. Oxidant, normally oxygen or air, is fed to the cathode and accepts electrons from the external circuit to accomplish a reduction reaction. The electron flow in the external circuit from the

anode to the cathode generates direct-current electricity, whilst the oxygen ions travels trough the electrolyte. Ideally, to obtain high current and to minimize voltage losses, fast reaction rates, high fluxes of molecules, ions and electrons are required. An individual cell can produce ~1 V on open circuit and ~0.6-0.7 V under load, as well as power of the order of 1 Wcm^{-2}. Multiplied cells can be combined to form fuel cell stacks providing higher power and output voltage appropriate for a particular applications. With the facility for modifying and adapting the cell configuration, stack designs, manufacturing processes and power plant sizes, SOFC technology is considered as the only type of fuel cells covering such a broad spectrum of power generation application [8].

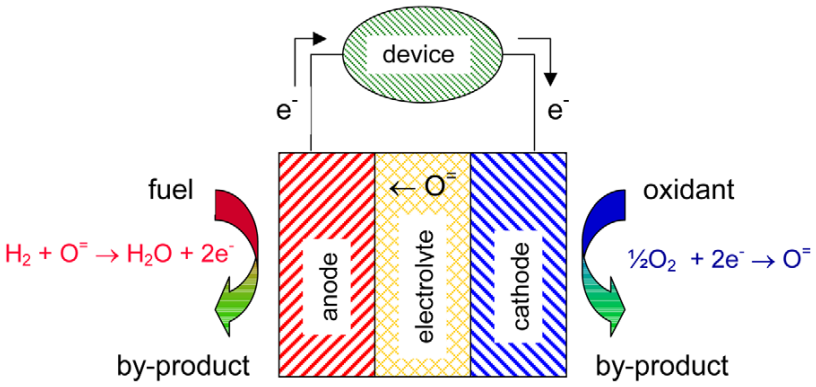

Figure 1.3 *Schematic of a electrolyte supported single SOFC cell [10]*

The brief requirements for the SOFC components in a single cell which operates at 700 °C are summarized below:

	Ionic conductivity (S cm^{-1})	Electronic conductivity (S cm^{-1})	Stability under atmosphere (atm)	Microstructure
Electrolyte	$\geq 10^{-2}$	void	$10^{-21} \leq P_{O_2} \leq 0.21$	dense
Cathode	$\geq 10^{-2}$	≥ 100	0.21	porous
Anode	$\geq 10^{-2}$	≥ 100	$\approx 10^{-21}$	porous

Table 1.2 Specifications for the material properties in SOFC single cell operating at 700 °C [11].

- Electrolytes

The most important requirement for an electrolyte material is the high ionic conductivity, as well as low electronic conductivity, stability in both oxidizing and reducing environments over a large range of oxygen partial pressure, good thermal and mechanic properties, and long-term stability with

respect to the dopant segregation. The mostly widely investigated families of electrolyte materials for SOFCs are the yttria-stabilized zirconia (YSZ), strontium, magnesium-doped lanthanum gallate (LSGM), and gadolinium- or samarium-doped ceria (CGO or SDC). Conductivity data of a broad range of materials are summarized in ***Figure 1.4*** [10]. The YSZ family is classically used at high temperatures (900-1000 °C) showing good ionic conductivity and mechanic properties, however their conductivity decreases significantly at lower temperature [12,13]. LSGM has higher ionic conductivity than YSZ, but its application is limited by the high price of gallium and elevated fabrication temperature. Ceria doped with rare earth metals has drawn considerable attention as an alternative electrolyte due to its highest conductivity a lower temperature range [13-15]. However, it is well known that at elevated temperature the reduction of Ce^{4+} to Ce^{3+} in reducing condition prevailing in the anode compartment gives rise to the introduction of electronic conductivity or/and deleterious lattice expansion thereby diminishing the fuel cell efficiency [16,17], nevertheless, this electronic conductivity become small and can be neglected if the operating temperature is lowered below 500 °C under typical fuel cell conditions [18,19].

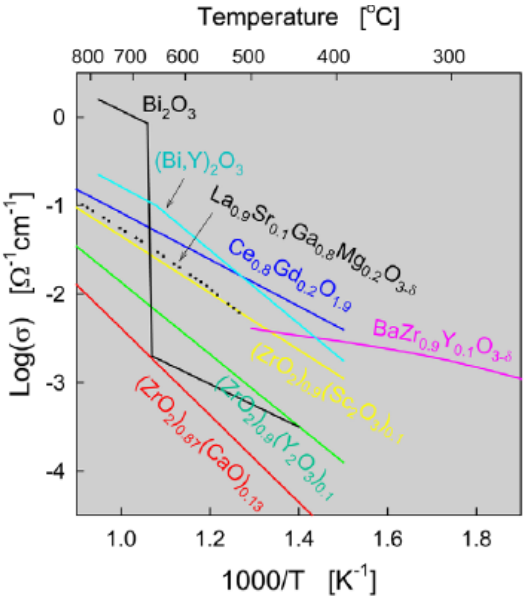

Figure 1.4 *Conductivities of selected electrolyte materials* [10]

As well, Table 1.3 listed the typical TEC values of the state-of-the-art solid oxide electrolytes in air condition, which can be used to evaluate the mechanical and thermal mechanical suitability of other fuel cell components providing a brief guidance for the materials thermomechanical compatibility. Compared to YSZ, doped ceria and transition metal substituted gallates exhibit moderately higer thermal expansions, especially Gd-doped ceria. Although, the thermal expansion of porous electrode layers can be optimized to match that of electrolytes by cell possessing and

configuration, the use of electrode materials having TECs higher than $15\sim17\times10^{-6}$ K^{-1} leads to insufficient stability and thereby reduce the fuel cell performance.

Composition	T (K)	TEC ($\times10^{-6}$ K^{-1})	Ref.
$Zr_{0.9}Y_{0.1}O_{2-\delta}$	300-1273	11	[20]
$Zr_{0.92}Y_{0.08}O_{2-\delta}$	300-1273	10.0	[21]
$Zr_{0.85}Y_{0.15}O_{2-\delta}$	300-1273	10.9	[20]
$Ce_{0.9}Gd_{0.1}O_{2-\delta}$	300-1100	13.4 ± 0.1	[22]
$Ce_{0.85}Gd_{0.15}O_{1.925}$		11.6	[23]
$Ce_{0.80}Gd_{0.20}O_{2-\delta}$	300-1100	11.8 ± 01	[22]
$Ce_{0.80}Gd_{0.18}Pr_{0.02}O_{2-\delta}$	300-1050	11.5 ± 0.1	[24]
$La_{0.9}Sr_{0.1}Ga_{0.8}Mg_{0.2}O_{2.85}$	300-1273	11.6	[25]
$La_{0.8}Sr_{0.2}Ga_{0.8}Mg_{0.2}O_{3-\delta}$	300-1273	11.4	[25]
$La_{0.8}Sr_{0.2}Ga_{0.76}Mg_{0.19}Co_{0.05}O_{3-\delta}$	300-1473	12.7	[26]
$La_{0.9}Sr_{0.1}(Ga_{0.9}Co_{0.1})_{0.8}Mg_{0.2}O_{3-x}$	300-1273	13	[25]
$Ce_{0.83}Sm_{0.17}O_{1.915}$		8.6	[27]
$Ce_{0.8}Sm_{0.12}O_{1.9}$	300-1173	11.4	[28]
$Ce_{0.8}Sm_{0.1}Mg_{0.1}O_{2-\delta}$	473-1073	12.34	[29]

Table 1.3 Average linear thermal expansion coefficient of currently used solid oxide electrolytes in air

- Electrodes

Electrodes are critical issues in SOFCs since they provide the interfaces between the chemical energy associated with fuel oxidation and electrical power. For both anode and cathode, high electrocatalytic activity and electronic conductivity are required to diminish the effective resistance, especially for cathode which is responsible for the major contribution to the cell voltage losses. Besides, the electrodes must be mechanically and chemically stable. The thermal expansion of electrodes should match that of electrolyte and current collector in order to obtain stable interfaces and avoid the thermal and fatigue stress which could effectively influence the fuel cell performance [30,31].

Moreover, the chemical compatibility of electrode materials with respect to the electrolyte and current collector as well as the stability of microstructure to maintain high specific surface areas and porosity under operating conditions, are also relevant issues. Various types of materials for SOFC electrode application have been summarized in detail in some reviews [10,32-37].

- Interconnectors

It is evident that the potential commercialization of SOFCs is highly limited by the expensive costs of interconnector materials employed at high temperature. The interconnectors form the connection between the anode of one cell and the cathode of the next in a stack arrangement [4]. It must have a good electronic conductivity and negligible ionic conductivity and meanwhile seal the gas chambers for the feed of fuel and oxidant gases at electrodes. The interconnector must have a thermal expansion coefficient (TEC) close to those of the other cell components to minimize thermal stresses, and include adequate mechanical strength, low permeability to oxygen and hydrogen, as well as reasonable thermal conductivity. In addition, cost-effective manufacture of fuels cells requires that the interconnect materials be easy to fabricate. The choice of interconnector materials is dependent on the stack design and majorly on the operating temperature. Ceramic interconnect materials which are oxides such as $LaCrO_{3-\delta}$ system [38,39], and are thus stable in oxidizing atmospheres, but typically have lower electrical conductivities as compared to metals. Lowering the operating temperature allows a switch from ceramic to metallic interconnects by effectively diminishing the oxidation rates for metals at the cathode side, showing remarkable advantages such as higher electrical and conductivity, negligible ohmic loss, low cost and easy manufacture [13,38,40,41].

Generally speaking, the combined area-specific resistivity of the cell components (electrolyte, anode and cathode) should be below 0.5 Ω cm^2 (and ideally approach 0.1 Ω cm^2) to ensure high power density aiming to the value of 1 kWdm^{-3} and 1 kW kg^{-1} as widely mentioned for transport application [42].

1.2.2 Advantages and challenges

Among those different types of fuel cells, the solid oxide fuel cells have recently drawn worldwide interests in building a decentralized, hydrogen based energy economy as a potential source of efficient, environmentally friendly, fuel versatile electric power [35]. The high operating temperature (600-1000 °C) enables the solid oxide fuel cells to provide several potentials and advantages over other fuel cells, such as high electric-conversion efficiency, cogeneration-combined heat and power application, reversible electrode reaction, high tolerance to typical catalyst poisons, high quality of

waste heat to recover, as well as the wide fuel flexibility offering the prospect for direct utilization of natural gas and biogas and other renewable fuels [8,10,35,36].

However, such elevated operation temperature imposes severe constraints on materials compatibility and stability resulting in utilization of expensive materials and short fuel cell life. Thus, recently, great research interests have been focused on lowering the operating temperature of SOFCs from traditional high temperature (800-1000 °C) to the intermediate-temperature (IT) range (500-800°C) while still maintaining the high power density and efficiency. This development of IT-SOFCs makes it possible to use less expensive construction materials in interconnects and heat exchanges, and also enhances the durability of SOFC systems by suppressing problems associated with thermal cycling and performance degradation arsing from interdiffusion or reaction of the individual component driven by the high temperature. On the other hand, the decrease in operating temperature diminishes the conductivity of electrolytes and increases the overpotentials at electrodes, which results in a reduction of fuel cell voltage and output power. Thus, the great challenge of IT-SOFCs development attributes to find appropriate electrolytes and electrodes providing both rapid ion transport across electrolyte and electrode-electrolyte interfaces and efficient electrocatalysis of oxygen reduction and fuel oxidation reactions in order to reduce the power losses in the commercially relevant temperature range. Diverse schools of thoughts contribute to the potentials solution, *e.g.* the use of thin electrolyte films which could allow to lower the operating temperature couple with modification of cell configuration with respect to mechanic strength [15,43-47], the utilization of composite electrodes [48]such as the typical LSM-YSZ [48-51], and the exploration of new electrode materials especially the cathode materials.

With lowering the temperature to the IT temperature range, the electrodes cover a higher percentage of the voltage loss due to higher activation energy with respect to the progress in manufacturing thinner and less resistive electrolytes [35]. Moreover, as mentioned above, the overpotential at cathode is much larger than that of anode since the oxygen reduction is generally thought to be a more difficult reaction to activate on SOFC operation from IT to low temperature. This makes the cathode become the major source of cell voltage losses for the whole system [52,53]. Consequently, the development of new cathode materials with mixed ionic-electronic conductivity shows a great potential for IT-SOFCs application and draws wide research interests.

1.3 Cathode materials for IT-SOFCs

Conventional cathode materials are only electronic conductors such as $La_{1-x}Sr_xMnO_{3-\delta}$ (LSM) possessing high electronic conductivity, good stability under oxidizing atmospheres, and moderate thermal expansion coefficients (TEC) compatible to commonly used solid electrolyte such as YSZ [38,54-59], which make LSM still considered as the state-of-the-art cathode materials for SOFCs operating at high temperature 800-1000 °C. However, for this kind of traditional porous electronic conducting cathodes, reduction of oxygen at cathode is generally thought to be limited to a narrow region near electrode/electrolyte interface, where the gas species has simultaneous access to both electronically conductive electrolyte and electronically conductive cathode phases. This limited and nearly one-dimensional region is called tree-phase boundary (TPB) where air, electrode and electrolyte are in intimate contact, as shown in ***Figure 1.5(a)***. Thus, fuel cell performance using this kind of cathode materials is highly dependent on the electrode morphology and is very sensitive to formation of interfacial secondary phase. Consequently, with respect to extend the active region for oxygen reduction, the improvement of performance devotes to either control the complex electrode morphologies by suitable cathode processing, or to increase the contact area between ionically and electronically conductive phases by combining the cathode materials with an ionic conducting oxides forming a porous composite microstructure as mentioned above, seen in ***Figure 1.5(b)***.

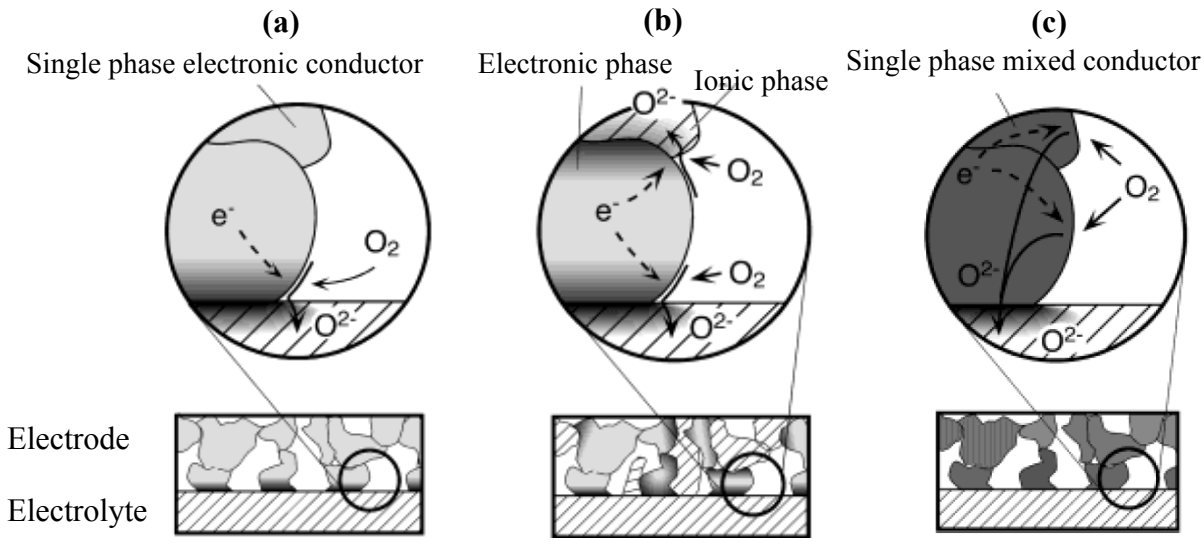

$$1/2O_2\left(gas\right)+2e^-\left(cathode\right)\rightleftharpoons O^{2-}\left(electrolyte\right)$$

Figure 1.5 *Function of cathodes in solide oxide fuel cells with: (a) porous single-phase conventional electronically conductive materials; (b) porous two-phase composite; (c) porous single phase mixed conductive materials* [35]

Another strategy to extend the electrochemically active region from the limited TPB at to the entire electrode/gas interfaces of cathode grains is the use of Mixed Ionic-Electronic Conductors (MIECs) as cathode materials. As depected in ***Figure 1.5(C)***, with application of MIEC cathode, oxygen molecules diffuse into the porous structure and form oxygen ions by the reduction reaction at the surface of the mixed conducting cathode and also TPB. The successive oxygen ions can diffuse either trough the cathode bulk or along the surface to the electrolyte. Even no universal agreement is achieved for the actual complex oxygen reduction mechanism at cathodes for MIECs due to several debatable or ambiguous issues, *e.g.* existence of oxygen intermediates, action region and rate-determing steps [60], the MIECs would be still highly expected to lower the resistance at IT temperature with respect to the larger active region available for reaction and ion transfer across the interface. To select new MIEC compounds for SOFC cathode candidate, the oxygen surface exchange and solid state diffusion should be taken into account in addition to electronic conductivity as the intrinsic properties of cathode materials. For example, the ALS model [61,62] was built to model the oxygen reduction for a porous MIEC cathode in terms of the oxygen ion diffusion coefficient D, surface exchange rate k, and electrode microstructure factors (surface area, tortuosity and porosity). As shown in ***Figure 1.6***, with given structure factors, the experimental diffusion coefficient D and surface exchange coefficient k for $La_{0.8}Sr_{0.2}CoO_{3-\delta}$ indicated by the arrow are corresponding to an area specific resistance of ~ 0.4 Ω cm^2, which could be lowered to 0.13 Ω cm^2 equal to the value for LSCO on CGO.

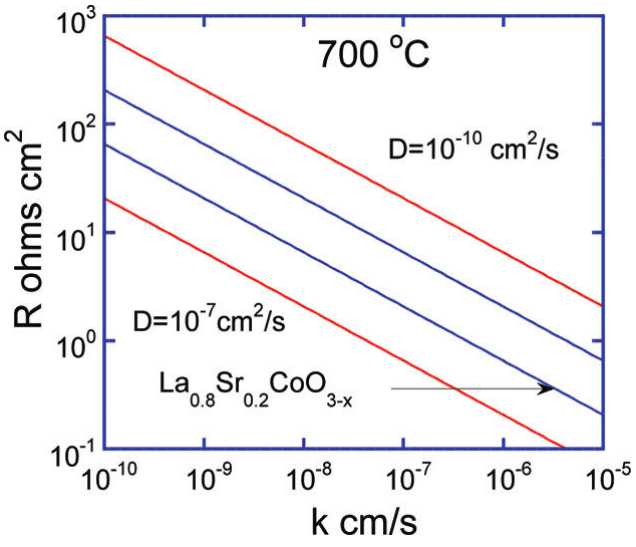

Figure 1.6 *Variation of the area specific resistance with D and k of $La_{0.8}Sr_{0.2}CoO_{3-\delta}$ calculated at 700 °C: surface area = 10000 cm^{-1}, particle size = 3 μm, porosity = 30%, tortuosity = 1.16* [33]

Perovskite-type mixed ionic-electronic conducting oxides have been intensively studied as potential cathode materials for IT-SOFCs application, including simple perovskites, Ruddlesden-

Popper phases, and double ordered perovskites. These materials are briefly summarized below with the emphasis on the double ordered perovskites which concerns the subject of this thesis.

1.3.1 ABO_3 perovskite oxides

Materials such as doped $LaCoO_3$, $BaCoO_3$ or $LaFeO_3$ have attracted extensive attention due to the possible use as ceramic membranes for the separation of oxygen and cathode materials for IT SOFC application. Their original structure can be represented by the general formula ABO_3 where A is rare earth or earth alkaline cation, B is a transition metal. One remarkable property of this kind of materials is that their defect structure, oxygen stoichiometry and charge transfer could be significantly altered by A-site acceptor substitution and both acceptor and donor B-site substitution, thereby giving rise to the possibility to alter oxygen vacancy concentration and oxygen diffusivity. The overall formula for substituted oxygen deficient perovskites could be modified to $A_{1-x}A'_xB_{1-y}B'_yO_{3-\delta}$. Large scale of studies have been done to investigate the influence of substitution (either A-site or B-site or both), defect structure and oxygen transport, as well as to analyze and model the relationship between the peculiarities of defect structure and transport properties with different dopant natures [63-65]. By modifying the type and proportion of A or B or both A and B sites substitution element, various systems have been developed, with extensive explorations focusing on the mixed conductivity, oxygen nonstoichiometry, oxygen surface exchange and solid state diffusion, and thermal expansion coefficient, *e.g.* $SrCo_{1-x}Fe_xO_{3-\delta}$ [66,67], $Sr_{1-x}Ce_xFe_{1-y}Co_yO_{3-\delta}$ [68], $Ba_{0.5}Sr_{0.5}(Co,Mn)_{0.8}Fe_{0.2}O_{3-\delta}$ [69,70], $Sm_xSr_{1-x}CoO_3$ [71-73], $La_{1-x}Ca_xCrO_{3-\delta}$ [56,59], $La_{1-x}Sr_xCoO_{3-\delta}$ [74-78], $La_{1-x}Sr_xFeO_{3-\delta}$ [79,80], $La_{1-x}Sr_xFe_{1-y}Ti_yO_{3-\delta}$ [81-83] and *et cetera*.

Among these materials, one attractive example refers to the well investigated $La_{1-x}Sr_xFe_{1-y}Co_yO_{3-\delta}$ (LSCF) system for which moderate dopant additions provide a significant enhancement in the total conductivity and electrochemical activity. The additions of the acceptor-type cations enhance the concentrations of mobile oxygen vacancies and *p*-type electronic charge carriers, in addition, the oxygen diffusivity is influenced by the content of lower-valence cations, thus the deficient structures caused by introduction and modification of A and B site substitution are expected to make this system suitable to cathode application. Nevertheless, increasing Sr^{2+} content above 50% and decreasing average cation radius in the Ln^{3+} sites promote vacancy-ordering and hole localization processes with a negative influence on the transport properties [37]. Stevenson *et al.* [84] studied the $La_{1-x}M_xCo_{1-y}Fe_yO_{3-\delta}$ (M = Sr, Ba, Ca) system by comparing there ionic and electronic conductivity, showing that at a constant temperature, the ionic and electronic conductivities as well as the diffusion coefficients are strongly dependent on both A and B sites substitution, which could differ by orders of magnitudes. This determines whether this material is suitable for IT-SOFCs application or not, *e.g.* LSCF-2882

($La_{0.2}Sr_{0.8}Co_{0.8}Fe_{0.2}O_{3-\delta}$) showed the highest ionic conductivity of 0.87 S cm^{-1} and electronic conductivity of 310 S cm^{-1} at 900 °C while LBCF-2828 exhibited the lowest electronic conductivity of 19 S cm^{-1}. Lankhorst *et al* [85] studied the $La_{06}Sr_{0.4}Co_{1-y}Fe_yO_{3-\delta}$ (y = 0-0.6) and found that the increase of iron content gives rise to a lower level of oxygen nonstoichiometry due to the fact that strontium doping is charge-compensated more readily by hole formation on iron than cobalt. Tai *et al.* investigated the LSCF system with low Sr content $La_{0.8}Sr_{0.2}Co_{1-y}Fe_yO_{3-\delta}$ [86] and low Co content $La_{1-x}Sr_xCo_{0.2}Fe_{0.8}O_{3-\delta}$ [87], respectively, indicating that the Sr content was compensated both electronically by valence change of B-site ions and ionically by formation of oxygen vacancies with the relative proportion being temperature dependent. They obtained a maximum electrical conductivity of 200-330 S cm^{-1} when x = 0.2-0.4 ranging from 600-800 °C in air, and also found that Co substitution increased the *p*-type electrical conductivity and thermal expansion coefficient. In addition, with respect to the application of porous MIEC cathode, oxygen transport properties such surface exchange, chemical diffusion, self-diffusion and oxygen permeation were extensively investigated. For example, the electrical conductivity relaxation measurement has been widely applied to investigate the chemical diffusion coefficient and surface exchange rate in LSCF, and by combing the isotope exchange or oxygen nonstocihiometry data further transport parameters such as tracer diffusion and oxygen vacancy diffusion could be obtained [80,88-92]. An optimum combination of transport, electrochemical properties, and thermomechanical properties in LSFC attributes to the compositions with x = 0.2-0.5 and y = 0.2, exhibiting promising potential for IT-SOFC cathode materials with ceria-base electrolyte. Moreover, with optimization of microstructure or adoption of cell designs, the cell performance might be improved significantly and thus match the IT-SOFCs requirements. For example, Bae *et al.* [93] obtained the low polarisation resistance of 0.5 Ω cm^2 at 520 °C for $La_{0.6}Sr_{0.4}Co_{0.2}Fe_{0.8}O_{3-\delta}$ double layer cathode comprising one thick porous layer and a thin dense film in conjunction with CGO electrolyte. Hsu *et al.* [94] has studied the NiO-$Sm_{0.2}Ce_{0.8}O_{1.9}$(SDC)/SDC/ $La_{0.6}Sr_{0.4}Co_{0.2}Fe_{0.8}O_{3-\delta}$ cell with either single layer or double layer cathode and obtained improved cell performance with introduction of a thin, porous intermediate cathode layer showing ASR of 0.05 Ω cm^2 at 600 °C and maximum power density of 0.91 W cm^{-2} at 600 °C and 1.18 W cm^{-2} at 700 °C. Similar high performance has been achieved by adding an interlayer in anode-supported Ni-YSZ/YSZ/SDC/$La_{0.6}Sr_{0.4}Co_{0.2}Fe_{0.8}O_{3-\delta}$ [47] cell, exhibiting an extraordinary high power density of 2.6 Wcm^{-2} at 0.7 V in flowing oxygen at 750 °C, as well as reduced ohmic resistance of 0.06 Ωcm^2 and polarization resistance of 0.03 Ωcm^2.

In comparison with the manganite or ferrite-based materials, perovskite-type cobalts show better mixed conductivity and exceptional electrochemical activity, but also higher thermal expansion coefficient (> 20×10^{-6} K^{-1}) which limits the compatibility with currently used solid oxide electrolyte. Thus their application as cathodes requires an intermediate barrier layer, the modification of the composition or formation of composite electrodes. In addition, some B-site substitutions for Co or Fe were found to be able to reduce the thermal expansion coefficient: *e.g.* increase of Fe substitution

could effectively decrease the thermal expansion coefficient in LSCF [86] and $Sm_xSr_{1-x}Co_{1-y}Fe_yO_3$ system [95], Ni substitution for Co was also found to decrease the TEC in the LSCFN and LSCN systems [96-98]. Moreover, $La_{1-x}Sr_xFe_{1-y}Ti_yO_{3-\delta}$ system has been investigated with respect to the lowering of TEC by Ti substitution for Fe, showing that the ionic and *p*-type electronic conductivities were both found to reduced with A-site deficiency and to increase with Fe content, and the average thermal expansion coefficients in air at 100-850 °C are in the range $(10.6\text{-}21.5)\times10^{-6}$ K^{-1} [81-83]. Recently, exceptionally remarkable performance was reported for $Ba_{0.5}Sr_{0.5}Co_{0.8}Fe_{0.2}O_{3-\delta}$ (BSCF) by Shao *et al.* [70] to give very low ASR values of 0.055-0.071 at 600 °C and 0.51-0.6 at 500 °C with BSCF/SDC symmetric cell configuration, and fuel cell test based on Ni+SDC/SDC/BSCF cell using humidified hydrogen as fuel and air as oxidant exhibited extremely high power density of 1010 mW cm^{-2} and 402 mW cm^{-2} at 600 °C and 500 °C, respectively. These values are considered as the best performance at such reduced temperature range and enable possible practical implementation of IT-SOFCs. Nevertheless, the excellent cathode performances are somehow thought to be related to the addition of silver in this system used as the current collectors [33].

1.3.2 Ruddlesden-Popper structure

The so called Ruddlesden-Popper (RP) perovskite oxides with the general formula $A_{n+1}B_nO_{3n+1}$ consist of $nABO_3$ perovskite layers sandwiched between two AO rock-salt layers, comprising A-site rare of alkaline earth and B-site transition metals. Of particular interest for SOFC cathode application, the $Ln_2NiO_{4+\delta}$ (Ln = La, Pr, Nd) based compounds, referring to n = 1 RP structure, haven been proposed, which exhibit suitable electronic conductivity and a relatively high ionic conductivity due to high oxygen overstoichiometry, TECs compatible with commonly used electrolytes and chemical compatibility with other SOFC components. Take the most studied $La_2NiO_{4+\delta}$ based compounds for instance; the structure of pure $La_2NiO_{4+\delta}$ can be described as succession of $LaNiO_3$ perovskite layers alternating (or sandwiched between) with LaO rock-salt layers, as depicted in ***Figure 1.7***. The oxygen excess in these materials results from the incorporation of interstitial oxygen anions into the rock-salt LaO layers, as well the bulk ionic transport occurs via diffusion of interstitial ions in the rock-salt layers, which possess fast diffusivity, and vacancies in the perovskite layers [99-101]. At ambient, maximum oxygen excess can be achieved in case of $La_2NiO_{4.18}$ and $Pr_2NiO_{4.22}$. The thermal expansion coefficients observed for $Ln_2NiO_{4+\delta}$ based compounds, ~$11\text{-}14\times10^{-6}$ K^{-1} [102-104], match well with the values of the electrolytes YSZ, CGO and LGSM. Moreover, similarly to the ABO_3 structure perovskites, the transport properties can be adjusted in a wide range by A-site and/or B site substitution.

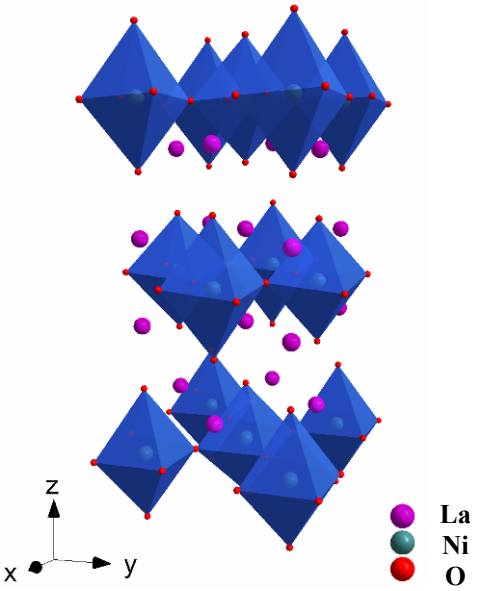

Figure 1.7 *Polyhedral view of Ruddlesden-Popper structure* La_2NiO_4

Skinner and Kilner [105] have investigated the surface exchange and self-diffusion coefficient by IEDP/SIMS experiment for $La_{2-x}Sr_xNiO_{4+\delta}$ (x = 0, 0.1) and found that A-site substitution by Sr lowered the tracer diffusion coefficient indicating a decrease of number of oxygen interstitials associated with a reduction in oxygen excess which was confirmed by TGA. Nevertheless, oxygen transport properties of $La_2NiO_{4+\delta}$ were found to be almost as good as current MIEC materials such as LSCF and LSC showing good thermomechanical stability at elevated temperature. This is in good agreement with recent study of $La_{2-x}Sr_xNiO_{4+\delta}$ (x = 0.1, 0.2) by Li *et al* [106], in which both experiments and defect calculation implied that Sr substitution led to higher jumping energy barrier for oxide ions to migrate which could thereby decrease the bulk diffusion, as well as to higher surface exchange rate with lower activation energy. Moreover, the incorporation of ionized atomic oxygen into surface vacancies was suggested to be the rate determining steps. EIS measurement of long-term stability of $La_2NiO_{4+\delta}$ with YSZ and CGO and reactivity tests showed an increase of ASR as a function of time indicating some chemical reactivity among cell components and formation of secondary phases [107]. B-site substitution for Ni with other transition metals has been widely studied. For example, oxygen transport properties have been extensively investigated in the Cu-substituted $La_2Ni_{1-x}Cu_xO_{4+\delta}$ systems [103,108-110], and the diffusion coefficient slightly lowered with increasing Cu content but no meaningful affect was obtained. Li *et al.* [111] studied the cathode performance of $La_{2-x}Sr_xNiO_{4+\delta}$ (x = 0.1, 0.3, 05) with CGO electrolyte and best performance was obtained in $La_{1.7}Sr_{0.3}NiO_{4+\delta}$ with the ASR of 0.16 Ω cm^{-2} at 700 °C and 1.2 Ω cm^{-2} at 500 °C in air. Aguadero *et al.* [112] investigated the $La_2Ni_{1-x}Cu_xO_{4+\delta}$ (0 ≤ x ≤ 1) by AC impedance with YSZ and CGO electrolytes in symmetric cell configuration, with

satisfactory total conductivity and thermal compatibility, but very high ASR values *e.g.* the best ASR is ~1 Ω cm^{-2} at 850 °C. By comparing the electrode properties of $Ln_2NiO_{4+\delta}$ based compounds with A-site La, Pr and Nd [113] in terms of impedance measurement with symmetric cell on YSZ electrolyte, $Pr_2NiO_{4+\delta}$ appeared to have the lowest ASR value but was chemically reactive with YSZ, and $Nd_2NiO_{4+\delta}$ exhibited promising electrode properties due to its high chemical stability and low polarization resistance compared to classical LSM, which is in consistency with good electrocatalytic properties and transport properties in these oxides [114]. Recently Ding *et al.* [115] has obtained attractive cathode performance for $Nd_{1.7}Sr_{0.3}CuO_{4+\delta}$ on SDC electrolyte, with polarisation resistances of 0.07 Ω cm^{-2} at 800 °C and 0.24 Ω cm^{-2} at 700 °C in air, which were consistent with high exchange current density of 390.7 mA/cm^2 and 76.1 mA/cm^2 at 800 and 700 °C, respectively, making this compound a promising cathode materials for the IT-SOFCs based on doped ceria electrolyte.

For the RP structure $Ln_2NiO_{4+\delta}$ materials, high ionic conductivities are expected due to their fast diffusion of oxygen interstitials. However, it should be noticed that the value of electrical conductivities in these materials is comparatively low with respect to other systems, which is usually less than or close to the standard value of 100 S cm^{-1} [103,108,116]. Their low thermal expansion coefficients compatible with currently used electrolytes are considered as one major advantage for potential application of cathode materials in IT-SOFCs, which is whilst limited by the low chemical stability and chemical reactivity with electrolytes observed for some compounds.

1.3.3 Ordered double layer perovskites

Recently, another type of mixed conducting perovskite oxides represented by the general formula $LnBaCo_2O_{5+\delta}$ (Ln = Pr, Nd, Sm, Eu, Gd, Tb, Dy, and Ho) has drawn tremendous attention as potential cathodes for IT-SOFCs due to the promising MIEC properties. These compounds are related to the "112" type structure and for a certain range of oxygen stoichiometry consist of double-pyramidal cobalt layers containing the Ba cations interleaved with Ln layers, as well as exhibit high electronic conductivity above the metal-insulator transition temperature and wide variation in oxygen nonstoichiometry [117]. Furthermore, Taskin *et al.* investigated the single crystal $GdBaCo_2O_{5+\delta}$ [118] on its structural, transport, magnetic, thermoelectric properties over a wide range of oxygen content, $0 \leq \delta \leq 0.77$. As depicted in ***Figure 1.8***, a simple cubic perovskite having the chemical formula $Gd_{0.5}Ba_{0.5}CoO_3$ with randomly occupied A sites Gd (a) can transform into a double layered crystal $GdBaCo_2O_6$ or a oxygen deficient double layered $GdBaCo_2O_{5+\delta}$ with a variability of oxygen content, $0 \leq \delta \leq 1$ (b)–(d). This transformation is driven by alternating lanthanide and alkali-earth planes, which reduces the oxygen bonding strength and provides disorder-free channels for ion motion, pointing to an efficient way to design new ionic conductors.

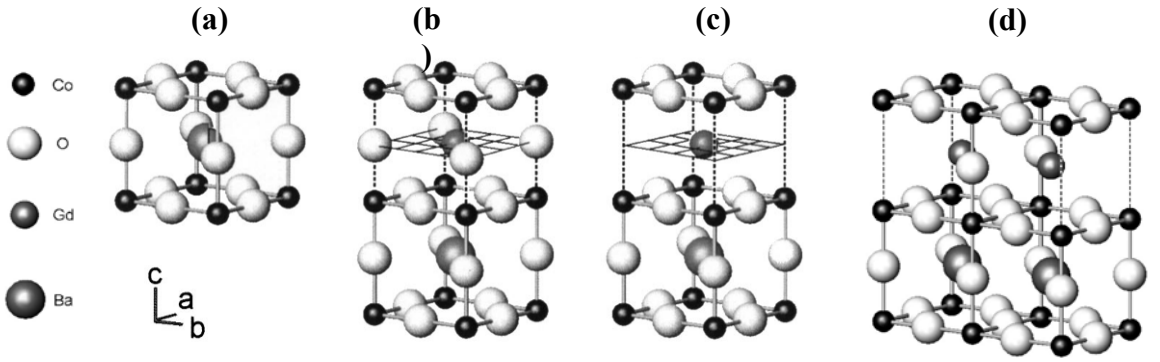

Figure 1.8 *Ordering of lanthanide Gd^{3+} and alkali-earth Ba^{2+} ions in the A-site sublattice of half-doped perovskites [118,119]: (a) simple cubic perovskite $Gd_{0.5}Ba_{0.5}CoO_3$ with random occupation of A-sites is transformed into (b) a layered crystal $GdBaCo_2O_6$ by doubling the unit cell, (c) Oxygen atoms can be partially or completely removed from lanthanide planes in $GdBaCo_2O_{5+\delta}$, providing a variability of the oxygen content, such as (d) $GdBaCo_2O_{5.5}$ when $\delta = 0.5$*

It has also been proved that oxygen diffusivity could be enhanced by orders of magnitude by inducing crystallographic ordering among lanthanide and alkali-earth ions in the A-site sublattice by Taskin *et al.* [119]. Rather fast oxygen diffusion, exceeding 10^{-5} cm^2 s^{-1} at 600 °C, and high surface exchange rates have been derived with quite low activation energy, moreover, as well, the ionic conductivity of ~ 0.01 S cm^{-1} could be achieved at nearly 500 °C, exhibiting promising potential for IT-SOFCs as MIEC cathode materials and having attracted extensive attention for this materials. Tarancón *et al.* [120] studied the stability of $GdBaCo_2O_{5+\delta}$ in CO_2 containing atmosphere (< 500 ppm to 100 % CO_2) showing excellent stability in air over the IT temperature range (500-700 °C), as well as good chemical stability with the state-of-the-art electrolytes for SOFCs, LSGM and CGO, except YSZ. Moreover, their electrochemical characterization using symmetric cells were carried out with both LSGM and CGO electrolytes and obtained ASR = 0.25 Ω cm^{-2} at ~650 °C. Fuel cells test carried out with the configuration GBCO/LSGM/CGO/Ni-CGO using Air and H_2 as oxidant and fuel respectively showed a maximum power density of 180 mW cm^{-2} at 800 °C, close to that using BSCF as cathode under the same condition, which was 240 mW cm^{-2} [121]. In addition, Tarancón *et al.* investigated the intrinsic oxygen transport and exchange of ceramic $GdBaCo_2O_{5+\delta}$ [122] using IEDP/SIMS method, and achieved suitable tracer diffusion coefficient and surface exchange coefficient with low activation energies compared to other cobaltites with mixed conducting such as LSC and LSCF. As discussed above and results from other works [46,123,124], excellent performance has been observed involving oxygen transport coefficients, polarisation resistance and electronic conductivity for $GdBaCo_2O_{5+\delta}$ in the temperature range of interest, indicating that this material is a good cathode candidate for intermediate even low temperature SOFC application.

Apart from $GdBaCo_2O_{5+\delta}$, analogues materials in $LnBaCo_2O_{5+\delta}$ family have also been investigated and evaluated for IT-SOFC application. Similar structural change and phase transition were observed in $PrBaCo_2O_{5.48}$, $NdBaCo_2O_{5+\delta}$, $TbBaCo_2O_{5+\delta}$ and $SmBaCo_2O_{5+\delta}$ [125-132]. Zhang *et al.* [133] found that the size of A site Ln^{3+} cation in $LnBaCo_2O_{5+\delta}$ is directly related to the stability of layered structure under reduction condition which could be kept for the composition with Ln = Pr, Nd, Sm and Gd but not for Ln = La or Y, and highest oxygen flux through was obtained across a membrane composed of $PrBaCo_2O_{5+\delta}$, and these compounds showed attractive electrode performances with SDC electrolyte, especially $PrBaCo_2O_{5+\delta}$ which possessed an ASR of ~0.213 Ω cm^{-2} at 600 °C. Moreover, excellent performance for a fuel cell for $PrBaCo_2O_{5+\delta}$ with SDC electrolyte have been reported [134,135], showing considerable maximum power density ~600 mW cm^{-2} at 600 °C. Zhou *et al.* reported very low ASR of $SmBaCo_2O_{5+\delta}$ on SDC and LSGM electrolyte of 0.098 and 0.054Ω cm^{-2} at 750 °C respectively.

Nevertheless, as usually observed in cobaltite compound, $LnBaCo_2O_{5+\delta}$ shows large thermal expansion coefficient, *e.g.* 16.0~20.0×10^{-6} K^{-1} [124,136,137] for the case $GdBaCo_2O_{5+\delta}$, considerably higher than those of typical electrolytes such as YSZ, CGO and LSGM, giving rise to mismatch during fabrication of cells and thermal cycling of operation process. One effective strategy is the use of composite electrodes with incorporation of electrolyte materials to cathode, which could reduce the thermal mismatch and also extend the TPB into electrode in addition to the electrode/electrolyte interface thereby enhancing the electrode performances. For example, Kim *et al.* [138] obtained a small ASR value of 0.05Ω cm^{-2} at 700 °C for a composite electrode SBCO:50 (50 wt% $SmBaCo_2O_{5+\delta}$ and 50 wt% $Ce_{0.9}Gd_{0.1}O_{2-\delta}$) on CGO91 electrolyte, as well as reduced the TEC from about 20 20.0×10^{-6} K^{-1} down to ~12.5×10^{-6} K^{-1} in the temperature range from 500 to 700 °C. Lee *et al.* investigated $GdBaCo_2O_{5+\delta}$ – $Ce_{0.9}Gd_{0.1}O_{1.95}$ (CGO) composited cathodes, and best performance was found with 30 wt% CGO-70wt % GBCO (GBCO:30) cathode, for which TEC was reduced to 14.7 ×10^{-6} K^{-1} and maximum powder density of GBCO:30/CGO/Ni-CGO cell was 340 and 525 mW cm^{-2} at 650 and 700 °C, respectively, showing a high performance for promising IT-SOFC cathode candidate. Moreover, another school of thought is the B-site substitution for Co by other transition metals such as Ni, Fe or Cu [139-141], with the aim to lower TEC and optimize the electrochemical performance.

Intrinsic properties of several MIEC electrode materials discussed above are summarised in Table 1.4. It can be noticed that in general the RP type layered perovskites show higher oxygen diffusivity than simple perovskite materials but also comparatively low overall electrical conductivity. The double layered $PrBaCo_2O_{5+\delta}$ shows highest transport properties at even lower temperature. However, these kinetics parameters, especially the surface exchange coefficient, are very sensitive to the sample quality and surface conditions, which may possibly give rise to a wide degree of variability and discrepant results for the same components obtained by different methods or authors.

Composition	Oxygen transport kinetics			Total conductivity		Ref.
	T (°C)	D^* ($cm^2\ s^{-1}$)	k^* ($cm\ s^{-1}$)	T (°C)	σ ($S\ cm^{-1}$)	
$La_{0.6}Sr_{0.4}FeO_{3-\delta}$	800	2.7×10^{-8}	1.05×10^{-5}	650-850	1000-1500	[80]
$(La_{0.6}Sr_{0.4})_{0.99}CoO_{3-\delta}$	700	3.1×10^{-8}		400-1000	1000-2000	[78,142]
$La_{0.8}Sr_{0.2}CoO_{3-\delta}$	700	1×10^{-8}	3×10^{-6}	500-7500	1500-1600	[143]
$La_{0.6}Sr_{0.4}Fe_{0.8}Co_{0.2}O_{3-\delta}$	800	7.3×10^{-10}	8.2×10^{-8}	300-1000	190-350	[89,91,92,142]
$La_{0.8}Sr_{0.2}Fe_{0.8}Co_{0.2}O_{3-\delta}$	716	7.6×10^{-12}	2.7×10^{-8}	500-1000	100-150	[86,144]
$La_2NiO_{4+-\delta}$	600	7.5×10^{-8}	1.0×10^{-6}	30-1000	25-60	[102,113,145,146]
$La_2Cu_{0.5}Ni_{0.5}O_{4+-\delta}$	700	7.5×10^{-8}	5.0×10^{-7}	500-900	30-50	[108]
$GdBaCo_2O_{5+\delta}$	496	4.8×10^{-10}	7.4×10^{-8}	500-800	450-900	[121,122]
	686	1.3×10^{-9}	1.3×10^{-7}			
$PrBaCo_2O_{5+\delta}$	500	3.7×10^{-7}	7×10^{-5}	500-800	400-700	[147]

Table 1.4 Oxygen self-diffusion and surface exchange coefficients and total conductivities for different SOFC cathode materials

1.4 Scope of the thesis

$GdBaCo_2O_{5+\delta}$, has shown attractive performance for IT-SOFC cathode application. Generally, cobaltites possess the best electrical conductivity and usually good ionic conductivity, but their potential for electrode materials is still limited by their large thermal expansion coefficients and chemical activity with YSZ. Substitution for Co by other transition metal such as Fe, Ni or Cu has been widely adopted to improve the material properties of cobaltite perovskites, and successively obtained great improvements such as lower thermal expansion, better chemical stability or enchanced electrode performance [86,88,95,97,148,149]. However, most of these works are focused on the LSC type perovskite materials, not much attention is paid on this kind of substitution in double layer perovskites materials, *e.g.* $GdBaCo_2O_{5+\delta}$.

The objective of present thesis is to explore new cathode materials based on the $GdBaCo_2O_{5+\delta}$ by Ni and Fe substitution aiming to altering the material properties and obtain better electrode performance.

- $GdBaCo_{2-x}M_xO_{5+\delta}$ (M=Ni or Fe, x = 0.1, 0.2 …) are synthesized by wet chemical method, seeking for solid solubility of Ni and Fe with moderate processing, these works are integrated in **Chapter 2**.

- **Chapter 2** is also focused on the chemical-physical characterizations for the as-synthesized materials: Structural evolution with substitution, oxygen nonstoichiometry, temperature dependent phase transition and thermal expansion coefficient are investigated.

- **Chapter 3** deals with the electrochemical performance of several selected composition serving as porous electrodes on different kinds of electrolyte, as well as intends to understand the oxygen reduction mechanism and look for the rate determining factor.

- **Chapter 4** is devoted to the electrical and oxygen transport properties coupled with oxygen nonstoichiometries in the investigated temperature range and atmospheres, more concerning the intrinsic properties of materials.

REFERENCES

[1] Carrette, L.; Friedrich, K. A.; Stimming, U. *ChemPhysChem* **2000**, *1*, 162-193.

[2] Winter, M.; Brodd, R. *Chemical reviews* **2004**, *104*, 4245.

[3] McCusker, L. B.; Von Dreele, R. B.; Cox, D. E.; Louer, D.; Scardi, P. *Journal of Applied Crystallography* **1999**, *32*, 36-50.

[4] Carrette, L.; Friedrich, K. A.; Stimming, U. *Fuel Cells* **2001**, *1*, 5-39.

[5] Williams, M. C.; Strakey, J. P.; Singhal, S. C. *Journal of Power Sources* **2004**, *131*, 79-85.

[6] Chalk, S. G.; Miller, J. F.; Wagner, F. W. *Journal of Power Sources* **2000**, *86*, 40-51.

[7] Dufour, A. U. *Journal of Power Sources* **1998**, *71*, 19-25.

[8] Minh, N. Q. *Solid State Ion.* **2004**, *174*, 271-277.

[9] Hart, D. *Journal of Power Sources* **2000**, *86*, 23-27.

[10] Haile, S. M. *Acta Materialia* **2003**, *51*, 5981-6000.

[11] LALANNE, C. Thèse, L'UNIVERSITE BORDEAUX 1, 24 Oct 2005.

[12] Manning, P. S.; Sirman, J. D.; DeSouza, R. A.; Kilner, J. A. *Solid State Ion.* **1997**, *100*, 1-10.

[13] Sahibzada, M.; Steele, B. C. H.; Barth, D.; Rudkin, R. A.; Metcalfe, I. S. *Fuel* **1999**, *78*, 639-643.

[14] Sahibzada, M.; Steele, B. C. H.; Hellgardt, K.; Barth, D.; Effendi, A.; Mantzavinos, D.; Metcalfe, I. S. *Chemical Engineering Science* **2000**, *55*, 3077-3083.

[15] Sahibzada, M.; Steele, B. C. H.; Zheng, K.; Rudkin, R. A.; Metcalfe, I. S. *Catalysis Today* **1997**, *38*, 459-466.

[16] Fergus, J. W. *Journal of Power Sources* **2006**, *162*, 30-40.

[17] Wang, S.; Kato, T.; Nagata, S.; Kaneko, T.; Iwashita, N.; Honda, T.; Dokiya, M. *Solid State Ion.* **2002**, *152-153*, 477-484.

[18] Steele, B. C. H. *Solid State Ion.* **2000**, *129*, 95-110.

[19] Xia, C.; Chen, F.; Liu, M. *Electrochem. Solid State Lett.* **2001**, *4*, A52-A54.

[20] Tietz, F. *Ionics* **1999**, *5*, 129-139.

[21] Mori, M.; Abe, T.; Itoh, H.; Yamamoto, O.; Takeda, Y.; Kawahara, T. *Solid State Ion.* **1994**, *74*, 157-164.

[22] Kharton, V. V.; Figueiredo, F. M.; Navarro, L.; Naumovich, E. N.; Kovalevsky, A. V.; Yaremchenko, A. A.; Viskup, A. P.; Carneiro, A.; Marques, F. M. B.; Frade, J. R. *Journal of Materials Science* **2001**, *36*, 1105-1117.

[23] Zajac, W.; Swierczek, K.; Molenda, J. *Journal of Power Sources* **2007**, *173*, 675-680.

[24] Kharton, V. V.; Kovalevsky, A. V.; Viskup, A. P.; Shaula, A. L.; Figueiredo, F. M.; Naumovich, E. N.; Marques, F. M. B. *Solid State Ion.* **2003**, *160*, 247-258.

[25] Ullmann, H.; Trofimenko, N.; Tietz, F.; Stöver, D.; Ahmad-Khanlou, A. *Solid State Ion.* **2000**, *138*, 79-90.

[26] Stevenson, J. W.; Hasinska, K.; Canfield, N. L.; Armstrong, T. R. *J. Electrochem. Soc.* **2000**, *147*, 3213-3218.

[27] Huang, W.; Shuk, P.; Greenblatt, M. *Solid State Ion.* **1998**, *113-115*, 305-310.

[28] Sameshima, S.; Ichikawa, T.; Kawaminami, M.; Hirata, Y. *Materials Chemistry and Physics* **1999**, *61*, 31-35.

[29] Zheng, Y.; Gu, H.; Chen, H.; Gao, L.; Zhu, X.; Guo, L. *Materials Research Bulletin* **2009**, *44*, 775-779.

[30] Majumdar, S.; Claar, T.; Flandermeyer, B. *J. Am. Ceram. Soc.* **1986**, *69*, 628-633.

[31] Hsiao, Y. C.; Selman, J. R. *Solid State Ion.* **1997**, *98*, 33-38.

[32] Steele, B. C. H. *Solid State Ion.* **1996**, *86-88*, 1223-1234.

[33] Jacobson, A. J. *Chem. Mat.* **2009**, *22*, 660-674.

[34] Haile, S. M. *Materials Today* **2003**, *6*, 24-29.

[35] Adler, S. B. *ChemInform* **2004**, *35*.

[36] Tsipis, E. V.; Kharton, V. V. *J. Solid State Electrochem.* **2008**, *12*, 1039-1060.

[37] Tsipis, E. V.; Kharton, V. V. *J. Solid State Electrochem.* **2008**, *12*, 1367-1391.

[38] Steele, B. C. H. *Journal of Materials Science* **2001**, *36*, 1053-1068.

[39] Fergus, J. W. *Solid State Ion.* **2004**, *171*, 1-15.

[40] Yang, Z.; Weil, K. S.; Paxton, D. M.; Stevenson, J. W. *J. Electrochem. Soc.* **2003**, *150*, A1188-A1201.

[41] Kurokawa, H.; Kawamura, K.; Maruyama, T. *Solid State Ion.* **2004**, *168*, 13-21.

[42] Steele, B. C. H.; Heinzel, A. *Nature* **2001**, *414*, 345-352.

[43] Tarancon, A.; Dezanneau, G.; Arbiol, J.; Peiro, F.; Morante, J. R. In *Conference on Scientific Advances in Fuel Cell Systems* Amsterdam, Netherlands, 2002, p 256-264.

[44] Tsuchiya, M.; Bojarczuk, N. A.; Guha, S.; Ramanathan, S. *The Journal of Chemical Physics* **2009**, *130*, 174711.

[45] Zhao, F.; Virkar, A. V. *Journal of Power Sources* **2005**, *141*, 79-95.

[46] Lee, Y.; Kim, D. Y.; Choi, G. M. *Solid State Ion.*, *In Press, Corrected Proof*.

[47] Lu, Z.; Hardy, J.; Templeton, J.; Stevenson, J. *Journal of Power Sources* **2011**, *196*, 39-45.

[48] Mogensen, M.; Primdahl, S.; JØrgensen, M. J.; Bagger, C. *J. Electroceram.* **2000**, *5*, 141-152.

[49] McIntosh, S.; Adler, S. B.; Vohs, J. M.; Gorte, R. J. *Electrochem. Solid State Lett.* **2004**, *7*, A111-A114.

[50] Jorgensen, M. J.; Mogensen, M. *J. Electrochem. Soc.* **2001**, *148*, A433-A442.

[51] Choi, M. B.; Jeon, S. Y.; Hwang, H. J.; Park, J. Y.; Song, S. J. *Solid State Ion.* **2010**, *181*, 1680-1684.

[52] Brandon, N. P.; Skinner, S.; Steele, B. C. H. *Annual Review of Materials Research* **2003**, *33*, 183-213.

[53] Fleig, J. *Annual Review of Materials Research* **2003**, *33*, 361-382.

[54] Kharton, V. V.; Naumovich, E. N.; Vecher, A. A. *J. Solid State Electrochem.* **1999**, *3*, 61-81.

[55] Huijsmans, J. P. P. *Current Opinion in Solid State and Materials Science* **2001**, *5*, 317-323.

[56] Yasuda, I.; Hishinuma, M. *Journal of Solid State Chemistry* **1995**, *115*, 152-157.

[57] Yasuda, I.; Hishinuma, M. *Solid State Ion.* **1995**, *80*, 141-150.

[58] Yasuda, I.; Hishinuma, M. *Journal of Solid State Chemistry* **1996**, *123*, 382-390.

[59] Yasuda, I.; Hikita, T. *J. Electrochem. Soc.* **1994**, *141*, 1268-1273.

[60] Li, Y.; Gemmen, R.; Liu, X. *Journal of Power Sources* **2010**, *195*, 3345-3358.

[61] Adler, S. B.; Lane, J. A.; Steele, B. C. H. *J. Electrochem. Soc.* **1996**, *143*, 3554-3564.

[62] Adler, S. B.; Lane, J. A.; Steele, B. C. H. *J. Electrochem. Soc.* **1997**, *144*, 1884-1890.

[63] Zuev, A.; Petrov, A.; Vylkov, A.; Tsvetkov, D. *Journal of Materials Science* **2007**, *42*, 1901-1908.

[64] Petrov, A.; Cherepanov, V.; Zuev, A. *J. Solid State Electrochem.* **2006**, *10*, 517-537.

[65] Dalslet, B. T.; Søgaard, M.; Bouwmeester, H. J. M.; Hendriksen, P. V. *Solid State Ion.* **2009**, *180*, 1173-1182.

[66] Vashuk, V.; Kokhanovskii, L.; Yushkevich, I. *Inorganic Materials* **2000**, *36*, 1043-1049.

[67] Ma, B.; Balachandran, U.; Park, J. H.; Segre, C. U. *Solid State Ion.* **1996**, *83*, 65-71.

[68] Trofimenko, N. E.; Ullmann, H. *J. Eur. Ceram. Soc.* **2000**, *20*, 1241-1250.

[69] Girdauskaite, E.; Ullmann, H.; Vashook, V. V.; Guth, U.; Caraman, G. B.; Bucher, E.; Sitte, W. *Solid State Ion.* **2008**, *179*, 385-392.

[70] Shao, Z.; Haile, S. M. *Nature* **2004**, *431*, 170-173.

[71] Wang, S.; Zhong, H.; Zou, Y. *Journal of Power Sources* **2006**, *161*, 1154-1160.

[72] Xia, C.; Liu, M. *Solid State Ion.* **2001**, *144*, 249-255.

[73] Xia, C.; Rauch, W.; Chen, F.; Liu, M. *Solid State Ion.* **2002**, *149*, 11-19.

[74] Lankhorst, M.; Bouwmeester, H. *J. Electrochem. Soc.* **1997**, *144*, 1268-1273.

[75] Lankhorst, M. H. R. a. B., H.J.M. *J. Electrochem. Soc.* **1997**, *144*, 4.

[76] Haar, L. M. v. d.; Otter, M. W. d.; Morskate, M.; Bouwmeester, H. J. M.; Verweij, H. *J. Electrochem. Soc.* **2002**, *149*, J41-J46.

[77] Van Der Haar, L.; Den Otter, M.; Morskate, M.; Bouwmeester, H.; Verweij, H. *J. Electrochem. Soc.* **2002**, *149*, J41.

[78] Søgaard, M.; Hendriksen, P. V.; Mogensen, M.; Poulsen, F. W.; Skou, E. *Solid State Ion.* **2006**, *177*, 3285-3296.

[79] Ten Elshof, J.; Lankhorst, M.; Bouwmeester, H. *J. Electrochem. Soc.* **1997**, *144*, 1060.

[80] Søgaard, M.; Vang Hendriksen, P.; Mogensen, M. *Journal of Solid State Chemistry* **2007**, *180*, 1489-1503.

[81] Fagg, D. P.; Kharton, V. V.; Frade, J. R.; Ferreira, A. A. L. *Solid State Ion.* **2003**, *156*, 45-57.

[82] Fagg, D. P.; Waerenborgh, J. C.; Kharton, V. V.; Frade, J. R. *Solid State Ion.* **2002**, *146*, 87-93.

[83] Park, C. Y.; Jacobson, A. J. *J. Electrochem. Soc.* **2005**, *152*, J65-J73.

[84] Stevenson, J. W.; Armstrong, T. R.; Carneim, R. D.; Pederson, L. R.; Weber, W. J. *J. Electrochem. Soc.* **1996**, *143*, 2722-2729.

[85] Lankhorst, M. H. R.; ten Elshof, J. E. *Journal of Solid State Chemistry* **1997**, *130*, 302-310.

[86] Tai, L. W.; Nasrallah, M. M.; Anderson, H. U.; Sparlin, D. M.; Sehlin, S. R. *Solid State Ion.* **1995**, *76*, 259-271.

[87] Tai, L. W.; Nasrallah, M. M.; Anderson, H. U.; Sparlin, D. M.; Sehlin, S. R. *Solid State Ion.* **1995**, *76*, 273-283.

[88] Hjalmarsson, P.; Søgaard, M.; Mogensen, M. *Solid State Ion.* **2009**, *180*, 1290-1297.

[89] Lane, J. A.; Benson, S. J.; Waller, D.; Kilner, J. A. *11th International Conference on Solid State Ionics (SSI-11)* **1997**, 201-208.

[90] Lane, J. A.; Kilner, J. A. In *12th International Conference on Solid State Ionics*; Elsevier Science Bv: Halkidiki, Greece, 1999, p 997-1001.

[91] Bouwmeester, H.; Den Otter, M.; Boukamp, B. *J. Solid State Electrochem.* **2004**, *8*, 599-605.

[92] Wang, S.; van der Heide, P. A. W.; Chavez, C.; Jacobson, A. J.; Adler, S. B. *Solid State Ion.* **2003**, *156*, 201-208.

[93] Bae, J.-M.; Steele, B. C. H. *Solid State Ion.* **1998**, *106*, 247-253.

[94] Hsu, C. S.; Hwang, B. H.; Xie, Y.; Zhang, X. *J. Electrochem. Soc.* **2008**, *155*, B1240-B1243.

[95] Lv, H.; Wu, Y.-j.; Huang, B.; Zhao, B.-y.; Hu, K.-a. *Solid State Ion.* **2006**, *177*, 901-906.

[96] Huang, K.; Lee, H. Y.; Goodenough, J. B. *J. Electrochem. Soc.* **1998**, *145*, 3220-3227.

[97] Nagamoto, H.; Mochida, I.; Kagotani, K.; Inoue, H.; Negishi, A. *Journal of Materials Research* **1993**, *8*, 3158-3162.

[98] Hjalmarsson, P.; Søgaard, M.; Hagen, A.; Mogensen, M. *Solid State Ion.* **2008**, *179*, 636-646.

[99] V. Kharton, V.; P. Viskup, A.; N. Naumovich, E.; M. B. Marques, F. *Journal of Materials Chemistry* **1999**, *9*, 2623-2629.

[100] Vashook, V. V.; Yushkevich, I. I.; Kokhanovsky, L. V.; Makhnach, L. V.; Tolochko, S. P.; Kononyuk, I. F.; Ullmann, H.; Altenburg, H. *Solid State Ion.* **1999**, *119*, 23-30.

[101] Kharton, V. V.; Viskup, A. P.; Kovalevsky, A. V.; Naumovich, E. N.; Marques, F. M. B. *Solid State Ion.* **2001**, *143*, 337-353.

[102] Boehm, E.; Bassat, J. M.; Dordor, P.; Mauvy, F.; Grenier, J. C.; Stevens, P. *Solid State Ion.* **2005**, *176*, 2717-2725.

[103] Kharton, V. V.; Tsipis, E. V.; Yaremchenko, A. A.; Frade, J. R. *Solid State Ion.* **2004**, *166*, 327-337.

[104] Al Daroukh, M.; Vashook, V. V.; Ullmann, H.; Tietz, F.; Arual Raj, I. *Solid State Ion.* **2003**, *158*, 141-150.

[105] Skinner, S. J.; Kilner, J. A. *Solid State Ion.* **2000**, *135*, 709-712.

[106] Li, Z.; Haugsrud, R.; Norby, T. *Solid State Ion.*, *In Press, Corrected Proof*.

[107] Hernández, A. M.; Mogni, L.; Caneiro, A. *International Journal of Hydrogen Energy* **2010**, *35*, 6031-6036.

[108] Mauvy, F.; Bassat, J. M.; Boehm, E.; Dordor, P.; Grenier, J. C.; Loup, J. P. In *8th International Conference on Electronic Ceramics and Their Applications (ELECTROCERAMICS VIII)*; Elsevier Sci Ltd: Rome, ITALY, 2002, p 1265-1269.

[109] Mauvy, F.; Bassat, J. M.; Boehma, E.; Dordor, P.; Loup, J. P. *Solid State Ion.* **2003**, *158*, 395-407.

[110] Mauvy, F.; Boehm, E.; Bassat, J. M.; Grenier, J. C.; Fouletier, J. *Solid State Ion.* **2007**, *178*, 1200-1204.

[111] Li, Q.; Zhao, H.; Huo, L.; Sun, L.; Cheng, X.; Grenier, J.-C. *Electrochemistry Communications* **2007**, *9*, 1508-1512.

[112] Aguadero, A.; Alonso, J. A.; Escudero, M. J.; Daza, L. *Solid State Ion.* **2008**, *179*, 393-400.

[113] Mauvy, F.; Lalanne, C.; Bassat, J.-M.; Grenier, J.-C.; Zhao, H.; Huo, L.; Stevens, P. *J. Electrochem. Soc.* **2006**, *153*, A1547-A1553.

[114] Mauvy, F.; Bassat, J. M.; Boehm, E.; Manaud, J. P.; Dordor, P.; Grenier, J. C. *Solid State Ion.* **2003**, *158*, 17-28.

[115] Ding, X.; Kong, X.; Jiang, J.; Cui, C. *International Journal of Hydrogen Energy* **2009**, *34*, 6869-6875.

[116] Tang, J. P.; Dass, R. I.; Manthiram, A. *Materials Research Bulletin* **2000**, *35*, 411-424.

[117] Maignan, A.; Martin, C.; Pelloquin, D.; Nguyen, N.; Raveau, B. *Journal of Solid State Chemistry* **1999**, *142*, 247-260.

[118] Taskin, A. A.; Lavrov, A. N.; Ando, Y. *Phys. Rev. B* **2005**, *71*, 28.

[119] Taskin, A. A.; Lavrov, A. N.; Ando, Y. *Appl. Phys. Lett.* **2005**, *86*, 3.

[120] Tarancon, A.; Pena-Martinez, J.; Marrero-Lopez, D.; Morata, A.; Ruiz-Morales, J. C.; Nunez, P. *Solid State Ion.* **2008**, *179*, 2372-2378.

[121] Pena-Martinez, J.; Tarancon, A.; Marrero-Lopez, D.; Ruiz-Morales, J. C.; Nunez, P. *Fuel Cells* **2008**, *8*,

351-359.

[122] Tarancon, A.; Skinner, S. J.; Chater, R. J.; Hernandez-Ramirez, F.; Kilner, J. A. *Journal of Materials Chemistry* **2007**, *17*, 3175-3181.

[123] Choi, M. B.; Jeon, S. Y.; Lee, J. S.; Hwang, H. J.; Song, S. J. *Journal of Power Sources* **2010**, *195*, 1059-1064.

[124] Li, N.; Lu, Z.; Wei, B. O.; Huang, X. Q.; Chen, K. F.; Zhang, Y. Z.; Su, W. H. *Journal of Alloys and Compounds* **2008**, *454*, 274-279.

[125] Streule, S.; Podlesnyak, A.; Sheptyakov, D.; Pomjakushina, E.; Stingaciu, M.; Conder, K.; Medarde, M.; Patrakeev, M. V.; Leonidov, I. A.; Kozhevnikov, V. L.; Mesot, J. *Phys. Rev. B* **2006**, *73*, 5.

[126] Streule, S.; Podlesnyak, A.; Pomjakushina, E.; Conder, K.; Sheptyakov, D.; Medarde, M.; Mesot, J. In *International Conference on Strongly Correlated Electron Systems (SECES 05)*; Elsevier Science Bv: Vienna, AUSTRIA, 2005, p 539-540.

[127] Lobanovskii, L. S.; Troyanchuk, I. O. *Jetp Lett.* **2005**, *82*, 719-722.

[128] Burley, J. C.; Mitchell, J. F.; Short, S.; Miller, D.; Tang, Y. *Journal of Solid State Chemistry* **2003**, *170*, 339-350.

[129] Taskin, A. A.; Lavrov, A. N.; Ando, Y. *Phys. Rev. B* **2006**, *73*, 121101.

[130] Kopcewicz, M.; Khalyavin, D.; Troyanchuk, I.; Szymczak, H.; Szymczak, R.; Logvinovich, D.; Naumovich, E. *J. Appl. Phys.* **2003**, *93*, 479-486.

[131] Moritomo, Y.; Akimoto, T.; Takeo, M.; Machida, A.; Nishibori, E.; Takata, M.; Sakata, M.; Ohoyama, K.; Nakamura, A. *Phys. Rev. B* **2000**, *61*, R13325.

[132] Conder, K.; Podlesnyak, A.; Pomjakushina, E.; Pomjakushin, V.; Stingaciu, M.; Karkin, A. E. In *17th International Conference on Magnetism (ICM 2006)*; Elsevier Science Bv: Kyoto, JAPAN, 2006, p 907-909.

[133] Zhang, K.; Ge, L.; Ran, R.; Shao, Z.; Liu, S. *Acta Materialia* **2008**, *56*, 4876-4889.

[134] Zhu, C.; Liu, X.; Yi, C.; Yan, D.; Su, W. *Journal of Power Sources* **2008**, *185*, 193-196.

[135] Chen, D.; Ran, R.; Zhang, K.; Wang, J.; Shao, Z. *Journal of Power Sources* **2009**, *188*, 96-105.

[136] Tang, Y. K.; Almasan, C. C. *Phys. Rev. B* **2008**, *77*, 5.

[137] Tarancon, A.; Marrero-Lopez, D.; Pena-Martinez, J.; Ruiz-Morales, J. C.; Nunez, P. *Solid State Ion.* **2008**, *179*, 611-618.

[138] Kim, J. H.; Kim, Y.; Connor, P. A.; Irvine, J. T. S.; Bae, J.; Zhou, W. *Journal of Power Sources* **2009**, *194*, 704-711.

[139] Ding, H.; Xue, X. *International Journal of Hydrogen Energy* **2010**, *In Press, Corrected Proof*.

[140] Kim, Y. N.; Kim, J. H.; Manthiram, A. *Journal of Power Sources* **2010**, *195*, 6411-6419.

[141] Wei, B.; Lü, Z.; Jia, D.; Huang, X.; Zhang, Y.; Su, W. *International Journal of Hydrogen Energy* **2010**, *In Press, Corrected Proof*.

[142] Petric, A.; Huang, P.; Tietz, F. *Solid State Ion.* **2000**, *135*, 719-725.

[143] Bouwmeester, H. J. M.; Burggraaf, A. J. In *Membrane Science and Technology*; Burggraaf, A. J., Cot, L., Eds.; Elsevier: 1996; Vol. Volume 4, p 435-528.

[144] Atkinson, A.; Chater, R. J.; Rudkin, R. *Solid State Ion.* **2001**, *139*, 233-240.

[145] Mauvy, F.; Lalanne, C.; Bassat, J. M.; Grenier, J. C.; Zhao, H.; Dordor, P.; Stevens, P. *J. Eur. Ceram. Soc.* **2005**, *25*, 2669-2672.

[146] Bassat, J. M.; Petitjean, M.; Fouletier, J.; Lalanne, C.; Caboche, G.; Mauvy, F.; Grenier, J. C. *Applied Catalysis A: General* **2005**, *289*, 84-89.

[147] Kim, G.; Wang, S.; Jacobson, A. J.; Reimus, L.; Brodersen, P.; Mims, C. A. Journal of Materials

Chemistry 2007, 17, 2500-2505.

[148] Ortiz-Vitoriano, N.; de Larramendi, I. R.; de Larramendi, J. I. R.; Arriortua, M. I.; Rojo, T. Journal of Power Sources 2009, 192, 63-69.

[149] Chiba, R.; Yoshimura, F.; Sakurai, Y. Solid State Ion. 1**999**, *124*, 281-288.

Chapter 2 Synthesis, Processing and Physical-Chemical Characterisation

2.1 Introduction

In this chapter, methods for powder fabrication and investigation are introduced in details, as well as the characterisation of physical and chemical properties of Ni and Fe doped $GdBaCo_2O_{5+\delta}$ cathode materials.

2.2 Synthesis of Ceramic Materials

Diverse fabrication methods for pure GBCO as well as doped GBCO have been applied in previous works, such as the floating zone method for GBCO single crystal [1,2], solid state reaction [3,4] and wet chemical routes [5-9] for ceramic polycrystalline powders. In this work, both solid state reaction and wet chemical routes have been attempted to obtain pure complex GBCO and Ni or Fe doped compounds.

2.2.1 Solid state reaction (SSR)

Traditional solid state reaction SSR is the most commonly used method for multi-component powder synthesis, which involves intimate mechanical mixing of precursors (oxides, carbonate or nitrates), repeated grinding and heating cycles, with the advantage of its simplicity and facility of large production. Previous works have proved SSR to be an effective route for pure $GdBaCo_2O_{5+\delta}$ powders synthesis [10-12], as shown in Table 2.1. In these works, starting materials, Gd_2O_3, $BaCO_3$ and Co_3O_4, were weighted in stoichiometric proportion and well mixed, followed by diverse high temperature thermal treatment processes, coupled with intermediate regrinding or repeated thermal cycles.

The nominal formation reaction of this solid state reaction can be written as follows:

$$1/2Gd_2O_3 + BaCO_3 + 2/3Co_3O_4 \rightarrow GdBaCo_2O_{5+\sigma} + CO_2 \uparrow \quad (2.1)$$

However, this classical method is unable to provide submicron powder with a controlled morphology, which is important for electrode materials. The multiple repetitions of grinding and prolonged thermal treatment cycles can easily induce uncontrolled crystalline growth, composition inhomogeneities and grain size non-uniformity, as well as apparently small solubility limits of doping elements.

Ref.	Process
A. Maignan [13]	Decarbonation at 1000ºC, pressed into bar then heated at 1100 ºC for 24h in air
Tarancón [6]	Calcination at 900 ºC and 1000 ºC for 20h
C. Frontera [3]	Firstly sintered as pellet at 1125 ºC for 24h, followed by repeated regrinding–compression–annealing–regrinding cycles
M.B Choi [14]	Precursors ball milled and calcined at 1000 ºC for 24h in air
D.S. Tsvetkov [15]	Step calcination from 800ºC to 1100ºC, 10h for every 100ºC step with mixture regrinding

Table 2.1 Diverse SSR thermal treatments for pure $GdBaCo_2O_{5+\delta}$

Both Ni and Fe substituted $GdBaCo_2O_{5+\delta}$ polycrystalline samples have been synthesized by solid state reaction method recently, reaching the solubility limit for Ni substitution at x = 0.4 *i.e.* $GdBaCo_{1.6}Ni_{0.4}O_{5+\delta}$ [8] and for Fe substitution at x = 0.2 *i.e.* $GdBaCo_{1.8}Fe_{0.2}O_{5-\delta}$ [7].

2.2.2 Gel Combustion Process

Apart from classical SSR route, wet chemistry routes proved to be an interesting alternative due to the possibility to mix the reagent species at the atomic scale in solution, and due to the high specific surface area and high reactivity of resulting oxide powders. Co-precipitation, spray-drying, freeze-drying, sol-gel and Pechini are the state-of-the-art methods in chemical ways for polycrystalline ceramic powders synthesis.

The traditional sol-gel method of synthesis starts from molecular precursors (generally alkoxides and/or organometallic compounds) and allows forming a solid network by hydrolysis-condensation reactions, with the disadvantages of difficulty in controlling the experimental process, as well as high cost of precursors. In 1967, Pechini [16] developed an alternative sol-gel approach, which mainly employs the inorganic salts as precursors, citric acid as chelating ligand and polyethylene glycol (PEG) as cross-linking agent. Tarancón *et al.* developed an improved polyacrylamide-gel combustion process and also another polymethacrylamide-gel combustion process to synthesize ultrafine and highly homogeneous powders for diverse electrolytes and cathodes as SOFC materials [17]. Such method was improved by introducing low cost and less toxic agents [18,19], such as acrylic acid instead of acrylamide. In this work, an acrylic acid polymerization method was used to fabricate original $GdBaCo_2O_{5+\delta}$, and Ni, Fe substituted $GdBaCo_{2-x}M_xO_{5+\delta}$ (M = Ni or Fe, x = 0.1, 0.2 …).

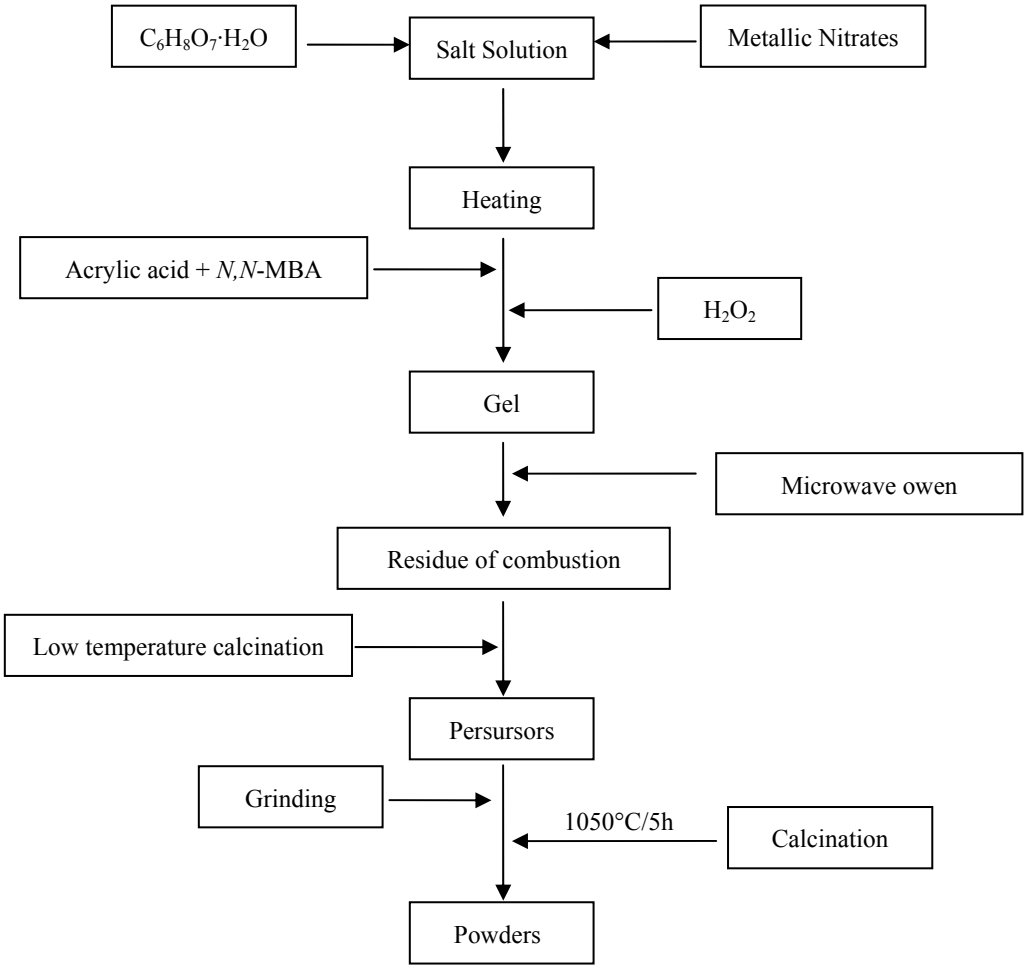

Figure 2.1 *Synthesis process of the methylenebisacrylamide-gel combustion route*

Nitrates precursors $Gd(NO_3)_3 \cdot 6H_2O$ (99.9%-Gd, STREM), $Ba(NO_3)_2$ (99%, Alfa Aesar), $Co(NO_3)_2 \cdot 6H_2O$ (99%, STREM), $Ni(NO_3)_2 \cdot 6H_2O$ (99.9%-Ni, STREM) or $Fe(NO_3)_3 \cdot 9H_2O$ (99%, STREM) were completely dissolved in de-ionized water in stoichiometric ratio by magnetic stirring, then citric acid monohydrate ($C_6H_8O_7 \cdot H_2O$, 99.5-100%, MERCK) was added as chelating agent with the proportion n(citric acid):n (total positive charges of metallic cations in solution) = 1:2, resulting in a clear transparent solution. And the pH value was adjusted to 6 at 70 °C by adding ammonia. The mixed solution was heated till boiling, afterwards acrylic acid (99%, SIGMA-ALDRICH) (1/10 of the original volume of solution) and N, N'-Methylene-bis-acrylamide (98%, SIGMA) with a concentration of 5.6g/L were added with continuous heating Then, several droplets of hydrogen peroxide were added as a polymerization initiator, until the two monomers reacted together forming an organic 3D tangled network, a transparent gel. In succession, the gel was dried in a microwave oven for 30 min, and then the dried and dehydrated gel was cracked, grinded and pre-heated at 500°C for 1.5 h. The obtained precursor was well grinded and finally thermal treated at 1050°C for 5h, resulting

in the desired $GdBaCo_{2-x}M_xO_{5+\delta}$ (M=Ni or Fe, x =0, 0.1, 0.2 …) compound.. The experimental process is presented in ***Figure 2.1***.

This gel method has been proved as a valid method for Ni, Fe-doped GBCO, by which the phase purity and high doping proportion could be guaranteed. But, the practical convenience of this method is limited by the vigorous swelling of polymer precursors during the thermal treatment and size of alumina crucibles, which gives rise to small amount of powders and to the risk of furnace pollution. To obtain sufficient quantity of products and to avoid the pollution of furnace, another microwave-assisted combustion method was used.

2.2.3 Microwave-assisted combustion synthesis

Among various chemical synthesis process, the combustion method is recognised as relatively simple to perform, low-cost, and easy to the control of stoichiometry [20]. The combustion process is actually a self-sustaining exothermic redox reaction between an oxidizer (metallic nitrate) and a fuel (such as ethylene glycol, citric acid). The fuel also acts as a complexing agent in the aqueous solution of nitrate salts.

A mirowave-assisted citric complex route was used in this work. The citrate solution was prepared by dissolving citric acid monohydrate ($C_6H_8O_7{\cdot}H_2O$, 99.5-100%, MERCK) in de-ionized water, by the proportion *n*(citric acid) : *n*(total positive charges of metallic cations in solution) = 1:1, heated and stirred by a magnetic agitator. After complete homogenization of the citrate solution, nitrates $Gd(NO_3)_3{\cdot}6H_2O$ (99.9%-Gd, STREM), $Ba(NO_3)_2$ (99%, Alfa Aesar), $Co(NO_3)_2{\cdot}6H_2O$ (99%, STREM), $Ni(NO_3)_2{\cdot}6H_2O$ (99.9%-Ni, STREM) or $Fe(NO_3)_3{\cdot}9H_2O$ (99%, STREM) were added in stoichiometric ratio. An aqueous transparent solution was obtained by continuous stirring and heating, and then moved into a domestic microwave oven, heated by the microwave irradiation with 600 W during 20-30 minutes. The residual product was heated at 500 ºC for 1.5 h, followed by grinding and finally thermal treated at 1050 ºC for 5 h in air. The experimental process is presented in ***Figure 2.2.***

Compared to the gel combustion method, the productivity has been effectively improved trough this citric acid combustion route. Due to a unique complexing agent and the rapid heating rate in microwave, the dehydration of solution, swelling and combustion of viscous gel could be accomplished in a short reaction time, without ignition or visible flame. The volume of residual precursors of citric acid combustion after microwave step is much smaller than that of gel combustion method, which significantly facilitates the following calcination steps by obtaining much larger amount of synthesized powders, in spite of limitation on the size of available crucibles.

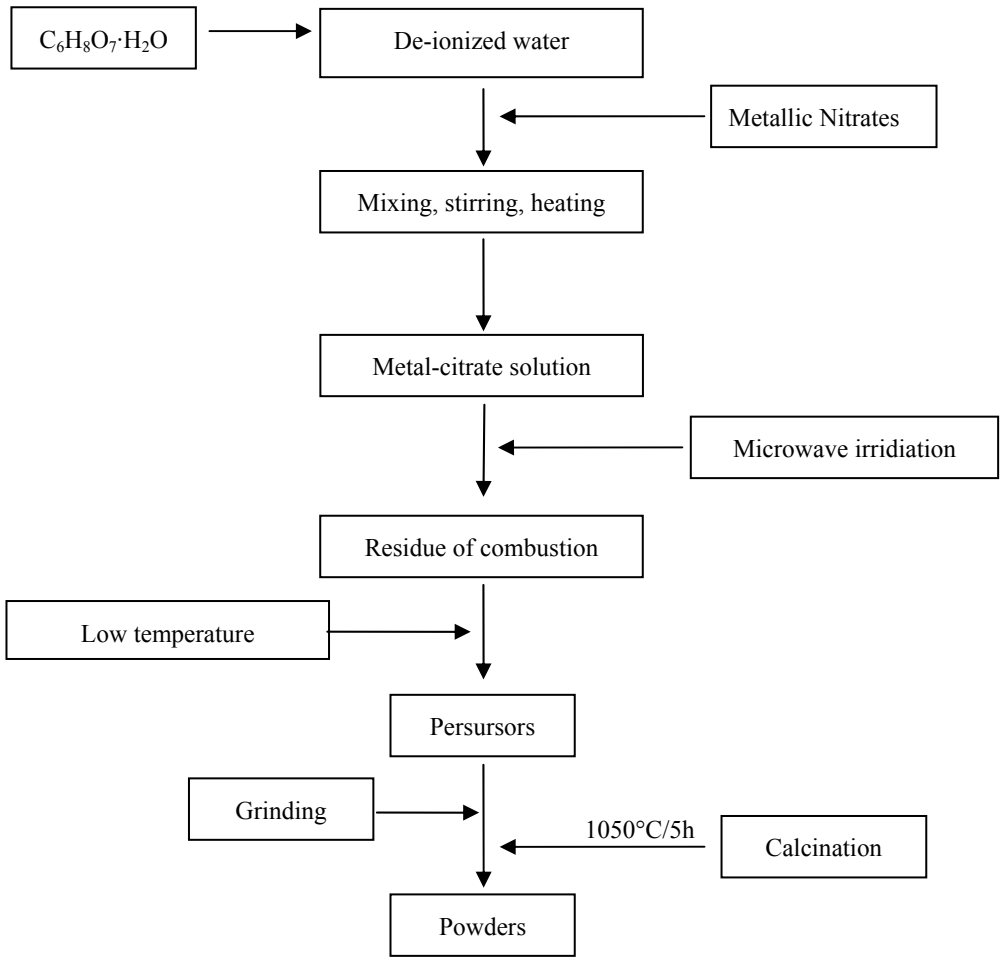

Figure 2.2 *Synthesis process of a microwave-assisted citric acid combustion method*

2.3 Structural and Microstructural properties

2.3.1 XRD characterization of synthesized compositions

The as-synthesized powders were characterized by X-ray powder diffraction (XRD, Rigaku D/max-2550/pc, Cu *K*α radiation, $\lambda_{K\alpha 1}$ = 1.5405 Å). The data were collected over the angular range from 20° to 60° with a step of 0.02°. ***Figure 2.3*** shows the result of Ni and Fe doped $GdBaCo_{2-x}M_xO_{5+\delta}$ synthesized by the gel route, calcinated at 1050 ºC for 5h at ambient. Higher substitution ratios of both Ni and Fe were achieved by this route, compared to the results of previous published work [7,8,21], respectively.

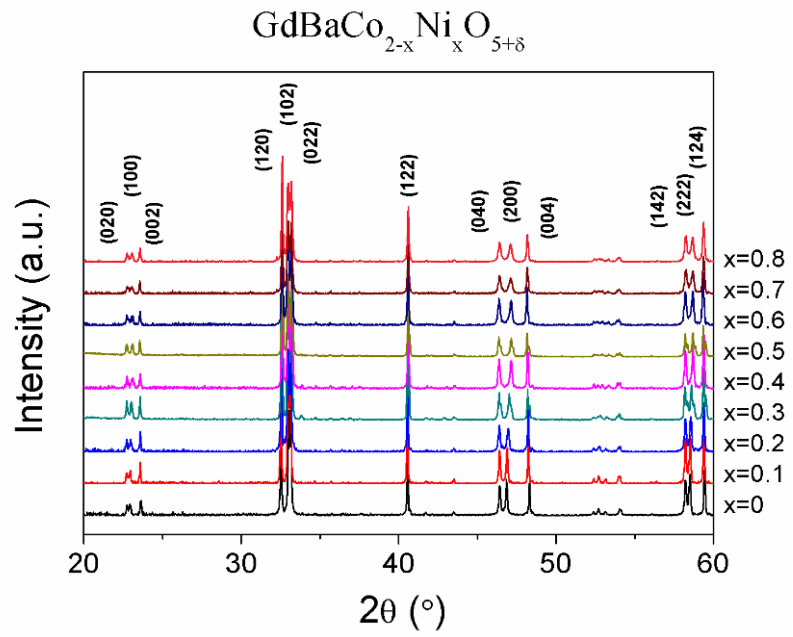

(a)

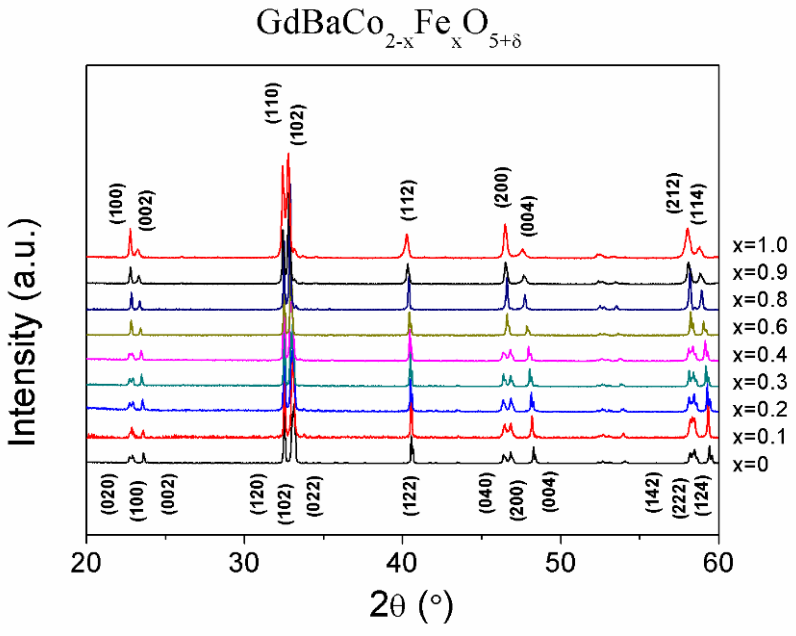

(b)

Figure 2.3 *XRD pattern of (a) $GdBaCo_{2-x}Ni_xO_{5+\delta}$, x = 0~0.8 indexed to orthorhombic structure with Pmmm symmetry and (b) $GdBaCo_{2-x}Fe_xO_{5+\delta}$, x = 0~1, showing a phase transition from orthorhombic Pmmm symmetry to tetragonal P4/mmm symmetry with increasing Fe content*

For the Ni substituted compounds, pure phase could be guaranteed up to the doping proportion x = 0.8. As $x \leq 0.8$, the compounds seem to maintain a structure similar to that of the GBCO

composition. For higher x values, extra phases have been observed (some several binary and ternary oxides).

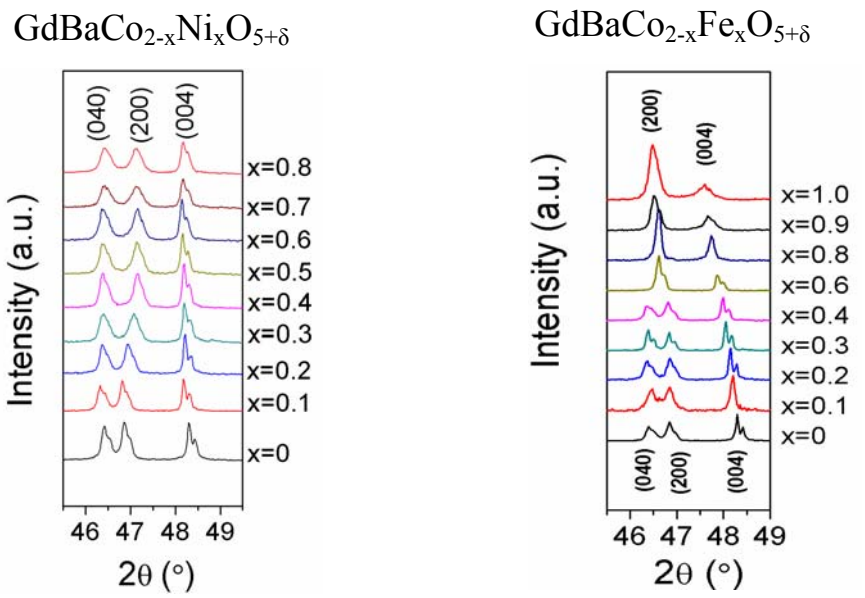

***Figure 2.4** Peak splitting in $GdBaCo_{2-x}Ni_xO_{5+\delta}$ and convergence of peaks in $GdBaCo_{2-x}Fe_xO_{5+\delta}$ with increase of Ni and Fe substitution, respectively*

With the increase of Ni substitution ratios, shifts of peak position and peak splittings appear on the XRD pattern. For instance, for the three peaks which represent the reflections of (040) (200) (004), respectively, shown in ***Figure2.4 (a)***. The (040) peak shifts to lower angular position while the (020) peak does in the opposite; meanwhile, other single peaks such as (122) and (004) show a tendency towards lower angular position. This phenomenon shows that the Ni substitution for Co could enhance the orthorhombic distortion in consistency with the systematic increase in "orthorhombicity" with Ni substitution in GBCO observed by Bharathi *et al.* [7,8].

For the Fe substitution compounds, pure phase could be obtained until the Fe fraction x = 1, by the same chemical route. XRD patterns (***Figure2.4 (b)***) exhibit the approaching and even convergence of peaks as a consequence of the increase of Fe substitution ratio. From x > 0.4, $GdBaCo_{2-x}Fe_xO_{5+\delta}$ shows a phase transition from the original orthorhombic structure to a tetragonal structure indexed in the P4/mmm space group. Apparently, Fe substitutions oppositely diminish the orthorhombic distortion and further give rise to the phase transition. This could be considered as consequence of oxygen content decrease due to Fe doping, as discussed in Chapter 2.4.

2.3.2 Powder morphology

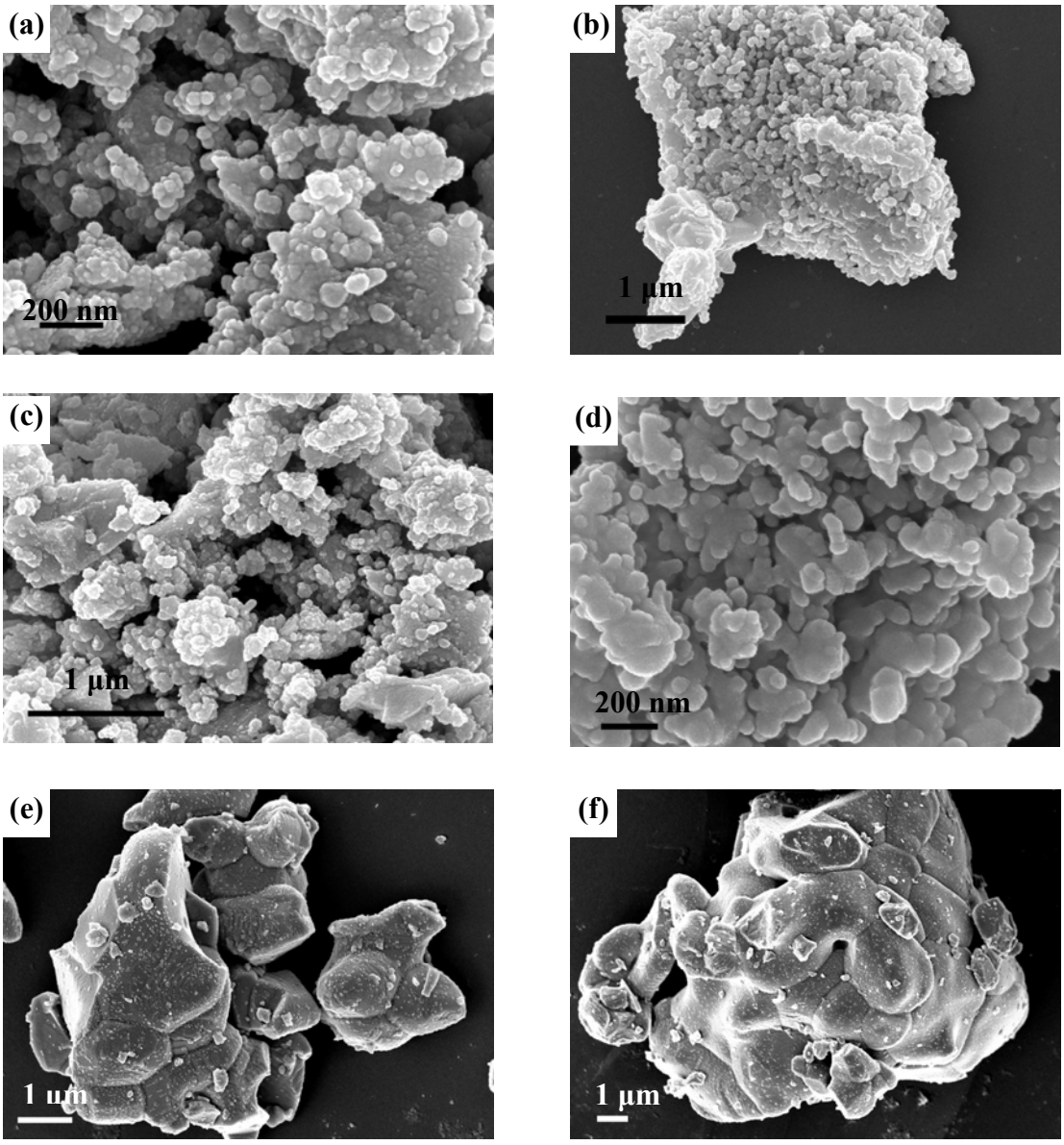

Figure 2.5 *SEM images of GBCO as-synthesized powders by gel combustion route calcinated at 800°C (a)(b), 1050°C(c)(d) by citric acid combustion route calcianted at 1050°C(e)(f), respectively*

Scanning electron microscopy (SEM) was used to investigate the morphology of as-synthesized powders. ***Figure2.5*** shows the images of $GdBaCo_2O_{5+\delta}$ powders obtained by gel combustion route calcinated at 800°C for 4h, with general grain size in the nano scale (a) and tendency of aggregation of single particles (b). the increase of grain size, especially the agglomeration has been observed for the same compound with successive thermal treatment at 1050°C for 5h (c)(d), by which pure phase could be guaranteed. At this stage, native particles agglomerate and form big grains of micron size. On the

other hand, $GdBaCo_2O_{5+\delta}$ powders obtained by citric acid combustion route at 1050°C exhibit significant agglomerate particles composed by grains on micron scale (e)(f).

2.4 Oxygen nonstoichiometry

XRD investigation has already revealed the different influences of Ni and Fe substitution on the $GdBaCo_{2-x}M_xO_{5+\delta}$ (M = Ni, or Fe) structures at room temperature. Besides of Ni, the structural transition with the increase of Fe substitution was considered to be related to the oxygen content change caused by the replacement of Co by Fe. Thus, oxygen nonstoichiometry becomes essential for a better understanding of the Ni and Fe substituted $GdBaCo_{2-x}M_xO_{5+\delta}$ (M = Ni, or Fe), with respect to the following analysis of crystal structural and high temperature transport properties.

2.4.1 Introduction

For transition metal oxides that are increasingly applied as functional materials, their desired properties (*e.g.* electric and ionic conductivity, superconductivity, electrical and magnetic properties, magnetoresistivity, and thermoelectricity) are highly dependent on the oxygen stoichiometry [20]. Great attention has been drawn on the precise determination of oxygen content its consequent variation of physical properties [22-25].

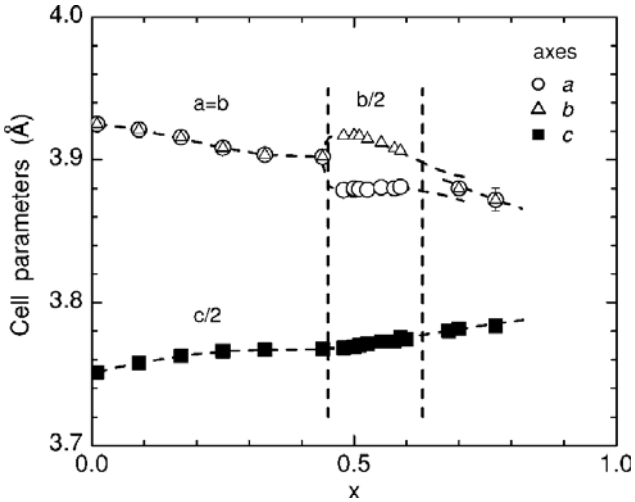

Figure 2.6 *Room-temperature parameters of the $GdBaCo_2O_{5+\delta}$ unit cell as a function of the oxygen content x (x = δ)* [1].

In two mostly studied classes of complex cobalt oxides (Ln, B)$CoO_{3-\delta}$ and $LnBCo_2O_{5+\delta}$ (Ln-rare earth, B-alkali earth elements) cobalt cations can adopt 2+, 3+ or 4+ oxidation state and therefore different δ are observed. Generally, the oxygen content in cobaltites depends both on the chemical

composition and on the synthesis procedure [24-32]. A previous work on $LnBaCo_2O_{5+\delta}$ synthesized in air gives $\delta \approx 0.7$ for Ln = Pr and Nd, but lower δ-values for other lanthanide cations with smaller Ln^{3+} size ($\delta \approx 0.4$ for Sm, Eu, Gd, Tb and $\delta \approx 0.3$ for Dy and Ho) [13].

The oxygen content can be tuned by annealing in controlled atmosphere (inert gas/oxygen or pure oxygen at high pressure) followed by quenching, or by gettering (with, e.g. metallic Zr, Y and Cu) in sealed ampoules. As revealed by Taskin *et al.* [1], the structural properties of $GdBaCo_2O_{5+\delta}$ at room termperature shows strong dependency on the oxygen nonstoichiometry (***Figure 2.6***).

i $0 \leq \delta < 0.45$, the system keeps a macroscopically tetragonal structure P4/mmm, where the unit cell smoothly expands in the c direction and shrinks in the in-plane directions with increasing x.

ii $0.45 \leq \delta < 0.60$, the oxygen ions order into alternating filled and empty chains running along with the *a* axis, which results in the orthorhombic structure Pmmm and in the doubling of the unit cell along the b axis.

iii $\delta > 0.60$, the system evolves towards a tetragonal symmetry.

A similar case has been found by Kopecewicz *et al.* [33] for the Fe substituted $TbBaCo_2O_{5+\delta}$, which is highly analogous to $GdBaCo_2O_{5+\delta}$ in the structural properties [34]; by means of MössBauer spectroscopy and TGA, they developed a modified chemical formula $TbBa(Co_{2-x}Fe_x)O_{5.5-x/2}$, describing that the increasing content leads to the reduction of Co^{3+} to Co^{2+} and to the decrease of oxygen content. Oxygen content changes in Ni and Fe substituted $GdBaCo_{2-x}M_xO_{5+\delta}$ (M = Ni, Fe) with smaller substitution ratio were also studied [7,8], and these results will be compared with those obtained from this work.

2.4.2 Experimental

The most accurate methods for establishing the precise oxygen content of transition metal oxides are all based on redox reaction. In these methods, the high-valent cations of the studied sample are reduced by a suitable reductant, *e.g.* I^-, Fe^{2+}, Cu^+ or H_2, followed by the determination of the exact amount of reductant left over or the oxidized form of the reductant formed, or even the weight change related to the reduction reaction, using appropriate analysis technique [22]. Iodometric titration and thermogravimetric hydrogen reduction analysis *etc.* were applied in this recent works as oxygen content determination methods. Nevertheless, the iodometry method is valid only for certain transition metals, *e.g.* it is not applicable to Fe oxides. Thus, iodometric titration method was only applied for Ni substituted compounds, and the thermogravimetric hydrogen reduction (TG/H_2 reduction) method was carried out on both Ni and Fe substituted compositions.

All the $GdBaCo_{2-x}M_xO_{5+\delta}$ (M = Ni, Fe) powder samples were obtained through those methods mentioned previously in 2.2, and their phase purities have been checked by X-ray diffraction. An air-annealing process was followed in order to eliminate possible nonuniformity of oxygen content during the thermal treatment: All the powders were grinded in an agate mortar, and then a three-hour isothermal heating period was applied at 900 ºC after which the samples were slowly cooled down to room temperature at the rate of 100 ºC/h in air.

Iodometry

The well grinded powder samples (*c.a.* 50 mg) of $GdBaCo_{2-x}Ni_xO_{5+\delta}$ was dissolved in 1 M HCl solution (100 ml) containing potassium iodide, in an Erlenmeyer flask isolated from air by using a nitrogen flow. Then the reduction of tri- and tetra-valent cobalt and nickel species of the sample takes place, forming a stoichiometric amount of iodine in the solution:

$$2Co^{3+} + 3I^- \rightarrow 2Co^{2+} + I_3^- \tag{2.2}$$

$$Co^{4+} + 3I^- \rightarrow Co^{2+} + I_3^- \tag{2.3}$$

$$2Ni^{3+} + 3I^- \rightarrow 2Ni^{2+} + I_3^- \tag{2.4}$$

$$Ni^{4+} + 3I^- \rightarrow Ni^{2+} + I_3^- \tag{2.5}$$

The amount of the liberated iodine is determined by titration with 0.01 mol/L $Na_2S_2O_3$ solution:

$$I_3^- + 2S_2O_3^{2-} \rightarrow 3I^- + S_4O_6^{2-} \tag{2.6}$$

The end point of the titration was detected by using starch as indicator, visually as the blue colour of the starch complex disappeared and the solution turned to light pink due the formation of Co^{2+} which was predominant compared to Ni^{2+}. The whole process was accomplished in the Erlenmeyer flask under protection of inert atmosphere by the N_2 flow.

Thermogravimetric reduction (TG/H_2 reduction)

In the TG/H_2 reduction method, the sample was heated in a reduction atmosphere (usually H_2), and from the weight loss (products of the reduction were supposed to be known) in situ at the temperature corresponding to the complete reduction, the oxygen content in the original sample could be calculated. K. Conder *et al.* provided the following equation cobaltites, as the cobalt is reduced to the metallic state [23].

$$LnBaCo_2O_{5.5+\delta} + (2.5+\delta)H_2 \rightarrow 0.5Ln_2O_3 + BaO + 2Co + (2.5+\delta)H_2O \tag{2.7}$$

In this work, TG/H_2 reduction of five chosen compounds are majorly studied: $GdBaCo_2O_{5+\delta}$, $GdBaCo_{1.7}Ni_{0.3}O_{5+\delta}$, $GdBaCo_{1.4}Ni_{0.6}O_{5+\delta}$, $GdBaCo_{1.7}Fe_{0.3}O_{5+\delta}$ and $GdBaCo_{1.4}Fe_{0.6}O_{5+\delta}$, abbreviated to GBCO, GBN03, GBCN06, GBCF03 and GBCF06, respectively. The measurements have been performed by G. Boemare using a SETARAM 92-1750 device with a thermobalance of high sensitivity. The powder samples (*c.a.* 100 mg) were heated up to 950 ºC at a rate of 2 ºC/min in a mixed 5% H_2 – 95% Ar gas flow (5 L/h), followed by an isothermal period of 5h. All the measurements have been carried out with correction of blank experiments, by performing with empty crucibles at the same condition, in order to eliminate the interference of Archimedes force for calculation. The overall reaction equations deduced from Eq. 2.7 are listed below:

$$GdBaCo_2O_{5.5+\delta} + (2.5+\delta)H_2 \rightarrow 0.5Gd_2O_3 + BaO + 2Co + (2.5+\delta)H_2O \quad (2.8)$$

$$GdBaCo_{2-x}Ni_xO_{5.5+\delta} + (2.5+\delta)H_2 \rightarrow 0.5Gd_2O_3 + BaO + (2-x)Co + xNi + (2.5+\delta)H_2O \quad (2.9)$$

$$GdBaCo_{2-x}Fe_xO_{5.5+\delta} + (2.5+\delta)H_2 \rightarrow 0.5Gd_2O_3 + BaO + (2-x)Co + xFe + (2.5+\delta)H_2O \quad (2.10)$$

2.4.3 Results and discussion

The oxygen content determined by iodometric titration method in this work is listed in Table 2.2.

Total oxygen content				
	$GdBaCo_{2-x}Ni_xO_{5+\delta}$		$GdBaCo_2O_{5+\delta}$	
Ni content x	This work	A. Bharathi *et al.* [8]	K. Conder *et al.* [23]	
0	5.51(4)	5.54 ± 0.01		
0.1	5.53(2)	5.53 ± 0.01	Iodometry	5.438 ± 0.002
0.2	5.55(2)	5.54 ± 0.01	Gas volumetry	5.505 ± 0.005
0.3	5.50(2)	5.50 ± 0.01	TG/H	5.42 ± 0.02
0.4	5.53(3)	5.54 ± 0.03		
0.5	5.50(2)			
0.6	5.50(1)			
0.7	5.48(2)			
0.8	5.34(2)			

Table 2.2 Oxygen contents of $GdBaCo_{2-x}Ni_xO_{5+\delta}$ obtained by iodometric titration in this work and from literature [8], as well as results of $GdBaCo_2O_{5+\delta}$ obtained with different methods [23]

The δ value of each composition was obtained from the average of several parallel experiments. It is evident that the total oxygen content remains roughly constant with the increase of Ni substitution and the value is very close to 5.5 when $x \leq 0.6$, suggesting that average valence of both Co and Ni in those compositions is close to 3+, which is in good agreement with the result of Bharathi *et al.* [8] in $GdBaCo_{2-x}Ni_xO_{5+\delta}$ as well as the oxygen content of $GdBaCo_2O_{5+\delta}$ obtained from Conder *et al.* [23] who have compared the different methods for oxygen content determination and the corresponding discrepancy is also shown in Table 2.2. On the other hand, for x = 0.7 and x = 0.8, the decrease of oxygen content was more important. XRD analysis has shown that both of these two compositions still maintain the orthorhombic symmetry with Pmmm space group. Moreover, for the particular case of x = 0.8, the situation is different from that of $GdBaCo_2O_{5+\delta}$, for which the orthorhombic structure corresponds to a strict oxygen content range $0.45 \leq \delta < 0.60$.

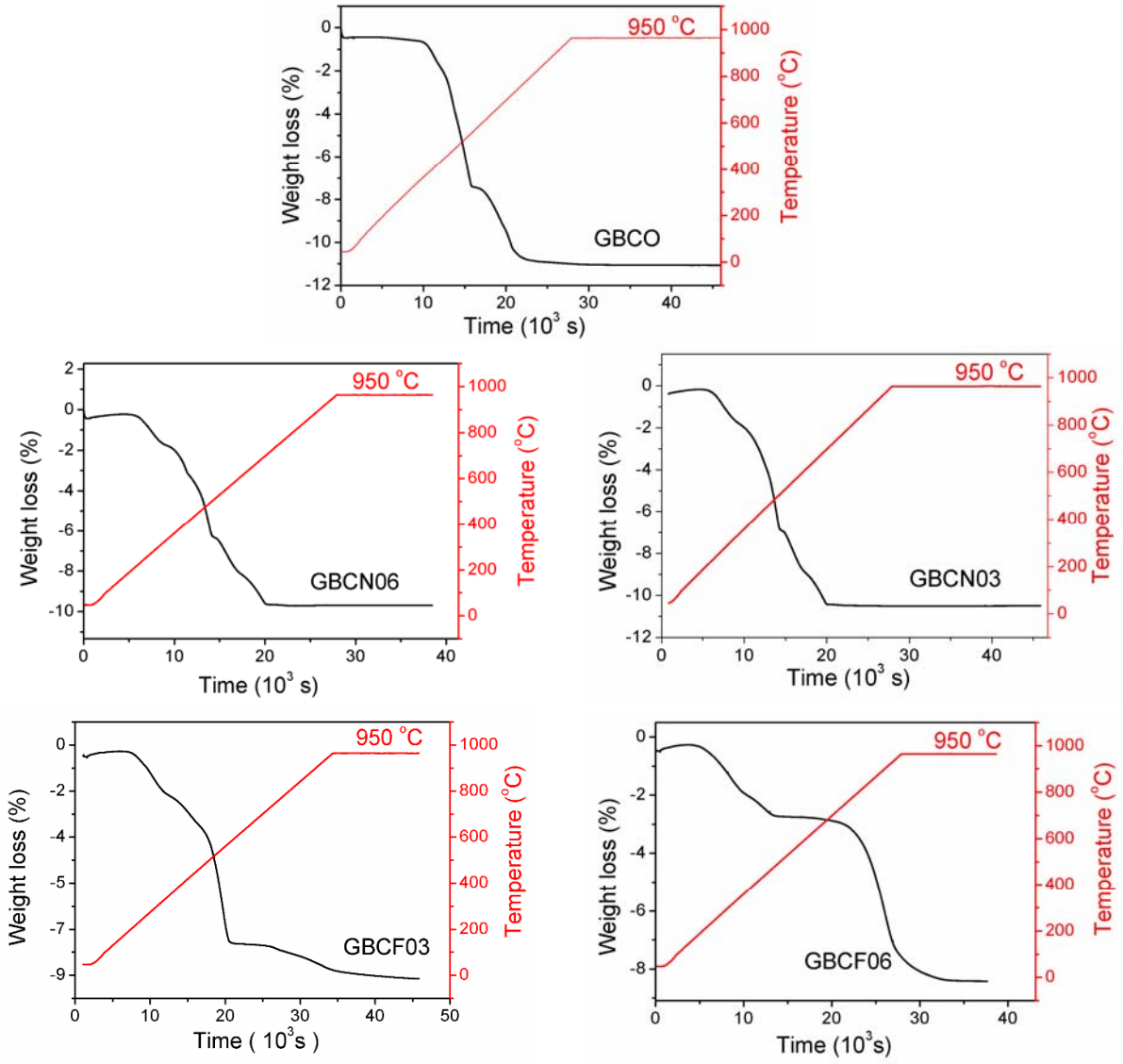

Figure 2.7 *TG curve of H_2 reduction for GBCO, GBCN03, GBCN06, GBCF03, and GBCF06. Black line and red line represent the mass loss in percentage and temperature, respectively.*

The reduction process by a reducing gas proceeds stepwise reactions [25], including desorption of surface water, decomposition of complex oxides and progressive reduction to metals, represented as weight losses at different reduction stages in the TG curve. In this work, the oxygen content analysis based on the overall weight loss is related to a "final plateau" of the TG weight loss (in percentage) curve, which was considered as the accomplishment of reduction process, referring to a residual pure oxide mixture and metallic cobalt and Ni or Fe. As shown in ***Figure 2.7***, the approximate starting temperature of the plateau is different for each composition. The weight plateau can be obtained at nearly 800 ºC for GBCO, which is in good agreement with the previous work of Conder *et a.l* [23], and at about 700 ºC for Ni substituted GBCN03 and GBCN06. On the other hand, for the Fe substituted GBCF03 and GBCF06, the weight "plateau" could only be obtained at 950 ºC, which is the highest in this work, after a period of isothermal process. This could probably be due to the difficulty of reduction of Fe oxides to metallic Fe.

Comparison of oxygen content determined by Iodometry method and TG/H2 method in this work, as well as the results from other work, is shown in Table 2.3. Oxygen content values determined by TG/H_2 are slightly higher than those obtained by Iodometry for pure GBCO and Ni substituted GBCN03, GBCN06. Generally speaking, these two methods seem in good accordance with each other. Remarkable decrease of oxygen content values with increase of Fe substitution is shown by TG/H_2. Considering the results of X-ray diffraction characterization for powder samples, the oxygen nonstoichiometry due to Fe substitution could be a major cause for the phase transition from orthorhombic to tetragonal with increase of Fe substitution in air-synthesized compounds.

Compounds	Total oxygen content		
	TG / H2	Iodometry	A. Bharathi et al [8] by Iodometry
GBCO	5.520	5.514	5.54 ± 0.01
GBCN03	5.512	5.502	5.50 ± 0.01
GBCN06	5.522	5.500	
GBCF03	5.356		
GBCF06	5.063		

Table 2.3 Oxygen content in $GdBaCo_{2-x}M_xO_{5+\delta}$ (M=Ni, Fe).obtained by different analytical methods used in this work

An oxygen content range $0.45 \leq \delta < 0.6$ referred to orthorhombic structure indexed in Pmmm symmetry was mentioned for single crystal $GdBaCo_2O_{5+\delta}$ sample by Taskin *et al.*[1]. In this work, nevertheless, both $GdBaCo_{1.2}Ni_{0.8}O_{5.338}$ and $GdBaCo_{1.7}Fe_{0.3}O_{5.356}$ with oxygen content $\delta < 0.45$, determined by Iodometry and TG/H_2, respectively, still sustain the orthorhombic Pmmm structure, as shown by X-ray diffraction.

2.5 Structural analysis

2.5.1 $GdBaCo_2O_{5+\delta}$

More recently, Maignan *et al.* [13] have studied the layered cobaltites $LnBaCo_2O_{5+\delta}$ ($0 \leq \delta < 1$, Ln = Pr, Nd, Sm, Eu, Gd, Tb, Dy, and Ho), with various oxygen stoichiometries. According to this study, the oxygen-deficient perovskites $LnBaCo_2O_{5+\delta}$ system showed a variation of oxygen content and of structure with the size of the lanthanide, which suggested a possible ordering between oxygen and vacancy in the lanthanide layer. Moreover, different superstructures depending on the sintering atmosphere were reported. ***Figure 2.8*** depicts the double layered oxygen-deficient structure of $GdBaCo_2O_{5+\delta}$ with orthorhombic Pmmm symmetry. In this structure, the Ba cations do not form a random distribution in the A perovskite sites but order in alternating (0 0 1) layers, following a stacking sequence along *c*-axis: – [BaO] – [CoO2] – [GdOδ] – [CoO2] – [BaO] –, characteristic of the 112 structure. Co ions are coordinated in square-pyramids (CoO_5) and octahedral (CoO_6), referred to intermediate spin state (IS) and low spin state (LS), respectively, with oxygen vacancies along (1 0 0) in the Gd plane.

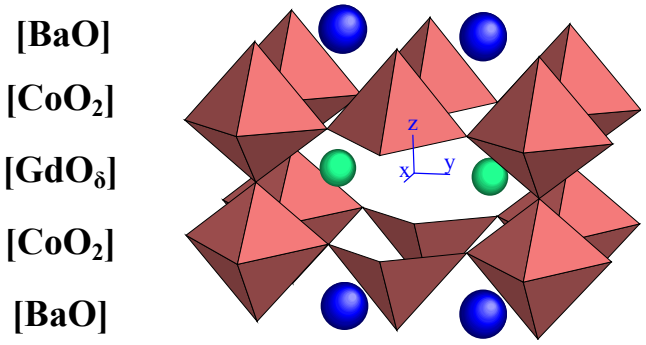

Figure 2.8 *Polyhedral view of the orthorhombic perovskite structure of $GdBaCo_2O_{5+\delta}$ indexed to Pmmm symmetry* [35]

Taskin *et al.* [1] concluded that, for the case of $GdBaCo_2O_{5+\delta}$, the presence of a particular distribution of oxygen vacancies located mainly in the rare earth plane [GdO_δ], observed for a certain range of oxygen stoichiometry, could improves the oxygen transport properties compared to non-ordered perovskites. And the following investigation [35] showed that this layered structure formed by cation ordering exhibited a remarkable enhancement of the oxygen diffusivity as well as a possibility to develop a class of materials suitable for applications requiring fast oxygen transport in the intermediate temperature range. For the crystal structural of $GdBaCo_2O_{5+\delta}$ at ambient, strong dependence on the oxygen stoichiometry has been proved as mentioned precisely in Chapter 2.4.

2.5.2 Structural analysis by Rietveld refinement

Apart from the original $GdBaCo_2O_{5+\delta}$, X-ray powder diffraction of $GdBaCo_{2-x}M_xO_{5+\delta}$ (M = Ni or Fe, x = 0.1, 0.2 …) has revealed the influence of Ni and Fe substitution for Co on the structural level, such as the enhancement of orthorhombic distortion with Ni and phase transition with Fe substitution. In this work, in order to obtain more detailed structural information, Rietveld refinement has been applied to analyze the XRD data.

Original structural information given by Frontera *et al.* [3] was used as starting model for the refinement of orthorhombic structure in case of all Ni substitutions and low Fe substitutions. As shown in ***Figure 2.9***, the schematic crystal structure of $GdBaCo_2O_{5+\delta}$, in which oxygen atoms are omitted and are only connected by lines. In the Pmmm orthorhombic structure, two cobalt sites and six oxygen sites are independent. The Co1 (0, 1/2, z) and Co2 (0, 0, z) sites correspond the octahedral and pyramidal sites, respectively. Among the six oxygen sites, three [O1 (0, 0, 0), O2 (0, 1/2, 0) and O3 (0, 1/2, 1/2)] sites are fixed in the Pmmm symmetry. On the other hand, the O4 (1/2, 0, z) and O5 (1/2, 1/2, z) site connect the neighboring pyramids and octahedral, respectively, along the ***a***-direction, whilst the O6 site does the neighboring pyramid and octahedron along the *b*-direction. O3' site corresponds to where the oxygen vacancies are located at (0, 0, 1/2) along the Gd plane. For the highly Fe substituted $GdBaCo_{2-x}Fe_xO_{5+\delta}$ ($x > 0.4$) with tetragonal structure, starting information was referred to the high temperature structure of $PrBaCo_2O_{5+\delta}$ given by Streule *et al.* [36] in P4/mmm space group, according to which, the oxygen vacancies locate at the O2 (0, 0, 1/2) site being proved by refinement of data from neutron diffraction. Detailed information of this model including atomic positions and Wyckoff coefficients are listed in Table 2.4, based on which the refinement are carried out.

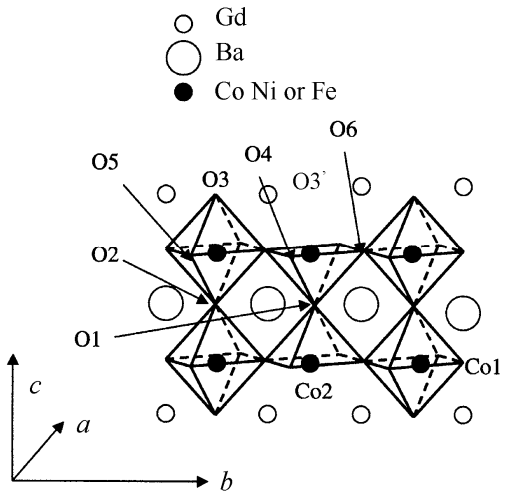

Figure 2.9 *Schematic model for crystal structure of orthorhombic* $GdBaCo_{2-x}M_xO_{5+\delta}$ *(M = Ni or Fe)* [34]

Orthorhombic (*Pmmm*)					Tetragonal (*P4/mmm*)				
atom	Wyckoff	X	Y	Z	atom	Wyckoff	X	Y	Z
Ba	2o	0.5	y	z	Ba	1c	0.5	0.5	0
Gd	2p	0.5	y	0.5	Gd	1d	0.5	0.5	0.5
Co(Ni or Fe)1	2r	0	0.5	z	Co(Ni or Fe)	2g	0	0	z
Co(Ni or Fe)2	2a	0	0	z	O1	1a	0	0	0
O1	1a	0	0	0	O2	1b	0	0	0.5
O2	1e	0	0.5	0	O3	4i	0	0.5	z
O3	1g	0	0.5	0.5					
O3’	1c	0	0	0.5					
O4	2s	0.5	0	z					
O5	2t	0	0	z					
O6	4u	0	y	z					

Table 2.4 Crystal structure models [36] *for Rietveld refinement in this work*

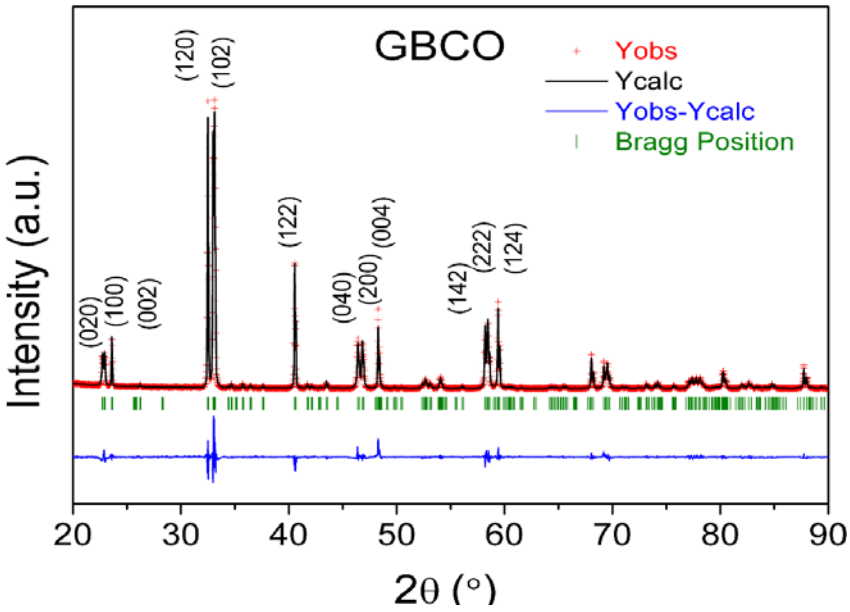

(a) $GdBaCo_2O_{5+\delta}$: R_{Bragg} = 4.83.4; R_F = 3.81 R_p =12.2; R_{wp} =15.3; R_{exp} = 9.43

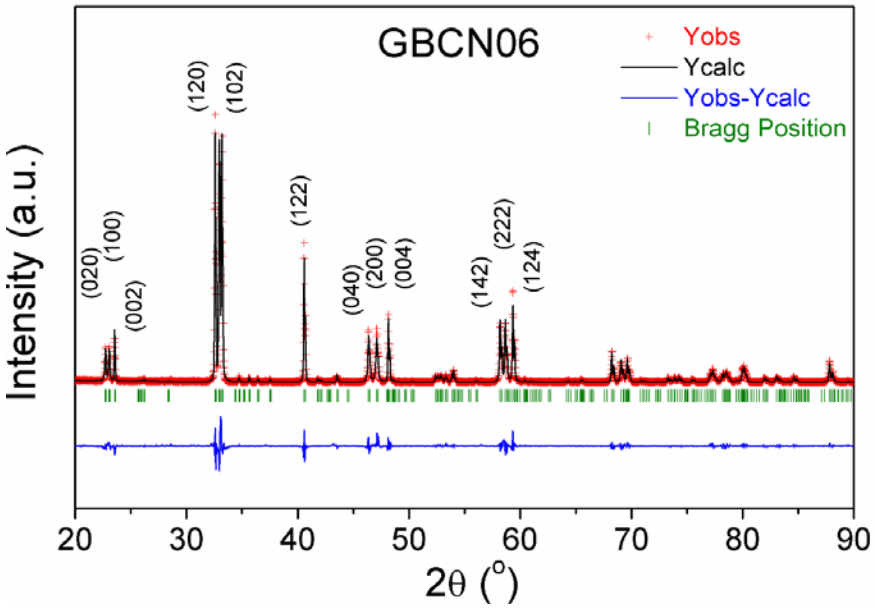

(b) $GdBaCo1_{1.4}Ni_{0.6}O_{5+\delta}$: R_{Bragg} = 4.86; R_F = 4.33; R_p = 13.3; R_{wp} = 17.1; R_{exp} = 9.96

Figure 2.10 *Diagrams of XRD powder diffraction data refined by Rietveld method for (a) $GdBaCo_2O_{5+\delta}$ and Ni substituted (b) $GdBaCo_{1.4}Ni_{0.6}O_{5+\delta}$; orthorhombic, space group Pmmm; reliability factors are listed below each pattern*

As-synthesized powder samples of $GdBaCo_{2-x}M_xO_{5+\delta}$ (M = Ni, Fe) followed by the same annealing process as described in 2.4.2 were characterized by X-ray powder diffraction (XRD, Rigaku D/max-2550/pc, Cu *K*α radiation, $\lambda_{K\alpha1}$ = 1.5405Å). Collected data were refined by the Rietveld method using Fullprof suite program. Information of cell parameters and atomic positions with Ni and

Fe substitutions were extracted from the Rietveld refinement. Oxygen content obtained by Iodometry and TG/H_2 methods in Chapter 2.3 were used as reference to determine the oxygen occupancy at the O3' site.

Figure 2.10 shows the results of Rietveld refinement for $GdBaCo_2O_{5+\delta}$ and $GdBaCo_{1.4}Ni_{0.6}O_{5+\delta}$. In the diagram, the crosses (+) and solid lines represent the experimental data and calculated curve, respectively, while the blue solid lines being their difference in the bottoms. The green vertical bars indicate the Bragg angle positions corresponding to the structure. Refined atomic coordinates and agreement factor are given in Table 2.5. For the Ni substitution, the occupancies of O3 and O3' sites are fixed according to the oxygen stoichiometry determined above by iodometry.

Atom		X GdBaCo$_{2-x}$Ni$_x$O$_{5+\delta}$								
		0	0.1	0.2	0.3	0.4	0.5	0.6	0.7	0.8
Ba(y)	2o	0.2507(3)	0.2503(3)	0.2494(3)	0.2483(3)	0.2488(3)	0.2481(5)	0.2480(3)	0.2492(3)	0.2489(4)
Gd(y)	2p	0.2718(3)	0.2712(2)	0.2707(3)	0.2690(3)	0.2683(3)	0.2688(5)	0.2684(3)	0.2681(3)	0.2677(4)
CoNi1(z)	2r	0.2519(10)	0.252(1)	0.252(1)	0.2519(9)	0.253(1)	0.250(2)	0.2515(10)	0.252(1)	0.251(1)
CoNi2 (z)	2p	0.2546(9)	0.255(1)	0.255(1)	0.2553(9)	0.255 (1)	0.255(2)	0.2542(10)	0.2548(10)	0.254(1)
O4(z)	2s	0.308(3)	0.318(3)	0.314(2)	0.315(2)	0.318(3)	0.313(4)	0.315(3)	0.313(3)	0.318(3)
O5(z)	2t	0.269(3)	0.277(3)	0.275(3)	0.271(3)	0.272(4)	0.275(6)	0.273(3)	0.273(3)	0.268(5)
O6(y)	4u	0.252(2)	0.248(2)	0.246(2)	0.232(2)	0.238(2)	0.239(3)	0.237(2)	0.238(2)	0.245(3)
O6(z)	4u	0.251(2)	0.300(2)	0.298(1)	0.292(2)	0.292(2)	0.295(2)	0.292(2)	0.292(2)	0.297(2)
Occ. O3	1g	1	1	1	1	1	1	1	0.964	0.676
Occ. O3'	1c	0.028	0.064	0.064	0.004	0.06	0.004	0	0	0
R_{Bragg}		4.83	5.77	3.76	4.29	3.98	4.5	4.86	4.43	4.01
R_F		3.81	4.51	3.23	3.81	3.46	4.89	4.33	3.84	3.52
χ		1.6	1.6	1.4	1.6	2.0	1.2	1.7	1.8	1.6

Table 2.5 Structural parameters and reliability factors for the Rietveld refinement of $GdBaCo_{2-x}Ni_xO_{5+\delta}$

The cell parameters and cell volume as a function of Ni doping content refined by rietveld method are shown in ***Fgure 2.11***. Cell volume is represented as unit cell volume ($a_p \times a_p \times a_p$) instead of the real double layered cell volume (($a_p \times 2a_p \times 2a_p$).

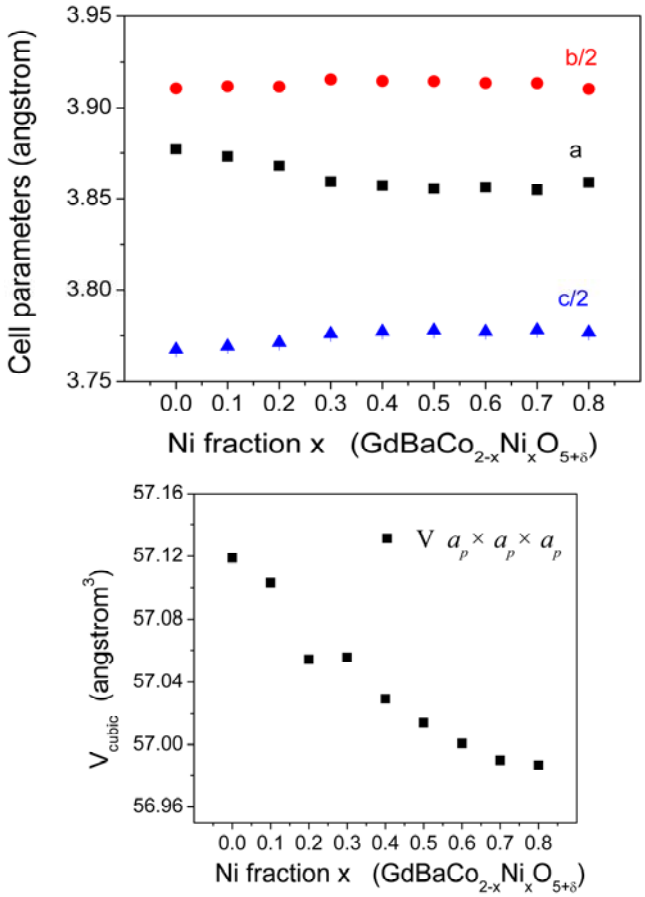

Figure 2.11 *Evolution of cell parameters and cubic cell volume with Ni substitution; by Rietveld refinement*

It can be seen that, for $x \leq 0.4$, a decrease of the *a*-lattice parameter is observed, whereas both *b* and *c* parameters show a small increase. This trend is in good agreement with some previous works of Ni substituted $GdBaCo_2O_{5+\delta}$ [8,21]. Along with the increase of Ni substitution, in case of $x > 0.4$, the lattice parameters show an inverse trend of evolution: Slight decrease of the *b*-lattice parameter is observed, whereas the *a*-lattice parameter shows a small increase, meanwhile the *c* parameter seems approximately constant. Nevertheless, the cell volume shows an uneventful decrease with Ni increasing substitution.

As investigated previously, the increase of Fe substitution in $GdBaCo_{2-x}Fe_xO_{5+\delta}$ gives rise to a phase transition from orthorhombic with space group Pmmm to tetragonal with space group P4/mmm and a successive decrease of oxygen content according to the X-ray diffraction and thermogravimetric

H_2 reduction results. Thus for $x \leq 0.3$, orthorhombic Pmmm structure was used in the characterization, and for $x > 0.4$, tetragonal P/4mmm structure was applied, as shown in ***Figure 2.12 (a) and (b)***. An unexpected difficulty in refining the X-ray diffraction data of air-annealed $GdBaCo_{1.6}Fe_{0.4}O_{5+\delta}$ powder sample with one phase, Pmmm or P4/mmm, has suggested a possibility of existence of mixture of two phases in this compound. Consequently, $GdBaCo_{1.6}Fe_{0.4}O_{5+\delta}$ was refined using two phases, as shown in ***Figure 2.13***.

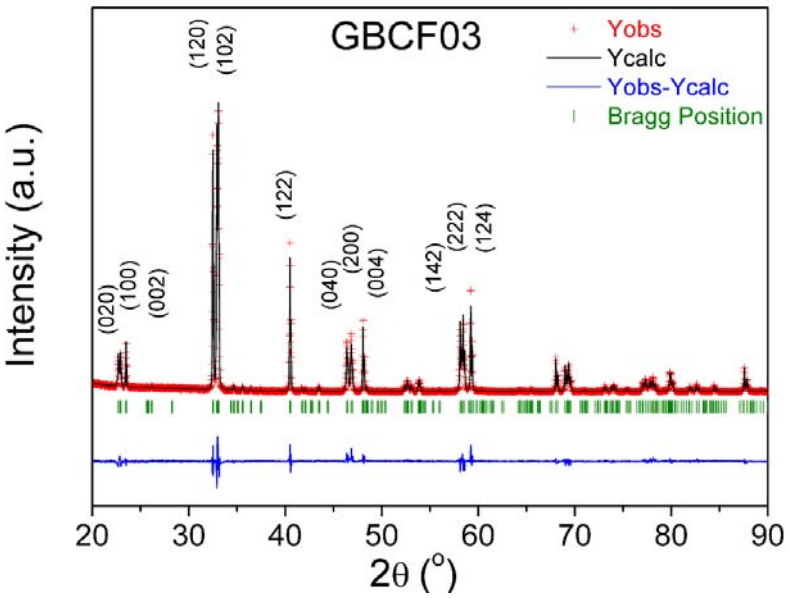

(a) $GdBaCo_{1.7}Fe_{0.3}O_{5+\delta}$: $R_{Bragg} = 6.94$; $R_F = 10.3$; $R_p = 14.8$; $R_{wp} = 16.6$; $R_{exp} = 10.7$

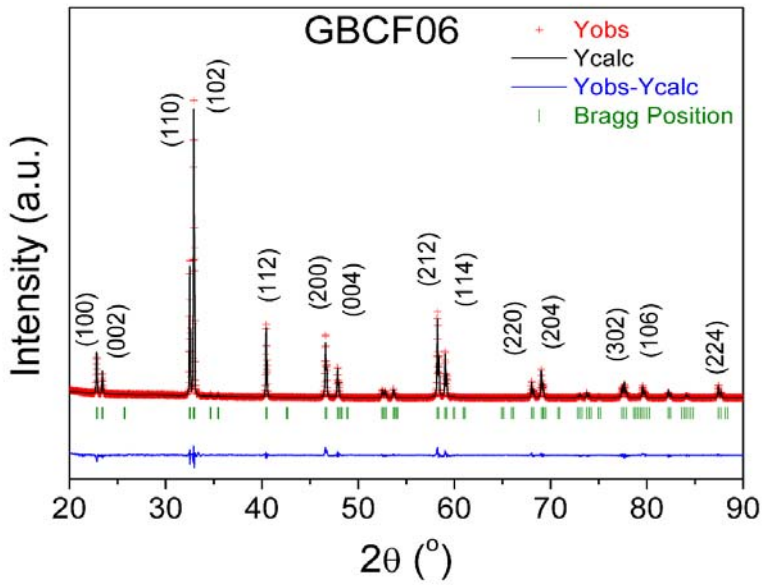

(b) $GdBaCo_{1.4}Fe_{0.6}O_{5+\delta}$: $R_{Bragg} = 4.92$; $R_F = 5.84$; $R_p = 13$; $R_{wp} = 16.5$, $R_{exp} = 10.33$

Figure 2.12 *Diagrams of results refined by Rietveld method for Fe substituted $GdBaCo_{2-x}Fe_xO_{5+\delta}$: a) x = 0.3 b) x = 0.6*

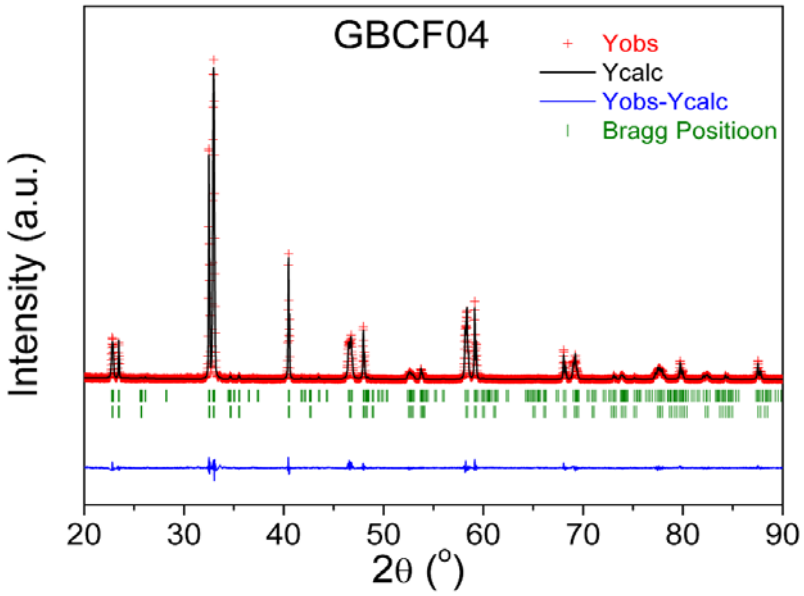

$GdBaCo_{1.6}Fe_{0.4}O_{5+\delta}$:

Pmmm: R_{Bragg} = 3.81; R_F = 6.19; R_p = 11.1; R_{wp} = 14.8, R_{exp} = 10.92

P4/mmm: R_{Bragg} =3.12; R_F = 4.53; R_p = 11.4; R_{wp} = 14.9, R_{exp} = 10.98

Figure 2.13 *Diagrams of results refined by Rietveld method for* $GdBaCo_{1.6}Fe_{0.4}O_{5+\delta}$:

Due to the fact that X-ray powder diffraction is not able to precisely define the oxygen occupancy and oxygen vacancy distribution, it is difficult to extract structural information about the oxygen nonstoichiometry introduced by Fe substitution. Neutron diffraction could have been considered as a better alternative but unfortunately this option is also unfeasible because of the presence of highly absorbing gadolinium in the investigated materials in present work. Nevertheless, structural information obtained by refining neutron diffraction data of some highly analogous materials, which have been proved to possess a wide range of similarities in structure such as space group, oxygen distribution, cation ordering, *etc.* can help to explore the structural evolution with Fe substitution for the materials studied in this work. For example, high temperature tetragonal phase of $PrBaCo_2O_{5+\delta}$ [8] and Fe substituted $TbBaCoCo_2O_{5+\delta}$ [36] revealed that with the P4/mmm tetragonal phase, the oxygen vacancy lies at O2 (0, 0, 1/2) site. The Refined parameters and reliability factors are listed in Table 2.6.

Cell parameters and unit cell volume ($a_p \times a_p \times a_p$) as a function of Fe substitution content obtained by by rietveld refinement are shown in ***figure 2.14(a)***. With the increase of Fe substitution, the lattice parameter *c* increases as well as the unit cell volume ($a_p \times a_p \times a_p$), which is partially in agreement with the work of Tang *et al.*[37]. This trend is independent of phase transition. On the contrary, no evidence

trend for *a* or *c* lattice parameter in the orthorhombic range is shown in this work, compared to the slight increase of *a* and *c* in the literature mentioned above, ***Figure 2.14 b)***. In the case of x > 0.4, with tetragonal structure, both lattice parameters *a* (*a* = *b*) and *c* increase regularly with Fe substitution.

		X	$GdBaCo_{2-x}Fe_xO_{5+\delta}$							
		Orthorhombic					Tetragonal			
Pmmm		0.1	0.2	0.3	0.4	*P4/mmm*		0.4	0.6	0.8	0.9
Ba(y)	2o	0.2505(5)	0.2501(3)	0.2504(3)	0.2503(4)	Ba	1c				
Gd(y)	2p	0.2697(4)	0.2703(3)	0.2688(3)	0.2626(4)	Gd	1d				
CoFe1(z)	2r	0.250(2)	0.252(1)	0.2526(9)	0.253(2)	CoFe1(z)	2g	0.254(2)	0.2521(9)	0.2539(8)	0.2527(9)
CoFe2(z)	2p	0.254(2)	0.255(1)	0.2536(9)	0.255(2)						
O4(z)	2s	0.323(4)	0.324(3)	0.314(3)	0.304(5)	O1	1a				
O5(z)	2t	0.265(7)	0.268(4)	0.277(3)	0.288(5)	O2	1b				
O6(y)	4u	0.250(4)	0.239(2)	0.243(2)	0.250(3)	O3	4i	0.312(4)	0.292(1)	0.293(1)	0.294(1)
06(z)	4u	0.293(3)	0.294(2)	0.293(2)	0.300(3)						
Occ. O3	1g	0.9	0.8	0.712		Occ. O2			0.063	0	0
Occ. O3'	1c	0	0	0							
R_{Brgg}		4.89	5.1	4.95	3.81			3.12	4.33	4.19	4.54
R_F		4.88	4.82	4	6.19			4.53	4.15	5.39	4.52
χ		1.00	1.06	1.24	0.62			1.36	1.04	0.78	1.00

Table 2.6 Structural parameters and reliability factors for the Rietveld refinement of $GdBaCo_{2-x}Fe_xO_{5+\delta}$

Kopcewicz *et al.* [33] have investigated the analogous $TbBaCo_{2-x}Fe_xO_{5.5-\delta}$ using Mössbauer spectroscopy, and found that the Fe^{3+} ions preferentially adopt a HS state at the pyramidal sites. In addition, the radius of 0.645 Å for the HS state Fe^{3+} ions is larger than the radius of 0.56 Å for the IS state Co^{3+} ions at the pyramidal sites [33], which are the ones replaced by the Fe^{3+} ions in the doping process. This could explain the increase in the unit cell volume of $GdBaCo_{2-x}Fe_xO_{5.5-\delta}$ with increasing Fe substitution for Co. In addition, their study conclude that Fe ions adopt 3+ charge states in a wide concentration range 0 < x < 1, which gives rise to the presence of Co^{2+}, in contrast to the case of Ni

substitution presenting Co^{4+} preferentially introduced by Ni^{2+}; moreover, the Fe substitution leads to the decrease of oxygen content, in agreement with what is observed in this work.

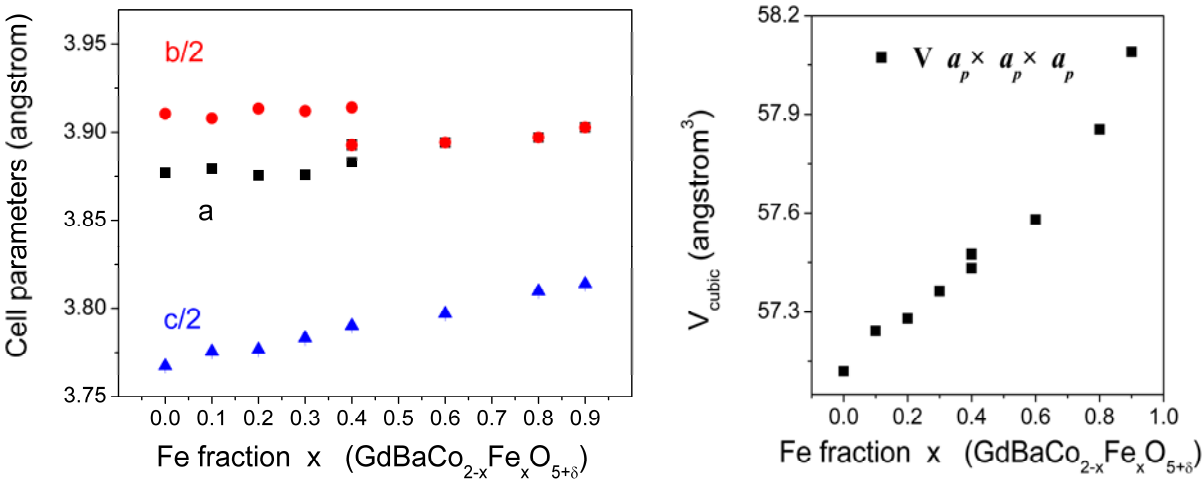

(a) Evolution of cell parameters and cubic cell volume with Fe substitution; by Rietveld refinement in this work

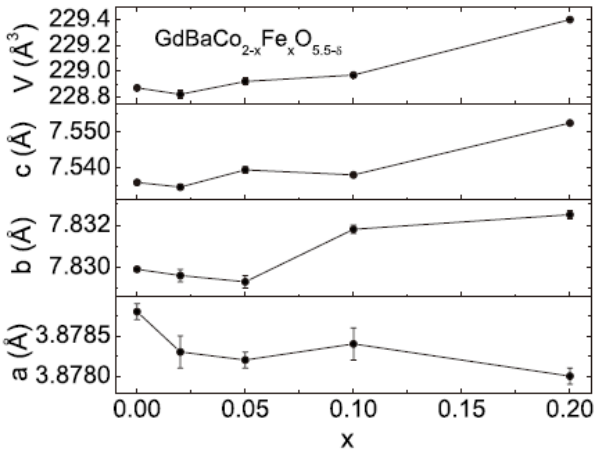

(b) Dependence of the structural parameters on the Fe concentration x in $GdBaCo_{2-x}Fe_xO_{5.5-\delta}$ by Tang *et al.* [7]

Figure 2.14 *Evolution of cell parameters with Fe substitution*

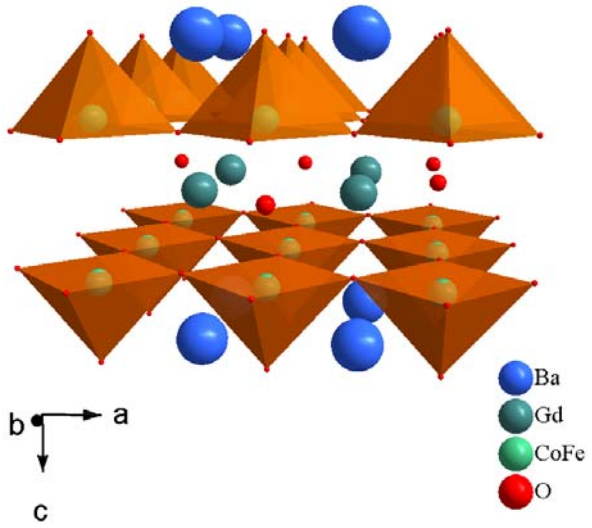

Figure 2.15 *Polyhedral view of $GdBaCo_{1.4}F_{e0.6}O_{5+\delta}$ based on refinement result*

Figure 2.15 shows the polyhedral view of the $GdBaCo_{1.4}F_{e0.6}O_{5+\delta}$ with tetragonal structure (P4/mmm) based on the information obtained from rietveld refinement, as can be seen in Table 2.6. With the phase transition from orthorhombic to tetragonal, the ordered perovskite goes trough a random two-dimensional distribution of oxygen vacancies in the Gd (100) layers. As the oxygen vacancies increase, using the oxygen content x = 0.063 determined by TG/H_2 method, the occupancy of O2 (0, 0, 1/2) site get close to 0. It could be assumed that a redistribution of oxygen ions takes place with Fe substitution: the oxygen O3' occupancy increases at the expense of the O3 one (O3' and O3 in orthorhombic phase), until the two sites display equivalent occupancies, transforming to O2 site (in tetragonal phase). This redistribution of oxygen leads to a disordered state in view of oxygen vacancies, since the planes of CoO_5 pyramids and CoO_6 octahedra no longer alternate along the *b* direction.

2.6 High temperature phase transition

Due to the importance of oxygen transport properties for electrode applications, it is essential to investigate the effects of the high temperature phase transition (orthorhombic Pmmm to tetragonal P4/mmm), which involves a rearrangement of oxygen vacancies going from low temperature one-dimensional distribution to high temperature two-dimensional distribution, on the electrical and electrochemical performance. Effect of phase transition on high-temperature electrical properties of $GdBaCo_2O_{5+\delta}$ has been studied by Tarancón *et al* [38].

Considering the structural evolution, oxygen stoichiometry variation in as-synthesized $GdBaCo_{2-x}M_xO_{5+\delta}$ (M = Ni or Fe, x = 0.1, 0.2 …) compounds, it is of interest to explore the existence of the high temperature phase transition and the possible influence by Fe and Ni substitution associated to this particular feature.

2.6.1 Differential Scanning Calorimetry (DSC)

Differential Scanning Calorimetry (DSC) is a thermoanalytical technique in which the difference of heat required to increase the temperature of a sample and a reference is measured as a function of temperature. When the sample undergoes a physical transformation such as phase transitions, more (or less) heat, depending on weather the process is exothermic or endothermic, will need to flow to it than to the reference to maintain both at the same temperature.

In this work, DSC has been applied to determine the existence of high temperature phase transition and the precise transition temperature (in case it exists). These measurements were carried out using a SETARAM TG/DSC, Model 92-1750 instrument, in static air condition, as well as Ar or O_2 atmosphere in certain cases, following a heating/cooling rate of 10 ºC/min till 700 ºC.

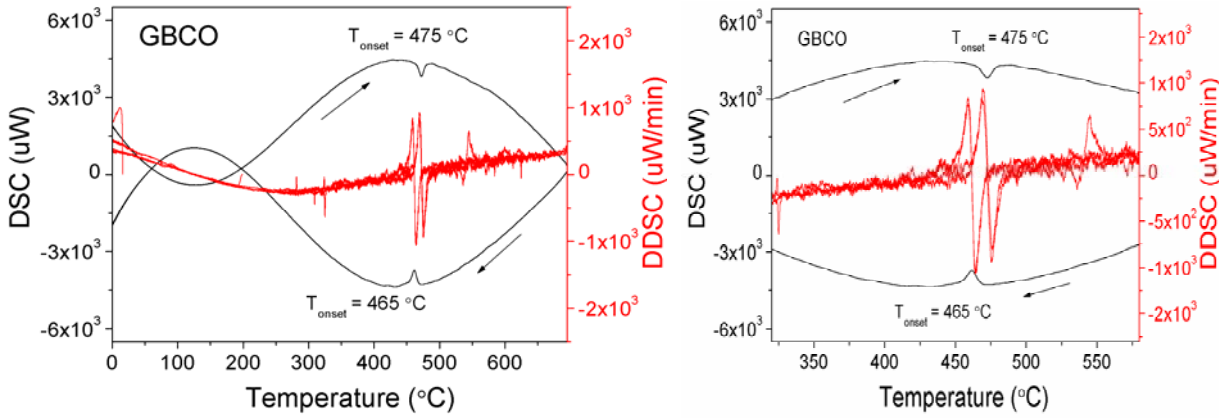

Figure 2.16 *Example of DSC curves for $GdBaCo_2O_{5+\delta}$: Arrows indicate the heating and cooling cycles, right pattern is enlarged zone covering the phase transition*

A typical DSC curve is shown in ***Figure 2.16***, obtained for GBCO sample. The small peaks on the DSC curve represent the appearance of phase transitions, corresponding to the structural change from orthorhombic Pmmm space group to tetragonal P4/mmm space group at high temperature, taking place at different temperatures in heating and cooling runs with a discrepancy of about 10 °C.

The results of high temperature phase transition in $GdBaCo_{2-x}M_xO_{5+\delta}$ (M=Ni or Fe, x = 0.1, 0.2 …) determined by DSC on the heating run in this work are shown in ***Figure 2.17.*** Both Ni and Fe substitution induce a decrease of the HT phase transition. With Fe content x > 0.4, no phase transition was observed on the DSC curve, which is in agreement with the fact that those compounds process a tetragonal structure with P4/mmm symmetry at room temperature.

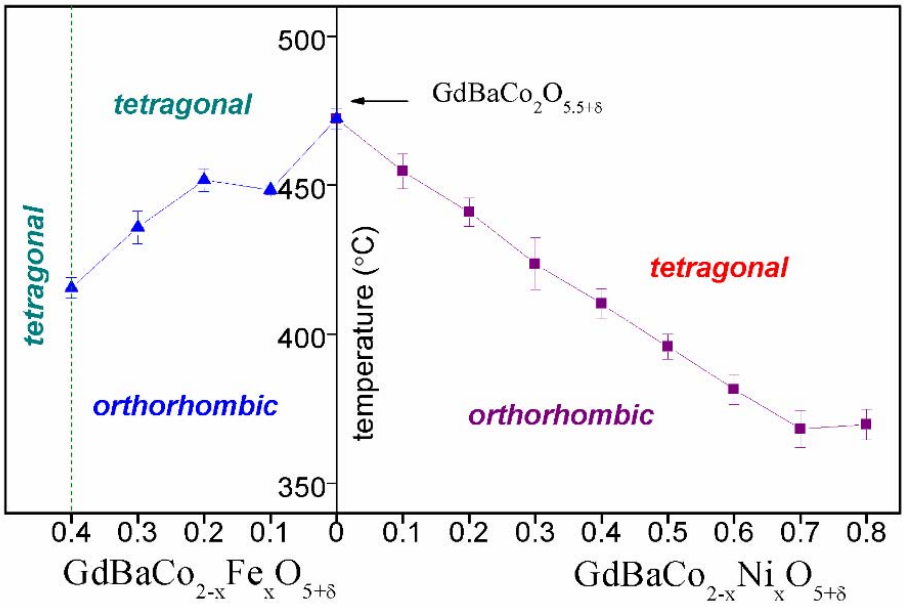

Figure 2.17 *DSC results of $GdBaCo_{2-x}M_xO_{5+\delta}$ (M=Ni or Fe, x = 0.1, 0.2 …), transition temperature determined from the T onset on the heating process*

2.6.2 High-temperature X-ray diffraction

In this work, 5 major compounds were studied by High-temperature XRD: $GdBaCo_2O_{5+\delta}$, $GdBaCo_{1.7}Ni_{0.3}O_{5+\delta}$, $GdBaCo_{1.4}Ni_{0.6}O_{5+\delta}$, $GdBaCo_{1.7}Fe_{0.3}O_{5+\delta}$ and $GdBaCo_{1.4}Fe_{0.6}O_{5+\delta}$, abbreviated as GBCO, GBCN03, GBCN06, GBCF03 and GBCF06, respectively. High-temperature XRD (25 –700 ºC) were carried out in air condition, on a laboratory diffractometer using Cu Kα1 radiation. Profile matching of the XRD pattern was preformed using Fullprof suite program using LeBail fitting. Atomic parameters were not refined. In accordance with previous works of Tarancón *et al.* [38] and Streule *et al.* [37], similar high temperature phase transition phenomenon was observed For GBCO in this work, as shown in ***Figure 2.18.***

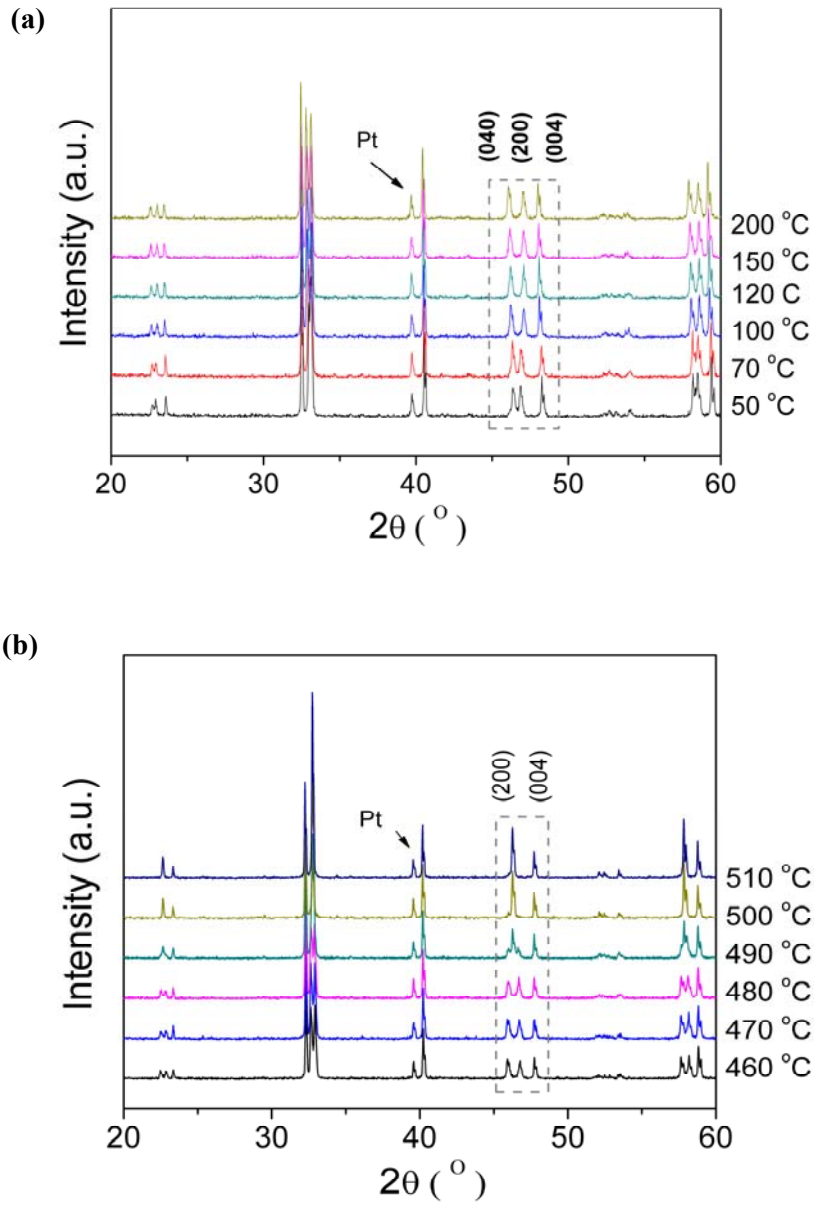

Figure 2.18 *Thermal evolution of GBCO by high temperature XRD: a) Low temperature transition; b) high temperature transition with space group change from Pmmm to P4/mmm*

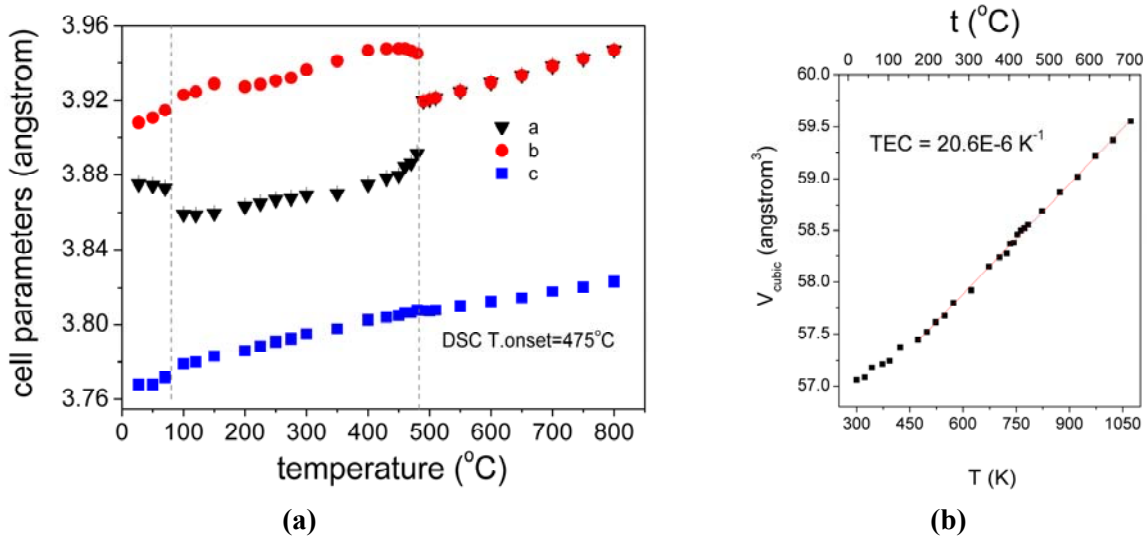

Figure 2.19 *Temperature dependent structural evolution of GBCO extracted from XRD: (a) evolution of cell parameters (dashed lines indicate the low- and high – temperature transition);(b) temperature dependence of unit cell volume and TEC from partially linear fitting of the volume curve*

Low temperature XRD patterns (T < 490 °C) were indexed using the orthorhombic Pmmm space group (unit cell $a_p \times 2a_p \times 2a_p$, with a_p as the lattice parameter of the cubic unit cell). While high temperature phase is tetragonal with space group P4/mmm (unit cell $a_p \times a_p \times a_p$). ***Figure 2.19*** shows the thermal evolution of the lattice parameters. This representation makes evident the presence of two different structural transitions for $GdBaCo_2O_{5+\delta}$. The low temperature (LT) structural transformation takes place at *ca.* 80 °C and corresponds to a sudden shrink of *a* lattice parameter, while lengthening of *b* and *c*. ***Figure 2.18 (a)*** clearly shows this anisotropic evolution with temperature of the unit lattice parameters by following the peaks indexed (0 4 0), (2 0 0) and (0 0 4) marked by the gray dashed rectangular frame .On the other hand, the high-temperature (HT) structural change takes place at ca. 490 °C and corresponds to a proper phase transition from the orthorhombic Pmmm space group ($a_p \times 2a_p \times 2a_p$) to the tetragonal space group P4/mmm ($a_p \times a_p \times a_p$). The vanish of peaks indexed (0 4 0) and (2 0 0) in Pmmm symmetry and successive generation of a new peak indexed (0 0 4) in P4/mmm symmetry at this transition temperature, which is in agreement with DSC result ca. 475 °C, is shown in ***Figure 2.18 (b)*** suggesting the lower symmetry of the high-temperature phase. ***Figure 2.19 (a)*** depicts the unit cell volume increases nearly linearly with the temperature although a phase transition occurs. Therefore, the linear thermal expansion coefficient (α_L) can be calculated (as derived from the volumetric thermal expansion coefficient, i.e. $\alpha_V \equiv 3\alpha_L$. The obtained value of linear thermal expansion coefficient (TEC) for $GdBaCo_2O_{5+\delta}$ at high temperature range is 20.6×10^{-6} K^{-1} in the range of

temperatures from 175 to 700 °C, in accordance with the TECs for cobaltites and published TEC for GBCO [38-40]. Moreover, GBCN03, GBCN06 and GBCF03 compounds show a similar phase transition from low temperature orthorhombic Pmmm structure to high temperature tetragonal P4/mmm structure, with an evolution of transition temperature in accordance with results determined by DSC. Thermal evolution of the cell parameters and unit cell volume obtained by LeBail refinement of high temperature XRD data are shown in ***Figure 2.20***.

In general, for Ni substituted $GdBaCo_{2-x}Ni_xO_{5+\delta}$ (x = 0.1~0.8) and low-proportional Fe substituted $GdBaCo_{2-x}Fe_xO_{5+\delta}$ (x = 0.1 ~ 0.4) both possessing orthorhombic structure indexed to Pmmm space group at ambient, two different transitions are expected over the investigated temperature range. One is the metal-insulator (MI) transition at low temperature, as the sudden shrink of lattice parameters mentioned above. This behavior has been reported previously by Frontera *et al*. [3] in GBCO, as well as similar MI transition observed in other analogous materials such as $TbBaCo_2O_{5+\delta}$ [41,42], $HoBaCo_2O_{5+\delta}$ [43,44] and $PrBaCo_2O_{5+\delta}$ [37,45]. In these oxides, Co can have multiple spin states in a given oxidation state Co^{3+}: low spin state (LS, $t_{2g}^6 e_g^0$), intermediate spin state (IS, $t_{2g}^5 e_g^1$) and high spin state (HS, $t_{2g}^4 e_g^2$), as well the small energy difference between the different spin states enables spin state transition [3]. In these investigated samples, it has been proposed that the Co^{3+} occupies the IS in the pyramidal environment and the LS in the octahedral environment at low temperature, whilst at high temperature the Co^{3+} in octahedral attains the IS state. The observed MI transition is devoted to a first-order spin-state transition, from LS to HS of the Co^{3+} ions located at the octahedral site, and the concomitant lattice distortion due to the larger ionic radius of the high-spin state cobalt ions, as the observed shrink of lattice parameters. However, in the present work, this phenomenon was only evident for pure GBCO according to the structural evolution extracted from the temperature dependent XRD results, and almost invisible in Ni and Fe substituted compounds. Recent studies in Ni and Fe substituted $LnBaCo_2O_{5+\delta}$ in s [7,8,33,46] revealed that Ni substitution could decrease the MI temperature as a consequence of the local structure distortions introduced by Ni^{2+}, while Fe substitution leads to the opposite due to the reducing of LS Co^{3+} ions located at octahedral site resulting from the oxygen vacancies introduced by Fe, as well as the larger thermal energy need to excite the Co^{3+} ions from LS to HS state with Fe substitution [33].

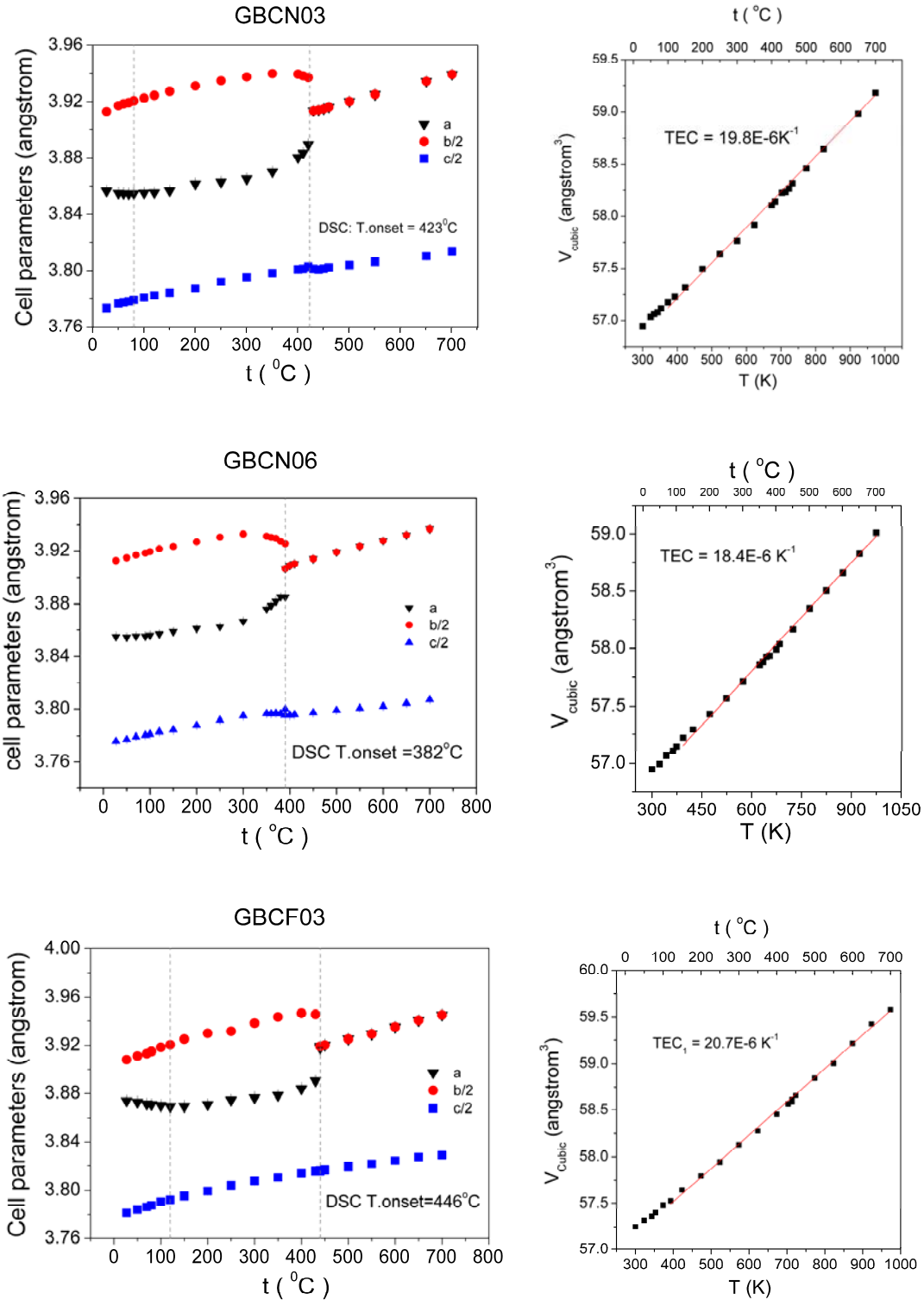

Figure 2.20 *Thermal evolution of lattice parameters and unit cell volume (on the right for each) of GBCN03, GBCN06 and GBCF03 Dashed lines mark the position of the low and high temperature structure transition.*

On the other hand, both Ni and Fe substitution seem to facilitate the occurrence of high-temperature phase transition from orthorhombic Pmmm structure to tetragonal P4/mmm structure by reducing the transition temperature, as certificated by both DSC and high-temperature XRD. The same phase transition could also take place with variation of oxygen stoichiometry, according to the work of Maignan *et al*. [13] and Taskin *et al*.[1]. Therefore, this phase transition can be achieved by either controlling the temperature or the oxygen stoichiometry. The highly Fe substitued $GdBaCo_{2-x}Fe_xO_{5+\delta}$ ($x > 0.4$) with tetragonal P4/mmm structure was supposed to avoid this orthorhombic-to-tetragonal phase transition at high temperature. Nevertheless, an intermediate temperature phase transition was accidentally observed in GBCF06 compound by the high-temperature XRD.

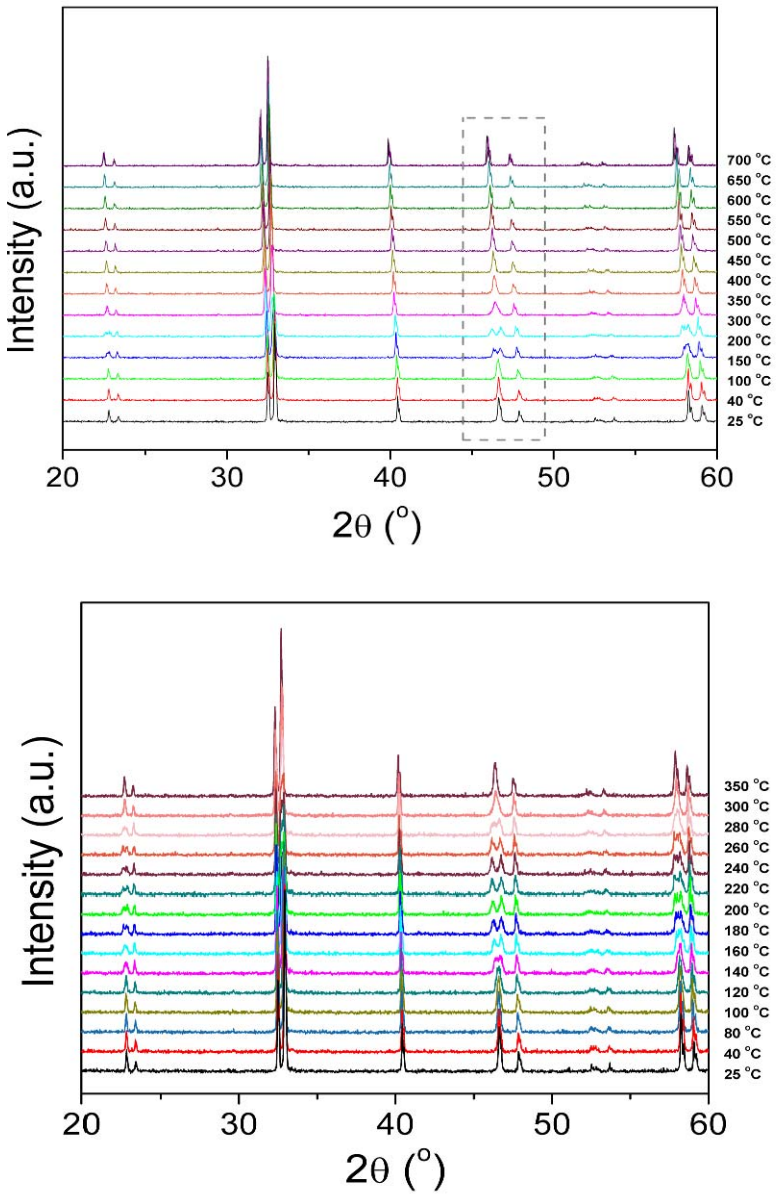

Figure 2.21 *High-temperature XRD pattern of $GdBaCo_{1.4}Fe_{0.6}O_{5+\delta}$ with a tetragonal-orthorhombic-tetragonal phase transition; orthorhombic phase exists in the temperature range 140~280 °C*

Figure 2.21 shows the high-temperature XRD patterns obtained in air condition from ambient temperature to 700 ºC. Former structural analysis has proved the tetragonal structure with P4/mmm space group of air-synthesized $GdBaCo_{1.4}Fe_{0.6}O_{5+\delta}$. However, it is evident that with the increase of temperature, the $GdBaCo_{1.4}Fe_{0.6}O_{5+\delta}$ compound undergoes a two step phase transition: tetragonal (P4/mmm, $a_p \times a_p \times 2a_p$)-orthorhombic (Pmmm, $a_p \times 2a_p \times 2a_p$)-tetragonal (P4/mmm, $a_p \times a_p \times 2a_p$). The diagram in ***Figure 2.21 (bottom)*** revealed the temperature range of existence of orthorhombic phase. First phase transition from tetragonal to orthorhombic is shown at *ca.* 140 ºC, whilst the second one from orthorhombic to tetragonal takes place at *ca.* 280 ºC. The presence of orthorhombic structure is limited in an intermediate temperature range between 100 ºC and 300 ºC.

Thermal evolution of the lattice parameters for $GdBaCo_{1.4}Fe_{0.6}O_{5+\delta}$ obtained by LeBail refinement is shown in ***Figure 2.22***. Uneventful increase of *c* lattice parameter is observed as a function of temperature, as well as a (= *b)* lattice parameter in tetragonal structure at low and high temperature. From *ca*. 140 ºC, after the orthorhombic to tetragonal phase transition, the difference between the values of *a* and *b* lattice parameters starts to increase. This could possibly indicate the oxygen rearrangement enhancing the orthorhombic distortion. After *ca*. 200 ºC, the *b* parameter starts to decrease as well the increase of *a* parameter, which exhibits the trend of phase transition towards the tetragonal P4/mmm structure involving a two-dimensional redistribution of oxygen vacancies in (0 0 1) layer, until the accomplishment of orthorhombic to tetragonal phase transition above 300 ºC.

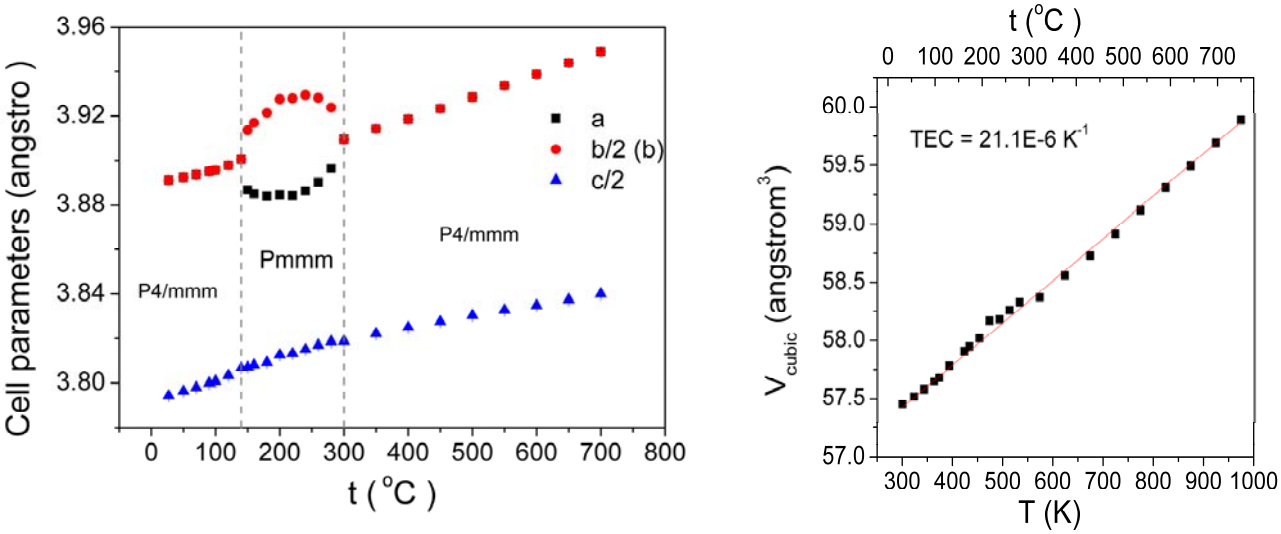

Figure 2.22 *Thermal evolution of lattice parameters for $GdBaCo_{1.4}Fe_{0.6}O_{5+\delta}$, dashed line mark the position of phase transition. Linear TEC coefficient is obtained by linear fitting of unit cell volume curve*

Some nonlinear dilatations of unit cell volume in the v-T line present in the orthorhombic temperature range. Considering the low oxygen stoichiometry of $GdBaCo_{1.4}Fe_{0.6}O_{5+\delta}$ determined by TG/H_2 in this work, which gives rise to the tetragonal P4/mmm structure at ambient, an assumption of oxygen uptake process upon heating could be supposed, even this is contradictory to the common sense that the oxygen deficient perovskites release oxygen on heating process and the oxygen loss is recovered when cooling in air condition. To certify the possibility of oxygen uptake with heating process for $GdBaCo_{1.4}Fe_{0.6}O_{5+\delta}$, thermogravimetric measurement was carried out under air as a function of temperature for air-annealed sample, as well as other two compounds GBCO and GBCF03 for comparison. In this condition, mass variation as a function of temperature is devoted to the incorporation or desorption of oxygen into/from the materials, as shown in ***Figure 2.22.***

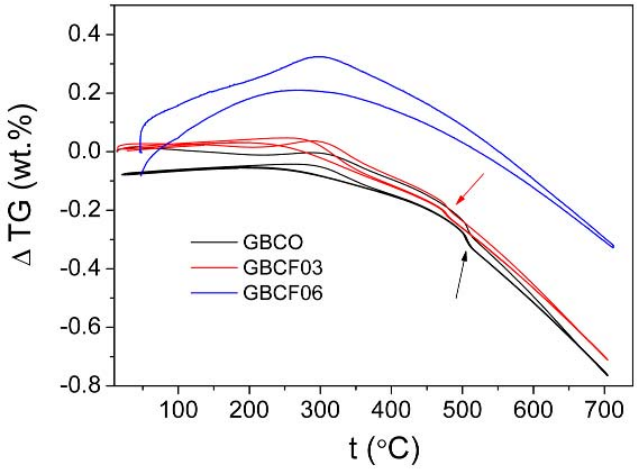

Figure 2.23 *Thermogravimetric patterns of GBCO, GBCF03 and GBCF06 measured in air condition, arrows indicate the phase transition*

Compared to the GBCO and GBCF03 which show almost constant weight below *ca.* 250 °C, GBCF06 exhibits an increase of mass until *ca.* 300 °C, which corresponds to the temperature of orthorhombic-tetragonal transition observed in XRD, in consistency with the assumption of oxygen uptake on heating process. The reproducibility of mass change on heating and cooling with small difference of inflection temperature is in accordance with the high-temperature TG data of $GdBaCo_2O_{5+\delta}$ given by Tarancón exhibiting an approximately pure mass loss during the heating process. It could be concluded that the oxygen nonstoichiometry induced by high level of Fe substitution is the major cause of this tetragonal-orthorhombic-tetragonal phase transition which can not exist in case of GBCO, GBCN and low Fe substituted GBCF.

A similar case in $TbBaCo_{2-x}Fe_xO_{5+\delta}$ ($0 < x < 1$) system with a coexistence of orthorhombic and tetragonal phases in the concentration range ($0.1 < x < 0.12$) has been investigated by Kopcewicz *et al*.

[33] using the Mössbauer spectroscopy. The Mössbauer data indicate three different positions of Fe ions in $TbBaCo_{2-x}Fe_xO_{5+\delta}$: one high symmetry position corresponds to the octahedral position (I); one low-symmetry position corresponds to square pyramidal position (II) in the ideal 122-type crystal structure. The second low-symmetry pyramidal position appears at octahedral position in this type of crystal structure by removing one oxygen atom from the $[TbO_{0.5}]$ layer. At high temperature when the diffusion processes of oxygen occur actively, the oxygen content in the sample is approximately 5 ($\delta \approx 0$) and all *B*-site cations with statistical distribution of the Fe and Co ions are placed within square pyramids with fivefold coordination. When the temperature decreases and absorption of the oxygen occurs, those lattice positions within the $[TbO_{0.5}]$ layer that normally possess one oxygen at the vertex of octahedral coordination of CoO_6 in the ideal ordered 122-type crystal structure, will remain vacant on condition that their corresponding coordinating Co are located in the neighborhood of Fe ions. Consequently, at the statistical distribution of the Fe ions at positions I and II, approximately half of these ions drive out oxygen atoms from the $[TbO_{0.5}]$ layer in octahedral position. In this case the chemical formula of the Fe-substituted compounds may be approximately expressed as $TbBaCo^{3+}_{2-2x}Fe^{3+}_xCo^{2+}_xO_{5.5-x/2}$. Assuming the same mechanism is suitable to $GdBaCo_{2-x}Fe_xO_{5+\delta}$, thus influence of the Fe substitution on the high temperature phase transition could also be considered as the consequence of extra oxygen vacancies introduced by Fe ions at the low symmetry octahedral positions which give rise to the oxygen vacant to the neighbouring site in $[GdO_\delta]$ player. However, the proposed new formula of Fe substituted $TbBaCo^{3+}_{2-2x}Fe^{3+}_xCo^{2+}_xO_{5.5-x/2}$ does not correspond perfectly to the $GdBaCo_{2-x}Fe_xO_{5+\delta}$ investigated in this work. For example, in the case x = 0.6, the chemical formula is $GdBaCo_{1.4}Fe_{0.6}O_{5.063}$ with oxygen content determined by TG/H_2, much lower than that should be obtained based on the proposed formula by replacing Tb with Gd: $GdBaCo_{1.4}Fe_{0.6}O_{5.2}$. Thus, the reliability of this formula or its suitability to analogous compounds with different A site cations except Tb is still doubtful and needs to be further discussed.

The linear thermal expansion coefficient (TEC) obtained from the XRD refinement data are listed below in Table 2.7. The Ni substitution gives rise to a slightly decrease of α_L , this trend is in agreement with the results from Bo Wei *et al*. [21] determined by dilatometry, whereas much larger decrease are shown in their work. Take the composition with the Ni substitution x = 0.3 for instance, they obtained the TEC = 15.5×10^{-6} K^{-1} compared to that of 19.8×10^{-6} K^{-1} in this work. On the contrary, Fe substitution shows an opposite influence leading to an increase of TEC.

Compounds	GBCO	GBCN03	GBCN06	GBCF03	GBCF06
α_L (K^{-1})	20.6×10^{-6}	19.8×10^{-6}	18.4×10^{-6}	20.7×10^{-6}	21.1×10^{-6}

Table 2.7 Linear TEC obtained from high-temperature XRD

2.7 Conclusion

This chapter mainly concerns the fabrication and physical-chemical characterization of $GdBaCo_{2-x}M_xO_{5+\delta}$ (M = Ni or Fe, x = 0.1, 0.2 …).

Comparing various synthesis method, highly substituted compounds with solubility until x = 0.8 for both Ni and Fe substitution are obtained by gel combustion process and microwave-assisted combustion route. Finally, five composition were selected for further investigation with x = 0, 0.3, 0.6, as GBCO, GBCN03, GBCN06, GBCF03 and GBCF06 for short.

Detailed crystal structural information was obtained by Rietveld refinement on the X-ray powder diffraction data. For the air-synthesized materials at ambient, increasing Fe substitution leads to an orthorhombic (Pmmm, $a_p \times 2a_p \times 2a_p$) to tetragonal (P4/mmm, $a_p \times a_p \times 2a_p$) phase transition when x >0.4, whilst Ni substitution seemed to sustain the orthorhombic structure and enhance the orthorhombic distortion. Oxygen contents were determined by iodometry and thermogravimetric for air-annealed samples, showing Fe substitution decreased the oxygen content and this is supposed to be responsible for the observed phase transition. As well, their structures at elevated temperatures corresponding to the SOFC operating condition were investigated. DSC results showed that both Ni and Fe substitution could reduce the temperature of the high temperature phase transition, except those GBCF compounds exhibiting already tetragonal phase at room temperature. This indicates that oxygen random distribution could be introduced at lower temperature by substitution of both Ni and Fe, which suggests a larger amount of oxygen vacancy at high temperature, especially for high Fe substitution, and the desired oxygen transport properties related to oxygen vacancy level could possibly be achieved at lower temperature.

A particular case was found in GBCF06, for which no phase transition was observed through DSC, but temperature dependent XRD showed a tetragonal-orthorhombic-tetragonal in the temperature range 100-300 °C.

In addition, the thermal expansion coefficients were calculated based on the evolution of structural parameters as a function of temperature extracted from refinement of XRD data. Ni substitution was shown to slightly decrease the TEC, while the Fe substitution showed the reverse. However, the obtained TECs are still too large compared to those of currently used electrolytes such as CGO which will be used in this work.

REFERENCES

[1] Taskin, A. A.; Lavrov, A. N.; Ando, Y. *Phys. Rev. B* **2005**, *71*, 28.

[2] Taskin, A. A.; Lavrov, A. N.; Ando, Y. *Physical Review Letters* **2003**, *90*, 227201.

[3] Frontera, C.; García-Muñoz, J. L.; Llobet, A.; Aranda, M. A. G. *Phys. Rev. B* **2002**, *65*, 180405.

[4] Taskin, A. A.; Ando, Y. *Journal of Magnetism and Magnetic Materials* **2007**, *310*, 969-971.

[5] Tarancon, A.; Pena-Martinez, J.; Marrero-Lopez, D.; Morata, A.; Ruiz-Morales, J. C.; Nunez, P. *Solid State Ion.* **2008**, *179*, 2372-2378.

[6] Tarancon, A.; Skinner, S. J.; Chater, R. J.; Hernandez-Ramirez, F.; Kilner, J. A. *Journal of Materials Chemistry* **2007**, *17*, 3175-3181.

[7] Tang, Y. K.; Almasan, C. C. *Phys. Rev. B* **2008**, *77*, 5.

[8] Bharathi, A.; Yasodha, P.; Gayathri, N.; Satya, A. T.; Nagendran, R.; Thirumurugan, N.; Sundar, C. S.; Hariharan, Y. *Phys. Rev. B* **2008**, *77*, 8.

[9] Tarancon, A.; Morata, A.; Dezanneau, G.; Skinner, S. J.; Kilner, J. A.; Estrade, S.; Hernandez-Ramirez, F.; Peiro, F.; Morante, J. R. *Journal of Power Sources* **2007**, *174*, 255-263.

[10] Pena-Martinez, J.; Tarancon, A.; Marrero-Lopez, D.; Ruiz-Morales, J. C.; Nunez, P. *Fuel Cells* **2008**, *8*, 351-359.

[11] Ding, H.; Xue, X. *International Journal of Hydrogen Energy* **2010**, *In Press, Corrected Proof*.

[12] Zhang, K.; Ge, L.; Ran, R.; Shao, Z.; Liu, S. *Acta Materialia* **2008**, *56*, 4876-4889.

[13] Maignan, A.; Martin, C.; Pelloquin, D.; Nguyen, N.; Raveau, B. *Journal of Solid State Chemistry* **1999**, *142*, 247-260.

[14] Choi, M. B.; Jeon, S. Y.; Lee, J. S.; Hwang, H. J.; Song, S. J. *Journal of Power Sources* **2010**, *195*, 1059-1064.

[15] Tsvetkov, D. S.; Sereda, V. V.; Zuev, A. Y. *Solid State Ion.* **2010**, *180*, 1620-1625.

[16] Pechini, M.; Adams, N. *US patatent* **1967**, *NO. 3330697*.

[17] Tarancon, A.; Dezanneau, G.; Arbiol, J.; Peiro, F.; Morante, J. R. In *Conference on Scientific Advances in Fuel Cell Systems* Amsterdam, Netherlands, 2002, p 256-264.

[18] Tarancón, A., University of Barcelona, 2007.

[19] Tarancón, A.; Dezanneau, G.; Arbiol, J.; Peiró, F.; Morante, J. R. *Journal of Power Sources* **2003**, *118*, 256-264.

[20] Gu, L.; Meng, G. *Materials Research Bulletin* **2007**, *42*, 1323-1331.

[21] Wei, B.; Lü, Z.; Jia, D.; Huang, X.; Zhang, Y.; Su, W. *International Journal of Hydrogen Energy* **2010**, *35*, 3775-3782.

[22] Karppinen, M.; Matvejeff, M.; Salomäki, K.; Yamauchi, H. *Journal of Materials Chemistry* **2002**, *12*, 1761-1764.

[23] Conder, K.; Pomjakushina, E.; Soldatov, A.; Mitberg, E. *Materials Research Bulletin* **2005**, *40*, 257-263.

[24] Chen, W. M.; Hong, W.; Geng, J. F.; Wu, X. S.; Ji, W.; Li, L. Y.; Qui, L.; Jin, X. *Physica C: Superconductivity* **1996**, *270*, 349-353.

[25] Liu, J.; Shen, J.; Gao, X.; Lin, L. *Journal of Thermal Analysis and Calorimetry* **1993**, *40*, 1245-1252.

[26] Boehm, E.; Bassat, J. M.; Dordor, P.; Mauvy, F.; Grenier, J. C.; Stevens, P. *Solid State Ion.* **2005**, *176*, 2717-2725.

[27] Burley, J. C.; Mitchell, J. F.; Short, S.; Miller, D.; Tang, Y. *Journal of Solid State Chemistry* **2003**, *170*, 339-350.

[28] Macklen, E. D. *J. Appl. Phys.* **1965**, *36*, 1022-1024.

[29] Rautama, E.-L.; Karppinen, M. *Journal of Solid State Chemistry* **2010**, *183*, 1102-1107.

[30] Tarascon, J. M.; Barboux, P.; Miceli, P. F.; Greene, L. H.; Hull, G. W.; Eibschutz, M.; Sunshine, S. A. *Phys. Rev. B* **1988**, *37*, 7458.

[31] Tarascon, J. M.; McKinnon, W. R.; Greene, L. H.; Hull, G. W.; Vogel; E, M. *Phys. Rev. B* **1987**, *36*, 226.

[32] Tikhonovich, V. N.; Zharkovskaya, O. M.; Naumovich, E. N.; Bashmakov, I. A.; Kharton, V. V.; Vecher, A. A. *Solid State Ion.* **2003**, *160*, 259-270.

[33] Kopcewicz, M.; Khalyavin, D.; Troyanchuk, I.; Szymczak, H.; Szymczak, R.; Logvinovich, D.; Naumovich, E. *J. Appl. Phys.* **2003**, *93*, 479-486.

[34] Kusuya, H.; Machida, A.; Moritomo, Y.; Kato, K.; Nishibori, E.; Takata, M.; Sakata, M.; Nakamura, A. *JOURNAL-PHYSICAL SOCIETY OF JAPAN* **2001**, *70*, 3577-3580.

[35] Taskin, A. A.; Lavrov, A. N.; Ando, Y. *Appl. Phys. Lett.* **2005**, *86*, 3.

[36] Streule, S.; Podlesnyak, A.; Sheptyakov, D.; Pomjakushina, E.; Stingaciu, M.; Conder, K.; Medarde, M.; Patrakeev, M. V.; Leonidov, I. A.; Kozhevnikov, V. L.; Mesot, J. *Phys. Rev. B* **2006**, *73*, 5.

[37] Streule, S.; Podlesnyak, A.; Pomjakushina, E.; Conder, K.; Sheptyakov, D.; Medarde, M.; Mesot, J. In *International Conference on Strongly Correlated Electron Systems (SECES 05)*; Elsevier Science Bv: Vienna, AUSTRIA, 2005, p 539-540.

[38] Tarancon, A.; Marrero-Lopez, D.; Pena-Martinez, J.; Ruiz-Morales, J. C.; Nunez, P. *Solid State Ion.* **2008**, *179*, 611-618.

[39] Tsipis, E. V.; Kharton, V. V. *J. Solid State Electrochem.* **2008**, *12*, 1039-1060.

[40] Li, N.; Lu, Z.; Wei, B. O.; Huang, X. Q.; Chen, K. F.; Zhang, Y. Z.; Su, W. H. *Journal of Alloys and Compounds* **2008**, *454*, 274-279.

[41] Moritomo, Y.; Akimoto, T.; Takeo, M.; Machida, A.; Nishibori, E.; Takata, M.; Sakata, M.; Ohoyama, K.; Nakamura, A. *Phys. Rev. B* **2000**, *61*, R13325.

[42] Troyanchuk, I.; Chobot, A.; Khalyavin, D.; Szymczak, R.; Szymczak, H. *Journal of Experimental and Theoretical Physics* **2002**, *95*, 748-752.

[43] Fauth, F.; Suard, E.; Caignaert, V.; Domengès, B.; Mirebeau, I.; Keller, L. *Eur. Phys. J. B* **2001**, *21*, 163-174.

[44] Malavasi, L.; Brunelli, M.; Diaz-Fernandez, Y.; Pahari, B.; Mustarelli, P. *Phys. Rev. B* **2009**, *80*, 153102.

[45] Frontera, C.; García-Muñoz, J. L.; Carrillo, A. E.; Ritter, C.; Martín y Marero, D.; Caneiro, A. *Phys. Rev. B* **2004**, *70*, 184428.

[46] Raveau, B.; Simon, C.; Caignaert, V.; Pralong, V.; Lefevre, F. *Journal of Physics: Condensed Matter* **2006**, *18*, 10237.

Chapter 3 Electrochemical Characterization

In SOFCs, the electrode provides the interface between chemical and electric energy and catalyzes the chemical reactions. Typically, an electrode is a complex structure that consists of a three-phase percolating composite of a metal or mixed conducting oxide, and oxide electrolyte and the pore space [1]. The transport and reactions in such porous structure are also complex. Thus the understanding of how the individual components determine the relative rate, the contributions from the various processes and thereby the overall electrode performance has been widely studied in order to guide the evaluation and optimization of the electrode properties. Moreover, it has been well accepted that in intermediate temperature SOFCs, oxygen reduction at the cathode is the main rate limiting factor to the performance of the whole system since the oxygen reduction is generally thought to be the more difficult reaction to activate on SOFCs operating in the intermediate to low temperature range [2-4]. Modeling and simulation techniques have been used to improve the understanding of the reaction mechanisms and kinetics of electrode processes in SOFCs. Electrochemical impedance spectroscopy (EIS), also known as AC impedance spectroscopy, is used for this purpose, as it seems to be an efficient experimental technique for fuel cell diagnosis and performance evaluation.

3.1 Characterization of cathodes

3.1.1 Electrochemical Impedance Spectroscopy (EIS): Technique tool

Electrochemical Impedance Spectroscopy (EIS) is a powerful diagnostic tool to characterize limitations and to improve the performance of fuel cells [5]. There are three fundamental sources of voltage loss in fuel cells: charge transfer activation or “kinetic” losses, ion and electron transport or “ohmic” losses, and concentration or “mass transfer” losses. Among other factors, EIS is an experimental technique that can be used to separate and quantify these individual losses [6].

Figure 3.1 depicts an example of AC impedance spectroscopy applied on a single cell. The impedance spectrum is taken by imposing a small amplitude AC voltage signal $U(\omega)$ on the tested cell under zero DC current conditions, which probes the linear responses of the sample and thereby resulting in a corresponding AC current response $I(\omega)$ with the same frequency f. The ratio between these two is the impedance $Z(\omega)$.

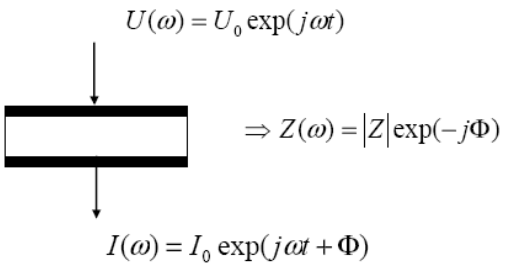

$U(\omega)$ – imposed sinusoidal voltage

$\omega = 2\pi f$ – angular frequency (f: frequency)

t – time,

Φ – phase shift

$Z(\omega)$ – Impedance

Figure 3.1 *Principle of impedance spectroscopy*

The quantity used for expressing models of impedance is the complex number, defined as:

$$Z(\omega) = \mathrm{Re}(Z) + j\,\mathrm{Im}(Z) = Z' + jZ'' \tag{4.1}$$

where the real part of the impedance ReZ (Z') comprises the resistive component (R), the imaginary part ImZ (Z''), includes capacitive and inductive components.

In impedance spectroscopy, complex impedance is measured over a range of frequencies. This enables to assign a number of discrete circuit elements to physical processes by using a certain model of their electrical response. The representation of imaginary impedance (Z'') versus the real part (Z') in a complex plane is called Nyquist plot, and normally it consists of more or less overlapping arcs each of which reflecting a physical or chemical process.

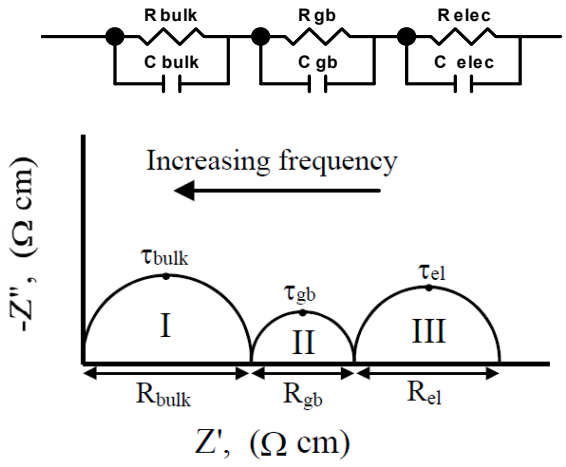

Figure 3.2 *Idealized Nyquist impedance plot with contributions of I) grain bulk, II) grain boundary, and III) electrode and its equivalent circuit. R-resistance, τ – apex frequency, C-capacitance*

A typical Nyquist impedance plot and its corresponding equivalent circuit are shown in ***Figure 3.2***. In an electrically inhomogeneous ceramic sample including different components (bulk, grain boundary, electrode *etc.*), different semicircles correspond to the contribution of grain, grain boundary and electrode, respectively. Each contribution could be represented by a single parallel RC circuit, for

which R is the resistance and C is the capacitance. An equivalent circuit consisted of a series of such individual RC sub-circuits represents the various processes in an ideal ceramic cell. The magnitude of R will give the resistance of the specific process, and the magnitude of C will serve to identify the process. The relaxation time for each process could be calculated from Eq. (4-2) using the apex frequency.

$$\tau_0 = \omega^{-1} = RC = \left(2\pi f_0\right)^{-1} \tag{4-2}$$

where ω is the angular frequency and f_0 is the relaxation frequency (Hz) which corresponds to the top of the semicircle.

However, instead of Nyquist plot comprising perfect semicircles**,** the experimental impedance data for many systems give rise to circular arcs with their center lying below the axis (depressing of semicircle into an arc). This is the so-called dispersing phenomenon. In this case, the double-layer capacitance and pseudo-capacitance involved in electrochemical reactions can not be simulated as pure capacitors, but as constant phase elements (CPE or Q). Admittance of impedance of CPE are defined as:

$$Y_{CPE} = Y_0 \left(j\omega\right)^n \tag{4-3}$$

$$Z_{CPE} = \frac{1}{Y_0 \left(j\omega\right)^n} \tag{4-4}$$

where Y_0 is the admittance magnitude and n is the exponential term, if $n = 1$ the expression is the same as for an ideal capacitor; if $n = 0$ it represents a pure resistor with Y_0 being the conductance.

In practice, an electrode in SOFC is a contact between two different phases (typically, one is a metal interconnector and the other an ionic conductor). Firstly, the interface comprises an interfacial layer of a particular kind (whatever properties), which is called the double-layer, and such a layer may comprise adsorbed species resulting in the double-layer capacitance. Next, the electrode or contact has a charge transfer conductance/resistance which represents the path electrons or ions use to jump the barrier, or, for electrode-electrolyte interfaces, the combined electrochemical process where both chemical species and electrons are involved. The charge transfer resistance is in parallel with the double-layer capacitance. Together they may thus form another semicircle in an impedance diagram, typically at much lower frequencies than the grain boundary and bulk semicircles characteristic to electrode performances. Several transport processes may take place in series with a charge transfer at an electrode. This includes adsorption – desorption, diffusion in condensed phases and gases or on materials surfaces, and reactions. This gives rise to a wealth of behaviors and corresponding electrical "equivalents" in EIS application for electrode SOFC estimation [7].

3.1.2 Oxygen reduction mechanisms and kinetics: Theoretical

To date, however, understanding of the mechanisms and kinetics of oxygen reduction under fuel cell operating conditions remains incomplete because of the geometrical complexity of the electrochemically active interfaces, and of the complex phenomena of adsorption and conversion of molecular O_2 into electrochemically active intermediate species. In addition to oxygen ad-atoms and O^{2-} anions, numerous forms of intermediates are often assumed to exist at electrode surface [8], as shown in ***Figure 3.3*** for mixed conducting electrode.

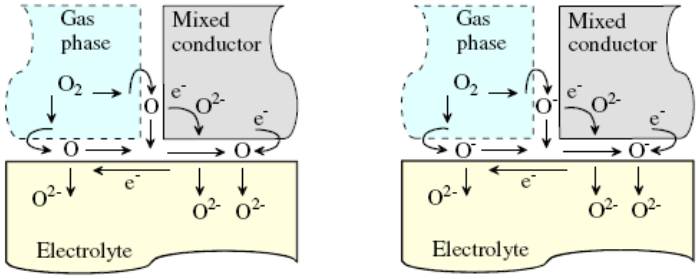

Figure 3.3 *Examples of the cathode reaction pathway for a porous mixed conducting electrode with surface diffusion of oxygen ad-atoms (left) and O- sub-ions (right)* [8]

The overall reaction for a *p*-type, oxygen-conducting SOFC cathode can be described as:

$$\frac{1}{2}O_2 + V_O^{\bullet\bullet} \rightarrow O_O^{\times} + 2h^{\bullet} \tag{4-5}$$

where, in the Kröger-Vink notation, $V_O^{\bullet\bullet}$ denotes an oxygen vacancy in the solid state (either in the electrolyte or in the MIEC) with two effective positive charges (with respect to the perfect crystal), $O_O^{\times}$ denotes a neutral oxygen ion in a solid state oxygen site, and $h^{\bullet}$ denotes a positively charged electron hole.

However, the electrochemical reduction of oxygen is composed of various elementary steps associated to different transport species and paths, including [9,10]:

- adsorption of gaseous molecular oxygen reduction and dissociation of the adsorbed molecule in (probably) multiple steps
- diffusion of adsorbates to various incorporation sites on the MIEC surface and at the TPB
- transport of vacancies to the incorporation sites and transport of electron holes away from the reduction sites
- the incorporation reaction (combination of adsorbed atomic oxygen and oxygen vacancies)
- the diffusion of vacancies from the electrolyte into the MIEC

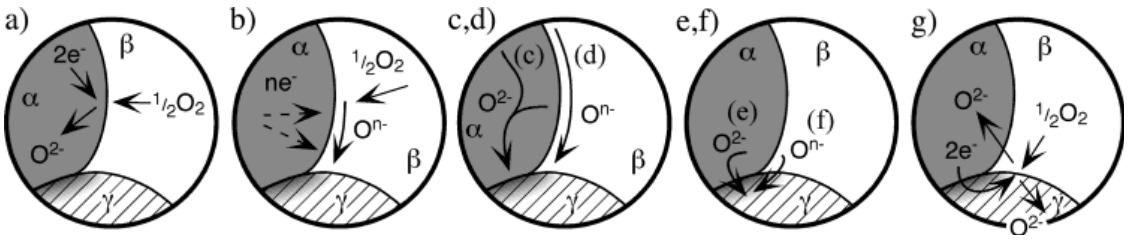

Figure 3.4 *[2] some mechanisms thought to govern oxygen reduction in SOFC MIEC cathodes. Phases α, β and γ refer to the electrode, gas, and electronic phase, respectively: (a) Incorporation of oxygen into the electrode phase (if mixed conducting); (b) adsorption and/or partial reduction of oxygen on the electrode surface ; (c) bulk or (d) surface transport of O^{2-} or O^{n-}, respectively, to the α/β interface, (e) Electrochemical charge transfer of O^{2-} or (f) combinations of O^{n-} and e^-, respectively, across the α/γ interface, and (g) generation and transport of electroactive oxygen species in electrolyte*

Adler [2] also outlines some of the mechanisms either known or theorized in the literature to be important in determining the rate of oxygen reduction in SOFC cathodes, these individual processes are schematically demonstrated as shown in ***Figure 3.4***. In order to understand and describe the complex oxygen reduction process, for further improvement of cathode properties, an enormous amount of works has been focused on how to develop a proper model to simulate the physical, chemical and electrochemical processes in the reaction system, based on experimental data or theoretical simulation, which have been summarized in some recent reviews [2,6,8,9,11,12].

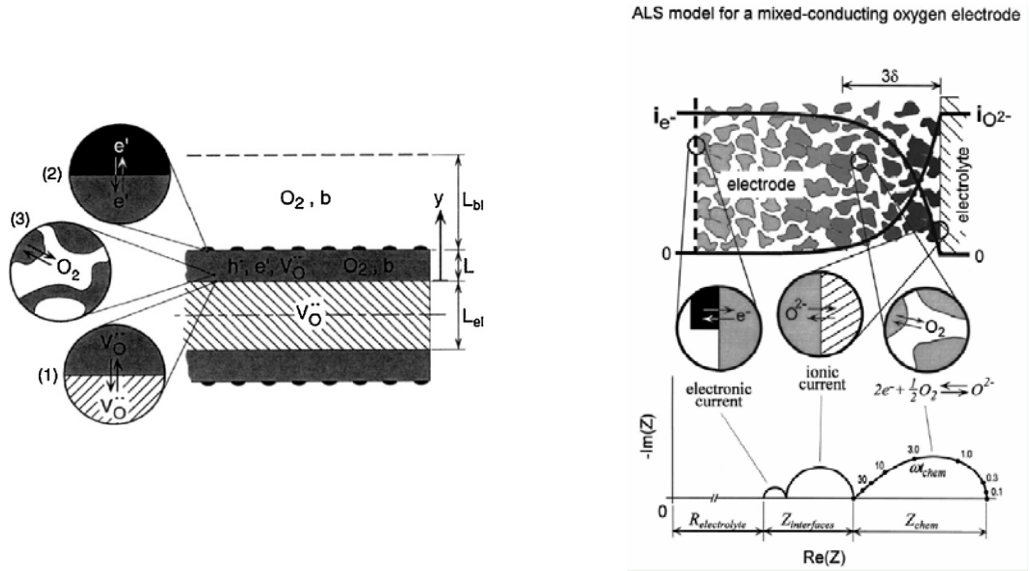

Figure 3.5 *Schematic of the ALS model for a porous mixed-conducting oxide electrode: cell geometry (left) Impedances of charge-transfer processes added in series. Impedance due to non-charge-transfer processes is convoluted (right) [13]*

For example, one attractive model for oxygen reduction with MIEC cathode with *p*-type electronic transport was considered by Adler *et al.* [14], as shown in ***Figure 3.5***. This so called Adler-Lane-Steel (ALS) model allows to analyze the reaction mechanism in combination with the AC

impedance for mixed-conducting electrodes [15]. In the ALS model, SOFCs cathode reaction was firstly treated as pure chemical process occurring via three separated interfacial reactions: (1) charge-transfer of oxygen ions/vacancies across the cathode/electrolyte interface; (2) charge-transfer of electrons across the current-connector/cathode interface; (3) chemical exchange of oxygen at the gas/cathode interface. Later, Adler explained the limits of this model for non-charge transfer reaction and provided a framework for defining "charge-transfer" and "non-charge-transfer" processes [13]: Charge-transfer represents any step that involves charged species and driven directly by gradients in electrical state, which always occurs at a rate proportional to the current; non-charge-transfer is any step that involves neutral species or neutral combinations of species and driven by gradients in chemical potential and occurs at a rate independent of current. This model can only be valid for the mixed conductors with high rates of oxygen surface exchange, *e.g.* $La_{1-x}Sr_xCoO_{3-\delta}$. For example, in the case of porous $La_{0.6}Sr_{0.4}Fe_{0.8}Co_{0.2}O_{3-\delta}$ electrodes on CGO electrolyte [13,16], ALS model agrees reasonably well with impedance data under conditions of high vacancy concentration.

The zero-bias impedance of a symmetrical cell (electrode/electrolyte/electrode) can be expressed as a sum of charge transfer resistances and impedances, plus a chemical impedance associated with non-charge-transfer process:

$$Z = Z_{\text{electrolyte}} + Z_{\text{interfaces}} + Z_{\text{chem}} \tag{4.6}$$

where $Z_{\text{electrolyte}}$ is the electrolyte resistance, $Z_{\text{interface}}$ is the impedance of the electron-transfer and ion-transfer processes occurring at the current collector and electrolyte interfaces, respectively, and Z_{chem} is the convoluted contribution of non-charge-transfer processes including oxygen surface exchange, solid –state diffusion, and gas-phase diffusion inside and outside the electrode. In the limit of a semi-infinite (thick) electrode with no gas-phase diffusion limitations, the non-charge-transfer term reduces to:

$$Z_{\text{chem}} = R_{\text{chem}}\sqrt{\frac{1}{1+j\omega t_{\text{chem}}}} \tag{4.7}$$

Where R_{chem} and t_{chem} are a characteristic resistance and time constant, respectively, related to the thermodynamic, surface kinetic, and transport properties of the mixed conductor:

$$R_{\text{chem}} = \left(\frac{RT}{2F^2}\right)\sqrt{\frac{\tau}{(1-\varepsilon)c_{\text{V}}D_{\text{V}}ar_0\left(\alpha_{\text{f}}+\alpha_{\text{b}}\right)}} \tag{4.8}$$

$$t_{\text{chem}} = \frac{c_{\text{V}}\left(1-\varepsilon\right)}{Aar_0\left(\alpha_{\text{f}}+\alpha_{\text{b}}\right)} \tag{4.9}$$

$$A = -1/\left(2n\right) = -1/2\partial\ln\left(P_{\text{O}_2}\right)/\partial\ln\left(c_{\text{V}}\right) \tag{4.10}$$

Where: c_V: vacancy concentration, A: thermodynamic factor, D_V: is the vacancy diffusion coefficient, ε: prosity, a: surface area,τ: solid state-phase tortuosity, r_0: exchange neutral flux density, α_f and α_b: kinetic parameters of the surface chemical exchange reaction [14]. This model also takes the distance from the electrode/electrolyte interface into account, bringing out a concept of characteristic length, δ, to describe the size of the active region, given by:

$$\delta = \sqrt{\frac{c_V D_V (1-\varepsilon)}{a r_0 (\alpha_f + \alpha_b)\tau}} \tag{4.11}$$

It has been concluded that in case of a porous mixed conducting peovskite electrode, the characteristic active utilization region for oxygen reduction is limited by oxygen exchange and diffusion, and may occur up to 20 μm from the electrochemical (charge-transfer) interface. Therefore, as discussed above, in addition to high electronic conductivity, the cathode performance strongly depend on the oxygen diffusion coefficient and surface exchange rate under different conditions. This ALS model has been proved as an effective method in explaining several important features of impedance data and electrode performance.

However, a number of papers expressed conflicting (or dissenting) views for the role of the bulk and interface in governing the mechanism and the extent of the utilization region, due to the neglecting of a parallel surface transport/reaction path, limitation of characteristic length being required to be much greater than the size of individual morphological feature, *etc* [2,16-18].

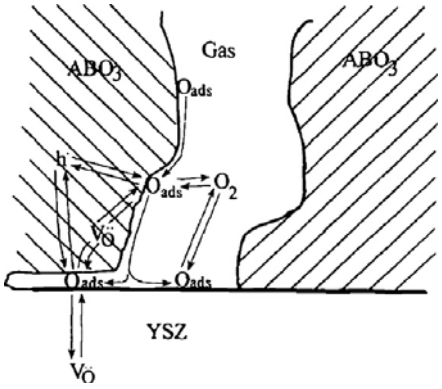

Figure 3.6 *Sketch of Svensson's macrohomogeneous model for the i-V characteristics of a porous mixed-conducting electrode, assuming both surface and bulk diffusion are active and that direct exchange of oxygen vacancies between the mixed conductor and the electrolyte may occur [19].*

Svensson *et al*. [19,20] developed a physical model to show the possible oxygen transport pathways on SOFC cathodes by modeling the current–overpotential (I–*η*) characteristics of porous mixed-conducting electrodes, shown in ***Figure 3.6***, where two step reactions for oxygen reduction are expressed as:

$$O_2(g) + 2ads \underset{kdes}{\overset{k_{ads}}{\rightleftharpoons}} 2O_{ads} \tag{4.12}$$

$$O_{ads} + V_O^{\bullet\bullet} \underset{k_O}{\overset{k_r}{\rightleftharpoons}} ads + 2h' + O_O^{\times} \tag{4.13}$$

This model takes a similar mechanistic approach as the ALS model, but additional physics has been considered. The gas/electrode interfacial reaction was also considered chemical in nature since no interfacial charge-transfer was involved, whilst the reaction at electrolyte interface was considered as an electrochemical process due to the possible existence of chargeable intermediate oxygen species, giving rise to the introduction of overpotential into their simulation expressing the departure of the surface exchange reaction occurring at electrolyte surface from equilibrium. In addition, other models including electrochemical process have been proposed including assumption of oxygen intermediates and corresponding sub-reactions, based on theoretical simulation or experimental data [21-25]. Nevertheless, based on the present investigations, there is still no effective technique to determine which intermediates actually exist in the reaction.

Besides, even these models have been built by studying a large number of materials and cases over a long period of time, significant uncertainties still remain due to the extreme sensitivity of the limiting factors to the exact structure, processing history, operating conditions and operation history of the electrode [2].

3.1.3 Concerning for characterization by EIS: practical

Investigation of electrode performance, including the understanding and modelling of oxygen reduction mechanism, is of great importance for optimizing the cathode performance and improving the fuel cell efficiency, according to which sub-reactions can be extracted to describe the overall reaction and to determine the rate-determining step under various conditions. The physicochemical processes within a SOFC can be classified as either internal factors *e.g.* material, composition, microstructures and component sizes, or external factors *e.g.* temperature, pressure, and fuel/air flows and concentration [2]. Thus, to diagnose the mechanism of a particular electrode under a specific set of conditions or to determine factors governing the rate of the various physical processes as well as their relevant importance in the mechanism, both the internal and external factors should be taken into account.

Concerning the EIS technique, the measured impedance $Z(j\omega)$ is the average result of overlapped responses from all microscopic processes. By combining the EIS with specific models and the operating conditions, information describing the electrode properties such as reaction kinetics, reaction activation, electrolyte conductivity and mass transfer can be extracted. One useful strategy is to model

the individual processes in terms of equivalent circuit elements, in most cases as a sum of the electrolyte impedance, interfacial impedance, and non-charge transfer impedance at high, medium, and low frequency range, respectively, such as the ALS model. Moreover, this description is often extended by introduction of additional empirically or theoretically derived circuit element according to the corresponding assumption of oxygen reduction mechanism as discussed in 1.2.

In this work, the investigated $GdBaCo_{2-x}M_xO_{5+\delta}$ (M = Ni or Fe) materials refer to the porous mixed conducting cathodes, which is a complex case. Symmetric electrode configuration is applied in order to help isolate the electrode contribution to the polarization losses from those of electrolyte from the overlap or dispersion of impedance date. Another key factor is the determination of the rate-determining step (RDS) among these electrode reaction processes, since the overall reaction could be divided into several sub-reactions according to the reaction mechanism, *e.g.* Jørgensen and Mogensen [26] claimed that at least five processes affected electrochemical phenomena and impedance plot.

However, same as the diversity of oxygen reduction mechanism models proposed, there is no universe agreement on RDS identification for all cathodes. Besides, quite different spectra could be obtained for nominally identical electrodes under different condition. Thus experimental results should be discussed in combination with the relative assumption of oxygen reduction mechanism in the RDS interpretation, even with the ambiguity and uncertainty remaining. Moreover, different mechanistic models for a given reaction often predict very similar impedance response after the governing equation have been linearized [27]. For example, in some case of EIS application, an obtained impedance result could be well fitted by different equivalent circuits, which will be discussed below in this chapter.

3.2 Experimental

3.2.1 GBCM electrodes based on ceria electrolyte

3.2.1.1 Symmetric cells

- Sample preparation

In this work, five compositions were chosen as electrodes for the impedance measurements, $GdBaCo_2O_{5+\delta}$, $GdBaCo_{1.7}Ni_{0.3}O_{5+\delta}$, $GdBaCo_{1.4}Ni_{0.6}O_{5+\delta}$, $GdBaCo_{1.7}Fe_{0.3}O_{5+\delta}$ and $GdBaCo_{1.4}Fe_{0.6}O_{5+\delta}$, which are abbreviated as GBCO, GBCN03, GBCN06, GBCF03 and GBCF06, respectively. As seen in the morphology characterization in Chapter 2, important agglomeration has been observed in the powders synthesized in this work, especially for those fabricated through the citric acid combustion

route. Thus, the as-synthesized powders were firstly ball milled with Zirconia balls in a laboratory benchtop planetary ball mill (Retsch PM 100) at a rate of 250 rpm for 4h. Ball milling allowed breaking the agglomerated big grains and obtaining good homogeneity in powder. ***Figure 3.7*** compares the SEM patterns of GBCF06 powders fabricated through citric acid combustion route before and after balling, showing smaller grain size and better homogeneity.

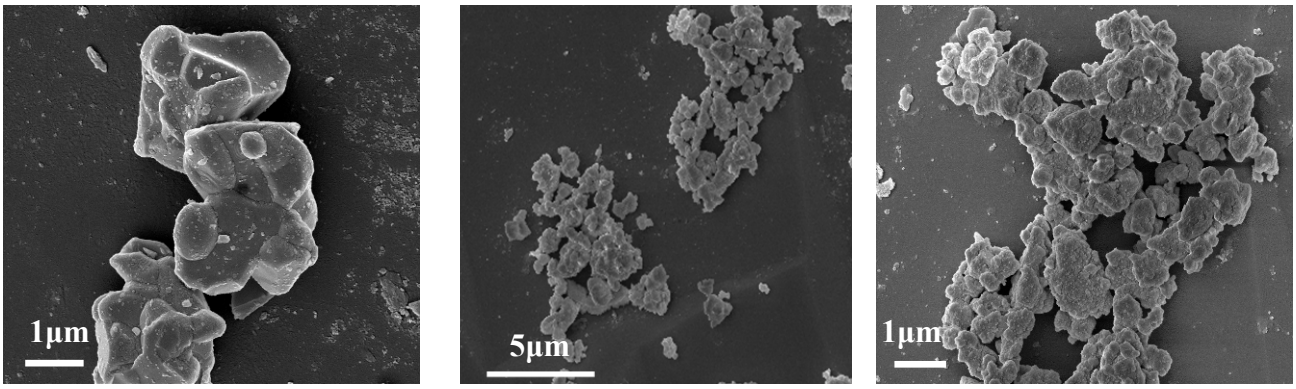

Figure 3.7 *SEM of GBCF06 powders: as synthesized powders (left), ball milled powders with the rate of 250 rpm for 4h (middle and right)*

Gadolinium-doped ceria, $Ce_{0.9}Gd_{0.1}O_{1.95}$ (CGO), was used as electrolytes for the electrochemical impedance measurement. A Commercial CGO nano-scale powder was firstly uniaxially pressed into pellets of diameter of 13mm, followed by high pressure cold isostatic pressing at 750 MPa. The pellets were then sintered at 1450 °C for 12 h, with a slow rate of 100 °C/h during the heating and cooling cycles. After polishing the obtained CGO pellets were of ~10 mm diameter and of ~1mm thickness, and high density (95-97% of theoretical density) were achieved (***Figure 3.8 (a)***). Electrodes were deposited on CGO electrolytes by the Screen-printing in a collaborative laboratory (Institut des Matériaux Jean Rouxel IMN), seeing ***Figure3.8 (b)***. It was expected to achieve identical electrode structure and comparability in electrochemical properties compared to hand painting. In order to obtain good contact, a viscous gold paste (METALORM, GOLD PASTE M-0034) was coated on cathode surfaces serving as current collector, then heated at 800 °C for 1h at a slow heating and cooling rate of 100 °C/h to obtain good adhesion between the gold layer and electrode, as shown in ***Figure 3.8 (c)***.

The morphology and microstructure of some samples were observed in cross section by using scanning electron microscopy (Hitachi S-4700 scanning electron microscope), in conjunction with EDS utilized with a link system digital spectrometer PFT (Princeton Gamma Tech, PRISM) to verify the absence of minor secondary phases.

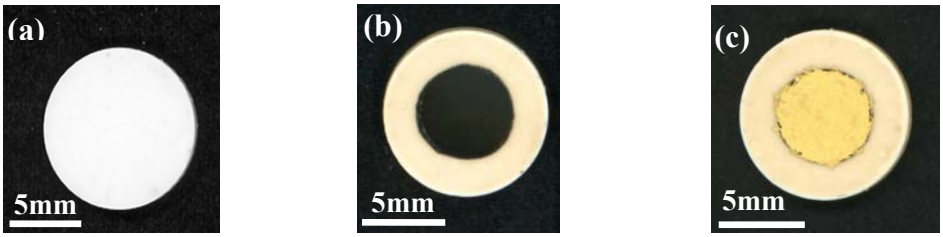

Figure 3.8 *Scanning images of (a) CGO pellet, (b)symmetrical cells with screen-printing deposited electrodes; (c) symmetric cell with gold layer*

- Measurements

Fabricated symmetrical cells were mounted with two-electrode configuration on a commercial sample-holder (Systems- Ionics). Electrochemical impedance measurements were performed at open circuit voltage (OCV) using a Solartron 1260 frequency response analyzer, with applied amplitude of 50 mV and the frequency range from 0.01 Hz to 10 MHz. The temperature dependence measurements were conducted in the temperature range of 300-750 °C in a 5L/h air flow. The oxygen partial pressure (pO_2) dependent measurements were obtained at 700 °C from 1 ppm (10^{-6} atm) to air (0.206 atm) with a constant flow rate of 5L/h. The oxygen partial pressure was controlled by mass flow controllers mixing O_2 and Ar in proportion and by an electrochemical pump (Zirox electrolysis cell) at low pO_2. A stabilization period of more than 40 min was carried out before each acquisition. *Z*view 2 electrochemical impedance software (Scribner Associates Inc.) was used for data analysis.

3.2.1.2 Fuel cell tests

Single cell tests were performed with the collaboration of A. Kulka and Prof. J. Molenda (AGH University of Science and Technology, Krakow, Poland) using the electrode powders fabricated in this work.

- Sample Preparation

$Ce_{0.8}Gd_{0.2}O_2$ electrolyte powders were prepared by a coprecipitation method, then pressed into pellets and sintered at 1500°C. The average thickness of the sintered electrolytes was close to 700 µm. The cathode consists of two layers, a transient layer with a mixture of GBCO, GBCF03 and GBCF06 with $Ce_{0.8}Gd_{0.2}O_2$ in 1:1 volume ration was deposited between the electrolyte and a pure GBCO, GBCF03 and GBCF06 cathode layer. Ni-YSZ was used as anodes. The cells were sintered with separate firings of the anode (at 1400 °C) and the cathode (at 1100 °C).

- Measurements

Button-type cell performance was studied using home-made SOFC testing unit equipped with Solartron SI 1287 electrochemical interface and Solartron 1252A frequency response analyzer. The anode was fuelled with humidified hydrogen (2.5 % H_2O) at different flow rates of 10, 20 and 40 cm^3/min, respectively, controlled by mass-flow controller. Air was provided at the cathode side with a flow rate around 500 cm^3/min. The impedance spectra and the current-voltage characteristics of the Ni-YSZ/ $C_{e0.8}Gd_{0.2}O_2$/GBCM cells were measured in the range of 600~800 °C, with frequency range of 0.1~300 kHz under 25 mV amplitude.

3.2.2 Electrodes in proton conducting fuel cells

These five materials, GBCO, GBCN03, GBCN06, GBCF03 and GBCF06, are also tested to attempt their possibility for utilization in proton conducting fuel cells.

- Sample preparation

Another series of high-temperature protonic–ionic conducting electrolyte pellets, $La_{0.995}Ca_{0.005}NbO_4$ ($LaNbO_4$), were provided by the collaborative laboratory (Institut des Materiaux Jean Rouxel, IMN), where the symmetrical cells GBCM/LNO/GBCM were prepared by screen-printing, then sintered at 950 °C for 2h. The morphology and microstructure of samples after EIS tests were also checked by SEM.

- Measurements

The measurements of symmetrical cells based on the $LaNbO_4$ electrolytes were carried out in dry and wet atmosphere. In the first case, an air flow of 5L/h was flowed through a column of P_2O_5 desiccant, and humidification was obtained by bubbling gas through water and water partial pressure was controlled by gas humidifier (OMISP280C- A, OMICRON Technologies). The impedance spectra were obtained in the frequency range of 0.1 Hz to 10 MHz, where the AC potential amplitude was 50 mV. ZView2 electrochemical impedance software of Scribner Associates Inc. was used for data analysis.

3.3 Results and Discussion

3.3.1 Symmetric cell

3.3.1.1 Morphology and Microstructure Characterization

Figure 3.9 show the SEM images of the cross-section of symmetric cell with GBCO electrode after the electrochemical measurement; focusing on the region in which the gold layer deposited on the electrode was still attached after the breaking up of cells. Here, Au paste was used as current collector in order to improve the measurement in addition to the utilization of Pt mesh, and it should introduce not influence on the cathode performance since it is more neutral compared to Pt or Ag paste used in other works [17,18,28]. Through the SEM images, clear morphological distinctions were observed for the interfaces between Au/electrode/electrolyte layers. EDS-SEM analysis confirmed that there was no insertion of Au paste into the electrodes or secondary phases at the electrode/electrolyte interfaces.

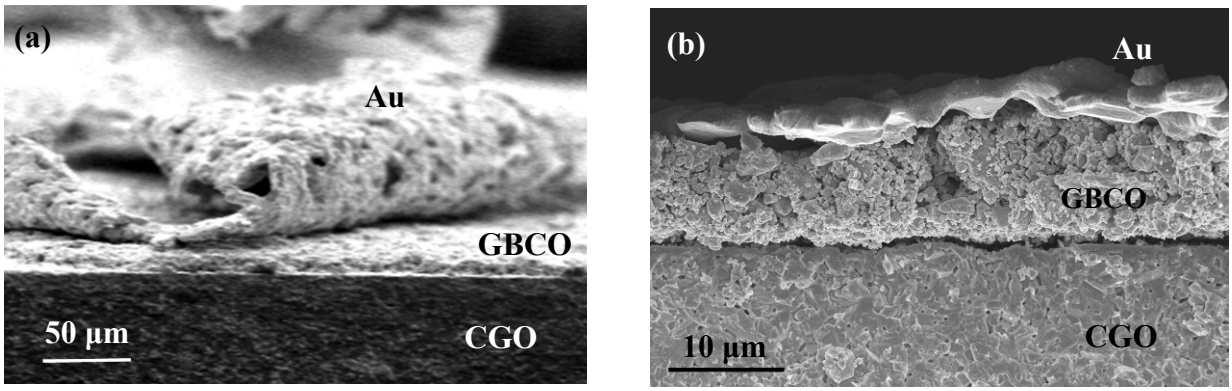

Figure 3.9 *SEM images of GBCO cathodes on CGO electrolyte with Au deposited using the gold paste: (a) peeled off (b) attached*

Figure 3.10 shows the cross-sectional SEM images of the symmetrical cells with CGO electrolytes with different electrodes deposited by screen-printing, with the sintering temperature of 950 °C for 2h. The quality and homogeneity of the CGO electrolytes are visible, whereas interfaces between the electrolytes and electrodes are clearly seen. No obvious reaction between the electrolyte and the electrode materials is observed in accordance with the investigation of chemical compatibility between GBCO and CGO indicating no significant reactions below 1000 °C [29]. Approximately identical microstructures could be seen whatever the composition. Nevertheless, the thickness of electrode layers measured by SEM analysis is of only 10 µm, which seems insufficient and might limit the cathode performance. Moreover, poor adhesion of electrode on the electrolyte surfaces is observed, a few gaps due to partial delamination of the cathode layer have been observed for these cells. This delamination is probably due to either the low roughness of the electrolyte layer, which would make cathode attachment difficult, or the different thermal expansion coefficients between CGO (TEC~10×10^{-6} K^{-1}) and cobaltites (e.g., TEC~22×10^{-6} K^{-1} for $LaCoO_{3-\delta}$). This poor connectivity between electrode and electrolyte phases could significantly influence the charge-transfer processes at the electrode/electrolyte interface, which possibly gives rise to a high frequency arc in impedance spectra

indicating the onset of interfacial electrochemical kinetic resistance. This could also reduce the apparent electrode-electrolyte contact surface. Besides, after the ball milling being applied to break the agglomeration in as-synthesized powders, similar inhomogeneity and poor porosity of electrode are observed in all cases with big size grains (>1 um) compared to other works [28-30]. Thus, in spite of good connectivity of grains in the electrode layer, the electrode performance could be strongly limited due to the insufficiency of electrode/gas interfaces on electrode grain surface which is considered as an importance electrochemical active zone for the oxygen surface exchange.

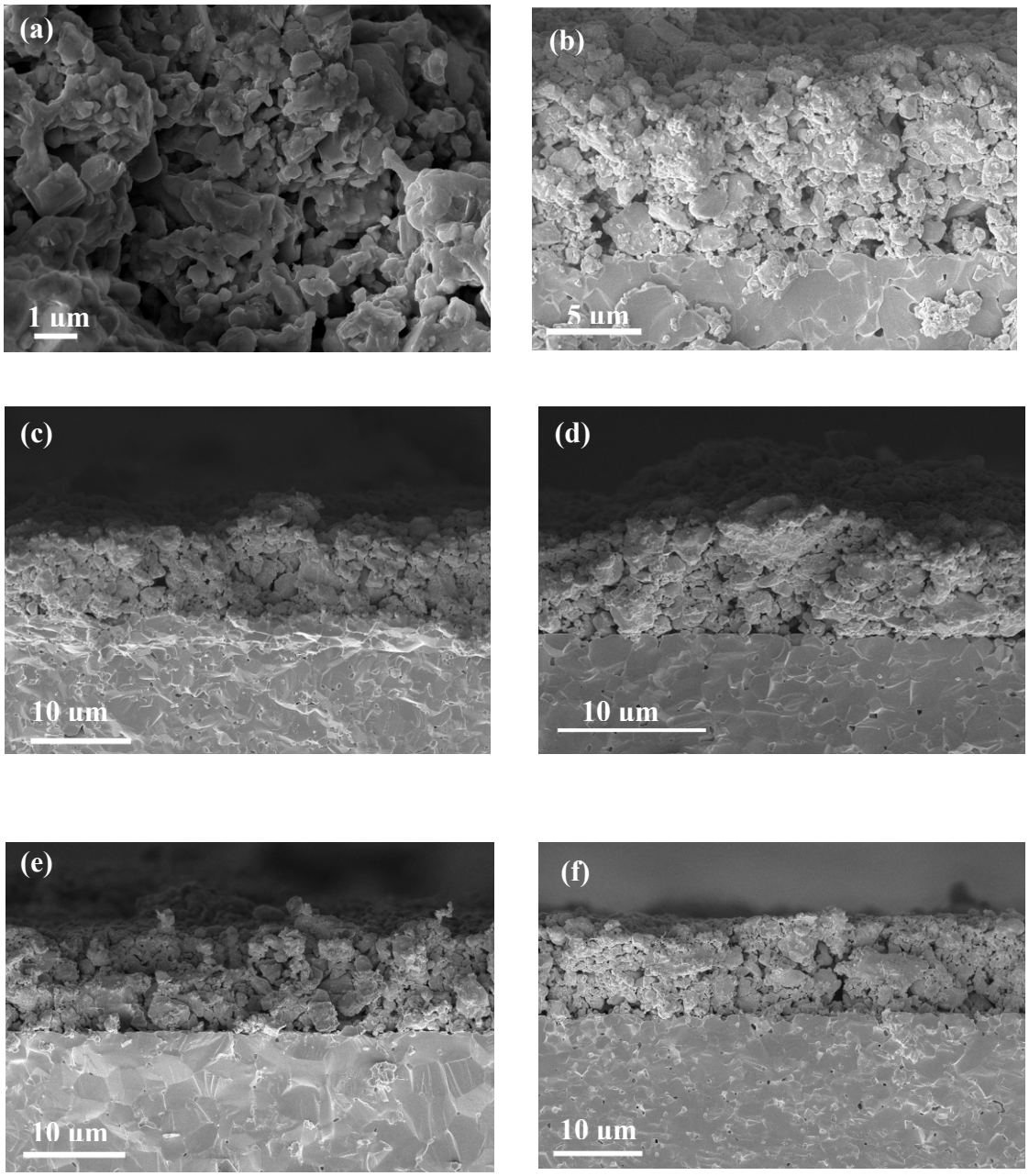

Figure 3.10 *SEM images of the cross section of GBCM/CGO/CGO symmetrical cells by screen-printing after the impedance spectroscopy measurements: (a) GBCO electrode microstructure, (b) GBCO, (c) GBCN03, (d) GBCN06 (e), GBCF03 and (f) GBCF06*

3.3.1.2 Electrochemical performance with CGO electrolytes

The impedance spectra under OCV of the symmetrical cells with CGO electrolytes may exhibit various contributions, due to the complexity of oxygen reduction mechanism as discussed above in this chapter. These spectra were analysed by the software Zview using equivalent circuits to separate the reaction processes, by which the cathode polarisation resistances (R_p) could be extracted. The term ASR was used to describe all resistance terms associated with the electrodes or electrodes/electrolyte interfaces, which is nominalised by the electrode surface area and corrected by a factor of 2 since as symmetric configuration was employed.

$$ASR = \frac{R_p \times S}{2} \tag{4.14}$$

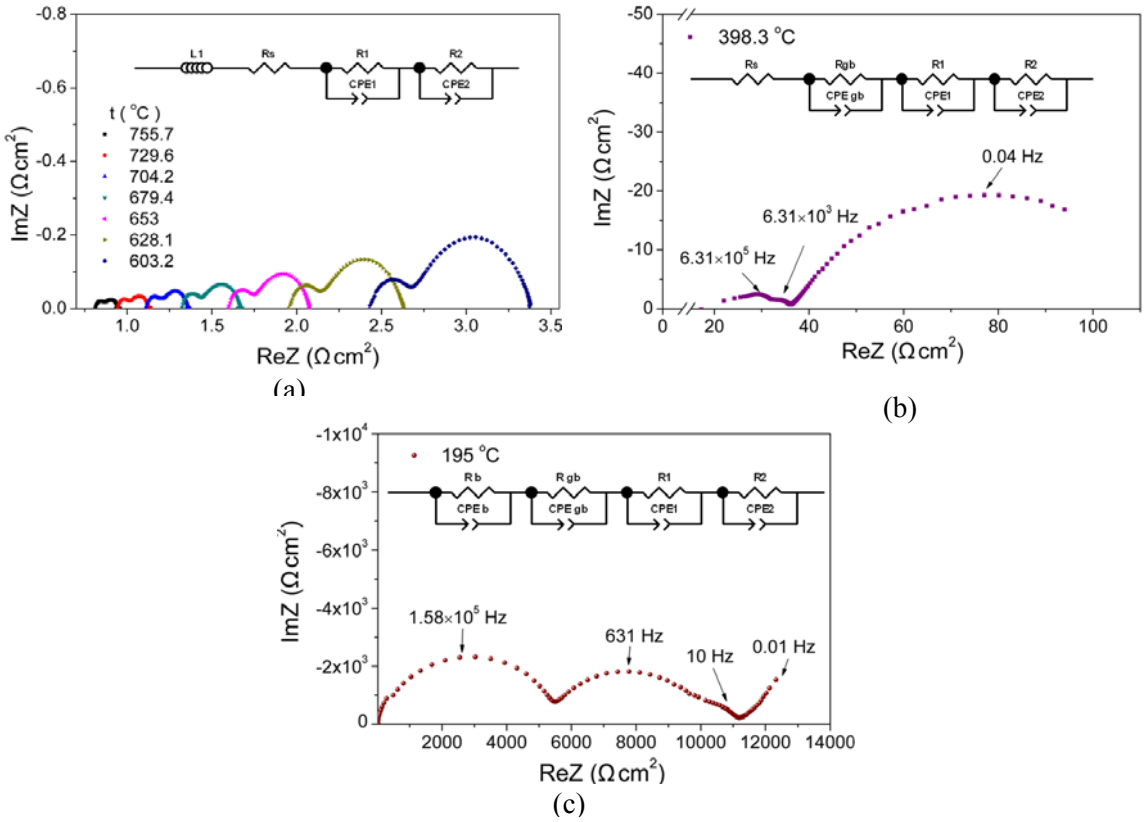

Figure 3.11 *Impedance spectra of GBCO/CGO/GBCO symmetrical cell at different temperatures under air and OCV condition; modified corresponding equivalent circuits depending on temperatures are applied to obtain cathode polarization resistance.*

Figure 3.11 shows the Impedance spectra of a GBCO/CGO/GBCO symmetrical cell measured at different temperatures under air and OCV condition, as well as the equivalent circuits applied and modified according to the temperature range. In the equivalent circuit, L is an inductance caused by the cable, the first resistance R_S corresponds to the ohmic series resistance; R_1 and R_2, each of which is

in parallel with a constant phase element (CPE1 and CPE2) and represent the comparatively high (actually in middle frequency range) and low frequency arc, respectively, are attributed to the electrode contribution, as shown in ***Figure 3.11(a)***. At lower temperature, additional high frequency arcs appear with decrease of temperature referring to the resistance associated to the CGO electrolyte, R_b for the bulk and R_{gb} for the grain boundary ***Figure 3.11(b) and (c)***, in accordance with other works [29]. This temperature dependence makes evident that the two depressed arc at the IT-temperature range (500~750 °C) correspond to the electrode contribution and also confirm the validity of the analysis with equivalent circuits to characterize the electrode performance of GBCO based cathodes [28-34]. Compared to the impedance spectra obtained in this work at higher temperature range (e.g >800 °C) which involves one major depressed arc in the impedance spectra, the two arcs are distinguishable, which indicates that there are two or two kinds of oxygen reduction processes, *e.g.* chemical, electrochemical or transport processes, involved in this intermediate temperature range. The overall polarisation resistance is the sum of R_1 and R_2, as $R_c = R_1 + R_2$. This model is applied for the analysis of the other cells with GBCN and GBCF electrodes, expect for the GBCN03 the low frequency (R_2CPE_2) element is replaced by a short Warburg (W_s) in parallel with a constant phase element to better fit the data, as shown in ***Figure 3.12***.

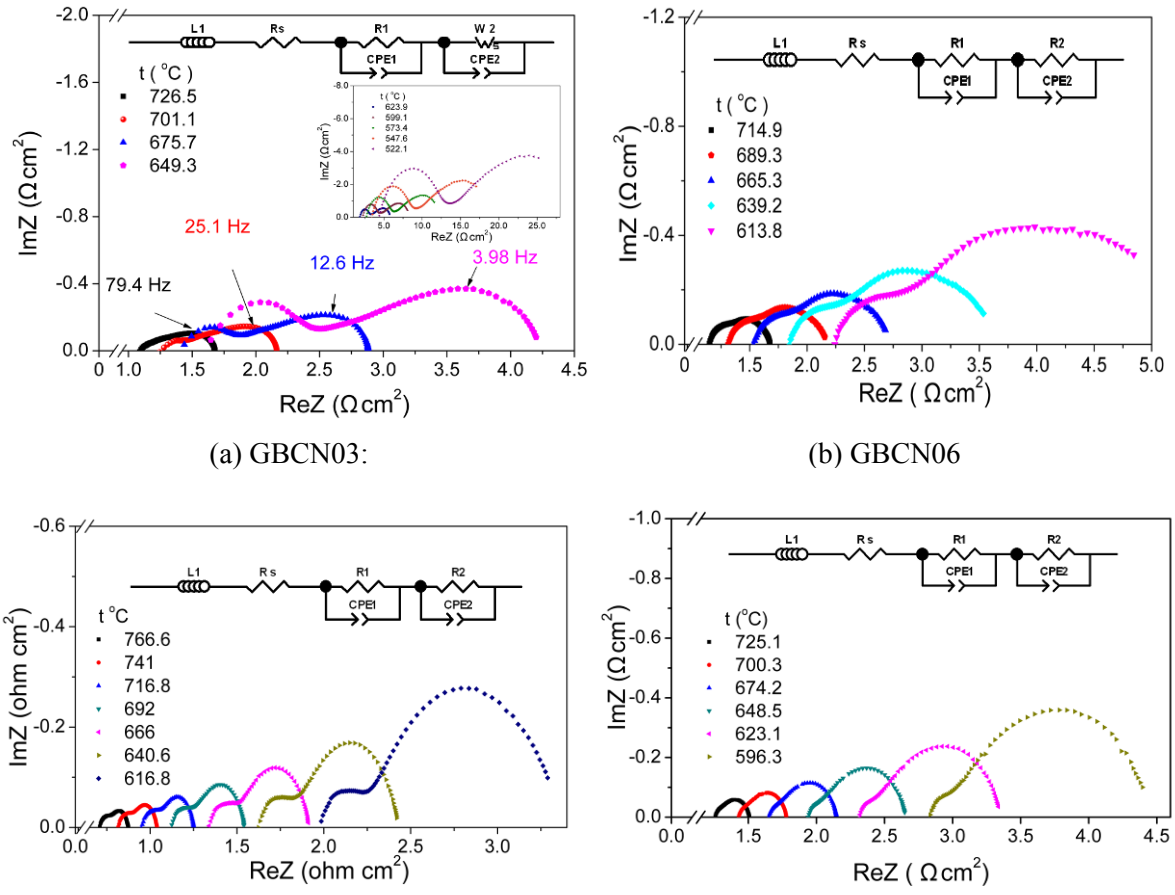

(a) GBCN03: (b) GBCN06

(d) GBCF03 (d) GBCF06

Figure 3.12 *Impedance spectra of symmetric cells with (a) GBCN03, (b) GBCN06, (c) GBCF03, and (d) GBCF06 electrodes, and their corresponding equivalent circuit.*

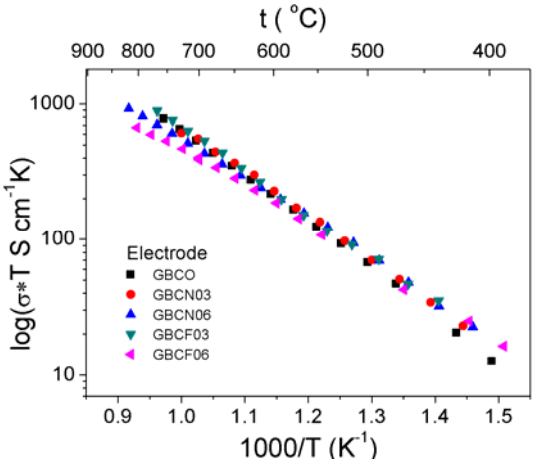

Figure 3.13 *Conductivity of CGO electrolyte with different electrode materials measured by symmetric cells in air*

The conductivity of CGO electrolytes shows good agreement whatever the electrodes used, as shown in ***Figure3.13,*** as well as the calculated activation energy *ca*. 0.54~0.66 eV. The overall polarisation resistances for these five electrodes at 700 °C are listed in Table 4.2. These values are much higher than those published, with the characteristic value of 0.25 Ω cm^2 at 650 °C for GBCO cathode performance [30,31]. Taking into account the previous SEM results and the comparatively large HF_C arc in impedance spectra associated with the charge transfer processes, this augmentation of ASR could be assumed mainly due to the poor connectivity between the electrode and electrolyte phases which enhances the electrochemical interfacial kinetic resistance and diminishes the electrode-electrolyte contact surface. In this case, the impedance is not only dominated by chemical dissociation and transport steps but also the exchange of oxygen ions across the of GBCM/CGO interface thereby increasing the ohmic resistance over the investigated temperature range, even if someone states that the electrochemical incorporation at the interface is usually considered largely equilibrated at least above 650 °C [2]. Besides, the microstructure defects of deposited electrodes by screen printing in this work might also contribute to the large ASR values. Thus, the electrode performance might be improved by ameliorating the preparation techniques: for example, polishing more roughly the CGO surface, increasing the ball milling time to obtain smaller grain size, or multiplying the deposits by screen printing to increase the electrode thickness. Another alternative strategy is the composite electrode, which has been proved as a promising option to improve the GBCO cathode performance [35-38]. By comparing the polarisation resistance of different compositions in this work at the same temperature, both Ni and Fe substitution are found to decrease the electrochemical performance, which is in agreement with the result from Wei *et al*. [28] in Ni-doped GBCO, with the polarization resistances of 0.40 Ωcm^2, 0.43 Ωcm^2, 0.48 Ωcm^2 and 0.54 Ωcm^2 at 600 °C for x = 0, x = 0.1, and x = 0.3, respectively.

Composition	GBCO	GBCN03	GBCN06	GBCF03	GBCF06
ASR 650 °C (Ω cm^2)	0.55	0.91	1.6	0.50	0.78
ASR 700 °C (Ω cm^2)	0.3	0.47	0.79	0.38	0.4

Table 3.2 ASR for GBCO, GBCN and GBCF, at 650 °C and 700 °C

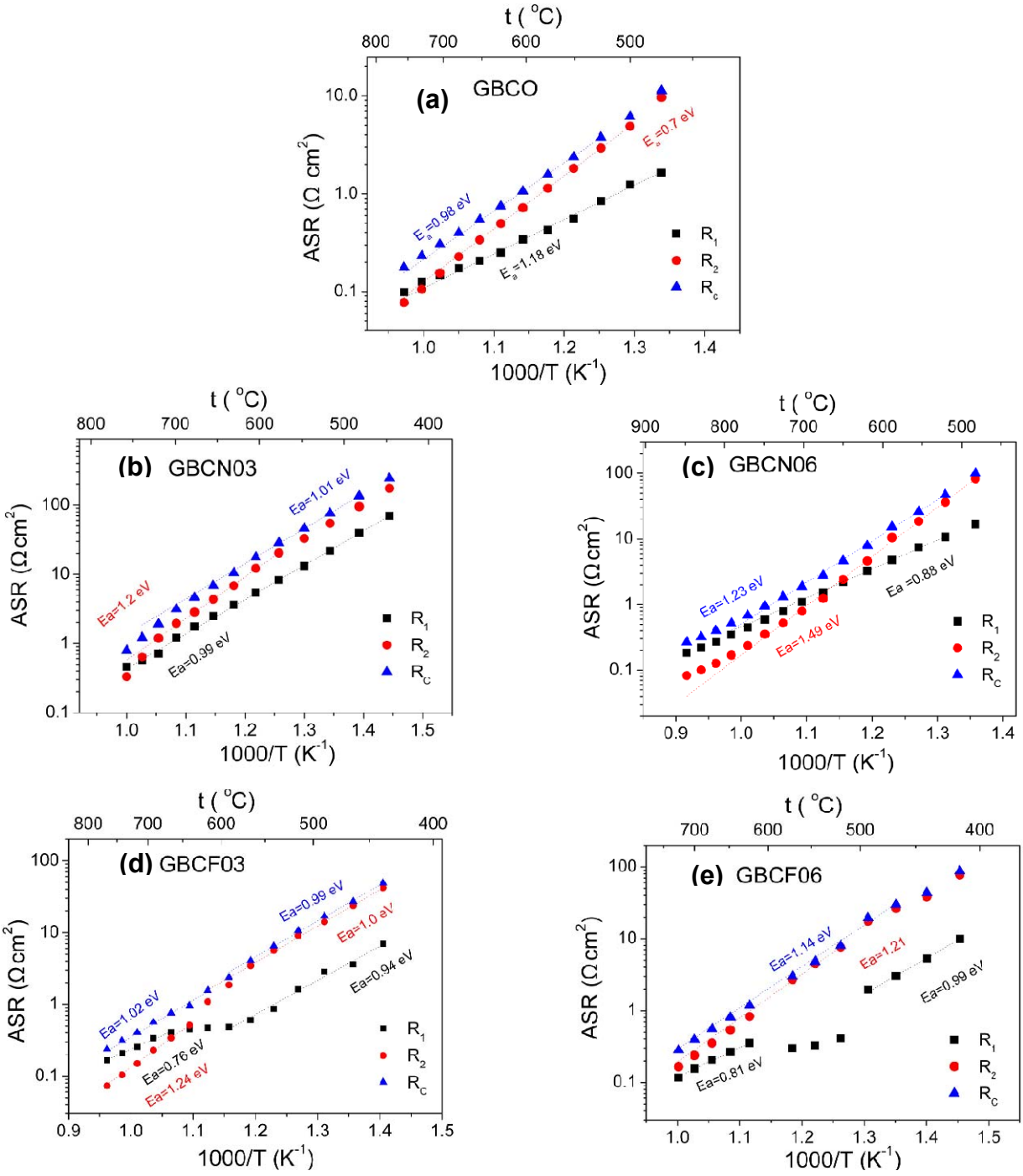

Figure 3.14 *Temperature dependence (Arrhenius plots) of the three polarization resistances R_1, R_2 and R_C (in term of ASR) and corresponding activation energies obtained by fitting these plots in certain temperature range.*

A common agreement assign to the high frequency arc (high frequency contribution to electrode performance HF_C) which is attributed to the electronic and ionic charge-transfer processes occurring across the current collector/electrode interface, bulk of mixed conductors, and electrode/electrolyte interfaces [13]. In contrast, the low frequency contribution range (LF_C) corresponds to the complex non-charge-transfer processes in oxygen reduction mechanism, such as oxygen surface exchange, solid-state diffusion and gas-phase diffusion in low oxygen partial pressure, which still remain debatable. Temperature dependent Arrhenius plots of polarisation resistances R_1 and R_2, associated with the HF_C and LF_C range respectively, as well as the overall polarisation resistances R_C which is the sum of R_1 and R_2 (all are in term of ASR), are shown in ***Figure3.14.*** Phenomenologically, these polarisation resistances exhibit the Arrhenius-like behaviour in the temperature range 500~750 °C, especially R_C and the R2 (LF_C) resistances. Exceptional behaviours of HF_C resistances are found in GBCF03 and GBCF06, seeing in ***Figure 3.14 (d)*** and ***(e)***, in which the HF_C resistance shows much slower increasing rate at lower temperature. Activation energies calculated for the HF_C, LF_C and overall resistance, respectively, as a function of reciprocal temperature (1000/T K^{-1}) are listed in table 3.3.

Electrode composition	Temperature range (°C)	Activation energy (eV)		
		R_1 HF	R_2 LF	R_c
GBCO	500-750	1.18	0.7	0.98
GBCN03	500-750	0.99	1.2	1.01
GBCN06	500-750	0.88	1.49	1.23
GBCF03	<550	0.94	1.24	0.99
	>600	0.76	1.0	1.02
GBCF06	<550	0.99	1.21	1.14
	>650	0.81		

Table 3.3 Activation energies obtained from impedance measurement for HF, LF processes and overall reaction on five compositions.

At high temperature (>750 °C) the polarisation resistance of HF_c arc is smaller than that of LF_C arc, which is inverse at lower temperature (< 700 °C), as the cross of R_1 and R_2 curves observed for all compositions, suggesting that at high temperature the charger transfer processes dominate the electrode performance since the oxygen reduction is assumed to be easily activated. With decreasing temperature, the non charge transfer processes become the limiting factor. In addition to the increased overall polarisation resistance, both Ni and Fe substitution are observed to increase the E_a contributing

to overall polarisation resistance. This is in consistency with the study of Ni substituted GBCN by Wei et al [28], showing the same influence of Ni substitution on electrode performance with similar activation energy (95.1 kJ mol^{-1} = 0.99eV) for GBCN03.

In case of Ni substitution for Co, the doping of nickel with a lower activity may account for the increased ASR values since the cobaltite are preferred for oxygen reduction reaction. Both Ni and Fe substitution are found to increase the activation energy E_a for R_2 greatly and meanwhile slightly decrease the E_a for R_1, compared to pure GBCO. If the R_1 and R_2 are attributed to specific electrochemical kinetic or processes according to their frequency dependence, Ni and Fe substitutions for Co in the studied materials are assumed to facilitate the charge-transfer processes and limit the chemical processes which possibly includes oxygen adsorption, solid-state diffusion, surface-path diffusion or gas phase diffusion *et al*., as discussed above. This is more obvious for the Fe substituted electrodes with predominant LF_C contribution to polarisation resistance as mentioned above. Nevertheless, a "break" and "slow down" of temperature dependent R_1 curve for GBCF03 and GBCF06 were observed. In order to better understand the oxygen reduction processes in GBCO, GBCN and GBCF, especially to identify the rate-limiting steps among possible sub-reactions steps, oxygen partial pressure (P_{O_2}) dependent impedance measurements were applied at a constant temperature 700 °C. ***Figure 3.15*** shows Nyquist-like impedance spectra of P_{O_2} dependent measurement under OCV for the symmetric GBCN03/CGO/GBCN03 cell as an example. Typically, at high oxygen partial pressure range (>0.01 atm), the impedance spectrum of GBCN03 is characterized by two individual arcs corresponding to equivalent circuits used in air condition. When the P_{O_2} decreases to ~10^{-3} atm, gas-phase effect appears as a separate arc at very low frequency, which is usually < 1Hz. Modified equivalent circuits according to variation of impedance spectra were used to analyze the polarization resistance, with high frequency (R_{HF}CEP1) and medium frequency (R_{MF}CPE2) elements being attributed to the interfacial charge-transfer processes and oxygen exchange and diffusion processes, respectively, as well as a short Warburg element added for describing the gas-phase diffusion at the very low frequency.

- In the HF range, the amplitude of the arc decreases with the increase of temperature and totally disappears above 800 °C in this work as discussed above. This arc shows almost no change with the oxygen partial pressure. According to the system and model used in this work, this arc would be attributed to the oxygen ions transferring through the electrolyte/ electrode interface.

- In the MF range, it seems that only one arc exists when the measurements are performed in air. However, under lower oxygen partial pressure, with careful examination, in some case such as the GBCN03 and GBCN06, one single (R_{MF}CPE) element is not sufficient to fit well the measured impedance spectra, which usually show a straight slope of 45° phase angle after the

HF arc indicating infinite diffusion phenomena. Thus the contribution of MF arcs is assumed to be the overlapping of several individual contributions characteristic of sub-reactions processes, *e.g.* oxygen exchange on electrode surface, oxygen diffusion in the solid state *etc.* Moreover, the amplitude of MF arcs increases with decreasing oxygen partial pressure which corresponds to the lack of oxidant, showing evident P_{O_2} dependency.

- In the LF range (< 1 Hz), a new arc or a straight line with a 45 ° angle appears at low oxygen partial pressure, normally below 0.01 atm. This contribution is commonly attributed to the gas phase diffusion that occurs on the electrode surface or in the pores of electrode structure. For this temperature 700 °C, under air condition or high oxygen partial pressure, this contribution to resistance becomes very small and comparatively neglectable, thus the corresponding impedance arc is highly overlapped and hard to distinguish or to separate.

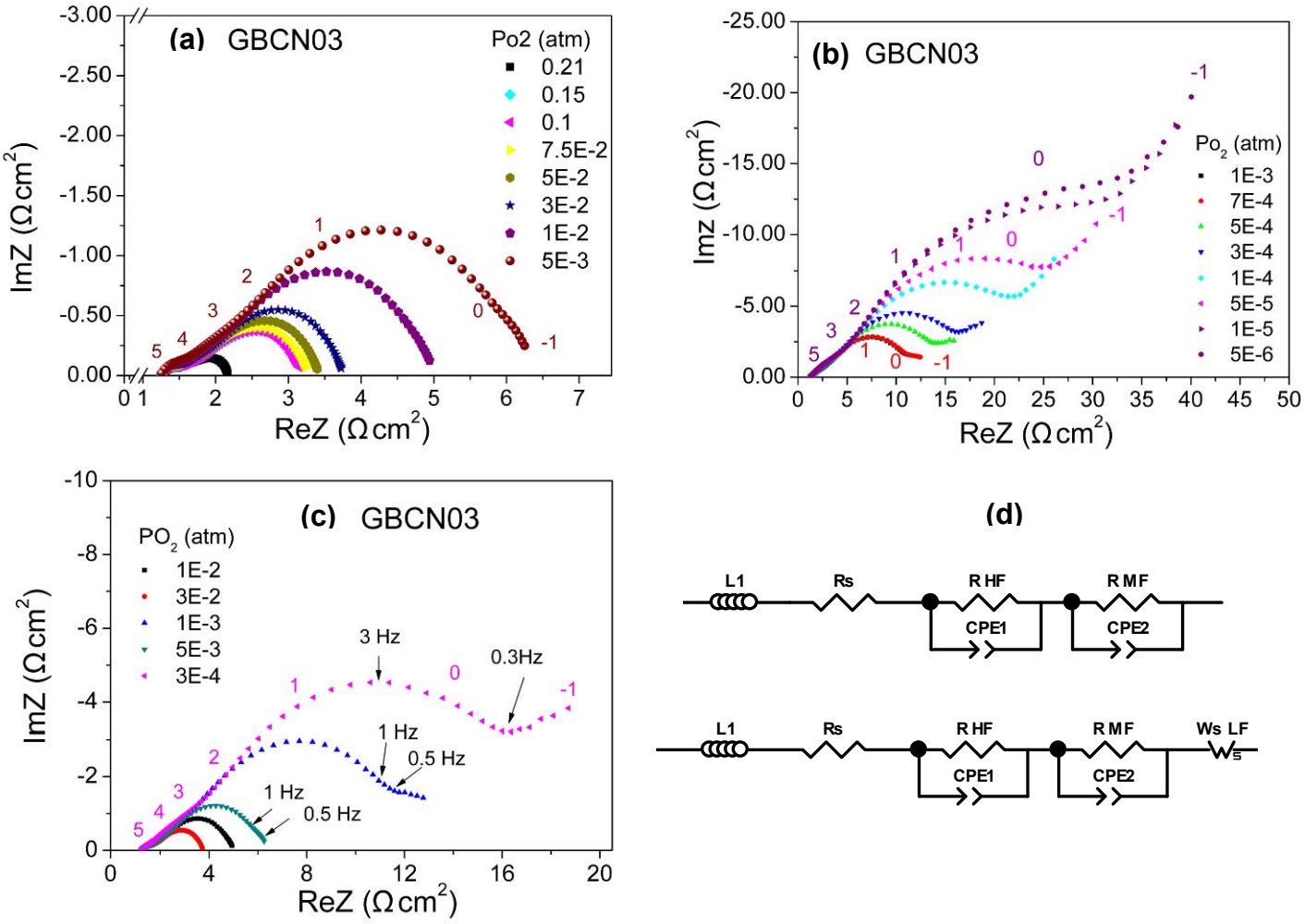

Figure3.15 *Impedance spectra of GBCN03 on CGO electrolyte at 700 °C under high (a) and low (b) oxygen partial pressure. (c)The appearance of a very low frequency arc (slope) characteristic of gas phase diffusion (d) Corresponding equivalent circuits.*

The oxygen dependence of polarisation resistance could be described by the law: $R_\eta \propto P_{O_2}^{-m}$, where the exponential factor m is well known to give information about the species involved in the electrode reactions [39-41] and can be used to find the main rate-determining steps (RDS) of electrode reaction in the MIECs, as shown in Table 4.4.

Reaction order m	Reaction steps [8,13,40,42-46]
1	Oxygen molecular absorption on the electrode surface or gas phase diffusion in the electrode microstructure
1/2	Oxygen dissociation (adsorption/desorption) and reduction, or oxygen surface diffusion with atomic oxygen involved in RDSs
1/3	Oxygen surface exchange
1/4	Charge-transfer reaction on the electrode (or O_2 incorporation into the bulk of mixed conductor)

Table 3.4 Elementary reaction steps and the value of reaction order (m) related to cathode reaction

Evolution of electrode resistance as a function of P_{O_2} at 700 °C is shown in ***Figure 3.16***. The values of reaction order (m) related to different frequency ranges are listed below in Table 4.5, which vary according to the P_{O_2} range.

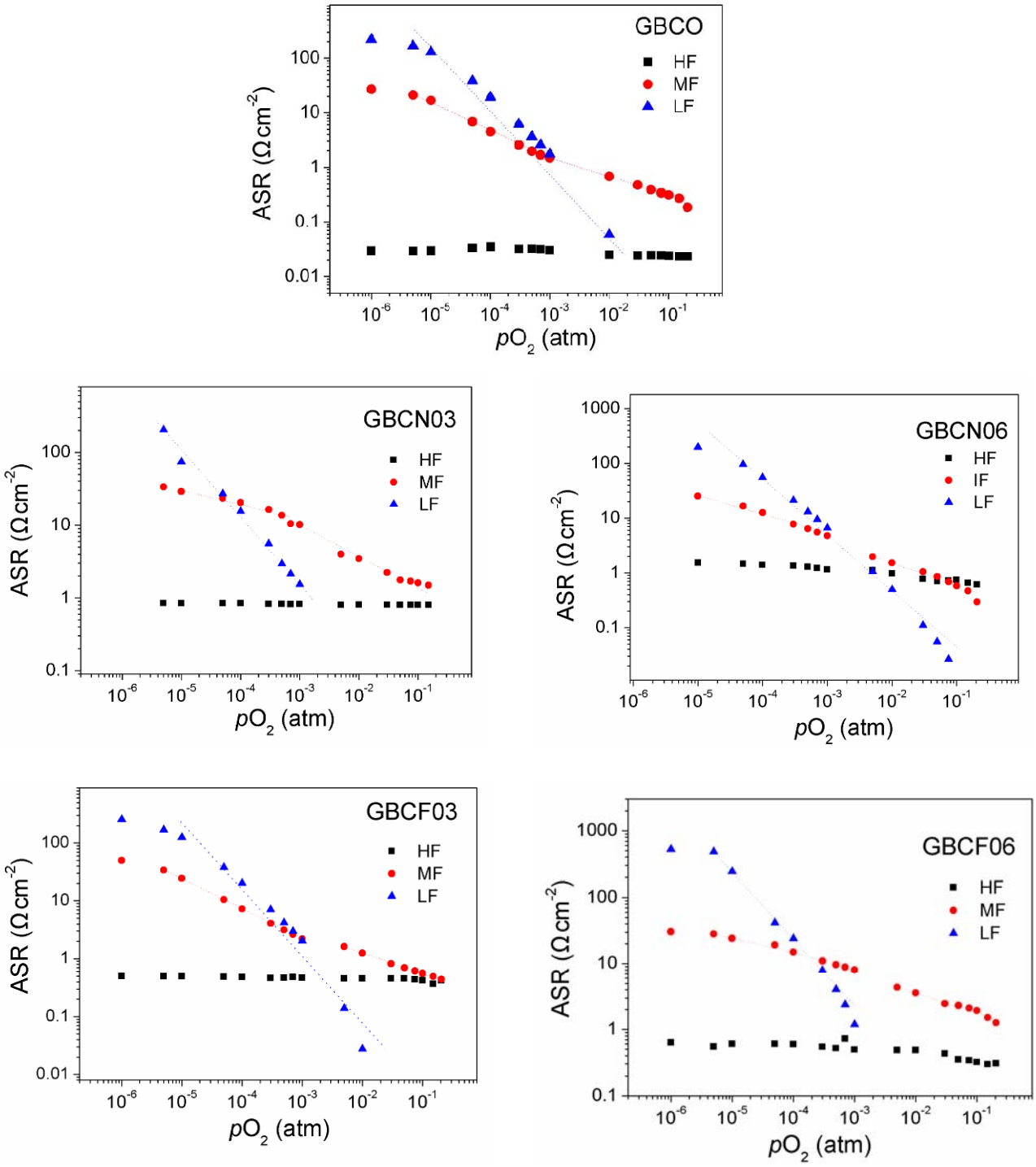

Figure 3.16 *Evolution of HF, MF and LF contributions to the electrode resistance as a function of oxygen partial pressure for the GBCO, GBCF03 and GBCF06 at 700 °C*

m ($R_\eta \propto P_{O_2}^{-m}$) / Electrode	HF	m for MF		m in $R_\eta \propto P_{O_2}^{-m}$ for LF
	10^{-5}~0.21 atm	> 10^{-3} atm	≤ 10^{-3} atm	< 10^{-3} atm
GBCO	0.02	0.34	0.53	0.96
GBCF03	0.01	0.36	0.51	0.95
GBCF06	0.05	0.24	0.31	1.01
GBCN03	0.01	0.39	0.22	0.89
GBCN06	0.08	0.38	0.41	1.05

Table 4.5 P_{O_2} dependence of polarization resistance of MF and LF arcs obtained from AC impedance measurement

- HF

The weak P_{O_2} -dependence of the HF arc suggests that neither atomic oxygen nor molecular oxygen is involved in this step. Therefor, the HF arc is associated with charger transfer processes such as oxygen ion transfer at the electrode/electrolyte interface as well as the reaction at TPB, as expressed by.

$$O_{ad}^{2-} + V_O^{\bullet\bullet}\left(CGO\right) \rightarrow O_O^{\times} \tag{4-16}$$

This is understandable that the oxygen vacancies created on the electrode surface due to change of oxygen partial pressure do not affect oxygen ion transfer, especially GBCO are considered as good ionic conductors. However, poor connectivity or even separation of the electrode-electrolyte could give rise to insufficient ion path way and thereby limit this processes.

- MF

The variation of P_{O_2} dependence in a wide range shows that more than one individual process may contribute to the MF arc, which may lead to serious contradictions in RDS identification [8,26]. The value of m is also used to indicate the rate-determining process of the oxygen reaction. For example, when m = 0.25, the $P_{O_2}^{1/4}$ dependence could be considered as charge transfer reaction or O^-/O_{ad} surface diffusion along the electrode surface [44,47], and in case of m = 0.5, the $P_{O_2}^{1/2}$ dependence may indicate that the dissociation of oxygen molecular is the dominant process. In this work, the m factors in MF range varies in the range *ca.* 0.25 ~ *ca.* 0.5, showing complex co-limitations. Nevertheless, at high

temperature range (> 10^{-3} atm), m is close to 1/3 which suggests surface exchange as rate-determining step.

- LF

The LF arc (< 1Hz) appearing only at low oxygen partial pressure (< 10^{-3} atm) exhibit strong oxygen dependence with reaction order close to 1. This process could be interpreted as the associative adsorption of O_2 molecular or the gas phase diffusion within the electrode pore system driven by the gradient in the chemical potential of gas, shown as.

$$O_2(gas) \rightarrow O_2(GBCM-pore1) \rightarrow O_2(GBCM-pore2) \quad (4\text{-}17)$$

$$O_2(gas) \rightarrow O_{2,ad} \quad (4\text{-}18)$$

$$O_{2,ad} \rightarrow 2O_{ad} \quad (4\text{-}19)$$

Through P_{O_2} dependent EIS, it is found that the Ni and Fe substituted GBCN and GBCF show the same general oxygen reduction behaviour as GBCO, especially in for the high frequency and low frequency range. The interfacial ion transfer and gas phase diffusion of all compositions indicated by reaction factor are in good agreement. The IF non-charge process could be considered mainly limited by the surface exchange, whilst the diffusion also contributes.

3.3.2 Fuel cell tests with Ni-YSZ/$Ce_{0.8}Gd_{0.2}O_2$/GBCM configuration

Single cell tests are measured at different temperatures with different flow rate of humidified H_2 as fuel. ***Figure 3.17*** shows an example of the cell voltage and the corresponding powder density of electrolyte-supported single cell configuration of Ni-YSZ/$C_{e0.8}Gd_{0.2}O_2$/GBCF06 in the temperature range of 600-800 °C. With the highest H_2 flow rate of 40 ml/min, the maximum power density obtained at 700 °C was 79 mW cm^{-2}, 78 mW cm^{-2}, and 72 mW cm^{-2} for GBCO, GBCF03 and GBCF06, respectively, which are lower than the results found in literature [31,36,38].

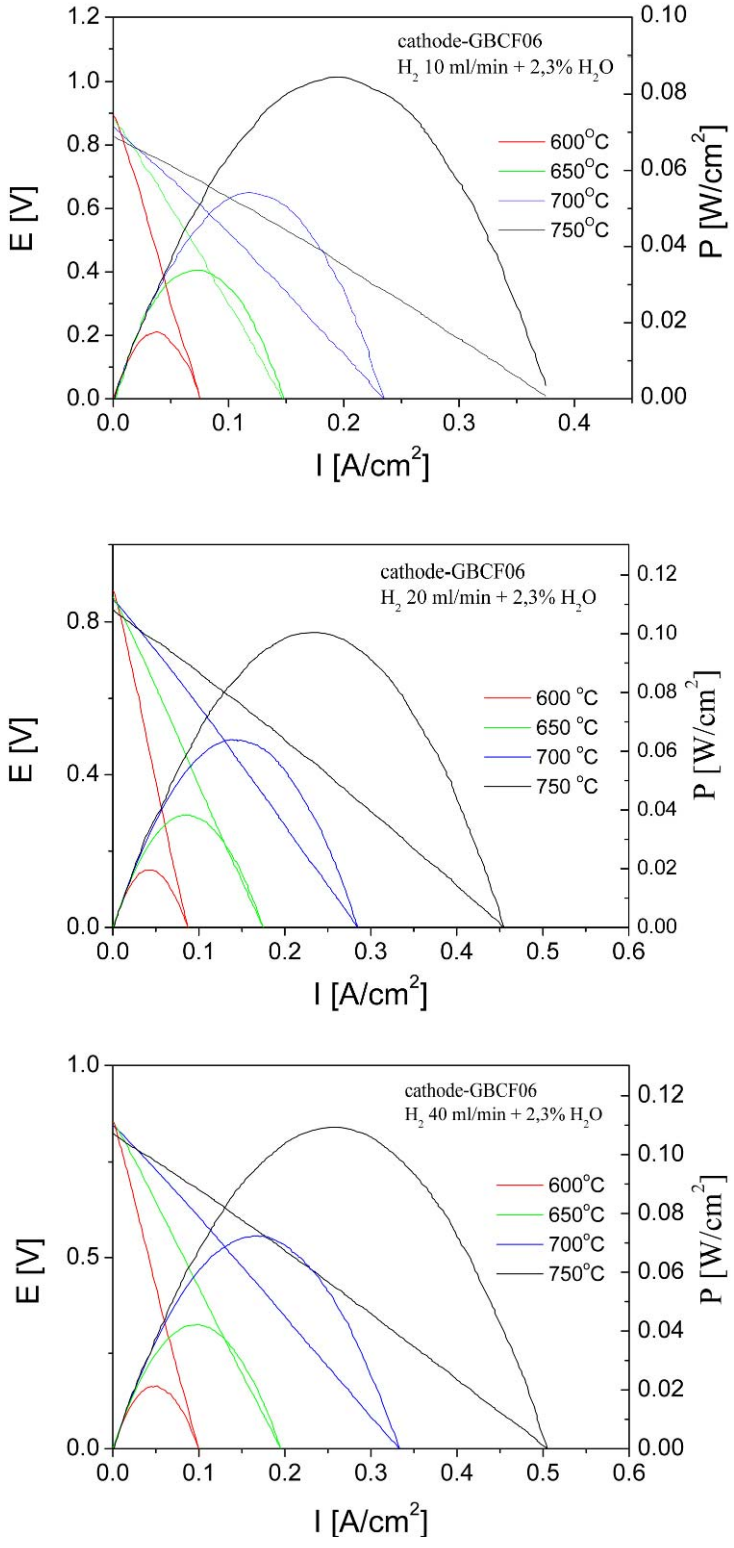

Figure 3.17 *Cell voltages (line) and power densities (arc) of Ni-YSZ/ $Ce_{0.8}Gd_{0.2}O_2$/GBCF06 single cell under humidified H_2 fuel and air oxidant at different temperatures and different H_2 flow rates*

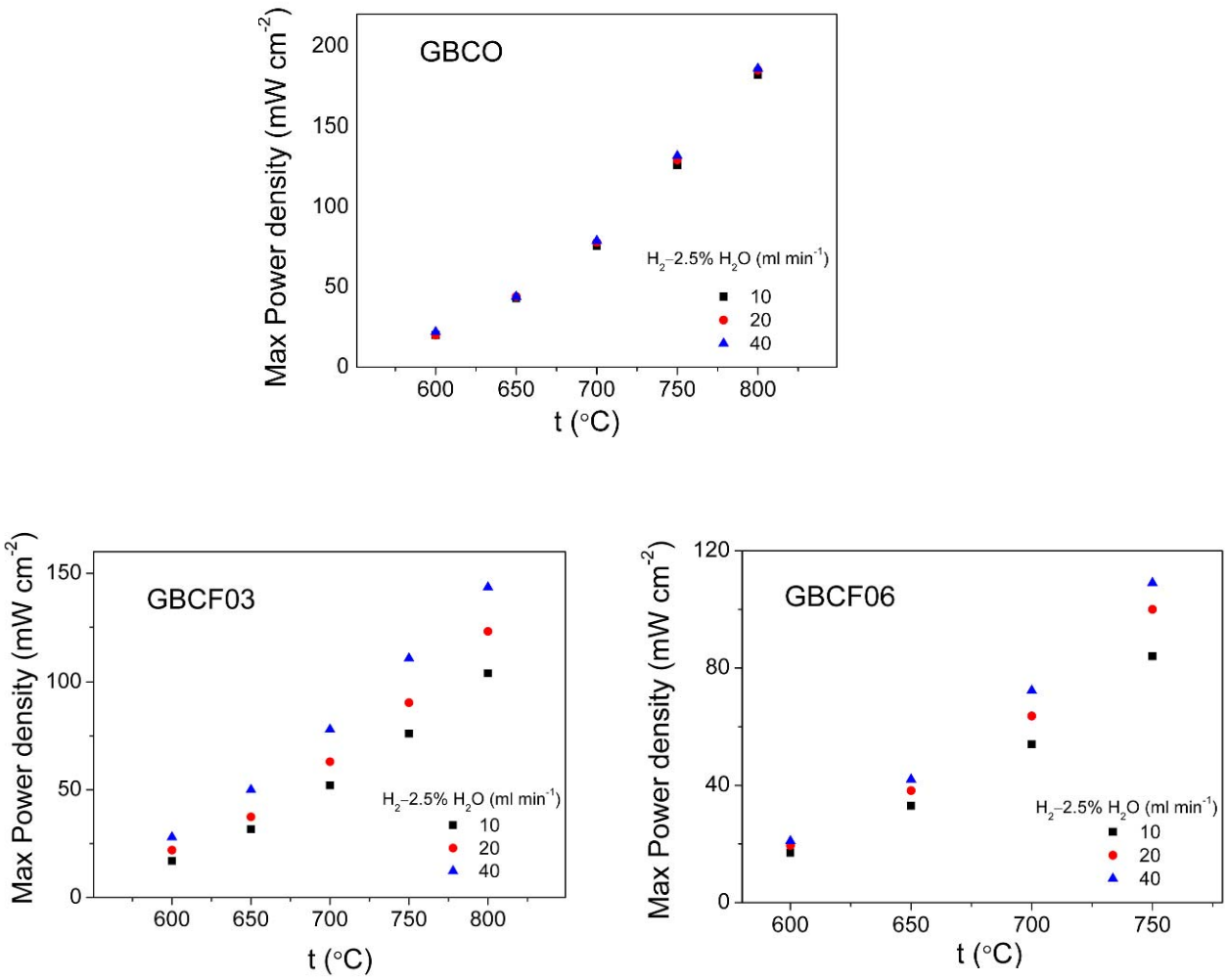

Figure 3.18 *Variation of Maximum power densities obtained from Ni-YSZ/$C_{e0.8}Gd_{0.2}O_2$/GBCM single cell tests under humidified H_2 fuel with different flow rate and different temperatures*

Figure 3.18 shows the maximum power densities varying with temperatures and flow rates of humidified H_2 fuel. It is observed that the performance of cell with GBCO cathode shows a weak flow rate dependency and highest power densities compared to those obtained from GBCF03 and GBCF06 under identical condition. For the GBCF03 and GBCF06 cathodes, the power densities are more sensitive to the flow rate of humidified H_2. Thus the cell performance could be assumed to improve at higher temperature and under higher H_2 flow rate. Moreover, lower cell performance was obtained with Fe substitution, according well with the results from symmetric cell tests in this work, and this is in good agreement with the consensus that cathode performance is the limiting factor for IT-SOFCs performance.

3.3.3 Electrochemical performance in proton conducting fuel cell

3.3.3.1 Morphology and Microstructure Characterization

The symmetrical cells with $La_{0.995}Ca_{0.005}NbO_4$ electrolytes exhibit very weak attachment of electrode on the electrolyte, e.g. ***Figure 3.19*** shows the SEM images of cross-sectional view of GBCF03/$La_{0.995}Ca_{0.005}NbO_4$/GBCF03 symmetrical cell. The electrode layer could be easily peeled off during the process of sample preparation for SEM, and the electrode shows better attachment to the Au layer than to the electrolyte. Nevertheless, the thickness of electrode layer could still be estimated close to 10 μm.

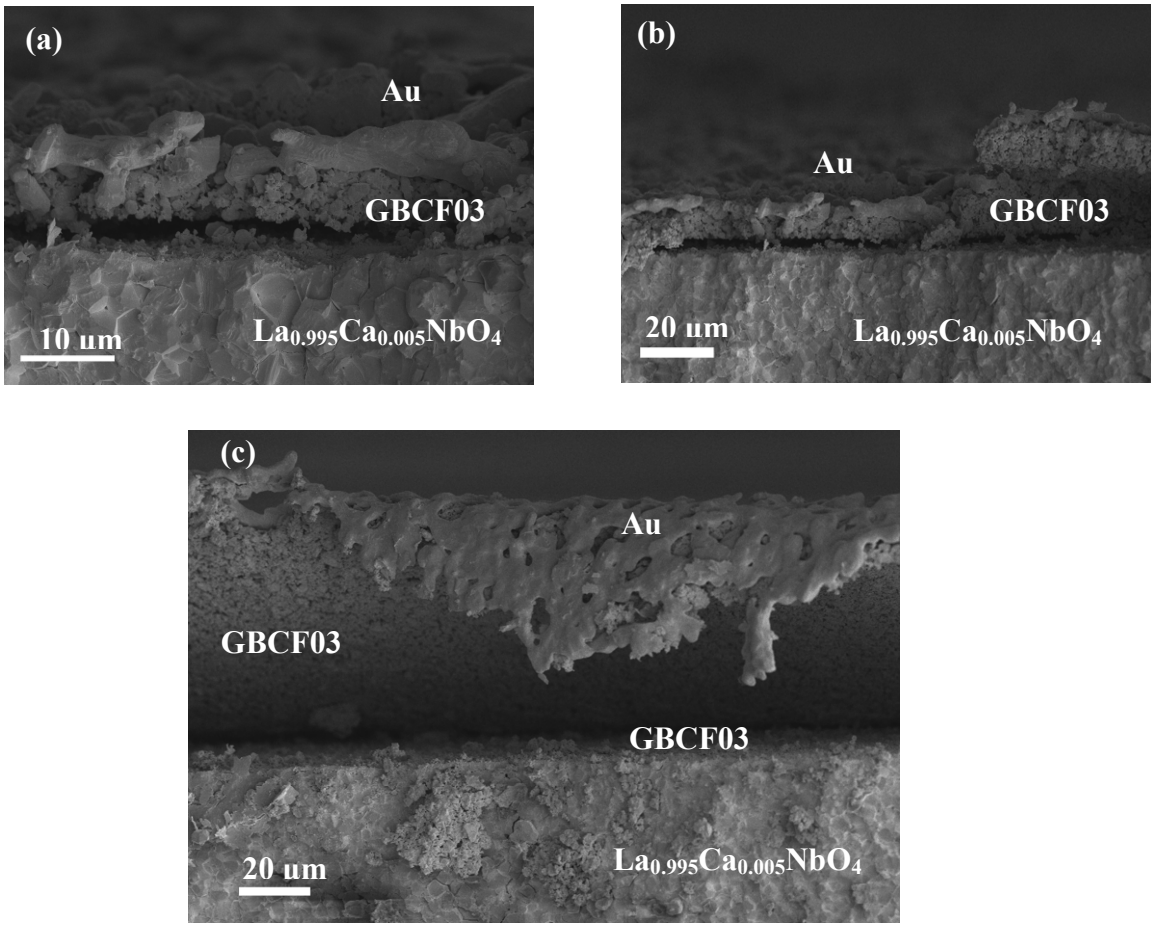

Figure 3.19 *SEM images of the cross section of GBCF03/$La_{0.995}Ca_{0.005}NbO_4$/GBCF03 symmetrical cells by screen-printing after the impedance spectroscopy measurements: (a) (b) and (c) represent different regions from the same cell.*

This extremely poor adhesion of electrode to electrolyte might come from the large mismatch of thermal expansion coefficient (TEC) between the GBCF/GBCN and $La_{0.995}Ca_{0.005}NbO_4$ electrolyte. As discussed in Chapter 2, the TEC values of electrodes studied in this work locate in the range of 19.8~21.1×10^{-6} K^{-1}, as well as 11.8~14.2 ×10^{-6} K^{-1} for $Ce(Gd)O_{2-\delta}$ [48]. In case of $LaNbO_4$, the most obvious challenge is the remarkable change in TEC above and below the monoclinic–tetragonal phase transition, with anisotropic expansion characteristics, particularly for the low temperature phase [49-52], as shown in Table 4.1. In addition, the very small thickness of $La_{0.995}Ca_{0.005}NbO_4$ electrolytes which are less than 0.2 mm seems to be responsible for the weak mechanic strength of the symmetrical cells on $La_{0.995}Ca_{0.005}NbO_4$ electrolyte which were thereby usually broken up in the sample holder after the electrochemical impedance measurement.

Materials	Temperature range	Linear TEC (α_L) (10^{-6} K^{-1})
$LaNbO_4$ [49,52]	473–773 K	14
	800–973 K	8.4
$Ce_{0.9}Gd_{0.1}O_{2-\delta}$ [48]		13.4 ± 0.1
$Ce_{0.8}Gd_{0.2}O_{2-\delta}$ [48]		11.8 ± 0.1
GBCN06 (this work)	373–973 K	18.4
GBCF06 (this work)	373–973 K	21.1

Table 3.6 Linear thermal expansion coefficients for the compositions used in this study

3.3.3.2 Electrochemical performance with $La_{0.995}Ca_{0.005}NbO_4$ electrolytes

Figure 3.20 shows the impedance spectra of GBCO/$La_{0.995}Ca_{0.005}NbO_4$/GBCO symmetric cell measured under OCV with 2.5%H_2O in air as an example as well as the corresponding equivalent circuits used. At high temperature, two contributions distinguished by frequency range are observed, which are assumed to be contribution attributed to the electrolyte grain boundary and electrode resistance, respectively [49,53,54]. With the decrease of temperature, the appearance of a high frequency arc represents the contribution of electrolyte bulk. Here the electrode contribution plays an important role in the overall resistance. The polarisation resistance (ASR) of electrode under dry air of humidified air (2.5%H_2O) calculated by equivalent fitting follows an Arrhenius-like behaviour, as shown in ***Figure3.20***.

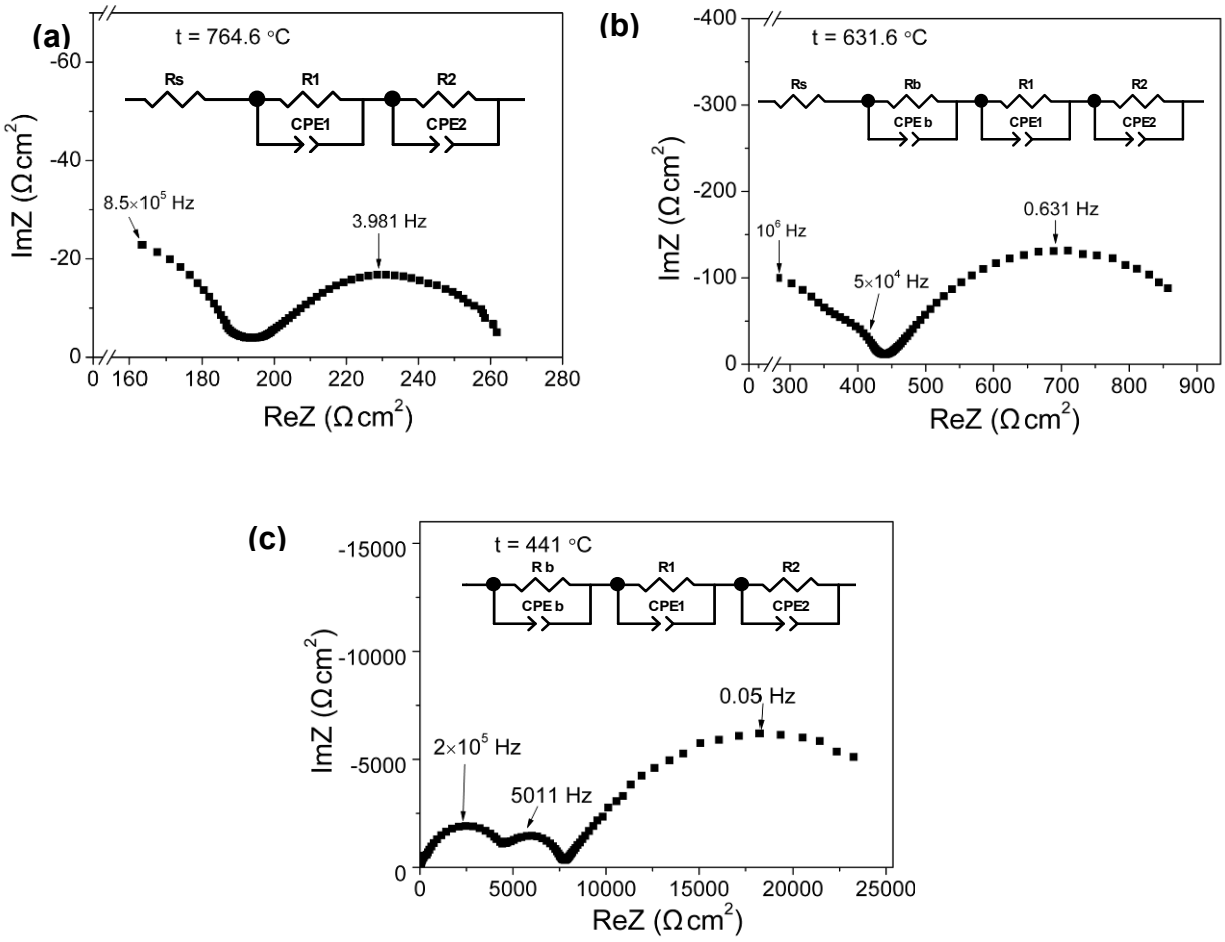

Figure 3.20 *Impedance spectra of GBCO/ $La_{0.995}Ca_{0.005}NbO_4$/GBCO cell under wet air with 2.5% H2O content at different temperature range and corresponding equivalent circuit used*

A dramatically large resistance of electrodes is obtained with this $La_{0.995}Ca_{0.005}NbO_4$ electrolyte. This is probably due to the great interfacial resistance related to the poor adhesion of electrode deposited by screen printing as observed by SEM, as well as the comparatively large thickness of the $La_{0.995}Ca_{0.005}NbO_4$ electrolyte, from 140 μm to 200 μm. The discrepancy in ASR measured under dry air and humidified air with 2.5% H_2O become more evident at lower temperature, and increases with the decrease of temperature, showing the water vapour contained in air effectively diminishes the electrode resistance. Unlike the impedance spectra with CGO electrolyte, electrode reaction steps are all overlapped to form a single arc in the low frequency range, whose summit frequency decrease with temperature and the electrodes resistance shows large contribution to the overall resistance in the whole temperature range measured.

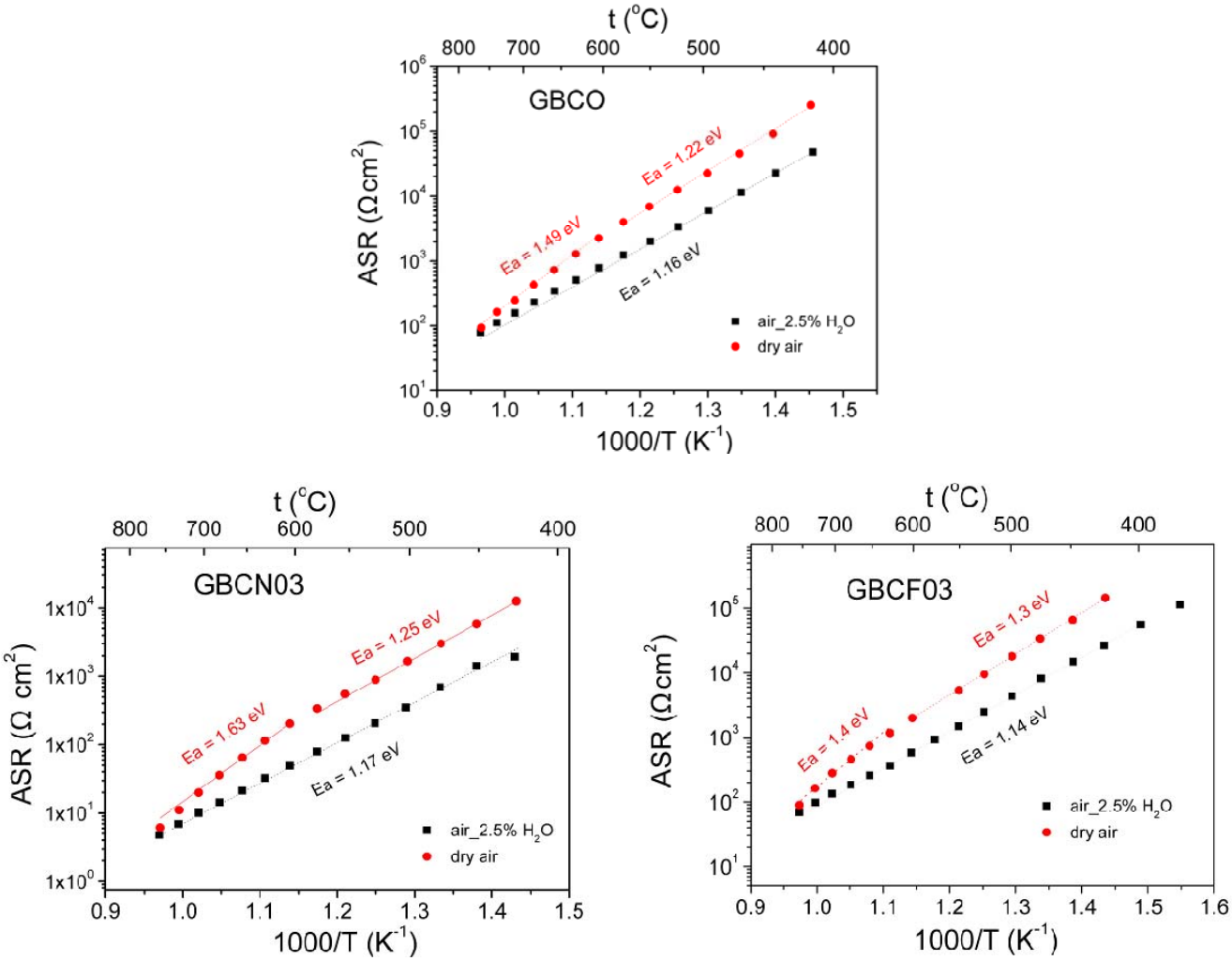

Figure 3.21 *ASR of electrode in GBCM/ $La_{0.995}Ca_{0.005}NbO_4$/GBCM symmetric cells as a function of temperature under humidified air and dry air, respectively*

Figure 3.22 shows the conductivity of electrolyte obtained by the impedance spectroscopy in this work. Compared to the maximum in protonic conductivity of acceptor-doped $LaNbO_4$ *i.e.* 1×10^{-3} S/cm at 950 °C in atmospheres containing ca 2% H_2O [49,50], the values obtained in this work are between one and two orders of magnitude lower, probably due to the poor electrode/electrolyte connectivity. In all cases, the conductivity is higher in wet air than that in dry air and the effect is stronger at lower temperature, showing the same trend with electrode performance. With respect to the study of this kind of electrolytes [49,50], at higher temperature, the proton concentration decreases, and above 1100 °C both oxygen ion conductivity and electronic conductivity surpass the protonic one, whilst below this temperature, positively charge native point defects, most probably oxygen vacancies take over. The conductivity is predominately ionic below 800 °C in air. At lower temperature, the protons are the major ionic charge carriers in the present of water vapour, and this explains the difference between the conductivity under dry air and wet air with water vapour.

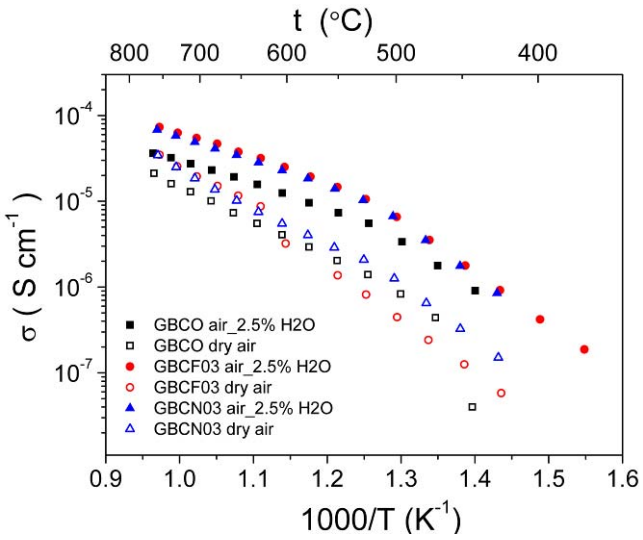

Figure 3.22 *Electrolyte conductivity obtained by impedance spectra of GBCO, GBCF03 and GBCN03, under dry air (open symbol) and wet air with 2.5% H_2O (solid symbols)*

Thus, due to the poor oxygen ionic conductivity in the intermediate temperature range, the electrode performance could possibly be limited by the charge-transfer process at the electrode/electrolyte interface. Moreover, compared to the small electrode resistance and electrolyte conductivity obtained for $BaZr_{0.1}Ce_{0.7}Y_{0.2}O_{3-\delta}$ with GBCO as cathode [54], the performance of GBCM/$La_{0.995}Ca_{0.005}NbO_4$/GBCO system is not satisfactory, probably attributing to the comparatively big electrolyte thickness or the poor electrode/electrolyte interfacial connectivity, and the relatively poor intrinsic conductivity of acceptor-doped $LaNbO_4$.

3.4 Conclusion

Electrochemical characterization have been carried out to investigate the electrode performance in GBCO and Ni, Fe-substituted GBCM (M=Ni, Fe) and the oxygen reduction reaction taking place on these materials. The temperature and oxygen partial pressure dependence of impedance spectra on GBCM/CGO/GBCM symmetric cells have been studied at OCV. Comparatively higher ASR values are obtained rather than the characteristic 0.25 Ω cm^2 obtained at 650 °C. Besides, it seems that both Ni and Fe substitutions increase the electrode resistance. The electrode polarization resistances were considered as a sum of two contributions distinguished by frequency and variation of impedance spectra with temperature. With the decrease of temperature, transfer process at the

electrode/electrolyte interface which is usually represented as impedance spectra arcs at high frequency, become predominant, especially in Fe-substituted GBCF.

In all cases, the whole oxygen reduction reaction is co-limited by the interfacial charge transfer process with very weak P_{O_2} dependence, and the oxygen surface exchange on the electrode or solid state diffusion associated with variation of reaction order m. With respect to the possible species involved and high ionic conduction in this series of materials, oxygen surface absorption/desorption involving atomic oxygen) and bulk diffusion are supposed to dominate rather than surface diffusion along the electrode to electrode/electrolyte interface or the gas phase diffusion. However, uncertainty still remains in the existence of oxygen intermediates and the influence of large electrode grain size. Both Ni and Fe doping has increased the electrode polarisation resistance compared with the pristine GBCO, which is in agreement with the single cell tests of GBCO and GBCF by A. Kulka with utilization of same electrode materials fabricated in this work. With proton conducting electrolyte $La_{0.995}Ca_{0.005}NbO_4$, the electrode performance is limited by the ionic charge transfer process especially at low temperature range, due to fact that the protons dominate the ionic conducting as major charge carrier at low temperature, which could be enhanced by the presence of water vapour. Comparatively large polarisation resistance values and low electrolyte conductivity are obtained due to the poor interfacial connectivity observed by SEM.

Several strategies could be expected to improve the cathode performance. For example, break the as-synthesized powders in order to obtain much smaller grain size, as well as increased electrode layer thickness, which could enlarge the effective active area for the oxygen reduction on electrode. The improvement of adhesion of electrode on electrolyte could also enhance the interfacial charge transfer process. Moreover, utilization of composite electrodes is another promising strategy as having been proved to be efficient to adapt the TEC mismatch between electrolytes and electrodes and to decrease the electrode polarization resistance in order to obtain appreciable cathode performance.

REFERENCES

[1] Jacobson, A. J. *Chem. Mat.* **2009**, *22*, 660-674.

[2] Adler, S. B. *ChemInform* **2004**, *35*.

[3] Princivalle, A.; Djurado, E. *Solid State Ion.* **2008**, *179*, 1921-1928.

[4] Zhao, H.; Mauvy, F.; Lalanne, C.; Bassat, J. M.; Fourcade, S.; Grenier, J. C. *Solid State Ion.* **2008**, *179*, 2000-2005.

[5] Barsoukov, E.; Macdonald, J. *Impedance spectroscopy: theory, experiment, and applications*; John Wiley and Sons, 2005.

[6] Huang, Q.-A.; Hui, R.; Wang, B.; Zhang, J. *Electrochimica Acta* **2007**, *52*, 8144-8164.

[7] Norby, T.; Departement of Chemistry, U. o. O., Ed. Oslo.

[8] Tsipis, E. V.; Kharton, V. V. *J. Solid State Electrochem.* **2008**, *12*, 1039-1060.

[9] Choi, Y.; Mebane, D.; Wang, J.-H.; Liu, M. *Topics in Catalysis* **2007**, *46*, 386-401.

[10] LALANNe, C. Thèse, L'UNIVERSITE BORDEAUX 1, 24 Oct 2005.

[11] Lai, W.; Haile, S. *J. Am. Ceram. Soc.* **2005**, *88*, 2979-2997.

[12] Tsipis, E. V.; Kharton, V. V. *J. Solid State Electrochem.* **2008**, *12*, 1367-1391.

[13] Adler, S. B. *Solid State Ion.* **2000**, *135*, 603-612.

[14] Adler, S. B.; Lane, J. A.; Steele, B. C. H. *J. Electrochem. Soc.* **1996**, *143*, 3554-3564.

[15] Adler, S. B.; Lane, J. A.; Steele, B. C. H. *J. Electrochem. Soc.* **1997**, *144*, 1884-1890.

[16] Adler, S. B. *Solid State Ion.* **1998**, *111*, 125-134.

[17] Lu, Y. X.; Kreller, C.; Adler, S. B. *J. Electrochem. Soc.* **2009**, *156*, B513-B525.

[18] Wilson, J. R.; Schwartz, D. T.; Adler, S. B. In *6th International Symposium on Electrochemical Impedance Spectroscopy*; Pergamon-Elsevier Science Ltd: Cocoa Beach, FL, 2004, p 1389-1402.

[19] Svensson, A. M.; Sunde, S.; Nisancioglu, K. *J. Electrochem. Soc.* **1997**, *144*, 2719-2732.

[20] Svensson, A. M.; Sunde, S.; Nisancioglu, K. *Solid State Ion.* **1996**, *86-88*, 1211-1216.

[21] Mebane, D. S.; Liu, Y.; Liu, M. *J. Electrochem. Soc.* **2007**, *154*, A421-A426.

[22] Janardhanan, V. M.; Heuveline, V.; Deutschmann, O. *Journal of Power Sources* **2008**, *178*, 368-372.

[23] Baumann, F. S.; Maier, J.; Fleig, J. *Solid State Ion.* **2008**, *179*, 1198-1204.

[24] Baumann, F. S.; Fleig, J.; Habermeier, H.-U.; Maier, J. *Solid State Ion.* **2006**, *177*, 1071-1081.

[25] Fleig, J. *Physical Chemistry Chemical Physics* **2005**, *7*, 2027-2037.

[26] Jorgensen, M. J.; Mogensen, M. *J. Electrochem. Soc.* **2001**, *148*, A433-A442.

[27] Li, Y.; Gemmen, R.; Liu, X. *Journal of Power Sources* **2010**, *195*, 3345-3358.

[28] Wei, B.; Lü, Z.; Jia, D.; Huang, X.; Zhang, Y.; Su, W. *International Journal of Hydrogen Energy* **2010**, *In Press, Corrected Proof*.

[29] Tarancon, A.; Pena-Martinez, J.; Marrero-Lopez, D.; Morata, A.; Ruiz-Morales, J. C.; Nunez, P. *Solid State Ion.* **2008**, *179*, 2372-2378.

[30] Pena-Martinez, J.; Tarancon, A.; Marrero-Lopez, D.; Ruiz-Morales, J. C.; Nunez, P. *Fuel Cells* **2008**, *8*, 351-359.

[31] Tarancon, A.; Morata, A.; Dezanneau, G.; Skinner, S. J.; Kilner, J. A.; Estrade, S.; Hernandez-Ramirez, F.; Peiro, F.; Morante, J. R. *Journal of Power Sources* **2007**, *174*, 255-263.

[32] Tarancon, A.; Skinner, S. J.; Chater, R. J.; Hernandez-Ramirez, F.; Kilner, J. A. *Journal of Materials Chemistry* **2007**, *17*, 3175-3181.

[33] Li, N.; Lu, Z.; Wei, B. O.; Huang, X. Q.; Chen, K. F.; Zhang, Y. Z.; Su, W. H. *Journal of Alloys and Compounds* **2008**, *454*, 274-279.

[34] Ding, H.; Xue, X. *International Journal of Hydrogen Energy* **2010**, *In Press, Corrected Proof*.

[35] Wei, B.; Lü, Z.; Jia, D.; Wei, T.

[36] Jo, S. H.; Muralidharan, P.; Kim, D. K. *Electrochemistry Communications* **2009**, *11*, 2085-2088.

[37] Lee, Y.; Kim, D. Y.; Choi, G. M. *Solid State Ion.*, *In Press, Corrected Proof*.

[38] Lee, S. J.; Kim, D. S.; Kim, D. K. *Current Applied Physics*, *In Press, Corrected Proof*.

[39] Siebert, E.; Hammouche, A.; Kleitz, M. *Electrochimica Acta* **1995**, *40*, 1741-1753.

[40] Takeda, Y.; Kanno, R.; Noda, M.; Tomida, Y.; Yamamoto, O. *J. Electrochem. Soc.* **1987**, *134*, 2656-2661.

[41] Schouler, E. J. L. *Solid State Ion.* **1983**, *9-10*, 945-951.

[42] Baek, S. W.; Bae, J.; Yoo, Y. S. *Journal of Power Sources* **2009**, *193*, 431-440.

[43] Mauvy, F.; Lalanne, C.; Bassat, J.-M.; Grenier, J.-C.; Zhao, H.; Huo, L.; Stevens, P. *J. Electrochem. Soc.* **2006**, *153*, A1547-A1553.

[44] Matsuzaki, Y.; Yasuda, I. *Solid State Ion.* **1999**, *126*, 307-313.

[45] Jiang, S. P. *Solid State Ion.* **2002**, *146*, 1-22.

[46] Kharton, V. V.; Tsipis, E. V.; Yaremchenko, A. A.; Frade, J. R. *Solid State Ion.* **2004**, *166*, 327-337.

[47] Kim, J.-D.; Kim, G.-D.; Moon, J.-W.; Park, Y.-i.; Lee, W.-H.; Kobayashi, K.; Nagai, M.; Kim, C.-E. *Solid State Ion.* **2001**, *143*, 379-389.

[48] Kharton, V. V.; Figueiredo, F. M.; Navarro, L.; Naumovich, E. N.; Kovalevsky, A. V.; Yaremchenko, A. A.; Viskup, A. P.; Carneiro, A.; Marques, F. M. B.; Frade, J. R. *Journal of Materials Science* **2001**, *36*, 1105-1117.

[49] Haugsrud, R.; Norby, T. *Solid State Ion.* **2006**, *177*, 1129-1135.

[50] Haugsrud, R.; Norby, T. *Nature Materials* **2006**, *5*, 193-196.

[51] Mokkelbost, T.; Lein, H. L.; Vullum, P. E.; Holmestad, R.; Grande, T.; Einarsrud, M.-A. *Ceramics International* **2009**, *35*, 2877-2883.

[52] Tolchard, J. R.; Lein, H. L.; Grande, T. *J. Eur. Ceram. Soc.* **2009**, *29*, 2823-2830.

[53] Fjeld, H.; Kepaptsoglou, D. M.; Haugsrud, R.; Norby, T. *Solid State Ion.* **2010**, *181*, 104-109.

[54] Lin, B.; Zhang, S.; Zhang, L.; Bi, L.; Ding, H.; Liu, X.; Gao, J.; Meng, G. *Journal of Power Sources* **2008**, *177*, 330-333.

Chapter 4 Oxygen nonstoichiometry and the transport properties

Oxygen transport properties, including oxygen nonstocihiometry, oxygen ion permeability and diffusion, and oxygen surface exchange [1], is of great importance in materials for SOFCs application. Thus to design materials demonstrating high oxygen conductivity at low temperature is also a scientific challenge in the IT-SOFC development. To be a good oxygen-ion conductor, two fundamental requirements must be met: large amount of oxygen vacancies in the oxygen sublattice and low energy barrier for oxygen migration from one site to another [2]. Most of the oxygen reduction mechanisms proposed, such as the ALS model [3], highlight that in porous mixed ionic-electronic conducting (MIEC) electrodes, the oxygen reduction reaction is complex and consists of chemical and electrochemical processes co-limited by the oxygen surface exchange and solid state diffusion. Furthermore, the oxygen non-stoichiometry, which reflects the concentration of oxygen vacancies, is a fundamental factor relating many important properties such as oxygen transport behaviour, electronic conductivity and catalytic activity [4]. Especially in deficient perovskite structures the bulk diffusion takes place by hopping of oxygen vacancies [5]. Therefore, these values are essential to assess the validity of those theoretical models or for predicting the performance of new materials [6].

In this work, the determination of the absolute values of oxygen stoichiometry δ in $GdBaCo_{2-x}M_xO_{5+\delta}$ (M=Ni or Fe, x =0, 0.3, 06) has been performed by thermogravimetric analysis versus temperature and oxygen partial pressure. Electrical conductivity relaxation (ECR) has been carried out in the temperature range of 600 to 800 °C and in the oxygen partial pressure range of 10^{-5} to 0.206 atm in order to investigate the oxygen surface exchange and chemical diffusion. The limitations of sample density, apparatus and especially the flush time are discussed.

4.1 Electrical conductivity relaxation (ECR)

High ionic conductivity in MIECs at elevated temperatures results from large oxygen vacancy concentration in conjunction with a high vacancy diffusivity [7]. For many mixed-conducting materials that are predominantly electronic conductor, a change in the oxygen partial pressure will result in a corresponding change in the electrical conductivity of the material due to, primarily, a change in the concentration of charge carriers [8]. If the ionic conductivity in a material is significantly less than the electronic conductivity, the time for this change to propagate throughout the material is considered almost exclusively controlled by the movement of ionic species. This time variation or “relaxation” of

the electrical conductivity of a sample after a stepwise change in the ambient oxygen partial pressure can be measured, giving rise to the electrical conductivity relaxation (ECR) technique. The relaxation data are fitted to theoretical equations from which the chemical diffusion coefficients and surface exchange coefficients can be extracted, based on the solutions proposed in literature [7,9-15].

4.1.1 General equation and solutions

To analyse the diffusion by relaxation technique, a flat thin sheet is considered with thickness 2*b*. At $t < 0$, the sample is assumed to be in thermodynamic equilibrium with the surrounding atmosphere. At $t = 0$, the corresponding P_{O_2} is changed stepwisely to a new value, associated with a new equilibrium in oxygen concentration c_∞. Driven by the gradient of oxygen concentration between c_0, the oxygen concentration at $t < 0$, and c_∞, the oxygen starts to diffuse into or out of the sample.

Starting point in the derivation is Fick's second law

$$\frac{\partial c}{\partial t} = \widetilde{D}\frac{\partial^2 c}{\partial x^2} \tag{4.1}$$

where $\widetilde{D}$ is the chemical diffusion coefficient. The surface reaction is assumed to proceed at a rate proportional to the difference between the actual concentration at the surface, $c(\pm b)$, and c_∞. The boundary conditions at both surfaces z = *b* and z = -*b* are given by [5,16]:

$$J(b) = -\widetilde{D}\left.\frac{\partial c}{\partial z}\right|_{z=b} = K_{tr}\left[c(b) - c_\infty\right] \tag{4.2}$$

$$J(-b) = -\widetilde{D}\left.\frac{\partial c}{\partial z}\right|_{z=-b} = -K_{tr}\left[c(-b) - c_\infty\right] \tag{4.3}$$

where *J* denotes the flux density and K_{tr} is the surface transfer coefficient controlling the rate of surface reactions. Thus, the solution for the concentration profile as a function of time, $c(z, t)$, is defined through an eigenfunction expansion of the initial oxygen concentration c_0 [17]:

$$\frac{c(z,t) - c_0}{c_\infty - c_0} = 1 - \sum_{n=1}^{\infty}\frac{2L_\beta \cos(\beta_n z/b)}{(\beta_n^2 + L_\beta^2 + L_\beta)\cos(\beta_n)} exp\left(-\frac{t}{\tau_n}\right) \tag{4.4}$$

where the time constants τ_n are given by

$$\tau_n = \frac{b^2}{\widetilde{D}\cdot\beta_n^2} \tag{4.5}$$

and the parameters β_n^2 are obtained from

$$\beta_n \tan\beta_n = \frac{bK_{tr}}{\widetilde{D}} = L_\beta \tag{4.6}$$

Since the total electrical conductivity of a mixed conductor is predominantly determined by the electronic conduction, in case of an oxide with *p*-type conduction *i.e.* decreasing with decreasing oxygen partial pressure, the change in electrical conductivity following step change in P_{O_2} results from the oxygen incorporation or generation of oxygen vacancies from the reaction with gas phase, thereby either forming two electrons or annihilating two electron holes, given by [18],

$$V_{\cdot\cdot} + \frac{1}{2}O_2 \rightleftharpoons O_O^{\times} + 2h^{\cdot} \tag{4.7}$$

The apparent conductivity change is related to oxygen ion conductivity which is the same as vacancy conductivity [18]. Equating the change in the oxygen nonstoichiometry to changes in electrical conductivity it is possible to express the conductivity transient as [13,16,19].

$$\overline{\sigma}(t) = \frac{\sigma(t)-\sigma_0}{\sigma_\infty - \sigma_0} = 1 - \sum_{n=1}^{\infty} \frac{2L_\beta \cos(\beta_n z/b)}{\beta_n^2\left(\beta_n^2 + L_\beta^2 + L_\beta\right)} exp\left(-\frac{t}{\tau_n}\right) \tag{4.8}$$

thus the parameters $\widetilde{D}$ and K_{tr} can be obtained from fitting the data of electrical relaxation experiments with this equation.

To evaluate the eigenvalues and validity of coefficients calculated, a characteristic length is given

$$L_c = \frac{\widetilde{D}}{K_{tr}} \tag{4.9}$$

within which diffusion limitation occurs if $b \gg L_c$ and surface limitation if $b \ll L_c$. By assuming a proportional relation between the electronic conductivity and the oxygen concentration, the dimensionless transient conductivity can be derived by integration of the concentration over the sample volume

$$\overline{\sigma}(t) = \frac{\sigma(t)-\sigma_0}{\sigma_\infty - \sigma_0} = 1 - \sum_{n=1}^{\infty} A_n \left(-\frac{t}{\tau_n}\right) \tag{4.11}$$

$$A_n = \frac{2L_\beta^2}{\beta_n^2\left(\beta_n^2 + L_\beta^2 + L_\beta\right)} \tag{4.12}$$

Limiting L_β between 0.03 and 30 in the procedure is considered the effective regime to evaluate both $\widetilde{D}$ and K_{tr} simultaneously. If the value of L_β from fitting is below 0.03, the chemical diffusion coefficient is to be ignored and *vice versa*.

4.1.2 Flush-time correction

The evaluation of chemical diffusion and surface exchange by the use of ECR technique requires an instantaneous change in surrounding atmosphere to match the derivation of the theoretical equations, and the accurate data of the conductivity transient should be measured at short times, i.e. immediately after the change in the surrounding oxygen partial pressure. Thus, the flushing behaviour of the reactor volume may significantly influence the early stage of the relaxation process and result in large errors in the transport parameters obtained.

Den Otter et al [16] provided a flush-time correction for the non-ideal step response, with a gradual equilibration of the oxygen partial pressure surrounding the sample, instead of ideal "instantaneous" change, due to the finite flush time of the reactor. An important time constant τ_f is taken into account, which is referred to the characteristic time needed to flush the reactor volume, by assuming continuously ideally stirred tank reactor (SISTR) behaviour in the actual reactor volume.

$$\overline{p}_{\mathrm{CRSTR}}(t)=\frac{p_{\mathrm{CISTR}}(t)-p_\infty}{p_0-p_\infty}=exp\left(-\frac{t}{\tau_{\mathrm{f}}}\right) \tag{4.12}$$

where the $p_{\mathrm{CISTR}}(t)$ denotes the oxygen partial pressure as a function of time, $\overline{p}_{\mathrm{CISTR}}(t)$ is the dimensionless oxygen partial pressure. This equation indicates that after a period of $4\times\tau_f$ has elapsed, only 1.83% of the original gas volume has not been replaced yet [16].

The final conductivity transient equation taking in account the flushtime is written as:

$$\overline{\sigma}_{\mathrm{CISTR}}(t)==1-\exp\left(-\frac{t}{\tau_{\mathrm{f}}}\right)-\sum_{n=1}^{\infty}A_n\frac{\tau_n}{\tau_n-\tau_{\mathrm{f}}}\left[exp\left(-\frac{t}{\tau_n}\right)-exp\left(-\frac{t}{\tau_{\mathrm{f}}}\right)\right] \tag{4.13}$$

$$A_n=\frac{2L_\beta^2}{\beta_n^2\left(\beta_n^2+L_\beta^2+L_\beta\right)} \tag{4.14}$$

They have also concluded that to be neglected, the flush time should be at least 500 times smaller than the duration of the experiment in the case of diffusion limitation, and 5000 times smaller in the case of pure surface limitation, with mixed control in the medium [16]. Den Otter *et al* [16] has concluded that,

both K_{tr} and $\widetilde{D}$ could be accurately evaluated simultaneously only in the region of $0.03 \le L_\alpha = aK_{tr} / \widetilde{D} \le 30$.

4.1.3 Equation for rectangular sample

Modified equations are also derived for other sample geometry, for two or three dimensional diffusion. For two-dimensional diffusion in beam-shaped samples with a rectangular cross-section $2a \times 2b$ which correspond to the sample geometry used in this work, the equations are given [20]:

$$\overline{\sigma}_{\text{CISTR}}(t) == 1 - \exp\left(-\frac{t}{\tau_{\text{f}}}\right) - \sum_{n=1}^{\infty}\sum_{n=1}^{\infty} A_{n,m} \frac{\tau_{n,m}}{\tau_{n,m} - \tau_{\text{f}}}\left[exp\left(-\frac{t}{\tau_{n,m}}\right) - exp\left(-\frac{t}{\tau_{\text{f}}}\right)\right] \tag{4.15}$$

$$A_{n,m} = \frac{2L_\alpha^2}{\beta_n^2\left(\beta_n^2 + L_\alpha^2 + L_\alpha\right)} \cdot \frac{2L_\beta^2}{\beta_m^2\left(\beta_m^2 + L_\beta^2 + L_\beta\right)} \tag{4.16}$$

$$\tau_{n,m} = \frac{1}{\widetilde{D} \cdot \left[\left(\frac{\alpha_n}{a}\right)^2 + \left(\frac{\beta_m}{b}\right)^2\right]} \tag{4.17}$$

$$\beta_n \tan\beta_n = \frac{bK_{tr}}{\widetilde{D}} = L_\beta \tag{4.18}$$

$$\alpha_n \tan\alpha_n = \frac{aK_{tr}}{\widetilde{D}} = L_\alpha \tag{4.19}$$

4.2 Experimental

4.2.1 Thermogravimetry (TGA) for oxygen nonstoichiometry determination

Thermogravimetric analysis (TGA) has been performed with G. Boemare using a SETARAM 92-1750 device. As synthesized powders GBCO, GBCN03, GBCN06, GBCF03 and GBCF06 were pressed into rectangular bars and sintered at 1200 °C for 12 h, followed by an annealing process identical to that for iodometry and TG/H_2 measurement. The rectangular bar samples were suspended vertically by Pt wire with a highly sensitive thermal balance. The buoyancy influence could be eliminated by this set-up, which allows neglecting blank measurement usually required for measurement of powder samples.

The samples are firstly heated in air to 800 °C followed by an isotherm period of 3h, then slowly cooled to room temperature at a rate of 2 °C/min to ensure the chemical equilibrium. The oxygen contents determined by iodometry and TG/H_2, as discussed in Chapter 2 were used as initial oxygen

stoichiometries for these re-equilibrated samples. The samples were then successively heated to different temperatures at which the oxygen partial pressure was changed from 10 ppm to air (details in next section). Oxygen contents were calculated using the resulting weight losses.

4.2.2 Set-up for Electrical conductivity relaxation (ECR)

- Sample preparation

As-synthesized powders were pressed in a rectangular die, followed by cold isostatic pressure at 750 MPa., then sintered at 1200 °C for 12 h. After sintering, distortion and bend were found in most cases. Thus the samples were polished to form bar-shape samples with rectangular cross-section $2a \times 2b$, indicating the suitability of the two-dimensional equations for fitting data obtained in this work. Then the surface of samples were carefully polished using 4000 SiC sand paper in order to obtain as smooth surface as possible, then ultrasonically cleaned in acetone prior to use. The prepared bar samples showed a relative density in excess of 90% (90% ~ 94%), as can be seen in Table 4.1. Gold wire (LS356875, Goodfellow) and gold paste (METALORM, GOLD PASTE M-0034) were used as electrodes to conduct a four-probe technique.

Sample	GBCO	GBCN03	GBCN06	GBCF03	GBCF06
Size (mm)	2.26×2.63×17.2	2.28×2.39×20.7	2.39×2.79×16.87	2.1×2.48×18.96	2.1×2.52×18.03
Density	93%	91%	90%	92%	94%

Table 4.1 Fabricated bar samples for electrical measurement

- Set-up of electrical conductivity measurement

Four-probe AC conductivity technique were carried out using a digital lock-in amplifier (SR850, Stanford research system). A current of 10 mA was applied throughout the sample and the voltage drop was measured over a well defined distance in the center of the sample. The sample was mounted in a sample holder placed in a quartz glass tube in which the atmosphere could be changed. Moreover, solid ceramic bars were filled in the space of this tube in order to diminish the flushtime, since the internal volume of this tube is too large, which is around 420 cm^3. Simple conductivity measurements were carried out in an air flux of 5L/h from ambient to 800 °C in order to get the electrical conductivity as a function of temperature and P_{O_2} . The electrical conductivity relaxation was measured at temperatures ranging from 600 °C to 800 °C with 50 °C incremental steps. Stepwise change of surrounding oxygen partial pressure (generally following an oxidation step in this work) were performed at each constant temperature, from 10 ppm to air (10^{-5}~0.206 atm), by switching between two continuous gas mixtures with constant flow rate of 10 L/h using a four-way valve at the

inlet of the reactor. The oxygen partial pressure was controlled by mixing O_2 and Ar in a mass flow controller when P_{O_2} >1000 ppm, whilst a Zirox SGM5 EL which combines an electrolysis cell with a potentiometric measuring cell was used for the case P_{O_2} <1000 ppm.

- Flushtime measurement

Considering the comparatively significant reactor volume used in this work, it is essential to determine the flushing characteristic of the reactor volume. Another Zirox was connected at the outlet of the reactor performing as an oxygen sensor. The non-ideal step response of the mounted reactor, with and without filled ceramic bars, was measured at the given flow rate and given temperatures for various oxidation steps. Flushtime τ_f was obtained by fitting the oxygen partial pressure equilibrium process using the Eq. 4.12.

- Acquisition and fitting

Data acquisition and instrument control were realised by the software LabView 7.1 (National Instruments, USA). The obtained data were fitted by a MATLAB program based on the Eq. 4.15 attributing for two-dimensional diffusion in beam-shaped samples with flushtime correction, from which either the chemical diffusion coefficient $\widetilde{D}$ or the surface exchange coefficient K_{tr} or both of them could be extracted according to the characteristic length.

4.3 Results and discussion

4.3.1 Oxygen nonstoichiometry

4.3.1.1 Oxygen nonstoichiometry at high temperature for GBCM

In this work, oxygen nonstoichiometry in GBCO, GBCN03, GBCN06, GBCF03 and GBCF06 at high temperature was studied by TGA as a function of temperature and oxygen partial pressure, attributing the mass loss to the release of oxygen from the crystal lattice. ***Figure 4.1*** shows the experimental process of GBCF03 as an example. After thermal equilibrium in air at 800 °C and slow cooling to room temperature, the absolute oxygen content in the sample, which corresponds to the plateau on the mass curve being marked as "equilibrium RT" in Figure 4.2 (a), is considered the same as that determined by iodometry and TG/H_2 (seeing Chapter 2). It is also used as reference in calculating the oxygen nonstoichiometry δ in $GdBaCo_{2-x}M_xO_{5+\delta}$ (M = Ni, Fe; x = 0, 0.3, 0.6). Then at a constant temperature (700, 750, and 800 °C), mass change was measured at the certain equilibrium plateau of weight curve following the corresponding stepwise change of oxygen partial pressure. The

measured data have been adjusted with the consideration of Archimedes effects resulting from the changes of density in mixed gas stream.

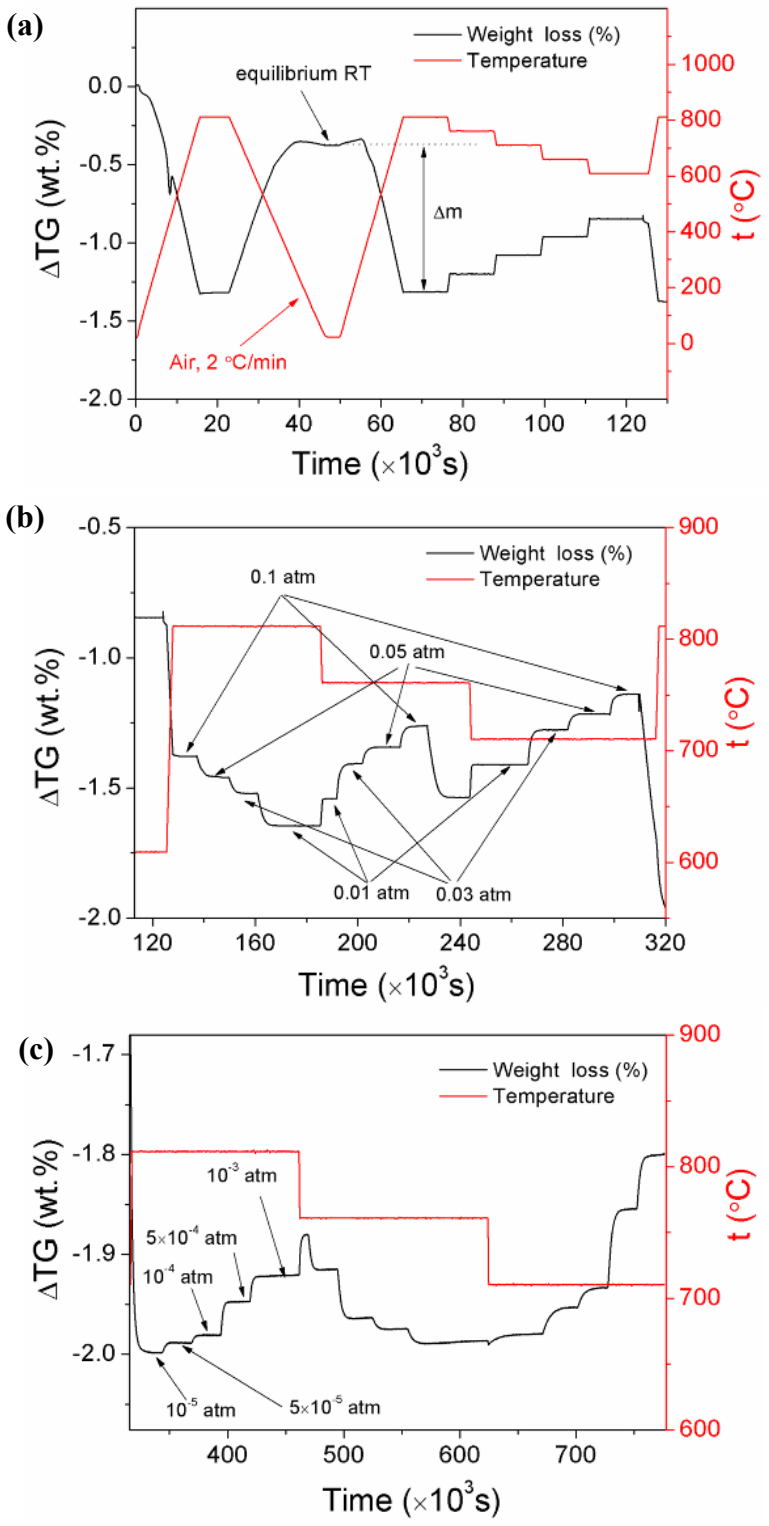

Figure 4.1 *Weight change of GBCF03 rectangular sample at three different temperatures under diverse atmospheres: (a) air, (b)* P_{O_2} *> 10⁻³ atm, controlled by mixing Ar and O_2 in a mass flow controller, (c)* $P_{O_2} \leq 10^{-3}$ *atm controlled by Zirox.*

Oxygen nonstoichiometries at different temperatures under air condition for $GdBaCo_2O_{5+\delta}$ (GBCO), $GdBaCo_{1.7}Ni_{0.3}O_{5+\delta}$ (GBCN03), $GdBaCo_{1.4}Ni_{0.6}O_{5+\delta}$ (GBCN06), $GdBaCo_{1.7}Fe_{0.3}O_{5+\delta}$ (GBCF03) and $GdBaCo_{1.4}Fe_{0.6}O_{5+\delta}$ (GBCF06), as well as the oxygen nonstoichiometry as a function of oxygen partial pressure P_{O_2} for pure $GdBaCo_2O_{5+\delta}$ at different temperatures, are shown in the ***Figure 4.2***. As can be seen, the oxygen nonstoichiometry depends on the composition, temperature and oxygen partial pressure, in agreement with previous works on GBCO [21-23] and many other perovskites including B-site Co, Ni or Fe [4,19,24-28].

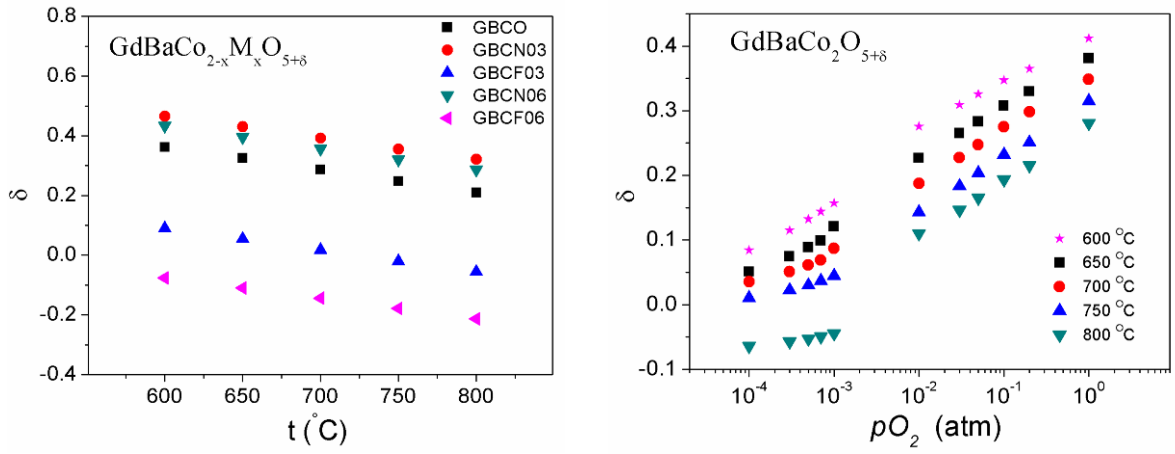

Figure 4.2 *The oxygen content δ:*

(Left) as a function of temperature in air condition, measured by TGA

(Right) as a function of oxygen partial pressure for $GdBaCo_2O_{5+\delta}$ at different temperatures

In the air condition, oxygen content decreases with the increase of temperature, representing release of oxygen from the crystal structure and formation of oxygen vacancies. Similar to the results of oxygen nonstoichiometry at ambient, at the investigated temperatures (> phase transition temperatures for all compositions) Fe substituted GBCF03 and GBCF06 show lower oxygen content δ with increasing Fe substitution for Co. Moreover, strong P_{O_2} dependency of the equilibrium oxygen content of GBCO shows good agreement with previous works [22,29], which could be directly related to the conductivity enhancement with increasing oxygen partial pressure [21]. Whilst, slightly higher oxygen content δ with Ni substitution are observed, however, the δ values in GBCN03 and GBCN06 are comparatively adjacent to those of GBCO, compared to Fe substitution.

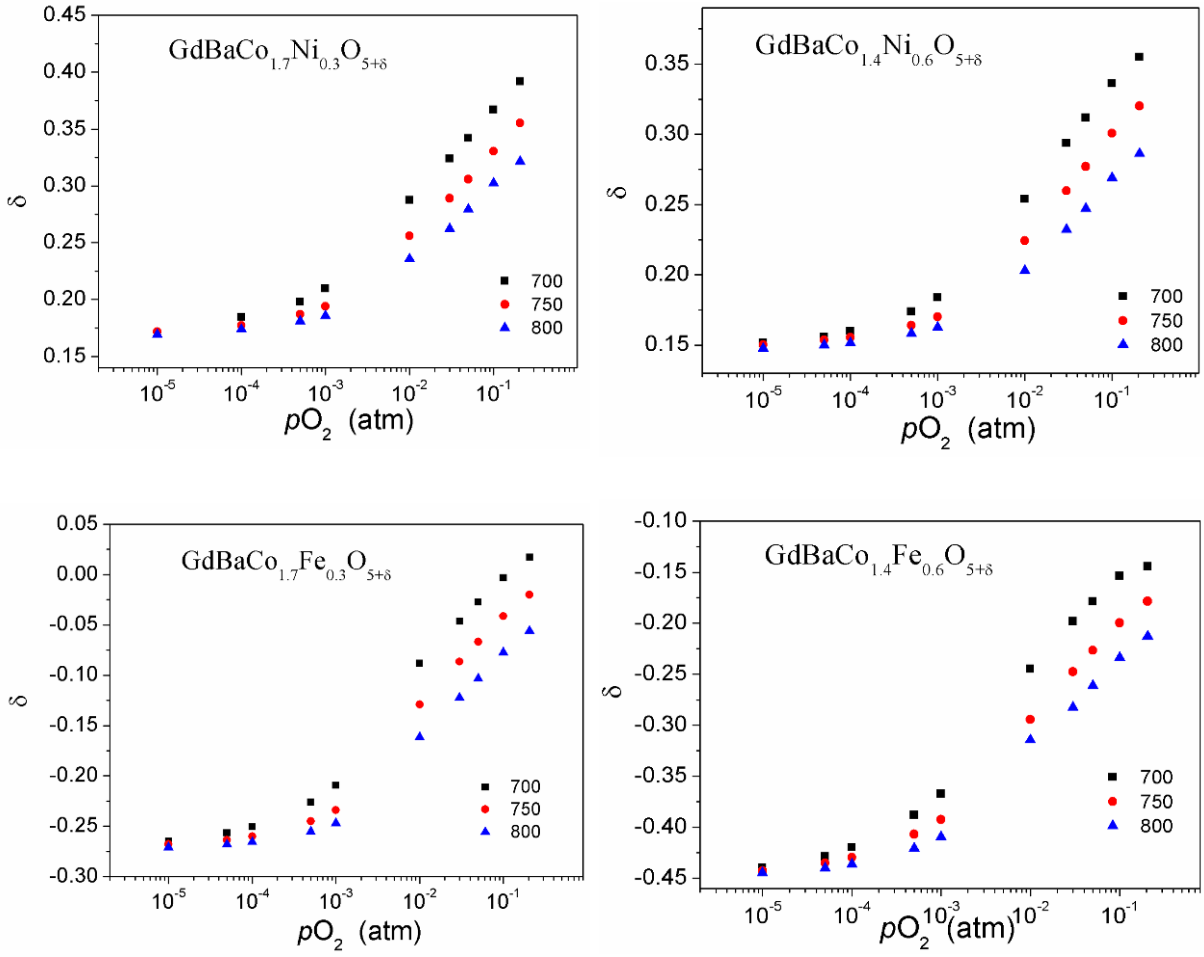

Figure 4.3 *Oxygen content δ as a function of oxygen partial pressure at different temperatures in GBCN03, GBCN06, GBCF03 and GBCF06*

Apart from the pristine GBCO, the oxygen nonsotichiometry δ, measured by TGA as a function of oxygen partial pressure in the range from air to 10^{-5} atm at 700, 750 and 800 °C, in other compositions is given in ***Figure 4.3***. As can be seen, for all compositions, the oxygen content at those elevated temperatures decrease almost linearly with decreasing log pO_2 until they approach a similar value, which is represented as a plateau or a trend of reaching a plateau (GBCO), at very low oxygen partial pressure < 10^{-5} atm.

The values of δ for GBCO (***Figure 4.2*** right) show an asymptotic trend from 10^{-4} atm, thus it can be assumed that if lower P_{O_2} (<10^{-4} atm) could be applied, the approximation to δ = 0 would be expected. This is in good agreement with previous work of Tsvetkov *et al.* [22] for pure GBCO, in which the measured P_{O_2} dependence of oxygen nonstoichiomery δ' in term of $GdBaCo_2O_{6-\delta'}$ at temperatures from 900 to 1050 °C exhibited inflection when δ' reached the value of 1, at the P_{O_2} close

to 10^{-4} atm. This approximation of oxygen nonstoichiometry δ indicating the weakening of temperature dependence is more evident in GBCN03, GBCN06, GBCF03 and GBCF06 for which δ has been obtained at lower P_{O_2} close to 10^{-5} atm, as shown in ***Figure 4.3***. The total changes in δ are less than 0.35, and the δ value of plateau differs according to the composition: GBCN03 and GBCN06 reach the δ value close to 0.17 and 0.15, respectively, which are higher than δ ≈ 0 for GBCO, and much lower δ values, ~0.26 for GBCF03 and ~0.437 for GBCF06, are obtained. Therefore, it can be concluded that the Fe substitution decreases the oxygen content at both low and high temperature with increasing Fe content, whilst the Ni seems to reduce the decrease in δ.

4.3.1.2 B site substitution on oxygen nonstoichiometry for other perovskites

The observed trends of influence of Fe substitution decreasing the oxygen content in this work are inverse to those previous works on $La_{1-x}Sr_xCo_{1-y}Fe_yO_{3-\delta}$ [4,19,27], in which the δ decreases with increasing Fe content at a given oxygen pressure and temperature, and this was attributed to an increasing binding energy of oxygen O^{2-} in the lattice and a large tendency of Fe to form holes rather than oxygen vacancies. Park *et al.* [25] studied the variation of oxygen nonstoichiometry for $La_{0.2}Sr_{0.8}Fe_{0.55}Ti_{0.45}O_{3-\delta}$ at different temperatures in a very wide P_{O_2} range ($10^{-18} \leq P_{O_2} \leq 0.3$ atm), in their study the plateau of δ vs P_{O_2} curve observed between 10^{-12} and 10^{-7} atm was attribute to the "ideal" stoichiometric composition. On the contrary, Kopcewicez *et al.* [30] has used the Mössbauer spectroscopy and TGA to reveal that the increase of Fe content leads to the decrease of oxygen content and suppose a change of the type of oxygen vacancy ordering according to the formula $TbBa(Co_{2-x}Fe_x)O_{5.5-x/2}$, leading to a phase transition from orthorhombic to tetragonal for annealed samples at room temperature. They stated the existence of there different positions of Fe ions in the lattice, in the contrast to the two positions of Co ions, CoO_5-square pyramidal coordinations and CoO_6-octahedral coordinations, with oxygen vacancies ordering in the $[LnO_{0.5}]$ layer in the ideal 112-type crystal structure for $LnBaCo_2O_{5+\delta}$ pervoskites [29,31,32]: one with higher symmetry with smaller quadrupole splitting corresponding to the Fe ions in octahedrons and two different low symmetries with large quadrupole splitting, one of which corresponds to the square pyramidal position while the other appears at octahedral position by removing on oxygen atom from the $[TbO_{0.5}]$ layer in this type of crystal structure. Applying this model on Fe substituted GBCF in this work, with the consideration of very similar structure between $TbBaCo_2O_{5.5}$ and $GdBaCo_2O_{5.5}$, Fe seems to prevent the formation of CoO_6 octahedral in the neighbourhood during the phase transition from high to ambient temperature, as discussed in Chapter 2. Thus the average valence state of Co ions should be considered as less than 3+ indicating partially reduction of Co^{3+} to Co^{2+}. However, by comparing the oxygen nonstoichiometry of GBCF measured in this work and that derivate from the formula $GdBaCo^{3+}_{2-x}Fe^{3+}_xCo^{2+}_xO_{5.5-x/2}$ according to the proposed formula $TbBaCo^{3+}_{2-x}Fe^{3+}_xCo^{2+}_xO_{5.5-x/2}$, shown

in Table 4.1, large discrepancy is observed in case of GBCF06, which give rise to the suspicion of reduction of Fe^{3+} to Fe^{2+} in addition to the Co ions.

Composition X	0	0.3	0.6
Oxygen content in $GdBaCo^{3+}_{2-x}Fe^{3+}_{x}Co^{2+}_{x}O_{5.5-x/2}$ derivated from [30]	5.5	5.35	5.2
Oxygen content in $GdBaCo_{2-x}Fe_xO_{5+\delta}$ measured in this work	5.514	5.356	5.063

Table 4.2 Oxygen content at room temperature in $GdBaCo_{2-x}Fe_xO_{5+\delta}$

4.3.2 Electrical conductivity

High electrical conductivity is one fundamental factor for MIEC materials used as electrodes for SOFC application. For this kind of oxides, there are two primary conduction mechanisms, electronic and ionic conduction, due to the simultaneous presence of both electronic holes and oxygen vacancies within these materials. Since the ionic conductivity is much lower than electronic conductivity, the values obtained herein are assumed to be electronically predominant.

4.3.2.1 Total conductivity as a function of temperature

- GBCO

Total electrical conductivity σ of GBCO measured in the range RT-800 °C is shown in ***Figure 4.4 (a)***. The conductivity increases with increasing temperature below about 100 °C, exhibiting a typical semiconductor-type behaviour, which corresponds to Metal-insulator (MI) transition consistent with the low-temperature phase transition observed by XRD in Chapter 2 of this work and other previous works [23,31,33], due to the sudden spin state switch in the Co^{3+} ions located at the cathedra from LS ($t_{2g}^6 e_g^0$) to HS ($t_{2g}^4 e_g^2$) states at this temperature (T_{MI}). Thereafter, the conductivity of GBCO gradually increases with the increasing temperature showing same semiconductor-type behaviour although with very weak temperature dependence, passing through a maximum value in σ in the temperature range 300-400 °C, where the materials starts to loose oxygen according to the TG results,. At higher temperature, especially after the orthorhombic-tetragonal phase transition which corresponds to a small abrupt change of conductivity on the δ curve (seeing the vertical bars), the total conductivity decreases with increasing temperature indicating a metallic-like behaviour, in accordance with references [21,23,34-36]. This is possibly due to the fact that the phase transition breaks down the alternation of CoO_5 pyramidal and CoO_6 octahedral planes along the *b* direction and therefore hampers the hole creation thus reduces the charge carrier (hole) concentration *p*; moreover, with the increase of

temperature, the thermally introduced loss of lattice oxygen and formation of oxygen vacancies accounts for the loss of charge carrier introduced by oxygen exchange with atmosphere.

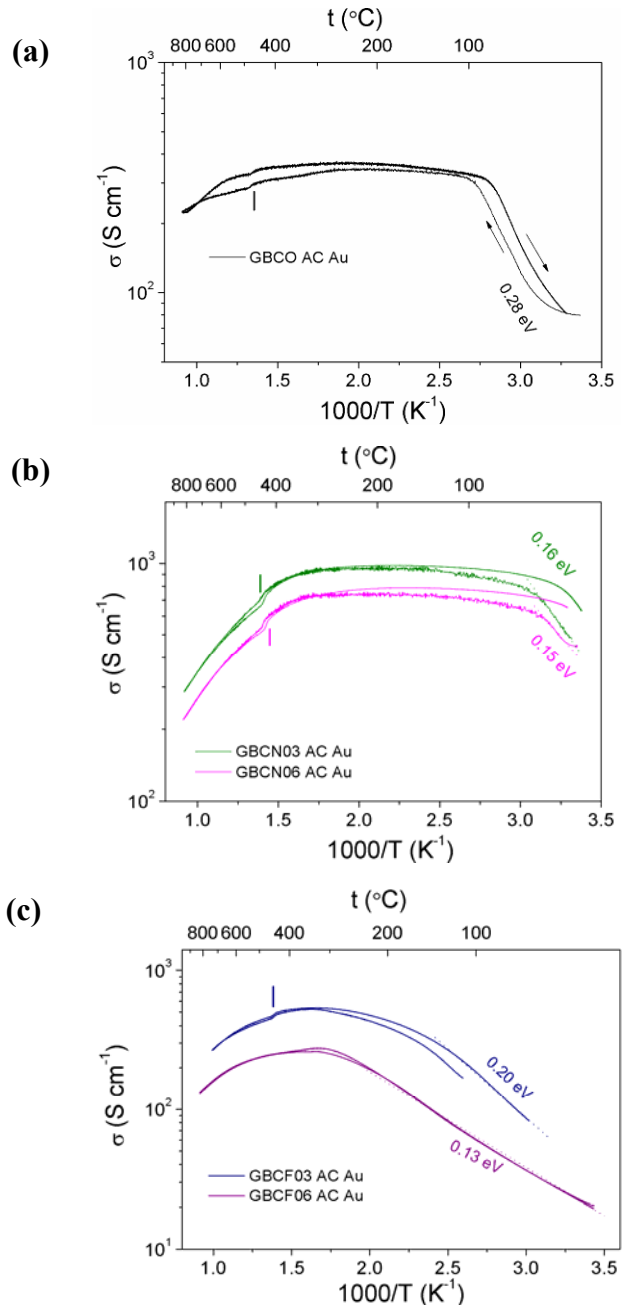

Figure 4.4 *Total electrical conductivity as a function of temperature measured by four-probe method under air with rectangular sample of (a) GBCO (b) GBCN03 and GBCN06 and (c) GBCF03 and GBCF06*

The small difference in conductivity values and the hysteresis of transition temperature between the heating and cooling process may be related to the kinetics of oxygen uptake/release process and valence variation of Co during heating and cooling and their first-order character of phase transition [23,36], respectively. Moreover, the electrical conductivities for GBCO reported in the references

mentioned above are quite different. Nevertheless, in this work, in the temperature range 300-800°C the total electrical conductivity of GBCO is higher than 200 S cm^{-1}, which is adequate for application as a cathode in IT-SOFCs requiring typically a conductivity of 100 S cm^{-1} at the operating temperature.

- GBCN

As can be seen from Figure (b), the total electrical conductivity of Ni substituted GBCN03 and GBCN06 shows similar semiconductor-type behaviour below ~50 °C, a temperature which is lower than that of GBCO. This is in consistency with previous work of Bharathi *et al*. [37] showing that the Ni substitution for Co in $GdBaCo_{2-x}Ni_xO_{5+\delta}$ led to a decrease of metal-insulator transition temperature (T_{MIT}), they have stated that the structure change with Ni substitution could result in the modification of the crystal field energies and consequently decrease the energy required for the spin stat transition driving the MI transition. The inflection in conductivity curves corresponding to high temperature phase transition, marked by the vertical bars, shifts to lower temperature with Ni substation, in consistency with the DSC and XRD results. Besides, seeing the high temperature metallic-like behaviour in conductivity, GBCN shows the strongest temperature dependence.

- GBCF

The total conductivity of Fe substituted GBCF03 and GBCF06 exhibits a remarkable enhancement of semiconductor-type behaviour which can be observed above 200 °C for GBCF and 300 °C for GBCF06, respectively, as shown in ***Figure 4.4 (c)***. Similar phenomena were observed for $GdBaCo_2O_{5+\delta}$ in a wide range of oxygen content by Taskin *et al*. [38,39], indicating the MI transition seems to be smeared for δ away from 0.5. Indeed, they have observed the temperature-independent MI transition for $0.45 \leq \delta \leq 0.55$ at $T_{MI} \approx 360$ K, and no MI transition was observed for $\delta = 0.165$ and $\delta = 0.7$, which corresponds well the case of GBCF in this study. In addition, Tang *et al*. has investigated the Fe doped $GdBaCo_{2-x}Fe_xO_{5.5-\delta}$ with low substitution ratio $0 \leq x \leq 0.2$ [40], and found that the spin-state transition slightly shifts to higher temperature with increasing Fe doping, from 365 to 372 K, due to the decrease of the oxygen amount in Fe-rich region and alsothe number of Co ions in octahedral positions which could undergo a spin state transition. More consistent result was reported in $TbBaCo_{2-x}Fe_xO_{5+\delta}$ [30], in which the Mössbaurer spectroscopy has been applied to prove that the Fe substitution slightly increased the T_{MIT}; and Fe doping also tended to increase the resistivity, which is in good agreement with our study, *e.g.* GBCF06 shows the lowest total electrical conductivity among all compositions. Similar decrease in electrical conductivity with higher Fe substitution was observed in LSCF and LCCF [19,41]. The hysteresis in conductivity of GBCF06 between cooling and heating at ~300 °C is related to the orthorhombic-tetragonal phase transition observed by XRD as discussed in Chapter 2. From this temperature, the conductivity starts to exhibit metallic-like behaviour as same as GBCO and GBCN.

Although the Fe substitution is shown to decrease the electrical conductivity, in the temperature range of 300-800 °C, the lowest σ value of GBCF06 is still larger than 100 S cm^{-1}, which guarantees the suitability for cathode application in IT-SOFCs.

4.3.2.2 Conductivity under decreasing P_{O_2}

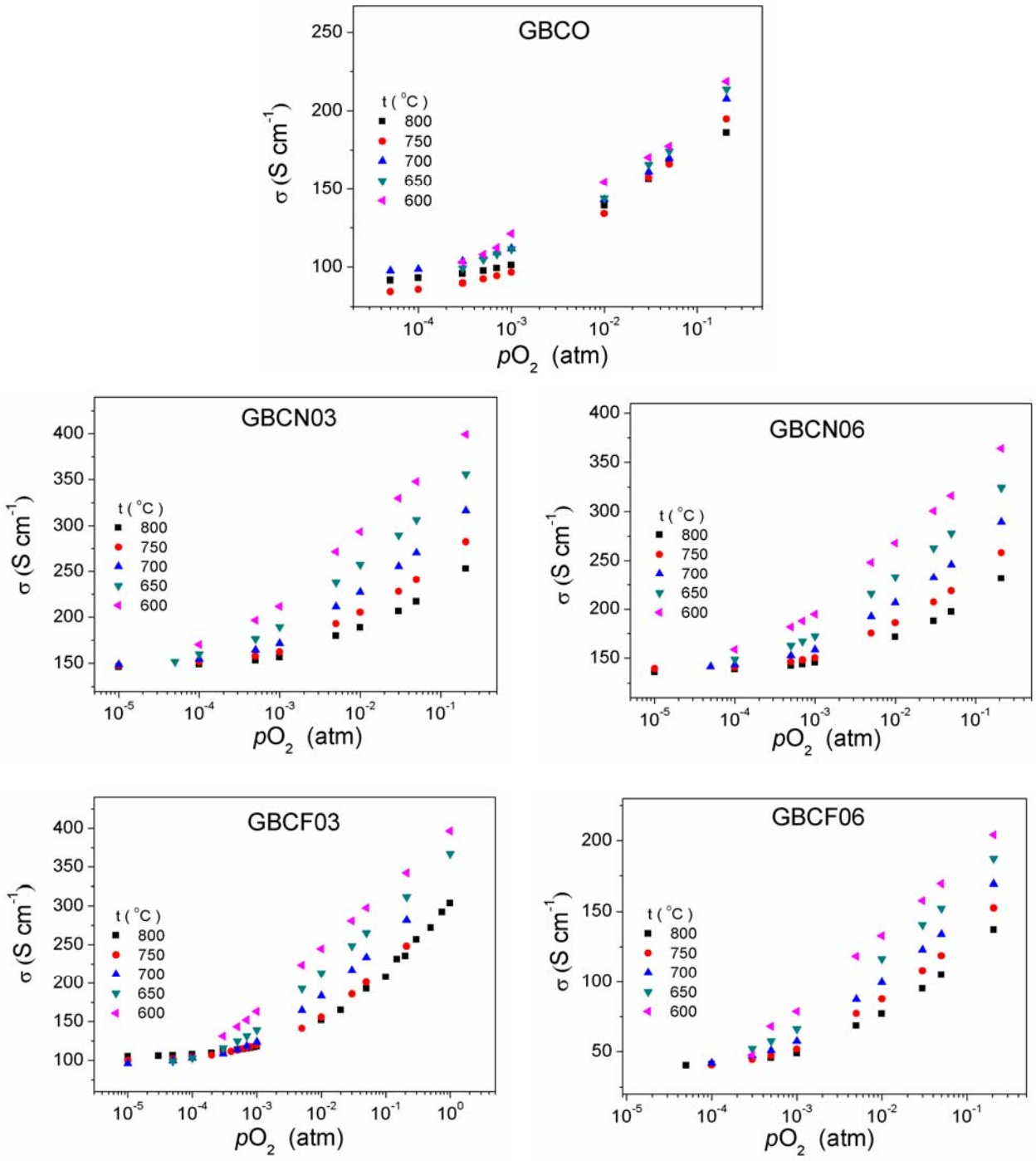

Figure 4.5 *Equilibrated total electrical conductivity as a function of oxygen partial pressure obtained from the electrical conductivity relaxation processes with AC four-probe setup at different temperatures (t = 600, 650, 700, 750 and 800 °C) for GBCO, GBCN03, GBCN06, GBCF03 and GBCF06*

Figure 4.5 shows the evolution of total electrical conductivity as a function of oxygen partial pressure at different temperatures. The values of δ were obtained conductivity relaxation processes at equilibrium state.

Generally, at a constant P_{O_2} , increasing temperature results in a decrease in the electrical conductivity, probably attributed a lowering of holes concentration. The total conductivities for all compositions decrease with decreasing oxygen partial pressure (P_{O_2}) at a constant temperature, exhibiting a typical *p*-type conductivity, due to the reaction forming of oxygen vacancies and consuming the charge carriers (electron holes), in consistency with the P_{O_2} and temperature dependency of oxygen nonstoichiometry in this work and previous works on GBCO [21,23].

For example, in case of GBCO, the charge disproportion and the process of oxygen release from the cobaltite lattice under reducing condition (lower oxygen partial pressure or increased temperature) which decrease the concentration of charge carriers could be described as [21,41,42]:

$$2Co_{Co}^{\times} \rightleftharpoons Co_{Co}' + Co_{Co}^{\bullet} \tag{4.20}$$

$$O_O^{\times} + 2Co_{Co}^{\bullet} \rightleftharpoons \frac{1}{2}O_2 + V_O^{\bullet\bullet} + 2Co_{Co}^{\times} \tag{4.21}$$

$$O_O^{\times} + 2Co_{Co}^{\times} \rightleftharpoons \frac{1}{2}O_2 + V_O^{\bullet\bullet} + 2Co_{Co}' \tag{4.22}$$

Nevertheless, the defect model at high temperature is still not clear for these materials, as well as the competition between concentration and mobility of these charge carriers.

4.3.3 Electrical conductivity relaxation (ECR)

4.3.3.1 Flush time

As discussed above, ideally, the oxygen partial pressure in relaxation experiments should be changed by switching between two gas flows with different oxygen partial pressures simultaneously. However, this assumption is hard to achieve with respect to actual experimental conditions in most cases. For the conductivity relaxation experiments, small reactor volumes and hence comparatively short flush times are needed, otherwise, if the relaxation time approaches the flush time of the reactor volume, the flush time correction is necessary. Otherwise the chemical diffusion coefficient and surface exchange coefficient cannot be accurately determined since the obtained relaxation could also be governed by gas flushing.

Since the quartz glass tube applied as rector in this work has a comparative large empty internal volume, *ca.* 420 cm^3 without sample holder, some alumina bars were added in order to diminish the time to flush the reactor volume. The flush time τ_f was obtained by fitting the simultaneous change of oxygen partial pressure in the reactor during the flushing of the reactor volume after the abrupt switch of gas stream followed in, according to Eq. 11.The the flow rate for all cases is controlled to be constant at 10 L/h. An example of step changes in P_{O_2} at 700 °C is shown in ***Figure 4.6***, the black squares are the measured oxygen partial pressure by Zirox as an oxygen sensor, for small pressure switch (a) 100-300 ppm, intermediate pressure switch (b) 0.01-0.03 atm and large pressure switch (c) 0.05-0.206 atm (air), and the red curve indicates the fitting for flush time τ_f according to Eq. 4.12.

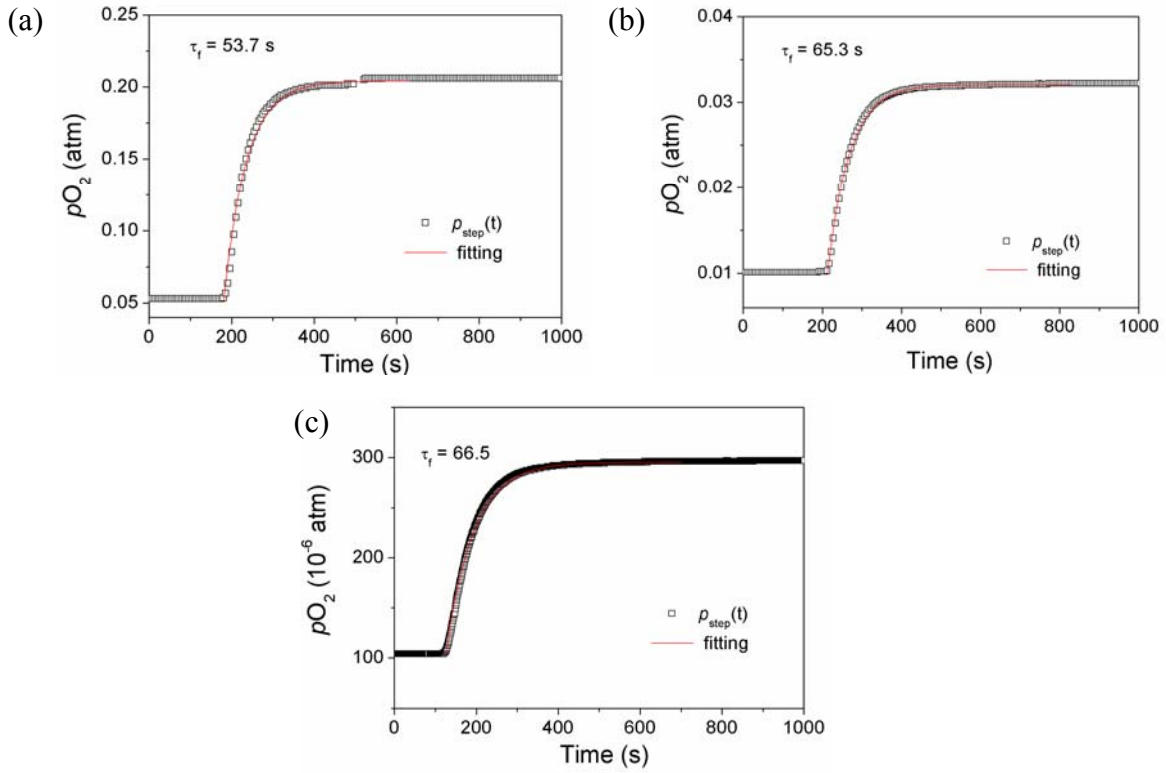

Figure 4.6 *Measurement of flush time following the re-equilibration of oxygen partial pressure in the reactor at different 700 °C, for different step changes: (a) 0.05-0.206(air) atm, (b) 0.01-0.03 atm, (c) 100-300 ppm*

The fitted flush times in all selective temperatures and P_{O_2} steps, which follow an oxidation direction, are listed in Table 4.2. As can been seen, at a constant flow rate, the reactor flushing behaviour is slightly thermally activated, with smaller τ_f at higher temperature for the same step change of P_{O_2} as well as the contribution of the values in ΔP_{O_2} . Nevertheless, the values of τ_f

measured in this work are significantly large, which is assumed to be due to the large reactor volume compared to other studies [6,16,20,43-46].

T (°C) \ P_{O_2}	Flushtime τ_f (s)								
	10(50)-100 ppm	100-300 ppm	300-500 ppm	500-700 ppm	700-1000 ppm	0.005-0.01 atm	0.01-0.03 atm	0.03-0.05 atm	0.05-0.206 atm
600	65	65.5	74	86.5	78	74	64.63	65	57.8
650	67	67.6	76	86	79.8	72	60.3	60	54.6
700	67.56	66.5	76	75.8	80	67.3	65.3	59	53.7
750	61.1	63.1	66.2	72.3	77.6	66	58	57.4	52.54
800	54	54	65.4	66	74	67.3	52.4	54.3	50

Table 4.3 Various oxygen partial pressure switches applied in this work for conductivity relaxation measurement and the corresponding flush times τ_f (s)

The conductivity relaxation plots of GBCF03 at different temperatures with oxygen partial pressure switches corresponding to those of ***Figure 4.6***, are shown in ***Figure 4.7***. The time dependent conductivities are normalized in term of $\overline{\sigma}(t)=\left[\sigma(t)-\sigma_0\right]/\left[\sigma_\infty-\sigma_0\right]$ in order to compare the relaxation processes at different temperatures.

As can been seen, the time to reach a new equilibrium in electrical conductivity after the change of surrounding atmosphere shows a temperature dependency and significant P_{O_2} dependency. For all oxygen partial pressure switches, at higher temperature, the conductivity re-equilibrium processes take place faster, showing higher oxygen transport kinetics associated with the oxygen surface exchange and bulk diffusion of oxide ions. For a constant temperature, the time of relaxation processes varies in a large range according to different P_{O_2} switches, even by orders of magnitude. Let's consider the GBCF03 sample for instance, seeing ***Figure 4.7***: (a) the re-equilibrium processes following the P_{O_2} change from 0.05 atm to air accomplish within 1000 s whatever the temperature; (b) for the P_{O_2} switch from 0.01 to 0.03 atm, the re-equilibrium in electrical conductivity accomplish within 2000-5000s, from 800 °C to 600 °C, exhibiting stronger temperature dependency than in the high P_{O_2} conditions; (c) at low oxygen partial pressure range, *e.g.* from 100 to 300 ppm, much longer time (>

2×10^4 s) is needed and it increases significantly with decreasing temperature. Moreover, in accordance with the small P_{O_2} dependency of σ at low P_{O_2}, as shown in ***Figure 4.5***, the changes in conductivity values at the initial and re-equilibrium P_{O_2} are small and thereby lead to low signal to noise ratio.

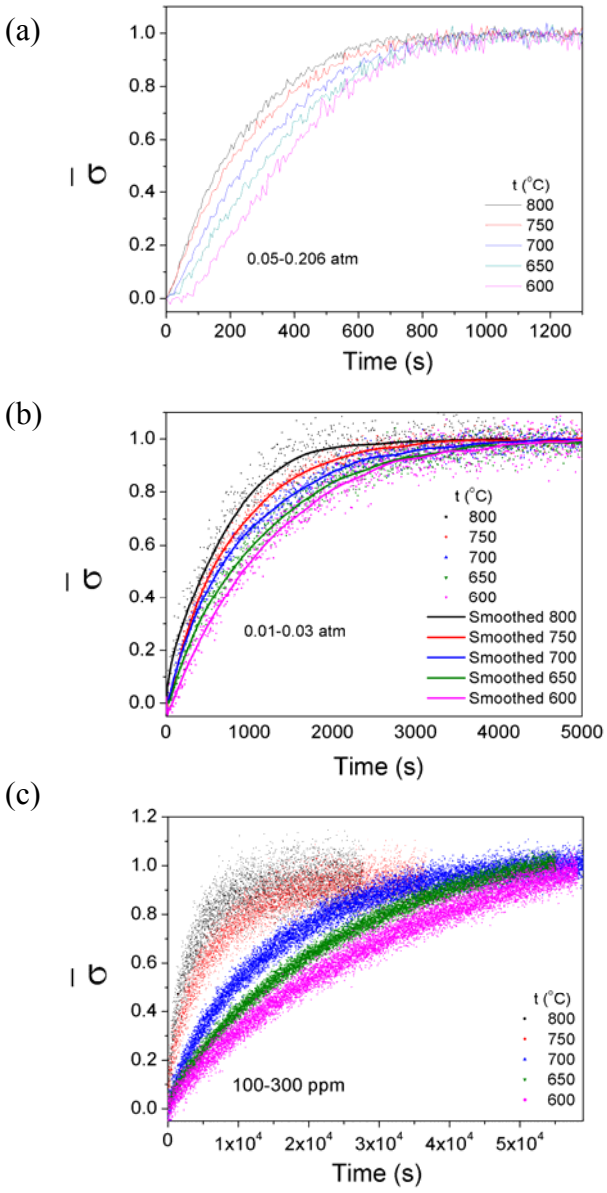

Figure 4.7 *Relaxation plots of GBCF03 at different temperatures for the indicated pressure switches: (a) 0.05atm-air (b) 0.01-0.03 atm, measured (points) and smoothed (solid lines) data, (c) 100-300 ppm*

Comparing the measured flush times τ_f with the conductivity relaxation processes, only at low P_{O_2} (≤ 1000 ppm) the flush time could be considered as "much smaller" than the duration of relaxation process, *ca.* by 3 orders of magnitude, which is supposed to allow accurate determination

for both surface exchange and chemical diffusion coefficients. In contrast, at higher P_{O_2}, the times of relaxation processes approach those for flushing the reactor volume with increasing oxygen partial pressure, from 2 orders to 1 order of magnitude higher than τ_f, exhibiting "non-ideal step process" and giving rise to the strong necessity for flush time correction.

4.3.3.2 Determination and evaluation of oxygen transport properties

As discussed in section 4.1, when the cross-section of the rectangular sample is 2a×2b (a>b), the parameter $L_\beta == b \bullet K_{tr} / \widetilde{D}$ is applied as an indicator for the evaluation of coefficients obtained by fitting the experimental relaxation data.

- If L_β < 0.03, the relaxation kinetics is entirely governed by the rate of surface reaction thus only K_{tr} could be obtained.
- If L_β > 30, the re-equilibrium in conductivity is not affected by the surface reaction only $\widetilde{D}$ can be obtained by the fitting.
- In the intermediate region 0.03 < L_β < 30, mixed controls coexist, and both $\widetilde{D}$ and K_{tr} can be derived from fitting the experimental relaxation data.

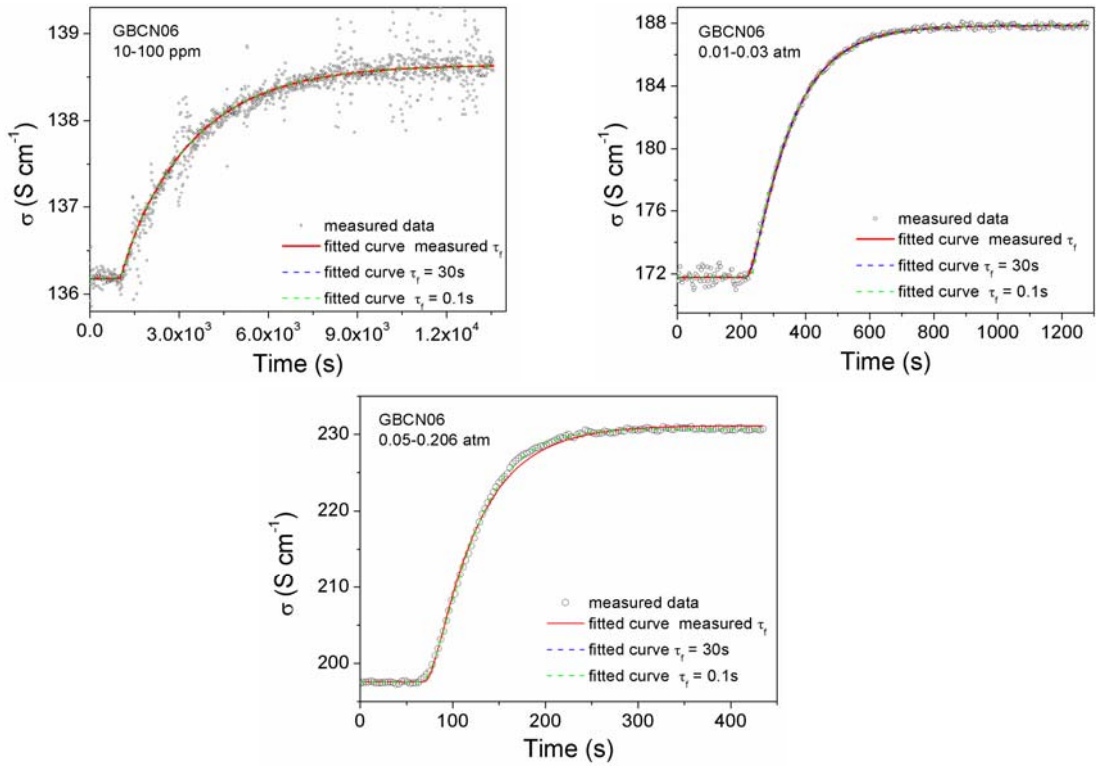

Figure 4.8 *Typical AC conductivity relaxation profiles for GBCN06 at 800 °C (open circle) and fitted curved using corresponding measured flush times (red line) as well as assumed flush times (blue and green dash lines)*

P_{O_2}	10-100 ppm		0.01-0.03 atm		0.05-0.206 atm (air)	
τ_f (s)	54	×	52.4	×	50	×
$\widetilde{D}$ (cm2 s-1)	3.53E-6	3.92E-6	3.22E-5	9.06E-4	6.77E-1	8.93E-1
Ktr (cm s-1)	4.03E-5	3.82E-5	3.71E-3	5.02E-4	6.08E-3	7.11E-3
Lβ	1.363	1.164	27.52	0.066	0.002	0.001

Table 4.4 Chemical diffusion and surface exchange coefficients obtained by fitting the relaxation data of GBCN06 at 800 °C with comparison of oxygen partial pressure, with (τ_f) and without (×) flush time correction

Figure 4.8 shows the typical AC conductivity relaxation profiles for GBCF03 with fitted curves. In order to interpret the importance of flush time correction, each profile is fitted with equation using actually measured flush time (τ_f) and the equation without flush time correction. The fitting results are listed in Table 4.4, showing clear evidence that both the two coefficients are sensitive to the flush time value. At low P_{O_2}, this influence of flush time is comparatively small, due to the long duration of conductivity re-equilibration process. In contrast, at high P_{O_2} where the re-equilibration usually takes place fast, especially with P_{O_2} switch towards air, the flush time is tremendously large compare to the requirement for mixed diffusion and surface control: between 500 and 5000 times smaller than time of relaxation process. Thereby, the fitting results are highly dependent on the τ_f values. For example, with the change of oxygen partial pressure from 0.05 atm to air at 800 °C for GBCN06, it took only 300 s to reach an new equilibrium in conductivity, with the flush time of 50 s, exhibiting very fast kinetics, and comparatively high $\widetilde{D}$ and K_{tr} values were obtained; the correspond L_β was less than 0.03 indicating a surface limitation. As a consequence, only the surface exchange coefficient K_{tr} was taken as results. In most cases of this work, L_β locates in the intermediate range which allows the determination of $\widetilde{D}$ and K_{tr} simultaneously. Nevertheless, at high oxygen partial pressure involving the conductivity re-equilibration in air condition, hardly both $\widetilde{D}$ and K_{tr} could be obtained.

4.3.3.3 Oxygen transport kinetics

The chemical diffusion coefficient $\widetilde{D}$ and surface exchange coefficient K_{tr}, obtained from the data fitting have been plotted in ***Figure 4.9*** and ***Figure 4.10*** as a function of the final P_{O_2} in each P_{O_2} step switch, respectively. For GBCN06, the chemical diffusion coefficient $\widetilde{D}$ from 0.05 atm to air is not plotted since they could not be extracted from the fitting procedure.

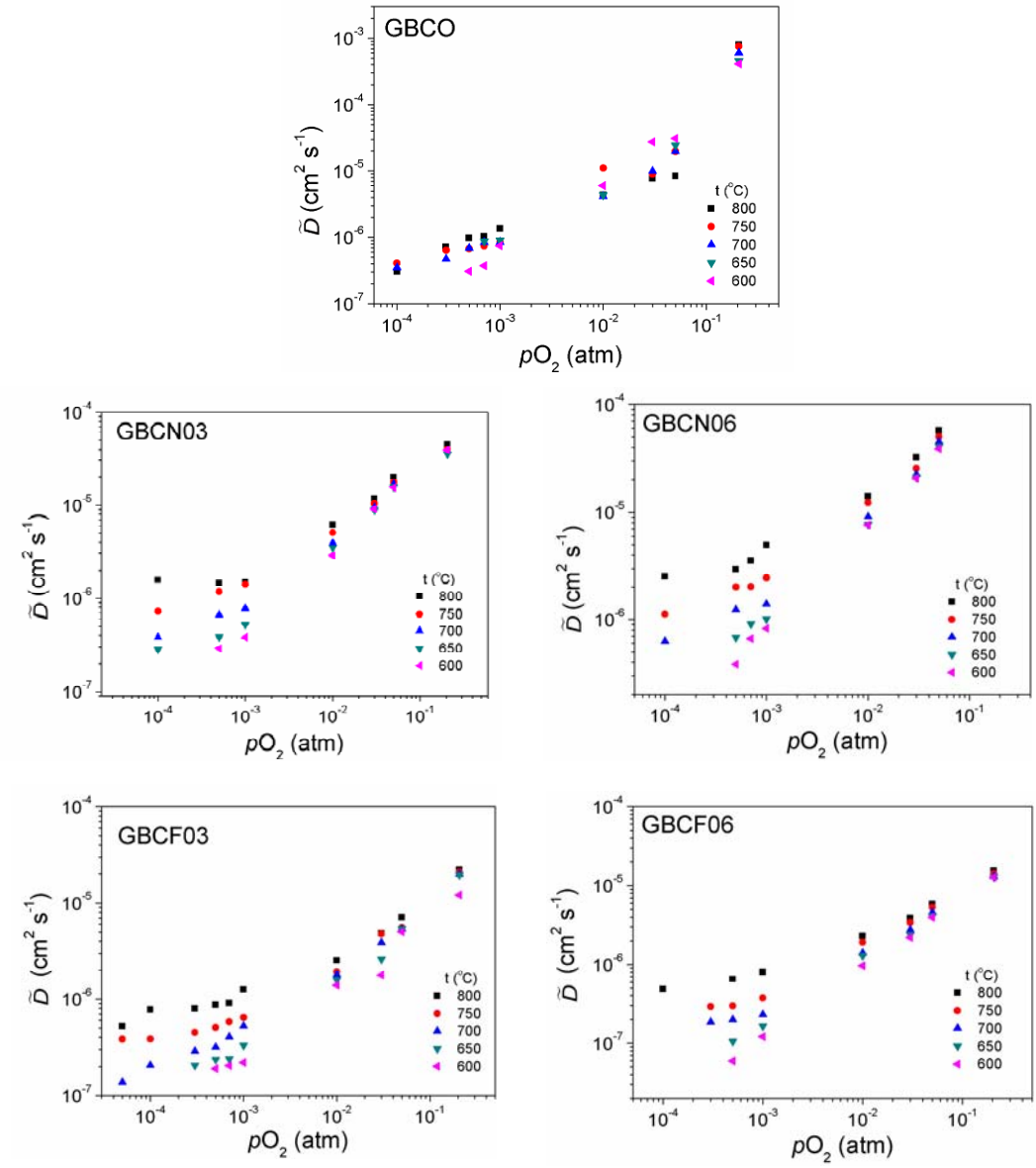

Figure 4.9 *Chemical diffusion coefficients as a function of final oxygen partial pressure from oxidation runs*

Generally, both the chemical diffusion coefficients and the surface exchange coefficients increase with increasing P_{O_2}, showing the same trend of P_{O_2} dependency, except the GBCO at high oxygen partial pressure. The surface exchange kinetics is of 2-3 orders of magnitude faster than bulk diffusion. It can be noticed that that the higher the oxygen partial pressure is, the weaker temperature dependency of $\widetilde{D}$ is shown. Among these five compositions, GBCO has the highest $\widetilde{D}$ values, even their reliability is doubtable which will be discussed in next section, and whilst lower values are obtained in Fe substituted GBCF03 and GBCF06 samples.

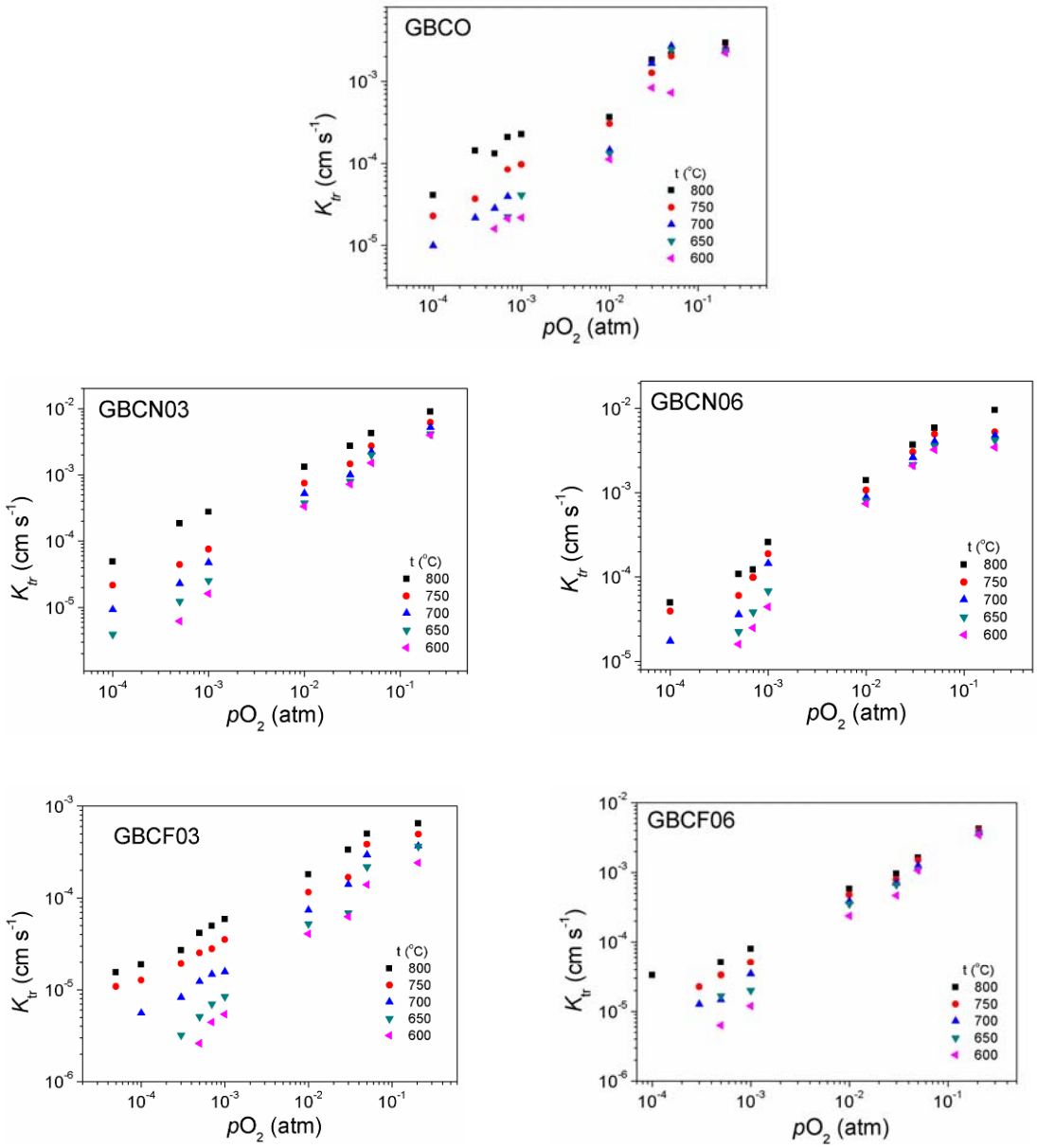

Figure 4.10 *Surface exchange coefficients as a function of final oxygen partial pressure from oxidation runs*

Nevertheless, both the chemical diffusion coefficients and surface exchange coefficients obtained in this work are much higher compared to previous work on GBCO [21]. Take the $\widetilde{D}$ and K_{tr} values at 700 °C for the step-wise switch from 0.05-0.206 atm for instance, as shown in Table 4.5, the $\widetilde{D}$ and K_{tr} values obtained in this work are 1-2 orders of magnitude higher, especially the surface exchange coefficients. In addition to the difference in ECR setups, this is also assumed to concern the lower density of measured samples, due to the inhomogeneity from the shaping and distortion of bar-shaped samples during the sintering procedure, which could definitely favour the bulk diffusion of oxygen.

700 °C 0.05atm-air	GBCO [21]	GBCO	GBCN03	GBCN06	GBCF03	GBCF06
$\widetilde{D}$ ($cm^2\ s^{-1}$)	1.93×10^{-6}	6.02×10^{-4}	3.86×10^{-5}	×	1.99×10^{-5}	1.30×10^{-5}
$K_{tr.}$($cm\ s^{-1}$)	2.74×10^{-5}	2.44×10^{-3}	5.18×10^{-3}	4.74×10^{-3}	3.68×10^{-4}	3.71×10^{-3}

Table 4.5 Comparaison of transport kinetics at 700 °C for 0.05atm-air

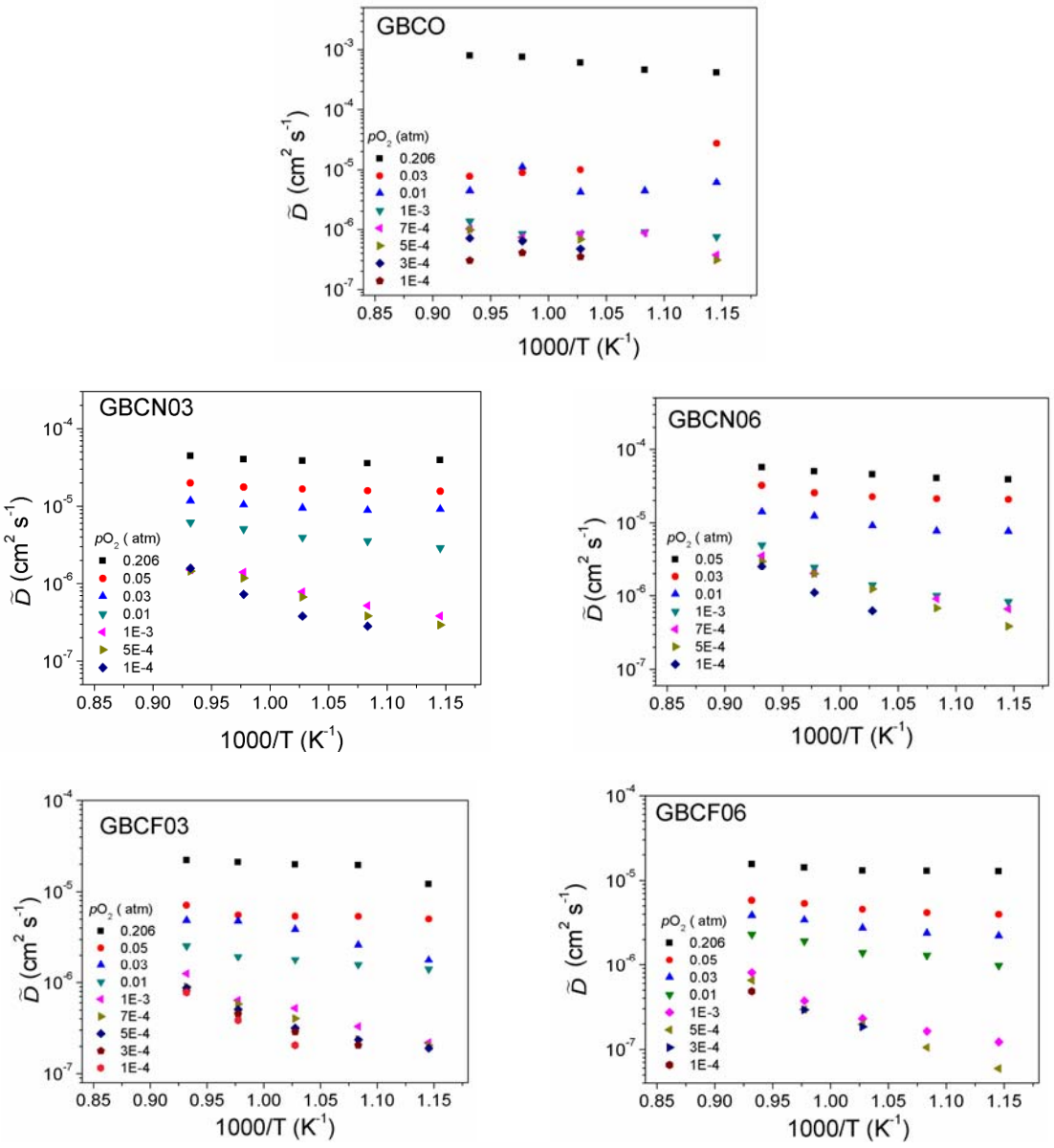

Figure 4.11 *Chemical diffusion coefficients as a function of reciprocal temperature from oxidation runs*

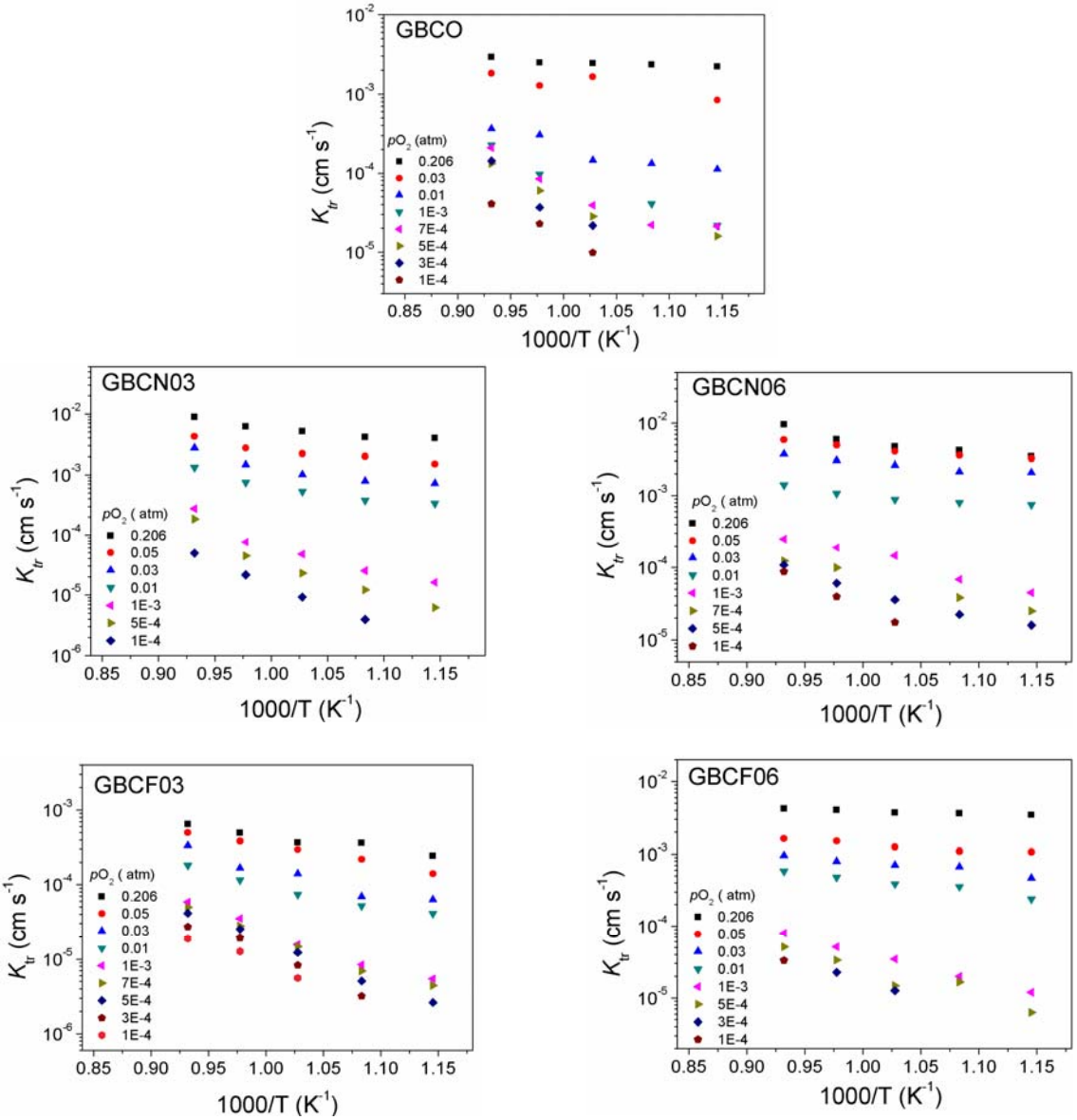

Figure 4.12 *Surface exchange coefficients as a function of reciprocal temperature from oxidation runs*

Temperature dependency of chemical diffusion coefficients $\widetilde{D}$ and surface exchange coefficients K_{tr} are depicted in ***Figure 4.11*** and ***Figure 4.12***, respectively, showing Arrhenius-type behaviour in general case. At high oxygen partial pressure, no big decrease is observed in either $\widetilde{D}$ nor K_{tr} over this temperature range, whilst at low oxygen partial pressure the two oxygen transport parameters show higher temperature dependency. Activation energies of $\widetilde{D}$ and K_{tr} over the temperature range 600-800 °C at various oxygen partial pressures are listed in Table 4.6, revealing quite low activation energies for both processes compared to previous works [2,21,32]. As a result, very fast oxygen transport kinetics in the investigated samples can be confirmed.

P_{O_2} (atm)	GBCO (eV)		GBCN03 (eV)		GBCN06 (eV)		GBCF03 (eV)		GBCF06 (eV)	
	$E^a_{\widetilde{D}}$	$E^a_{K_{tr}}$	$E^a_{\widetilde{D}}$	$E^a_{K_{tr}}$	$E^a_{\widetilde{D}}$	$E^a_{K_{tr}}$	$E^a_{\widetilde{D}}$	$E^a_{K_{tr}}$	$E^a_{\widetilde{D}}$	$E^a_{K_{tr}}$
0.206	0.29	0.10	0.12	0.38		0.46	0.18	0.38	0.08	0.08
0.05			0.13	0.44	0.16	0.26	0.13	0.49	0.17	0.19
0.03		0.25	0.16	0.72	0.19	0.26	0.37	0.85	0.25	0.25
0.01	0.09	0.59	0.32	0.84	0.30	0.28	0.24	0.71	0.35	0.33
1×10^{-3}	0.21	1.25	0.57	1.14	1.03	0.64	0.80	1.08	1.05	0.77
5×10^{-4}	0.42	1.38	0.68	1.06	0.81	0.94	0.85	1.08	1.14	0.84

Table 4.6 Activation energies of $\widetilde{D}$ and K_{tr} at various oxygen partial pressures

Oxygen transport in defective perovskite oxides is generally considered to occur via vacancy-hopping mechanism. The diffusivity of oxygen is thus related to the extent of oxygen nonstoichiometry exhibited by the oxide. For a material with prevailing electronic conductivity, as the investigated materials in this work, knowing the chemical diffusion coefficient and the oxygen nonstoichiometry as a function of temperature and oxygen partial pressure, it is possible to calculate other parameters describing the oxygen transport such the vacancy and self-diffusion coefficient using corresponding thermodynamic factors [5,6,18,19,45].

Theoretically, the ionic conduction can be deduced from the Nernst-Einstein relation:

$$\sigma_{ion} = \frac{\left(z_O F\right)^2 \mathrm{D^*C_O}}{RT} \tag{4.29}$$

where $z_O F$ represents the electrical charge of an oxygen mole. D* and C_O are the tracer self-diffusion coefficient and the concentration of oxide ions, respectively. The chemical diffusion coefficient can be related to the tracer self-diffusion coefficient with thermodynamic factor γ following the relation [43,47]

$$\widetilde{D} \approx \gamma \times D^* \tag{4.30}$$

$$\gamma = \frac{1}{2RT} \times \frac{\partial \mu_{O_2}}{\partial \ln \mathrm{C_O}} = \frac{1}{2} \times \frac{\partial \ln P_{O_2}}{\partial \ln \mathrm{C_O}} \tag{4.31}$$

where μO_2 is the oxygen chemical potential, P_{O_2} is the oxygen partial pressure. Experimentally, the chemical diffusion coefficients can be obtained by electrical conductivity relaxation, and the thermodynamic factor can be obtained by thermogravimetric analysis (TGA). By assuming the oxygen oxygen ion concentration as proportional to the oxygen content 5+δ [43,46,48], the thermodynamic factors

could be derived from $\gamma = 1/2\left(\partial \ln P_{O_2} / \partial \ln\left(5+\delta\right)\right)$ by fitting the oxygen nonstoichiometry data in section 4.3.1, from 700 to 800 °C over the oxygen partial pressure range from 10^{-3} atm – air, as listed in Table 4.7.The measured values lies in the range 50-100.

T (°C)	GBCO	GBCN03	GBCN06	GBCF03	GBCF06
800	56 ± 1	102 ± 2	111 ± 2	67 ± 4	64 ± 2
750	67 ± 3	87 ± 3	91 ± 2	60 ± 1	58 ± 2
700	69 ± 2	78 ± 2	80 ± 4	57 ± 1	51 ± 2

Table 4.7 Thermodynamic factors γ from 10^{-3} atm – air as a function of temperature

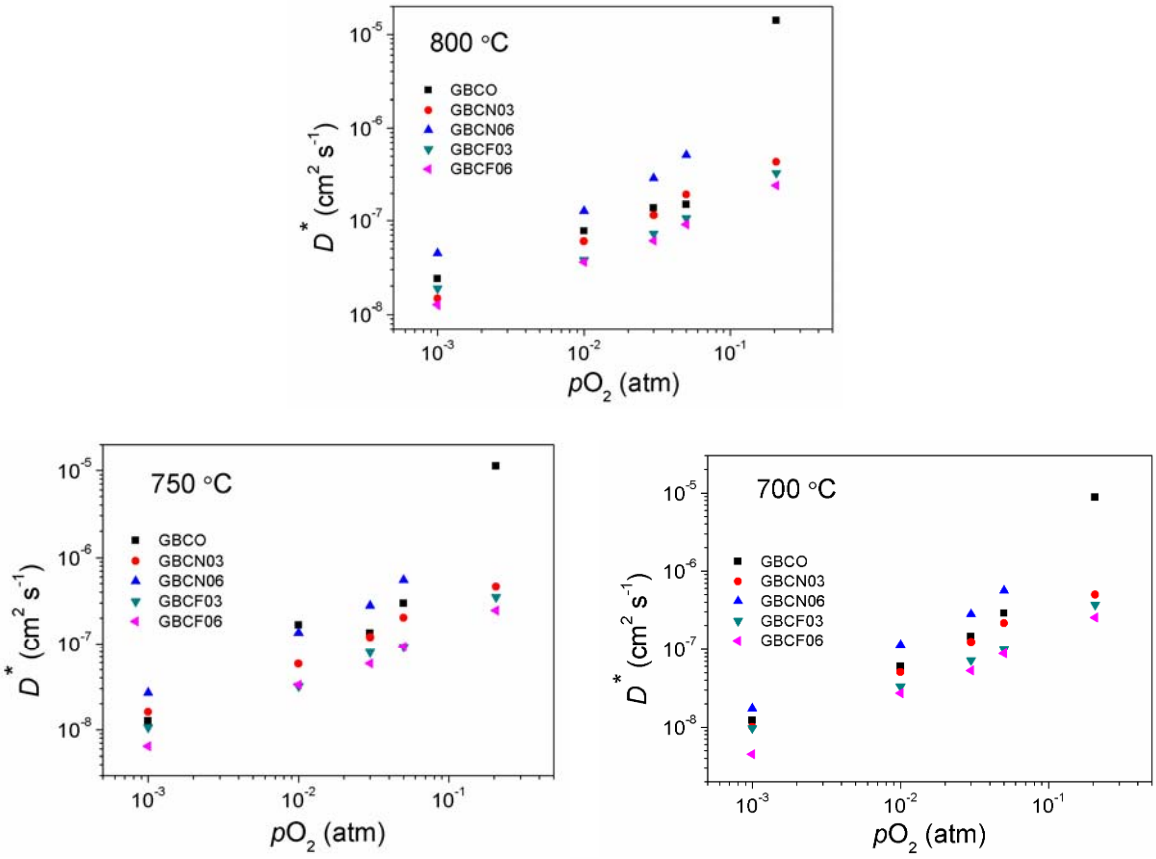

Figure 4.13 *Tracer self-diffusion coefficients D^* calculated from chemical diffusion coefficients and thermodynamic factor obtained in this work*

The tracer self-diffusion coefficients for the five investigated compositions were calculated as shown in ***Figure 4.13***. It seems that with the Fe substitution, the calculated tracer self-diffusion coefficient decrease over the investigated temperature range, in accordance with the trend for chemical diffusion coefficient. But this is in contrast to the expectation that the higher oxygen vacancies introduced by Fe substitution should facilitate the oxygen ion diffusion. Nevertheless, compared to the self diffusion coefficient for the dense sample of pure GBCO, which was determined from the depth profiles obtained with the IEDP technique in combination with SIMS analysis by Tarancón *et al* [49], the tracer diffusion coefficient obtained in this work shows still significantly higher values, *e.g.* $D^* = 8.85\times10^{-6} \sim 2.4\times10^{-7}$ $cm^2\,s^{-1}$ at 700 °C in this work compared to $D^* = 1.3\times10^{-9}$ at 686 °C in their study, due the high chemical diffusion coefficients measured here.

4.3.3.3 Experimental limitations and propositions

The reliability of $\widetilde{D}$ and K_{tr} obtained, however, should be examined carefully. From the practical experiences, both errors from the fitting and experimental procedures should be taken into account.

In fact, the $\widetilde{D}$ and K_{tr} values from the fitting procedure are to some extend related to the input fitting parameters, and are extremely sensitive to the input flush time. The low signal to noise ratio also plays an important role, especially at relative high temperature and high oxygen partial pressure with small P_{O_2} step change, which makes it difficult to precisely identify the starting point of relaxation process.

For the ideal conductivity relaxation measurement, higher the density is, more reliable the results will be. Unfortunately, none of the studied samples in this work is of high density in excess of 95%, due to the distortion of bar-shape sample during the sintering process. Consequently, the surface of sample is difficult to avoid the existence of porosity even being polished by very thin sand paper.

In addition, degradation at the surface of the samples is confirmed by XRD measurement for all the five samples. After slightly polishing the surface, the degraded layer could be easily removed and the bar samples remain their original phases, therefore the surface degradation is supposed to mainly affect K_{tr} coefficient. Moreover, after the relaxation measurement, a remarkable decrease in the electrical conductivity for bar sample was observed for GBCO sample as shown in Figure under identical air condition, which could be attributed to the degradation from either the surface or the Au electrode during long-time measurement.

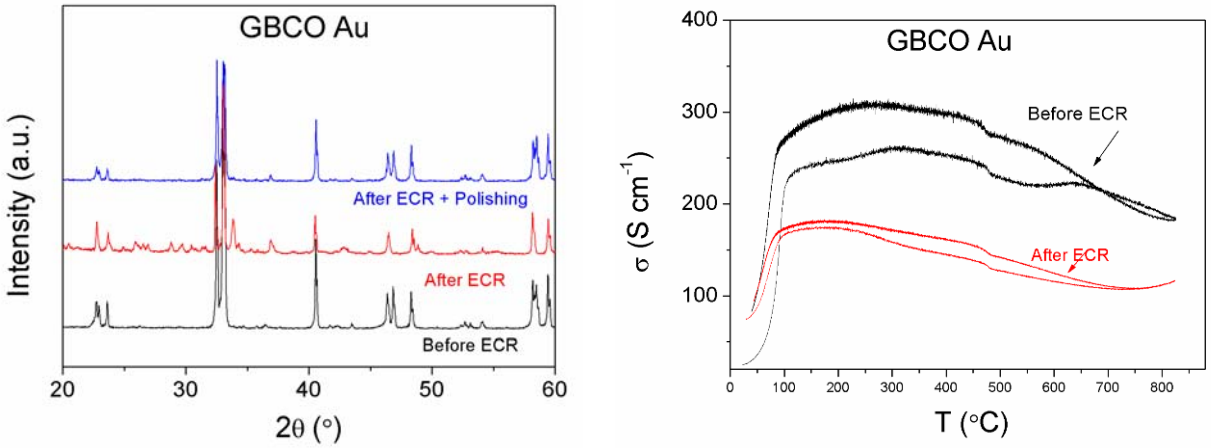

Figure 4.14 *Surface phase transition and degradation of electrical conductivity observed in GBCO bar sample*

Based on these discussions, several optimizations could be considered with respect to acquire reliable oxygen diffusion coefficients and effective surface exchange coefficients from conductivity relaxation experiment.

1) Utilizing bar sample cut off from a sintered big pellet instead of being formed in bar shape before sintering, with following careful polishing as smoothly as possible.

2) Optimizing the mounting of apparatus in the system in order to diminish the reactor volume in order to obtain the flush time much shorter than the relaxation time.

3) Increasing the stepwise changes in oxygen partial pressure at high P_{O_2} in order to obtain good signal to noise ration, which requires adjusting the gas control equipments.

4.4 Conclusion

The oxygen nonstoichiometry at high temperature has been measured by thermogravimetry analysis (TGA) as a function of oxygen partial pressure, meanwhile the thermodynamic factor γ is obtained by the linear regression over the investigated P_{O_2} ranges. It has been confirmed that the Fe substitution gives rise to decrease of oxygen content at high temperatures, whereas the materials show a tetragonal structure with two-dimensional distribution of oxygen vacancies.

The total electrical conductivity has been measured by four-probe AC method under air as a function of temperature. It seems that the Fe substituted samples show a decrease in conductivity with increasing Fe proportion. Nevertheless, over the temperature range of 300-800 °C, all the investigated materials have a total electrical conductivity larger than 100 S cm^{-1}, strongly supporting the potential for cathode materials in IT-SOFCs at the operation temperature. The measurements of electrical conductivity as a function of oxygen partial pressure at constant temperatures indicate a *p*-type metallic-like behaviour for all the materials at high temperature after the order-disorder phase transition. The decrease of conductivity attributes to the consumption of electron holes by the generation of oxygen vacancies from the external reaction with atmosphere.

The oxygen transport kinetics has been investigated by electrical conductivity relaxation measurement. The chemical diffusion coefficients and surface exchange coefficients were obtained by fitting the transient re-equilibrium in electrical conductivity following a stepwise change of surrounding atmosphere. Based on the obtained $\widetilde{D}$ and K_{tr} values over the investigated temperature ranges, all the five materials could be taken as fast oxygen ion conductors. Both temperature and oxygen partial pressure dependences have been observed, as well as very small activation energies for both $\widetilde{D}$ and K_{tr}. Moreover, the tracer-self diffusion coefficients have been calculated by using the thermodynamic factors. It should be noticed that the values of $\widetilde{D}$ and K_{tr} values, as well as D^*, obtained in this work are significantly higher compared to previous work on GBCO, which makes it necessary to examine carefully the reliability of these kinetics, due to the experimental limitations such as sample density, surface condition, large reactor volume, especially the noises in conductivity signal and surface degradation. Thus, some suggestions to improve the electrical conductivity measurement have been proposed for further works.

The Ni substitution does not show obvious influence on neither electrical conductivity nor oxygen transport. On the contrary, the Fe substitution which increase the oxygen nonstoichiometry at the investigated temperatures was supposed to enhance the electrical or electrochemical properties shows inverse results throughout these measurement. For example, the GBCF06 possesses the highest oxygen vacancies concentrations, which is supposed to favour the oxygen diffusion, shows lowest electrical conductivity and chemical diffusion coefficient. Nevertheless, this needs further investigation with improved experimental setup in order to avoid or diminish the external influence such as sample density and signal quality.

REFERENCE

[1] Haoshan, H.; Lu, Z.; Yingfang, W.; Shijiang, L.; Xing, H. Journal of Rare Earths 2007, 25, 275-281.

[2] Taskin, A. A.; Lavrov, A. N.; Ando, Y. Progress in Solid State Chemistry 2007, 35, 481-490.

[3] Adler, S. B.; Lane, J. A.; Steele, B. C. H. J. Electrochem. Soc. 1996, 143, 3554-3564.

[4] Mantzavinos, D.; Hartley, A.; Metcalfe, I. S.; Sahibzada, M. Solid State Ion. 2000, 134, 103-109.

[5] Van Der Haar, L.; Den Otter, M.; Morskate, M.; Bouwmeester, H.; Verweij, H. J. Electrochem. Soc. 2002, 149, J41.

[6] Lane, J. A.; Benson, S. J.; Waller, D.; Kilner, J. A. 11th International Conference on Solid State Ionics (SSI-11) 1997, 201-208.

[7] Lankhorst, M. H. R. a. B., H.J.M. J. Electrochem. Soc. 1997, 144, 4.

[8] Lane, J. A.; Kilner, J. A. In 12th International Conference on Solid State Ionics; Elsevier Science Bv: Halkidiki, Greece, 1999, p 997-1001.

[9] Yasuda, I.; Hishinuma, M. Journal of Solid State Chemistry 1996, 123, 382-390.

[10] Yasuda, I.; Hishinuma, M. Solid State Ion. 1995, 80, 141-150.

[11] Yasuda, I.; Hishinuma, M. Journal of Solid State Chemistry 1995, 115, 152-157.

[12] Yasuda, I.; Hikita, T. J. Electrochem. Soc. 1994, 141, 1268-1273.

[13] Ten Elshof, J.; Lankhorst, M.; Bouwmeester, H. J. Electrochem. Soc. 1997, 144, 1060.

[14] Haar, L. M. v. d.; Otter, M. W. d.; Morskate, M.; Bouwmeester, H. J. M.; Verweij, H. J. Electrochem. Soc. 2002, 149, J41-J46.

[15] Ma, B.; Balachandran, U.; Park, J. H.; Segre, C. U. Solid State Ion. 1996, 83, 65-71.

[16] den Otter, M. W.; Bouwmeester, H. J. M.; Boukamp, B. A.; Verweij, H. J. Electrochem. Soc. 2001, 148, J1-J6.

[17] Crank, J. The mathematics of diffusion; Oxford University Press, USA, 1979.

[18] Yoo, J.; Verma, A.; Wang, S.; Jacobson, A. J. J. Electrochem. Soc. 2005, 152, A497-A505.

[19] Bouwmeester, H.; Den Otter, M.; Boukamp, B. J. Solid State Electrochem. 2004, 8, 599-605.

[20] Otter, M. W. d., 2000.

[21] Choi, M. B.; Jeon, S. Y.; Lee, J. S.; Hwang, H. J.; Song, S. J. Journal of Power Sources 2010, 195, 1059-1064.

[22] Tsvetkov, D. S.; Sereda, V. V.; Zuev, A. Y. Solid State Ion. 2010, 180, 1620-1625.

[23] Tarancon, A.; Marrero-Lopez, D.; Pena-Martinez, J.; Ruiz-Morales, J. C.; Nunez, P. Solid State Ion. 2008, 179, 611-618.

[24] Dalslet, B. T.; Søgaard, M.; Bouwmeester, H. J. M.; Hendriksen, P. V. Solid State Ion. 2009, 180, 1173-1182.

[25] Park, C. Y.; Jacobson, A. J. J. Electrochem. Soc. 2005, 152, J65-J73.

[26] Søgaard, M.; Vang Hendriksen, P.; Mogensen, M. Journal of Solid State Chemistry 2007, 180, 1489-1503.

[27] Lankhorst, M. H. R.; ten Elshof, J. E. Journal of Solid State Chemistry 1997, 130, 302-310.

[28] Hjalmarsson, P.; Søgaard, M.; Hagen, A.; Mogensen, M. Solid State Ion. 2008, 179, 636-646.

[29] Taskin, A. A.; Lavrov, A. N.; Ando, Y. Phys. Rev. B 2005, 71, 28.

[30] Kopcewicz, M.; Khalyavin, D.; Troyanchuk, I.; Szymczak, H.; Szymczak, R.; Logvinovich, D.; Naumovich, E. J. Appl. Phys. 2003, 93, 479-486.

[31] Maignan, A.; Martin, C.; Pelloquin, D.; Nguyen, N.; Raveau, B. Journal of Solid State Chemistry 1999, 142, 247-260.

[32] Taskin, A. A.; Lavrov, A. N.; Ando, Y. Appl. Phys. Lett. 2005, 86, 3.

[33] Frontera, C.; García-Muñoz, J. L.; Llobet, A.; Aranda, M. A. G. Phys. Rev. B 2002, 65, 180405.

[34] Pena-Martinez, J.; Tarancon, A.; Marrero-Lopez, D.; Ruiz-Morales, J. C.; Nunez, P. Fuel Cells 2008, 8, 351-359.

[35] Zhang, K.; Ge, L.; Ran, R.; Shao, Z.; Liu, S. Acta Materialia 2008, 56, 4876-4889.

[36] Li, N.; Lu, Z.; Wei, B. O.; Huang, X. Q.; Chen, K. F.; Zhang, Y. Z.; Su, W. H. Journal of Alloys and Compounds 2008, 454, 274-279.

[37] Bharathi, A.; Yasodha, P.; Gayathri, N.; Satya, A. T.; Nagendran, R.; Thirumurugan, N.; Sundar, C. S.; Hariharan, Y. Phys. Rev. B 2008, 77, 8.

[38] Taskin, A. A.; Lavrov, A. N.; Ando, Y. Phys. Rev. B 2006, 73, 121101.

[39] Taskin, A. A.; Ando, Y. Physical Review Letters 2005, 95, 176603.

[40] Tang, Y. K.; Almasan, C. C. Phys. Rev. B 2008, 77, 5.

[41] Stevenson, J. W.; Armstrong, T. R.; Carneim, R. D.; Pederson, L. R.; Weber, W. J. J. Electrochem. Soc. 1996, 143, 2722-2729.

[42] Zuev, A.; Petrov, A.; Vylkov, A.; Tsvetkov, D. Journal of Materials Science 2007, 42, 1901-1908.

[43] Mauvy, F.; Bassat, J. M.; Boehm, E.; Dordor, P.; Grenier, J. C.; Loup, J. P. In 8th International Conference on Electronic Ceramics and Their Applications (ELECTROCERAMICS VIII); Elsevier Sci Ltd: Rome, ITALY, 2002, p 1265-1269.

[44] Kim, S.; Wang, S.; Chen, X.; Yang, Y.; Wu, N.; Ignatiev, A.; Jacobson, A.; Abeles, B. J. Electrochem. Soc. 2000, 147, 2398-2406.

[45] Wang, S.; van der Heide, P. A. W.; Chavez, C.; Jacobson, A. J.; Adler, S. B. Solid State Ion. 2003, 156, 201-208.

[46] Girdauskaite, E.; Ullmann, H.; Vashook, V. V.; Guth, U.; Caraman, G. B.; Bucher, E.; Sitte, W. Solid State Ion. 2008, 179, 385-392.

[47] Bassat, J. M.; Petitjean, M.; Fouletier, J.; Lalanne, C.; Caboche, G.; Mauvy, F.; Grenier, J. C. Applied Catalysis A: General 2005, 289, 84-89.

[48] Mauvy, F.; Bassat, J. M.; Boehma, E.; Dordor, P.; Loup, J. P. Solid State Ion. 2003, 158, 395-407.

[49] Albert Tarancón, S.; Chater, R.; Hernández-Ramírez, F.; Kilner, J. Journal of Materials Chemistry 2007, 17.

Chapter 5 Conclusion

Summary

This work is mainly concerned with the mixed conducting double layered perovskite $GdBaCo_2O_{5+\delta}$ which has been investigated as potential cathode materials for solid oxide fuel cells operating in the intermediate to low temperature range, aiming to improve the electrode performance by Ni and Fe substitution for Co as well as better understand the oxygen transport properties in these materials and the oxygen reduction performance for cathode application.

Firstly $GdBaCo_{2-x}M_xO_{5+\delta}$ (M=Ni or Fe, x = 0.1, 0.2 …) have been synthesized trough different methods, and highly substituted compounds with solubility until x = 0.8 for both Ni and Fe cases are obtained by either modified gel combustion process or microwave-assisted combustion route. Finally, five composition were selected for further investigation with x = 0, 0.3, 0.6, as GBCO, GBCN03, GBCN06, GBCF03 and GBCF06 for short.

Detailed crystal structural information was obtained by Rietveld refinement on the X-ray powder diffraction data. By increasing Fe substitution, an orthorhombic (P4/mmm, $a_p \times a_p \times 2a_p$) to tetragonal (P4/mmm, $a_p \times a_p \times 2a_p$) phase transition was shown when x >0.4, whilst Ni substitution seemed to enhance the orthorhombic distortion. Combined with the oxygen contents determined by iodometry and thermogravimetric for air-annealed samples, showing Fe substitution decreased the oxygen content, this observed phase transition could be related to the oxygen re-odering caused by Fe substitution. DSC results showed that both Ni and Fe substitution could reduce the temperature for the high temperature phase transition, except those GBCF compound exhibiting already tetragonal phase at room temperature. A particular case was found in GBCF06, for which no phase transition was observed through DSC, but temperature dependent XRD showed a tetragonal-orthorhombic-tetragonal in the temperature range 100-300 °C.

In addition, the thermal expansion coefficients were calculated based on the evolution of structural parameters as a function of temperature extracted from refinement of XRD data. Ni substitution was shown to decrease the TEC, while the Fe substitution showed the inverse. However, the obtained TECs are still too large compared to those of currently used electrolytes such as CGO applied in this work.

Electrochemical characterization have been carried out with different configurations to evaluate the electrode performance in GBCO and Ni, Fe-substituted GBCM (M=Ni, Fe) and also to understand the oxygen reduction reaction taking place on these materials. Symmetric cells on CGO electrolytes were fabricated trough screen-printing deposition and measured under both air and reducing atmosphere. However, SEM showed some negative electrode morphologies, such as big electrode grains and poor electrode thickness (~10 μm) which could possibly lower the cathode performance and contribute to the large ASR values obtained in this work.

Under air condition; with the decrease of temperature, transfer process at the electrode/electrolyte interface, which is usually represented as impedance spectra arcs at high frequency, became predominant, especially for Fe-substituted GBCF. This gives rise to the assumption that Fe substitution might enhance the oxygen charge transfer process, by introducing higher oxygen vacancy concentration in combination with the higher level of oxygen nonstoichiometry caused by Fe substitution. In all cases, the whole oxygen reduction reaction is co-limited by the interfacial charge transfer process with very weak P_{O_2} dependence, and the oxygen surface exchange or/and solid state diffusion on cathode, which is associated with variation of reaction order m. With respect to the possible species involved and high ionic conduction in this series of materials, oxygen surface absorption/desorption involving atomic oxygen and bulk diffusion are supposed to dominate rather than surface diffusion along the electrode to electrode/electrolyte interface or the gas phase diffusion. Both Ni and Fe doping has increased the electrode polarisation resistance compared with the pristine GBCO, which is in agreement with the single cell tests of GBCO and GBCF by A. Kulka using same electrode materials fabricated in this work. With proton conducting electrolyte $La_{0.995}Ca_{0.005}NbO_4$, the electrode performance is limited by the ionic charge transfer process especially at low temperature range, due to fact that the protons are the major charge carrier and dominate the low temperature ionic conducting which could be enhanced by the presence of water vapour. Comparatively large polarisation resistance values and low electrolyte conductivity are obtained due to the poor interfacial connectivity observed by SEM.

The oxygen nonstoichiometry at high temperatures has been measurement by thermogravimetry analysis (TGA) as a function of oxygen partial pressure, meanwhile the thermodynamic factor γ is obtained by the linear regression over the investigated P_{O_2} ranges. It has confirmed that the Fe substitution give rise to an increase of oxygen nonstoichiometry at high temperatures, whereas the materials show a tetragonal structure with two-dimensional distribution of oxygen vacancies. The

overall electrical conductivity in air exhibits a low temperature metal-insulator transition as well as a *p*-type metallic-like behaviour at high temperature, which was confirmed by the measurements of electrical conductivity as a function of oxygen partial pressure at constant temperatures. A remarkable decrease in overall conductivity with increasing Fe proportion was observed. Nevertheless, over the temperature range of 300-800 °C, all the investigated materials have a total electrical conductivity larger than 100 S cm^{-1}, being suitable for cathode materials in IT-SOFCs at the operating temperature.

An electrical conductivity relaxation measurement system has been mounted to investigate the oxygen transport kinetics using dense bar sample. Unfortunately, identical high density was not achieved, thus low density value and discrepancy between different samples require careful examination for the reliability of fitted results. Based on the chemical diffusion coefficients $\widetilde{D}$ and surface exchange coefficients K_{tr} values obtained from fitting the experimental data over the investigated temperature ranges, all the five materials could be taken as fast oxygen ion conductors. In addition, both temperature and oxygen partial pressure dependences have been observed, as well as very small activation energies for $\widetilde{D}$ and K_{tr}. Moreover, the tracer-self diffusion coefficients have been calculated by using the thermal dynamic factors. The obtained values of $\widetilde{D}$ and K_{tr}, as well as D^*, in this work are comparatively significant, even orders of magnitudes higher than the results from previous work on GBCO, possibly due to the inconsistent sample density, large reactor volume or bad signal and noise. .

In general, the Ni substitution does not show obvious influence on neither electrical conductivity nor oxygen transport. On the contrary, the Fe substitution which increased the oxygen nonstoichiometry at the investigated temperatures was initially supposed to enhance the electrical and electrochemical properties, but finally it shows inverse results throughout these measurements. For example, the GBCF06 possesses the highest oxygen vacancies concentrations, which were supposed to have high concentration of electron holes, was firstly assumed to favour the oxygen bulk diffusion and electrical conductivity, respectively. In the contrast, lowest electrical conductivity values and chemical diffusion coefficient have been obtained for GBCF06. Nevertheless, this needs further investigation with improved experimental setup in order to avoid or diminish the external influence such as sample density and signal quality.

Perspectives

Further studied could be devoted to improve in several ways.

Firstly, the evaluation of oxygen transport kinetics concerns more experimental optimizations, including ameliorating the measurement system such adoption of small reactor or elimination of signal noise, and also fabrication of identical samples. Referring to results in this work, considered oxygen diffusion and surface exchange rate could be expected.

Even Ni substitution was proved to be able to reduce the TEC to some extend, generally its effect is still far from the requirement matching other cell components, especially the electrolyte. Thus, morphology optimization seems to be necessary. Firstly, the electrode should be deposited with thicker layers than those used in this work, for example ~15-30 μ m, to proved sufficient active zone for the oxygen reduction reaction. Also, the precursor powders of electrode materials is suggested to be well ball milled to get smaller grain size, and in conjunction with processing control, larger specific surface on electrode could be obtained, providing increasing gas/electrode interfaces for oxygen incorporation. In addition, utilization of interlayer between electrolyte and electrode or composite electrodes is still promising technology.

As Ni and Fe have been test as substitution for Co, and different influences on the investigated properties are obvious in evidence. Some other transition metals which haven been used as B-site substation in perovskites and RP structure oxide compounds could also be considered, such as Cu, Mn, and Cr.